Towards Compact Laser-Driven Neutron Sources

A numerical study of liquid leaf targets for high repetition rate laser experiments and neutron production using deep learning.

Zur Erlangung des Grades eines Doktors der Naturwissenschaften (Dr. rer. nat.)
Genehmigte Dissertation von Benedikt Schmitz aus Büren
Tag der Einreichung: 28.03.2023, Tag der Prüfung: 27.06.2023

1. Gutachten: Prof. Dr. rer. nat. Oliver Boine-Frankenheim
2. Gutachten: Prof. Dr. rer. nat. Markus Roth
Darmstadt, Technische Universität Darmstadt

TECHNISCHE UNIVERSITÄT DARMSTADT

Electrical Engineering and Information Technology Department

Particle Acceleration and Electromagnetic Fields

Accelerator Physics

Towards Compact Laser-Driven Neutron Sources
A numerical study of liquid leaf targets for high repetition rate laser experiments and neutron production using deep learning.

Accepted doctoral thesis by Benedikt Schmitz

Date of submission: 28.03.2023
Date of thesis defense: 27.06.2023

Darmstadt, Technische Universität Darmstadt

Bitte zitieren Sie dieses Dokument als:
URN: urn:nbn:de:tuda-tuprints-243356
URL: http://tuprints.ulb.tu-darmstadt.de/24335
Jahr der Veröffentlichung auf TUprints: 2023

Dieses Dokument wird bereitgestellt von tuprints,
E-Publishing-Service der TU Darmstadt
http://tuprints.ulb.tu-darmstadt.de
tuprints@ulb.tu-darmstadt.de

Für Josef.

Erklärungen laut Promotionsordnung

§ 8 Abs. 1 lit. c PromO

Ich versichere hiermit, dass die elektronische Version meiner Dissertation mit der schriftlichen Version übereinstimmt.

§ 8 Abs. 1 lit. d PromO

Ich versichere hiermit, dass zu einem vorherigen Zeitpunkt noch keine Promotion versucht wurde. In diesem Fall sind nähere Angaben über Zeitpunkt, Hochschule, Dissertationsthema und Ergebnis dieses Versuchs mitzuteilen.

§ 9 Abs. 1 PromO

Ich versichere hiermit, dass die vorliegende Dissertation selbstständig und nur unter Verwendung der angegebenen Quellen verfasst wurde.

§ 9 Abs. 2 PromO

Die Arbeit hat bisher noch nicht zu Prüfungszwecken gedient.

Darmstadt, 28.03.2023

Benedikt Schmitz

Abstract

More than 20 years ago, the first ion acceleration experiments were performed using Target Normal Sheath Acceleration (TNSA). Most TNSA experiments relied on low repetition rates and fixed foil targets. Recent technological advances have enabled the development of laser-plasma accelerators with high repetition rates. The core aspect of the high repetition rate is gas or liquid-based targets, of which the liquid leaf target seems particularly promising. Despite the potential to achieve high repetition rate laser pulses for TNSA, the predictive capabilities of the proposed Liquid Leaf target remain limited.

This research investigates the plasma generated by a Liquid Leaf target and its interaction with any laser using particle-in-cell simulations. A surrogate model is developed to predict the full spectrum of the generated beam and the maximum ion energy. This model also allows numerical optimization of the experiment. A surrogate model for the neutron yield is also developed based on Monte Carlo simulations and artificial neural networks. Combining these models makes it possible to determine the potential of a compact laser-driven neutron source.

Optimizing a laser plasma experiment is performed as an example for two different optimization conditions, focusing on maximizing the proton yield. The optimized solutions utilize an effect caused by different ions, oxygen, and hydrogen, propagating in the same expanding plasma. These ions interact, causing spectra to deviate from plasma expansion models. This effect can be predicted and applied to other applications outside neutron production.

The neutron model allows comparing different designs of compact neutron sources. This allows determining the particle numbers and repetition rates required to make laser-driven neutron sources competitive. Since simulations are insufficient for real-world applications, a new method is proposed to improve data analysis using radiochromic film stacks. The method uses algorithmic solutions to reduce operator inaccuracy while increasing the evaluation speed, allowing Big Data analysis of laser-plasma acceleration data to be performed soon.

Zusammenfassung

Vor mehr als 20 Jahren wurden die ersten Ionenbeschleunigungsexperimente mit der Target Normal Sheath Acceleration (TNSA) durchgeführt. Die meisten dieser TNSA Experimente beruhen auf niedrigen Wiederholungsraten und festen Folientargets. Jüngste technologische Fortschritte haben es ermöglicht, Laser-Plasma-Beschleuniger mit hoher Repetitionsrate zu entwickeln. Der Kernaspekt für die hohe Repetitionsrate sind auf Gas oder Flüßigkeiten basierende Targets, von dem das Liquid Leaf-Target besonders vielversprechend erscheint. Trotz des Potenzials, Laserpulse mit hoher Repetitionsrate für TNSA zu erzielen, sind die Vorhersagemöglichkeiten des vorgeschlagenen Liquid Leaf-Targets nach wie vor begrenzt.

In dieser Forschungsarbeit wird das von einem Liquid Leaf-Target erzeugte Plasma und seine Wechselwirkung mit einem beliebigen Laser mit Hilfe von Particle-in-Cell-Simulationen untersucht. Es wird ein Ersatzmodell entwickelt, um das gesamte Spektrum des erzeugten Strahls und die maximale Ionenenergie vorherzusagen. Dieses Modell ermöglicht auch eine numerische Optimierung des Experiments. Auf der Grundlage von Monte-Carlo-Simulationen und künstlichen neuronalen Netzen wird außerdem ein Ersatzmodell für die Neutronenausbeute entwickelt. Die Kombination dieser Modelle ermöglicht, das Potential einer kompakten lasergetriebenen Neutronenquelle zu bestimmen

Die Optimierung eines Laser-Plasma-Experimentes wird exemplarisch für zwei verschiedene Optimierungsbedingungen durchgeführt, wobei der Schwerpunkt auf der Maximierung der Protonenausbeute liegt. Die optimierten Lösungen nutzen einen Effekt, der durch verschiedene Ionen, Sauerstoff und Wasserstoff, verursacht wird, die sich im selben expandierenden Plasma ausbreiten. Diese Ionen wechselwirken untereinander, sodass die Spektren von Plasmaexpansionsmodellen abweichen. Dieser Effekt kann vorhergesagt und auf andere Anwendungen außerhalb der Neutronenproduktion angewendet werden.

Das Neutronenmodell ermöglicht es verschiedene Designs kompakter Neutronenquellen zu vergleichen. Damit werden die erforderlichen Teilchenzahlen und Wiederholungsraten bestimmt, damit lasergetriebene Neutronenquellen wettbewerbsfähig werden. Da Simulationen für reale Anwendungen nicht ausreichen, wird eine neue Methode zur Verbesserung der Datenauswertung unter Verwendung radiochromatischer Filme vorgeschlagen. Die Methode nutzt algorithmische Lösungen zur Verringerung der Ungenauigkeit durch den Operateur und erhöht gleichzeitig die Auswertegeschwindigkeit, was in naher Zukunft die Durchführung von Big-Data-Analysen von Laser-Plasma-Beschleunigungsdaten ermöglicht.

Contents

1. Introduction

"Pleasure to me is wonder – the unexplored, the unexpected, the thing that is hidden and the changeless thing that lurks behind superficial mutability."
– H.P. Lovecraft

In recent years, there has been growing interest in developing compact, high-intensity neutron sources for various applications ranging from materials science and engineering, via nuclear medicine, to homeland security applications. Compact laser-driven ion accelerators are promising candidates for compact high-intensity neutron sources. These sources use lasers to accelerate protons or deuterons, which collide with a target material to produce neutrons via nuclear reactions.

Compactifying Ion Acceleration

Conventional radio-frequency-based particle accelerators have played a significant role in advancing fields such as physics, biology, and medicine since the 1930s, and they still belong to some of the largest and most complex machines ever built (Livingston 1980) (Bryant 1994) (Crockcroft et al. 1932). These conventional accelerators are restricted to specific sizes for needed energy and beam parameters. A major limiting factor is the accelerating field, which is limited by the resonator's material. Superconducting niobium based cavities can reach up to $35\,\mathrm{MV\,m^{-1}}$ (Padamsee et al. 1998, Sec. 13.2) while normal conducting copper cavities can reach up to $100\,\mathrm{MV\,m^{-1}}$ (CLIC et al. 2018, Sec. 1, Sec. 3.2.1). An accelerating field, several orders of magnitude larger, can be reached if acceleration is induced inside a plasma, which does not have similar boundaries.

The acceleration in a plasma relies on the capability to heat the plasma as quickly and efficiently as possible. The development of chirped pulse amplification by Donna Strickland and Gérard Mourou in 1985 (Strickland et al. 1985) paved the way to high intensity and high energy short pulse laser systems, which enable this kind of acceleration. Strickland and Mourour received the Nobel prize in 2018 for their work on chirped pulse amplification.

The resulting high-power laser system allowed the acceleration of ions from the laser-plasma interaction via different mechanisms. One of those mechanisms – Target Normal Sheath Acceleration (TNSA) – was measured first by Snavely et al. in 2000 (Snavely et al. 2000). TNSA accelerates ions from a plasma with a high acceleration gradient in the order of $10^6\,\mathrm{MV\,m^{-1}} \sim \mathrm{TV\,m^{-1}}$ Some centimeters of acceleration space can acquire the same energy as hundreds of meters long conventional accelerators.

This process has some disadvantages, though. One of which is the resulting exponential ion spectrum. It complicates beam transport and its subsequent usage in applications that need well-defined energies, such as ion therapy (Katayama et al. 2022) (Eickhoff et al. 2003) (Schardt et al. 2010) (Linz et al. 2007) or as an injector for conventional accelerators (Aymar et al. 2020).

A first application for which these ion beams could be used is a compact neutron source, which converts most if not all ions to neutrons independent of the beam quality (Katayama et al. 2022) (Favalli et al. 2019) (Kleinschmidt et al. 2018) (Roth, Jung, et al. 2013). The disadvantage of having an exponential spectrum does not matter in this case, and the high beam current becomes favorable for a maximized neutron yield.

Advanced Scientific Tools with Neutrons

James Chadwick first discovered neutrons in 1932 (Chadwick 1932). In the decades since their discovery, neutrons have been used in a wide range of scientific research, from understanding the fundamental properties of materials to exploring the structure of biological molecules.

One of the earliest applications of neutrons was in nuclear physics, where they were used to study the structure of atomic nuclei. In the 1940s and 1950s, researchers began using neutron scattering to study the structure of materials, including metals and polymers (Hahn et al. 1939). The first neutron scattering experiment was conducted in 1946 by Clifford Shull and Ernest Wollan, who used neutrons to study the crystal structure of a single crystal of zinc sulfide (Shull et al. 1948).

The development of more powerful neutron sources in the 1960s and 1970s, such as the high-flux reactor at the Institute Laue-Langevin (ILL) in France, allowed researchers to use neutrons to study the structure and behavior of a broader range of materials, including complex biological molecules. It led to the development of several scattering methods, such as small-angle scattering and reflectometry using neutrons. Refer for a detailed discussion to (Ashkar et al. 2018, and the sources therein). In addition to neutron scattering, neutrons are used in various other analysis methods, such as neutron activation analysis and neutron radiography. While activation analysis can be used to identify the elemental composition of a sample, radiography is used to create images of the internal structure of objects.

Neutrons are an important tool for industrial and scientific applications because they have unique properties that allow them to probe the structure and composition of materials in ways other probes cannot. Neutrons have no electrical charge, which makes them ideal for studying the structure of materials without altering their electrical properties. Ions would change the electrical properties through ion implantation (Ziegler 1988). No charge means no Coulomb interaction, such that the only reaction possible is with the nucleus of an atom with the strong nuclear force.Although they have no charge, they have a non-vanishing magnetic momentum and a non-zero spin. These traits make them useful for various magnetic and structural studies (Lakey 2009, and the sources therein). Since neutrons can be produced with a large range of energies the spectrum of possible applications is also enlarged further. High energy neutrons can penetrate deep into dense matter, such as metals and concrete, which allows for testing and imaging areas where no gamma ray has imaged before. This makes neutrons invaluable for various industrial and scientific applications, including material science, biology, semiconductor and microelectronics, oil and gas exploration, quality control, and nuclear reactors.

1.1. The Demand and Supply Mismatch in the European Neutron Landscape

Neutrons are an essential tool, and the demand for neutrons is not only high but increasing. A study by Gutberlet et al. evaluated the peer-reviewed publications for neutrons scattering experiments and found that Europe's scientific community published $42\,689$ peer-reviewed articles from 2005 to 2015 (Gutberlet et al. 2018, Fig. 2). This is more than half of all publications worldwide about neutron scattering in the respective time frame ($81\,307$) and therefore underlines the importance of the neutron landscape in Europe.

How does this split up into research area, and how does the field behaves after 2015? To answer this, the published data of a representative of the neutron-producing facilities is investigated. Due to the well-documented publication counts, the Heinz Maier-Leibnitz Zentrum's (MLZ) research neutron reactor FRM II is selected as a field representative. The information from the corresponding annual reports can be split into different counts and estimate a trend from 2015 to 2021. The publication trend for the source increases over the years until 2021, as displayed in Figure 1.1b. This figure also shows the split between Grand Challenges, Keys Technologies, and Basic Research MLZ. Figure 1.1c shows the three areas split into the more complex fields it comprises. Considering the trend of the displayed data, it can be deduced that demand for neutron radiation for experimentation will continue to increase in the following years.

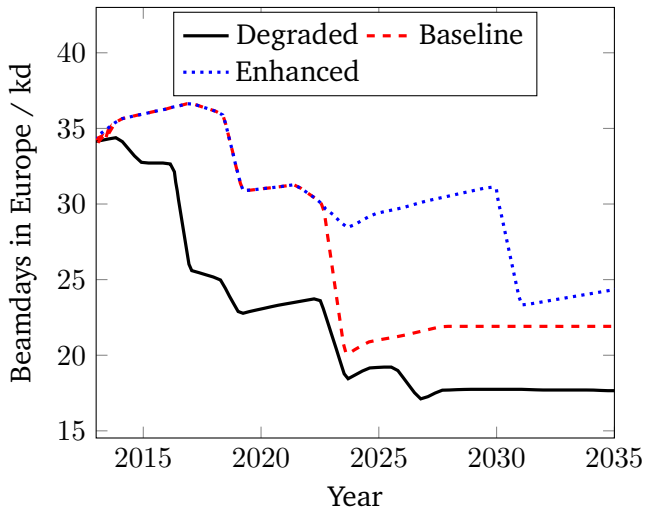

(a) Prediction of the available beam days for neutron radiation in Europe. Three potential scenarios are displayed. The explanation for each scenario is given in the text.

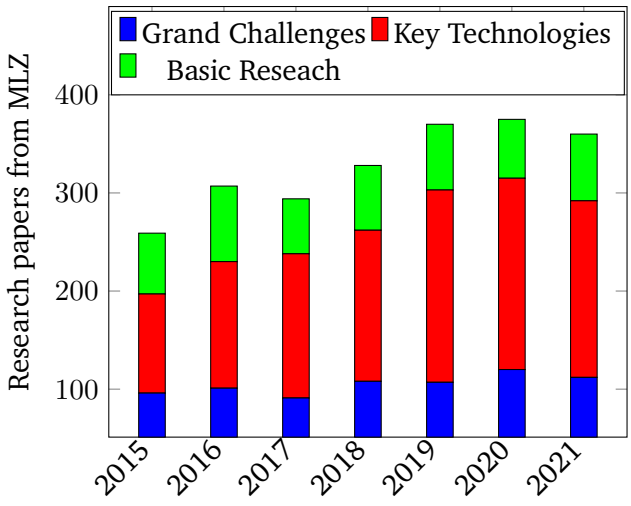

(b) Publication count for the MLZ. Yearly reports discriminate neutron radiation paper counts into the three given categories.

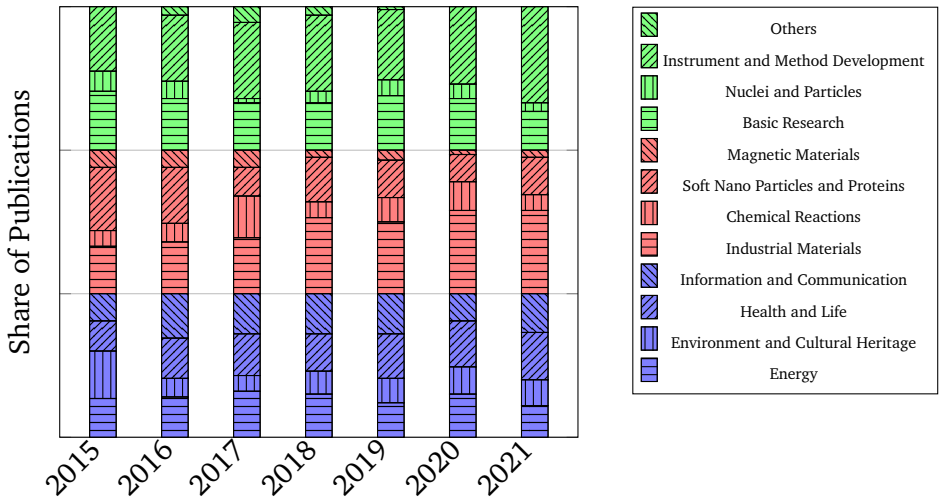

(c) Indicators on how many peer-reviewed articles are submitted in which field for neutron applications. The data is for the FRM II HML neutron source and is taken as representative of the field. Each color with different shades corresponds to a mono-colored bar in (b). The sum of each color type – greenish, reddish, blueish – is normalized to its count.

Figure 1.1.: The decreasing neutron supply (a) and indicator for the increase in demand (b) and (c). Data for (a) taken from (ESFRI Physical Sciences and Engineering Strategy Working Group - NeutronLandscape Group 2015, pp. 66-77). Data for (b) and (c) taken from (FRM II – Forschungs-Neutronenquelle Heinz Maier-Leibnitz 2016, pp. 126-127),(FRM II – Forschungs-Neutronenquelle Heinz Maier-Leibnitz 2017, pp. 96-97),(FRM II – Forschungs-Neutronenquelle Heinz Maier-Leibnitz 2018, pp. 110-111), (FRM II – Forschungs-Neutronenquelle Heinz Maier-Leibnitz 2019, pp. 96-97),(FRM II – Forschungs-Neutronenquelle Heinz Maier-Leibnitz 2020, pp. 106-107),(FRM II – Forschungs-Neutronenquelle Heinz Maier-Leibnitz 2021, pp. 94-95),(FRM II – Forschungs-Neutronenquelle Heinz Maier-Leibnitz 2022, pp. 100-101).

This, on the one hand, underlines the diverse range of applications of neutron radiation. On the other hand, many applications are part of research topics such as environmental research, energy research, or industrial applications, none of which will decrease demand in the following years. If further innovation for neutron applications shows up, the demand will increase further.

Although the demand increases, reactor-based neutron sources are successively being shut down. This reduces the number of available beam days for neutron-based experiments. Three cases of the predicted beam days in Europe can be found in Figure 1.1a. Some facilities of the European research landscape are currently under construction or are being expanded; even if they are finished in time and the run time of some reactors is prolonged, the decrease can not be compensated. Three scenarios for available beam times were investigated in (ESFRI Physical Sciences and Engineering Strategy Working Group - NeutronLandscape Group 2015, pp. 66-77). The Enhanced scenario assumes Institute Laue-Languvin (ILL) operation until 2030 and European Spallation Source (ESS) operation with 35 instruments beyond 2035. The Baseline scenario assumes ILL operation at the full output until 2023 and ESS operation with 22 instruments beyond 2028, while the Degraded scenario assumes ILL operation at the reduced output until 2023 and ESS operation with only 22 instruments beyond 2028 while more reactors are shut down.

Considering different conditions for the operation of large-scale neutron sources, all three predicted scenarios have a net beam day loss in the order of thousand beam days. To counteract and close the emerging gap, small, compact, fast-to-construct, and easy-to-operate neutron sources are needed.

Fill the Void with Compact Laser-Driven Neutron Sources

The proposed solution's concept for decentralized compact neutron sources is sketched in Figure 1.2a, where the relevant degrees of freedom are visible. Different energy spectra can be used based on the acceleration mechanism, either mono-energetic particle bunches from conventional or exponential or varying shapes from laser-driven accelerators. On one side, the spectrum of incoming ions can vary to a large degree, depending on the accelerator and the converter can also have any arbitrary shape. To grasp the physical situation, a photograph of a laser-based neutron source during interaction is presented in Figure 1.2b.

More applications for neutron radiation have been discussed recently, resulting in a higher demand for neutrons despite the mentioned loss in beam days. These applications include integrity tests for concrete bridges or buildings, nuclear waste management and test of castor integrity, or homeland security application at airports or customs (Nakai et al. 2010; Alvarez et al. 2014). These innovative applications need small, portable devices that provide high-quality neutron radiation.

Accelerator-based neutron generators are normally used in a pitcher-catcher configuration (Mima et al. 2022, Ch. 2, Fig. 2) as displayed in Figure 1.2b and Figure 1.2c. The accelerator is pitching ions, which are then converted into neutrons. Neutrons can not be directly accelerated since they have no charge and only exist inside a nuclear bound (Krieger 2018, Sec. 13.1 and 13.5.3). Therefore, a large amount of energy has to be transmitted onto the neutron to split this bound and pass kinetic energy. The full setup is sketched in Figure 1.2c.

1.2. Outline of the Thesis

This thesis deals with the modeling and physical optimization of a setup for compact laser-driven neutron sources that can achieve high repetition rates and therefore become competitive with the yield of conventional sources while being smaller.

Chapter 2 explains the fundamental physics and lays the foundations to understand the subsequent system and its behavior. At first, the laser-based acceleration processes are displayed and TNSA with its relevant physics is discussed. Then, the fundamental physics of nuclear conversion and the relevant traits of the neutron converters are discussed.

Chapter 3 gives the necessary concepts about the numerical methods used in the course of the thesis. The first point is the particle-in-cell method, followed by the Monte Carlo method for nuclear reactions. Followed by definitions and descriptions of artificial neural networks and how they can be used for surrogate modeling. The chapter closes with a section on sensitivity analysis.

Chapter 4 shows how the Maxwell-Vlasov set of equations can be simplified and its relevant dimensionality can be reduced. Furthermore, a developed model for the cut-off energy is displayed.

Chapter 5 addresses the main problem of surrogate modeling with artificial neural networks; how to get consistent data. It expands on measuring laser-accelerated beams via radiochromic film stacks and introduces a procedure to evaluate a large data set consistently. The procedure developed evaluates a detailed data set and uses simulated data to test and ensure its validity.

Chapter 6 models the surrogates for the ion accelerations and the neutron production. Their traits and sensitivities are discussed, and a case study for the optimization is presented. It further introduces a parameter that has to be measured experimentally to fit the model onto a real machine.

Chapter 7 concludes the thesis. It reviews the surrogates developed, correlates several observations from different chapters with each other, and discusses the application of the developed models in real-world applications. It finally outlines the next steps for a more precise model to achieve a full design study.

1.3. Scientific Contribution

The summary of the scientific contributions of this thesis is given below. Further references to papers and codes are given in the corresponding chapters and the bibliography.

Development of a Tool for Automatized Data Evaluation for Radiochromic Film Based Particle Spectra

Data-driven modeling for laser-accelerated ions was, until now, not possible for the full particle spectrum. A tool and an innovative evaluation method for radiochromic film stacks were developed and published. It allows evaluating these stacks with a constant bias despite the current individual bias of each user. This enables comparable data sets over a large number of data and further accelerates the evaluation, allowing more data to be evaluated and revisited.

Development of a Liquid Leaf Surrogate Model from Particle In Cell Simulations

An extensive simulations study of ample parameter space was done for the high repetition system utilizing a liquid leaf target. This allowed determining a surrogate based on this data and deriving optimum working points under variable conditions. It is further possible to evaluate the importance of the parameters from the total variation, allowing for global insights into the physics of the spectrum and cut-off energy formations of laser-accelerated ions.

Development of a Surrogate Model for Thick Target Yields of Neutrons

A second surrogate model maps any arbitrary light ion spectrum to neutron yields. It is based on an extensive data set based on nuclear Monte Carlo simulations. Due to its generality, it is a valuable model for comparing different accelerator concepts with the same assumptions and cross-sections. This comparability is essential to check the efficiencies of different setups to minimize bias and variations from individual numerical configurations. For this model, a Monte Carlo-like setup was developed and implemented to map the uncertainty of the input data to the model's final predictions.

First optimization results for Neutron Yields from Ion Beams from Liquid Leaf Targets

The combination of the different surrogates allows to design and predict parameters for a compact neutron source with an arbitrary amount of conditions. A first suggestion for a working point is made and its limitations are discussed.

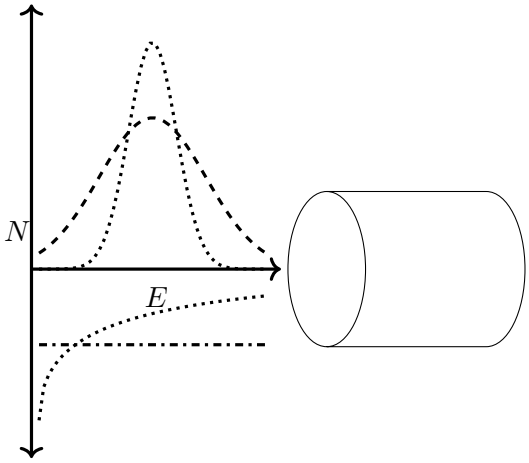

(a) Generalized compact neutron source with light ions. The curves on the left display several different possibilities of ion bunch spectra to be used. The cylinder represents the neutron converter. Particle count N is mirrored at the E axis to clearer plot different shapes more and is always positive as indicated by both arrows.

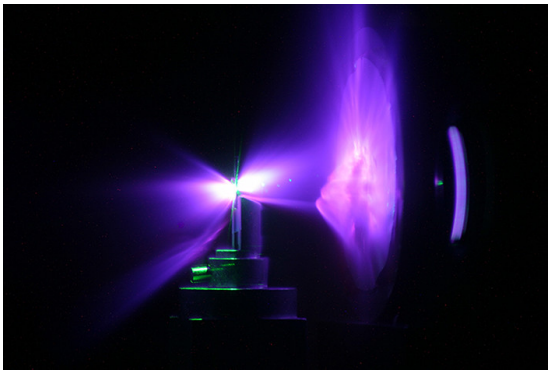

(b) Experimental neutron production at Los Alamos National Lab. Laser target interaction is visible in the center of the image; the neutron converter is visible on the right. Courtesy of Markus Roth.

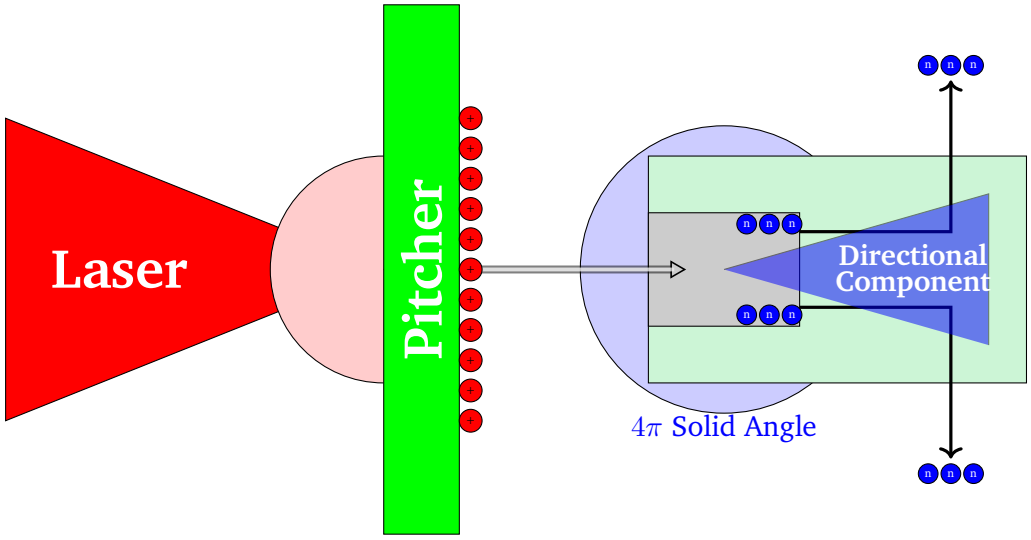

(c) Pitcher catcher representation for a laser-driven ion source. The laser comes from the left and hits a plasma target (Pitcher). The laser heats the system, and ions are accelerated. They impinge on the catcher, where the ions convert to neutrons. Two neutron components are displayed, a homogeneous 4π distributed component, and a directional superposed element in the forward direction. The neutron flux is moderated by a moderator surrounding the catcher; changes in the moderator's geometry do allow for adjustment of the final spectrum.

Figure 1.2.: Overview about the concept for a compact neutron source and its implementation using laser-driven ion acceleration.

2. Physical Fundamentals

"Our best ideas are often those that bridge between two different worlds."
– Marvin Minsky

Laser-driven particle accelerators are a new branch of particle acceleration technology that overcomes the limitation of acceleration field gradients. They are generally capable of creating much higher acceleration fields of $10^6\,\mathrm{MV\,m^{-1}}$ compared to classical particle accelerators with some $\mathrm{MV\,m^{-1}}$. This allows much shorter accelerators but also has complications, as shown in the following section.

Several acceleration methods have emerged utilizing lasers, which have been tailored for different particle species. This is done before an in-depth discussion on laser-based ion acceleration. All are based on the Lawson–Woodward theorem (Lawson 1975) (Sprangle et al. 1996), which states that an electromagnetic wave can accelerate particles if at least one of the following conditions is violated:

i) The electromagnetic field exists in a vacuum with no boundaries present.

ii) The particle is highly relativistic ($v \approx c$) along the acceleration path.

iii) No additional static electric fields are present.

iv) The expansion of the wave is infinite.

In the case investigated here, real laser pulses are applied. These real pulses have a finite spatial size, follow a Gaussian-like intensity distribution, and are also limited in time. Furthermore, particles are supposed to be part of a plasma. Therefore, the condition that a boundary-free vacuum exists is also not fulfilled. The intensities of the investigated lasers are also so high not only the electric field but also the magnetic field has to be taken into account ($I\lambda_\mu^2 \approx 10^{17}\,\mathrm{W\,\mu m^2\,cm^{-2}}$) (Kruer et al. 1985, Eq. 1). Assuming furthermore that in a natural system, the target starts "cold" either as part of a liquid or a solid target negates the condition of the highly relativistic movement. This allows several flavors or types of laser-driven particle acceleration (section 2.1). As will be shown, most of them rely on the acceleration of particles from a plasma. Therefore, traits for this principle will be given as well (section 2.2) just before the relevant process is described in detail (section 2.3).

2.1. Laser Acceleration Schemes

An implemented system violates at least one condition of the Lawson Woodward Theorem. Violating the conditions ii) and iv) can be achieved by using a laser to irradiate matter to accelerate particles.

Properties of Laser-Induced Electromagnetic Waves

Electromagnetic waves created by "Light Amplification by the Stimulated Emission of Radiation" (short LASER) have the traits of being monochromatic, directional and coherent (Sigrist 2013, Sec. B 3) (Demtröder 2016,

Ch. 8). Monochromatic means that the wavelength contains only one central wavelength λ_L and a very small bandwidth of superposing wavelengths $\Delta\lambda_L$, in an ideal case $\Delta\lambda_L = 0$. Directional means that it is emitted in a specific direction with a narrow size inside the focus. Coherent means that all waves in the laser pulse are in phase in space and time. Utilizing the chirped pulse amplification (Strickland et al. 1985) method allows the laser to reach highest intensities which results in creating hot plasmas from solid or liquid matter and triggering the processes that result in particle acceleration. The following section will briefly describe some of these to complement the field and the detailed ion acceleration discussion.

A real laser pulse is the sum of the different frequency components the laser generates. The amplified spontaneous emission is strongly damped for modern laser systems, so it is irrelevant compared to the main pulse. Pre-pulses are preceding the main pulse and have a lower intensity. They are created through multiple reflections and nonlinear coupling (Keppler, Sävert, et al. 2015) (Didenko et al. 2008). An example pulse is displayed in Figure 2.1.

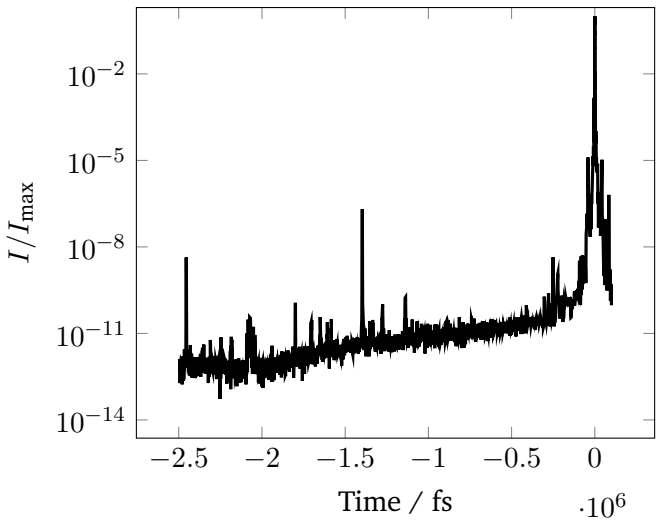

Figure 2.1.: PHELIX contrast spectrum from shot database with number 20180905. The full spectrum has a length of 2.5 ns, while the main pulse (at $t = 0$) has a length of around 500 fs and 200 Joule beam energy.

Dielectric Laser Acceleration

Dielectric laser acceleration is an acceleration scheme that utilizes the deformation of electrical fields inside a dielectric structure. The field distribution of the electric field can be varied and optimized by introducing dielectric structures. These structures can be varied and implemented to use accelerator components for electrons, additionally violating condition i). (Schmickler 2020, pp. 265-284) (Niedermayer et al. 2021) (Egenolf 2020) It is important to note that the laser field is not supposed to destroy the structure and hence needs low-intensity laser light. DLAs can reach arbitrary high energies, enabling high-energy beam target interactions for a high-energy collider. The major limitation for DLA is the bunch current, which is limited to a maximum of $7.3\,\mathrm{fC}$ per bunch (Egenolf 2020). This maximum bunch current is too low and, together with the necessary staging, is a disadvantage if not even a show stopper for using compact neutron sources based on the electron-target interactions.

Wakefield Acceleration

Wakefield Acceleration is a type of particle acceleration for electrons based on a plasma. The idea is that a plasma wave is excited, accelerating electrons in the plasma. This plasma wave can be excited by either a laser pulse and its corresponding ponderomotive force or by an external particle beam injected into the plasma. Therefore, the literature distinguishes between laser-driven wakefield accelerators (LWFA) and particle-driven wakefield accelerators (PWFA). These accelerators consist of plasma cells containing gas. The gas is pre-ionized, for example, using a high-voltage discharge just before the wave is excited. Due to construction, repetition rates of up to $0.5\,\mathrm{kHz}$ were already achieved (He et al. 2013). Details about this type of acceleration can be found, for example, in the proceeding of the CERN accelerator school on high wakefield accelerators (Schmickler 2020).

Ion Acceleration

A laser can be used to accelerate ions from plasmas. The starting point is a solid state, a liquid, or a gaseous target. Irradiating the target with a high-intensity laser ionizes the existing atoms and heats the target. The energy deposited while heating up is deposited in the electrons, which drive the acceleration process inside the plasma. Depending on the laser parameters, this dynamic process deviates for different intensities and target densities. The Target Normal Sheath Acceleration (short TNSA) is a process thoroughly investigated and is therefore the acceleration type, discussed in this thesis. A detailed discussion of the TNSA process is given in section 2.3.

2.2. Fundamentals of High Energy Density Physics

Plasma-based acceleration relies on the understanding of the relevant basic quantities and concepts of plasma physics. This will be presented concisely in the following section together with an explanation of the most important processes for the subsequent laser-plasma interaction.

2.2.1. Basic Plasma Quantities

A plasma is a state of matter that contains ions and their freed electrons. The degree of the ion's ionization is in general non homogeneous and is a result of the different processes to be presented. In contrast to conventional gas, collective effects govern the dynamics of a plasma. These collective effects are a direct result of the long-range Coulomb interaction due to the material's ionization. While a gas molecule is electrically neutral and only interacts via collisions, plasma ions, and electrons do interact via the Coulomb interaction.

If an additional charge is introduced, this charge gets screened over a specific distance. This length scale after which the charge effect is not measurable anymore is called Debye length. The Debye length can be derived from the system's Poisson equation (Piel 2017, Ch. 2.2.1) and is given as

$$\frac{1}{\lambda_D^2} = \underbrace{\frac{e^2 n_{e0}}{\varepsilon_0 k_B T_e}}_{1/\lambda_{De}^2} + \underbrace{\frac{Z^2 e^2 n_{i0}}{\varepsilon_0 k_B T_i}}_{1/\lambda_{Di}^2}, \tag{2.1}$$

where ε_0 is the vacuum permittivity, Z the ion's charge number, e the elementary charge, k_B Boltzmann's constant, $n_{\alpha 0}$ and T_α are the particle density and the temperature of the ions and electrons respectively. In many cases, the ion temperature is low compared to the hotter electron temperature, which allows the ion's term to be dropped. If a system with several ion species is investigated the ion term is substituted by a sum.

Assuming a non-isothermic plasma makes it necessary to consider different temperatures for the different ion species. This modifies the equation to

$$\frac{1}{\lambda_D^2} = \frac{e^2 n_{e0}}{\varepsilon_0 k_B T_e} + \sum_j \frac{Z_j^2 e^2 n_j}{\varepsilon_0 k_B T_j} \tag{2.2}$$

$$\lambda_D = \sqrt{\frac{\varepsilon_0 k_B / e^2}{n_e/T_e + \sum_j Z_j^2 n_j / T_j}} \tag{2.3}$$

The plasma appears neutral from the outside for lengths larger than the Debye length. But since the plasma is not neutral over smaller length scales, plasma is said to be quasi-neutral. Overall positive and negative charges must be present in approximately the same number. The quasi-neutrality condition is then

$$\left| \sum_j Z_j e n_{i0,j} - e n_{e0} \right| \ll e n_{e0}. \tag{2.4}$$

The Debye length and particle's thermal velocity can define a characteristic plasma time scale τ. This time scale describes how long electrons need to get to the screening position and how long it needs to screen the plasma. Since ions are heavier and less mobile than electrons, the ion influence can be neglected. Hence, the plasma's time scale and the corresponding plasma frequency can be defined as

$$\omega_{\text{pe}} = \tau^{-1} \approx \frac{v_e}{\lambda_{\text{De}}} = \frac{(k_B T_e / m_e)^{1/2}}{\lambda_{\text{De}}} = \left(\frac{n_{e0} e^2}{\varepsilon_0 m_e} \right)^{1/2}. \tag{2.5}$$

These relations are unique features of a plasma. To show the collective behavior, plasma has to be larger than the Debye length and exist longer than the characteristic time scale τ, otherwise, the collective effects do not manifest. Furthermore, these quantities must be resolved in numerical simulations to model a plasma properly. This gives a physical constraint for the Courant-Friedric-Lewy conditions, which is further discussed in section 3.1.

2.2.2. Laser Plasma Interaction

As plasma dynamics are largely dictated by electron movement, understanding and controlling the electron temperature is essential to control the full process. The temperature increases when more energy is deposited inside the target, leaving the main question open, which processes coupled energy into the plasma and how significant are they?

For an incoming electromagnetic wave, plasma can be described as a boundary condition similar to dielectric materials. Therefore the plasma can be categorized as over- or under-dense respectively. This state is defined by the ratio of the plasma frequency ω_{pe} and the laser frequency ω_L,

$$\omega_{\text{pe}} \begin{cases} < \omega_L & \text{under dense} \\ = \omega_L & \text{critically dense} \\ > \omega_L & \text{over dense.} \end{cases} \tag{2.6}$$

If the system is under-dense, the electromagnetic wave can propagate into the plasma. The plasma behaves slowly compared to the wave's oscillation and the effective refraction index inside the plasma is nonlinear. If the system is over-dense, the plasma boundary behaves like a mirror. If the system is critically dense, incoming

Table 2.1.: Atom densities, full ionization intensities, and critical wavelength for several elements utilized as targets in laser-plasma experiments. The ionization threshold energies were taken from the NIST database (Kramida 2006) all other quantities were calculated by the relations given in this thesis.

Elements	Z	Full Ionisation at /W cm^{-2}	Atom Density n_i in cm^{-3}	comment	λ_c in nm
Hydrogen	01	1.4E14	5.3E22		137
Carbon	06	6.4E18	1.1E23		95
Oxygen	08	3.6E19	∼E19	gaseous	10 000
Silicon	14	1.1E21	4.9E22		143
Copper	29	8.6E22	8.5E22		108
Gold	79	4.8E25	5.9E22		130
Water (H2O)	8+2	6.4E18	3.3E22	molecule	174

light excites evanescent waves in the plasma, getting exponentially damped. Hence, the critical density at which $\omega_p = \omega_L$ characterizes a system,

$$1 \stackrel{!}{=} \frac{\omega_p^2}{\omega_L^2} = \frac{e^2 n_{e0}}{\varepsilon_0 m_e} \cdot \frac{\lambda_L^2}{4\pi^2 c^2} \quad \Rightarrow \quad n_c \simeq 10^{21} \lambda_\mu^{-2} \text{cm}^{-3}, \tag{2.7}$$

where λ_μ is the laser wavelength given in microns. Several densities for some materials relevant to laser-plasma experiments are given in Table 2.1. The incoming laser deposits energy in the plasma. This increases the electron temperature T_e and causes the ionization of atoms.

Ionization

The governing effect for ionization is dependent of the laser's intensity:

$$I_0 \begin{cases} \leq 1 \times 10^{10}\,\text{W cm}^{-2} & \text{impact ionization} \\ \leq 1 \times 10^{12}\,\text{W cm}^{-2} & \text{multi photon interaction} \\ \leq 1 \times 10^{13}\,\text{W cm}^{-2} & \text{tunnel ionization} \\ \geq 1 \times 10^{13}\,\text{W cm}^{-2} & \text{direct ionization} \end{cases} \tag{2.8}$$

The low-intensity part is dominated by collisions, while collision-based ionization can be neglected for high intensities. Both, tunnel and direct ionization, are due to the laser's electric field suppressing the atomic potential barrier. If the electric field suppresses the barrier's threshold E'_{ion} below $0\,$MeV the atom is ionized directly. Otherwise, the tunnel effect allowing an electron to tunnel out of the atom is boosted. This behavior is sketched in Figure 2.2. These relations can be expressed mathematically by superposing the atom's Coulomb potential with the potential of an external electric field, for an ion at position x_0:

$$V(x) = -\frac{1}{4\pi\varepsilon_0} \frac{Ze}{|x_0 - x|} - E_{\text{ext}} x \tag{2.9}$$

The calculation of the extrema yields a local maximum at x_{max}, inserting $V(x_{\text{max}})$ allows to determine the threshold field for direct ionization as well as the intensity needed to achieve this field:

$$E_{\text{ext}} = \frac{E_{\text{ion}}^2}{4Z} \quad \Rightarrow \quad \frac{I_{\text{th}}}{\text{W cm}^{-2}} \approx 4 \times 10^9 \frac{E_{\text{ion}}^4/\text{eV}}{Z^2} \tag{2.10}$$

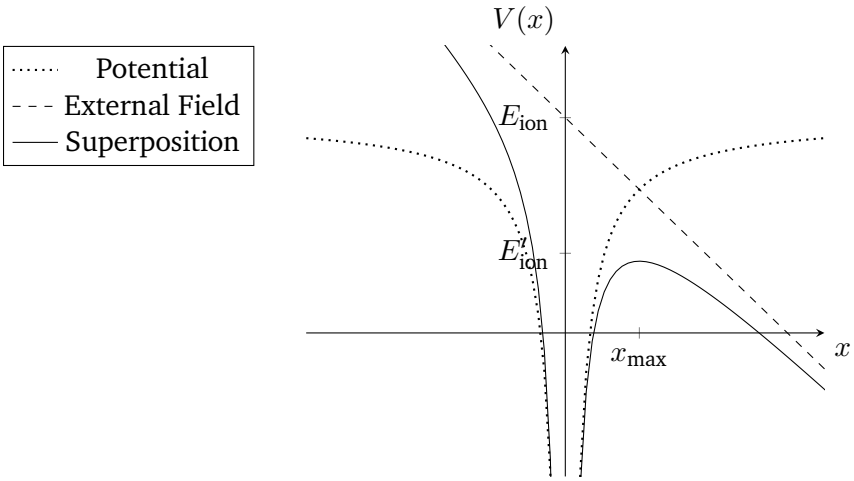

Figure 2.2.: Illustration of the barrier suppression model. The dotted line indicates the undisturbed electric potential, and the dashed lines show the externally applied field which strengthens the potential on one side and weakens the potential on the other. The solid line gives the superposition of both.

2.2.3. Heating Processes

The relevant heating process depends on the specific laser/plasma setup and so far there is no global theory about which process is relevant in which case (Gibbon 2005, Ch. 5.5.6). For this work high laser intensities ($I_L \geq 1 \times 10^{18}\,\mathrm{W\,cm^{-2}}$) are investigated.

In this regime, the particle-particle collision frequency is low and negligible compared to the collision-free processes and the discussion is limited to the collision-free processes. These processes are discussed in this section.

Ponderomotive Force

The acceleration of electrons in the laser field, caused by the spatial and temporal limits of the pulse is a result of the ponderomotive force. Particles in an electromagnetic field experience the Lorentz force

$$\vec{F}_L = q\left(\vec{E} + \vec{v} \times \vec{B}\right), \tag{2.11}$$

where $\vec{E}$ and $\vec{B}$ are the electric and magnetic field of the electromagnetic wave, q and $\vec{v}$ are the particle's charge and velocity respectively. The ponderomotive force results from the electric field strength's gradient along the transverse component of a real laser. It describes the resulting movement of charged particles inside the laser's electric field. It can be derived by time averaging the electric field component of the Lorentz force for the time-constraint laser. Detailed step-by-step derivation can be found in many books on plasma physics (e.g. (Piel 2017, Sec. 3.7.1.) (Gibbon 2005, Sec. 3.2.)), the ponderomotive force is given as

$$\vec{F}_p = -\frac{q^2}{4m\omega_{\mathrm{L}}^2}\vec{\nabla}E_0^2. \tag{2.12}$$

Where ω_{L} is the field's oscillation frequency, e and m are the particle's charge and mass respectively and E_0 is the electric field.

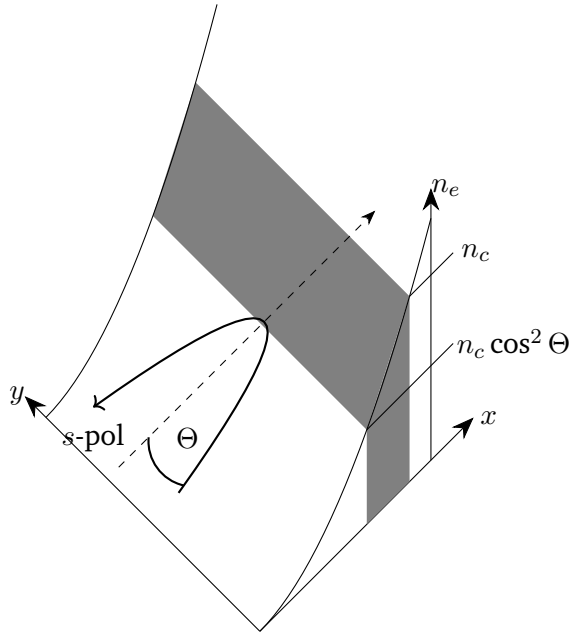

Figure 2.3.: Situation for the laser hitting a pre-expanded target under an angle Θ. The plasma is underdense for most of the domain.

Some remarks concerning the behavior of the ponderomotive force: Firstly, the charge is taken into account with a quadratic dependency, the direction of the force is therefore independent of the particle's charge. Secondly, the particle oscillates with the field's oscillation frequency. Thirdly, the particle drifts along the negative gradient of the squared electric field and therefore towards the region of the lower field. The derivation of the ponderomotive force includes linearization and time averaging of the Lorentz force. This implies that higher-order terms are neglected and only the lower-order electric field contributes.

Relativistic j x B Heating

If the intensity of an electromagnetic wave is high enough, then the higher order terms of the Lorentz force's $\vec{v} \times \vec{B}$-term have to be taken into account as well. This was firstly considered by Kruer and Estabrook (Kruer et al. 1985, Eq. 1) who arrived at the expression for a modified ponderomotive force, including the magnetic field term

$$\begin{aligned} \vec{F}_p &= -\frac{m}{4}\frac{\partial v_{\text{os}}^2(x)}{\partial x}\left[1-\cos\left(2\omega_L t\right)\right]\vec{e}_x \quad \text{inserting} \quad v_{\text{os}} = \frac{q\vec{E}_0(x)}{m\omega_L} \\ &= -\frac{q^2}{4m\omega_L^2}\frac{\partial \vec{E}_0^2(x)}{\partial x}\left[1-\cos\left(2\omega_L t\right)\right]\vec{e}_x \end{aligned} \tag{2.13}$$

where x denotes the longitudinal direction into the plasma direction as indicated in Figure 2.3. The first summand is the regular ponderomotive force, while the second summand introduces a fast oscillating part caused by the magnetic field acting on the charged particles in the longitudinal direction. Further calculations by Wilks et al. (Wilks et al. 1992, Eq. 2, Fig. 3) yield the so-called Ponderomotive Scaling model of the hot electron temperature

$$T_{\text{e}}^{\text{pm}} = m_{\text{e}}c^2\left(\sqrt{1+\frac{a_0^2}{2}}-1\right) \quad \text{with} \quad a_0 = \frac{eE_0}{cm\omega_L} \tag{2.14}$$

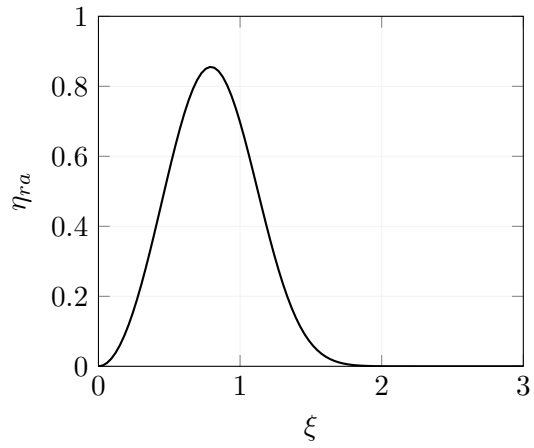

(a) Self-similar solution for the resonance absorption plotted for ξ. The maximum of the curve is at $\xi \approx 0.793$.

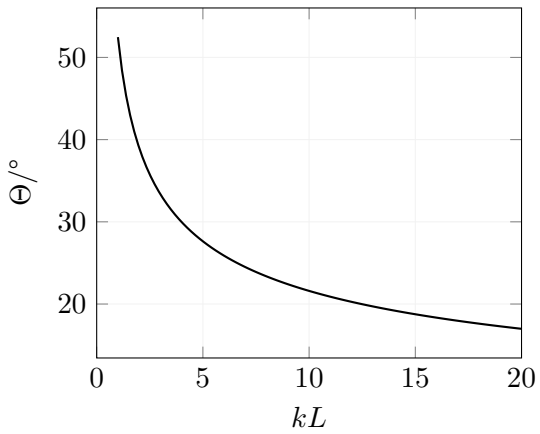

(b) Plot of the maximum absorption angle in dependence of the kL parameter.

Figure 2.4.: Traits of the resonance absorption. The curve for the absorption in (a) and the curve for the ideal absorption angle in (b).

This ponderomotive heating is frequently used as an approximation of the hot electron temperatures, although it has the tendency to overestimate the hot electron temperature (Cui et al. 2013, Eq. 2, Sec. 4), (Kluge et al. 2011, Eq. 9, Fig. 1. Fig 3), (Flacco et al. 2010, Fig. 5), (Cialfi et al. 2016, Fig. 5). Concluding, different heating processes are more dominant in different regimes.

Resonance Absorption

Laser light is generally reflected at the density $n_c \cos\Theta$, where n_c is the critical density and Θ the incidence angle, as displayed in Figure 2.3. An evanescent wave can penetrate the plasma further towards the n_c limit, while p-polarized laser light can trigger waves in the area between $n_c \cos\Theta$ and n_c. The reason for the latter is due to p-polarised waves an electric field component parallel to the gradient of the electron density exists. This field can excite plasma oscillations. The efficiency of this process is dependent on the plasma scale length and the incidence angle. If the scale length is large, then a self-similar solution exists, which depends on the wave vector $k = 2\pi/\lambda_L$ and the scale length $L^{-1} = |\partial_x \ln(N_e)|_{x=x_c}$, where N_e is the number of electrons. The fractional absorption η_{ra} for $kL \gg 1$ can be determined self-similarly as (Gibbon 2005, Ch. 5.5.1.)

$$\eta_{ra} = \frac{1}{2}\left[2.3\xi \exp\left(\frac{-2\xi^3}{3}\right)\right] \quad \text{with} \quad \xi = (kL)^{1/3}\sin\Theta \tag{2.15}$$

η_{ra} is displayed in Figure 2.4a. The ξ value at the maximum is $\xi_{\max} = 0.793$. Solving the ξ identity for the angle $\xi = \xi_{\max}$ allows predicting the ideal angle for the maximal resonance absorption.

Brunel Absorption

Resonance absorption does break down for very steep plasma gradients. If a steep gradient exists and is irradiated by a laser with some electric field component normal to the plasma surface, this component causes electrons to accelerate back and forth around the plasma boundary, heating the plasma during the deceleration inside the plasma. The derivations from Brunel (Brunel 1987, Eq. 10) and Gibbon (Gibbon 2005, Ch. 5.5.2.)

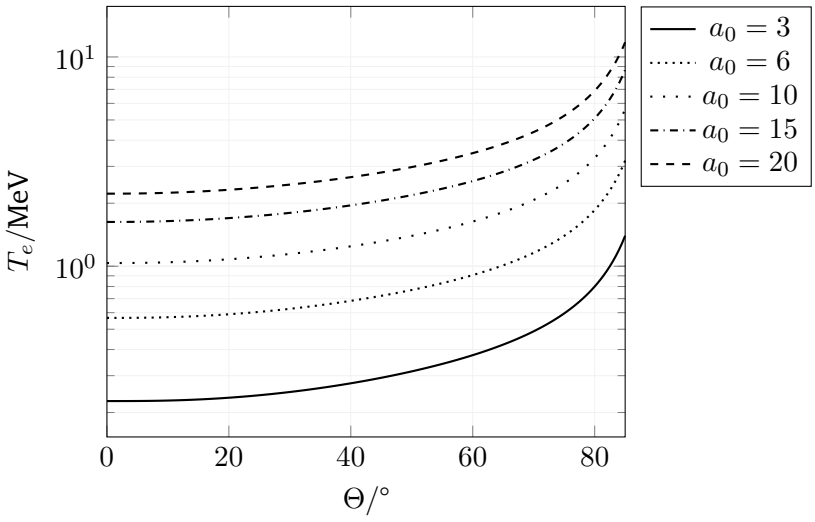

Figure 2.5.: Plot for hot electron temperature T_e for different a_0 values following Equation 2.17. With $C_1 \approx 0.33$ and $C_2 \approx 0.06$.

both result in the same expression for the Brunel absorption η_B as

$$\eta_B = \frac{1}{\pi a_0} f \left[\left(1 + f^2 a_0^2 \sin^2\Theta\right)^{1/2} - 1 \right] \frac{\sin\Theta}{\cos\Theta} \quad \text{with} \quad f = 1 + \sqrt{1 - \eta_a}, \tag{2.16}$$

where f is the field amplification factor and $\eta_a = (4/\pi) a_0 (\sin^3\Theta / \cos\Theta)$ the fractional absorption rate.

Hot Electron Prediction

Cialfi (Cialfi et al. 2016, Eq. 5, Fig. 4) developed a model capable of reproducing the hot electron temperature for many targets. The model combines the ponderomotive scaling with the Brunel absorption weighted by empirically determined values:

$$\begin{aligned} T_e/\text{MeV} = {} & C_1 \times 0.511 \left[\sqrt{1 + \frac{a_0^2}{2}} - 1 \right] \\ & + C_2 \times 0.511 \left[\sqrt{1 + f^2 \frac{a_0^2}{2} \sin^2\Theta} - 1 \right] \tan\Theta, \end{aligned} \tag{2.17}$$

where C_1 and C_2 are the process's empirical weighting factors dependent on the laser and target parameters. They are in good approximation constant for the variation of a_0 but vary for different laser and target parameters and the different simulation dimensions.

2.3. Target Normal Sheath Acceleration

The following section first discusses the physics of TNSA. Secondly, an analytical model for understanding TNSA time evolution will be discussed. The third part explains the basic idea of multi-species interaction. The fourth part considers the beam divergence, while the fifth part focuses on the different types of targets. The final part of this section discusses some further literature about TNSA. Further details and numerous studies

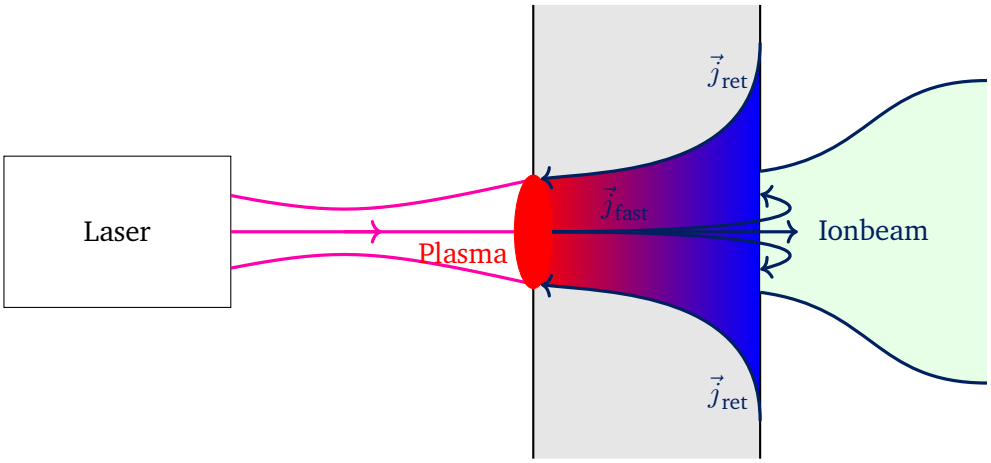

Figure 2.6.: TNSA setup. A high-intensity short-pulse laser hits the target. The target is heated up and electrons start to move along the target and are scattered. Idealized electron trajectories are indicated by black errors. The laser follows a Gaussian profile indicated by the purple lines.

can be found in the literature. Exemplary for these studies are (Roth and M. Schollmeier 2014) (Snavely et al. 2000) (Berglund et al. 1998) (Borghesi et al. 2013) (*Laser-Driven Sources of High Energy Particles and Radiation* 2019, and the sources therein), where the work from Snavely et al. presented the first experimental result measuring TNSA.

Physical Description of the Process

TNSA is a process for the acceleration of ions from a plasma. The process starts, when the target, placed inside a vacuum, from which the ions should be accelerated is irradiated by a short-pulse laser. Short pulse in this context means in the order of ps or shorter. Short pulsed lasers do not follow a single ideal Gaussian distribution. Instead, these pulses follow a complex time and spatial distribution, as mentioned in section 2.1 and exemplary depicted in Figure 2.1. These corrections result in an effective train of pulses hitting the target. The pulses hitting the target before the main pulse hits are generally orders of magnitude smaller than the main pulse. This smaller intensity domain is triggering the first ionization of the target as described in section 2.2.2, which also causes the first expansion of the plasma into the vacuum and therefore creates a plasma in front of the target. The plasma created before the main pulse hits is called pre-plasma.

The main pulse with intensities $\geq 1 \times 10^{18}\,\mathrm{W\,cm^{-2}}$ further ionizes and significantly heats up the plasma. Plasma heating results from several competing processes as described in subsection 2.2.3. As discussed before, plasma heating can be regarded as heating electrons exclusively. The hot electrons can then be characterized by at least one hot electron temperature T_e and the underlying Maxwell-Jüttner distribution (Jüttner 1911b) (Jüttner 1911a). This process's hottest electron's Debye length can be larger than the target's extension. We can estimate the order of magnitude using the approximate electron density of $\eta \cdot n_e \approx \eta \cdot 3.3 \times 10^{23}\,\mathrm{cm^{-3}}$, where η is the number of electrons with high kinetic energy and the result for T_e from Figure 2.5. Assuming a low number of high energy electrons $\eta < 1\,\%$ with a high temperature of $T_e > 2\,\mathrm{MeV}$, the Debye length is $\lambda_{De} > 130\,\mathrm{nm}$. Schollmeier reported in his thesis Debye lengths of a tenth of micrometers, while the targets under investigation are maximal $3\,\mu\mathrm{m}$ thick (M. S. Schollmeier 2009, p. 25). The plasma is neutral at the start of the process, but since the hottest and fastest electrons can leave the target, the plasma gets charged over time.

The hot electron flux through the target creates strong magnetic fields. These magnetic fields need a large

current to be induced and this current is limited by the Alfven limit, which would have to be exceeded during the process (Roth and M. Schollmeier 2016a, p. 233) (Alfvén 1942). Luckily, the plasma can sustain a large current that exceeds the Alvfen limit for a short time scale and short distances. For larger times beam filamentation and subsequent return currents have to be taken into account (Davies 2006). These currents transport electrons from the low-temperature part of the plasma back to the hot spot. They get heated and follow the flow toward the ends of the target, further charging up the plasma. The strong magnetic field created by the flux of hot electrons forces the electrons, leaving the target, onto curved trajectories. These trajectories resemble a fountain as indicated in Figure 2.6.

Over time, the increasing charge of the target and the large fields trap more and more hot electrons, which form an electron sheath behind the target. The hottest and fastest electrons are in the middle of the laser focus which deviates over the full depth of the target and causes an approximately Gaussian electron distribution centered around the projected focus point (M. S. Schollmeier 2009, p. 69).

After a characteristic time for the individual ion species, the corresponding ions also start to move and see the electric field from the charge separation. This field is similar to that of a plate capacitor and allows a first simple estimation of the reached maximum particle energies via the energy transfer in a homogeneous electric field

$$E_{\text{kin}} \propto \frac{q_i^2}{m_i} \tag{2.18}$$

The electron sheath has a finite width and the time that the field is seen can be determined. The ions reaching the sheath first, see the full field and start to screen the electron charge, reducing the effective electric field for all slower ions. The acceleration process's important part is the number of electrons and the charge in the sheath created. Despite the goal of accelerating ions, the process is driven by electron dynamics. For highest intensities of $\sim 10^{24}\,\mathrm{W\,cm^{-2}}$ calculations predict, that ions can be accelerated directly in the laser field enabling higher energies than possible with TNSA, refer to section 4.1 and (*Laser-Driven Sources of High Energy Particles and Radiation* 2019, and the sources therein).

The full process can not be solved analytically and we can give neither an approximate nor a closed solution. Evaluating the full dynamics of the process is only possible by using numerical simulations. Different simulation schemes exist and are valid in different parts of the process, while hydrocodes (Fryxell et al. 2000) (Büchner et al. 2010, and the sources therein) can model and calculate the first part of the process, from laser irradiation over the initial ionization towards the initial heating up, particle-in-cell method, which is described in section 3.1, has to be used to model the main pulse interaction, the particle dynamics, and the time until the acceleration phase is over. The scope of this work is to model the TNSA main pulse interaction until the end of the acceleration phase. Hence particle-in-cell simulations are used, for the initial particle and temperature distributions are chosen to represent the impact of the pre-pulse effect. The dedicated parameters for this are given in subsection 6.1.1.

Several models to describe the acceleration have been developed (Mora 2003) (Mora 2020) (Passoni, Zani, et al. 2014) (Perego, Batani, et al. 2012) (Passoni, Bertagna, et al. 2010). These models reduce the system's dimensionality and either model the situation with a fluid approach or approximate the problem with a static charge separation approach. An alternative as presented in section 2.3.4 relies heavily on experimental data and only reproduces observations. The model used in this work is based on a fluid approach and was developed by Patrick Mora. With this model, several predictions can be made which are consistent with PIC simulations. The model can further be expanded to accommodate several effects observed, as will be presented for multi-species plasmas in subsection 2.3.2. The base model is discussed further which allows quantifying the hot electrons' influence on the ion spectrum and increases the understanding of relevant effects.

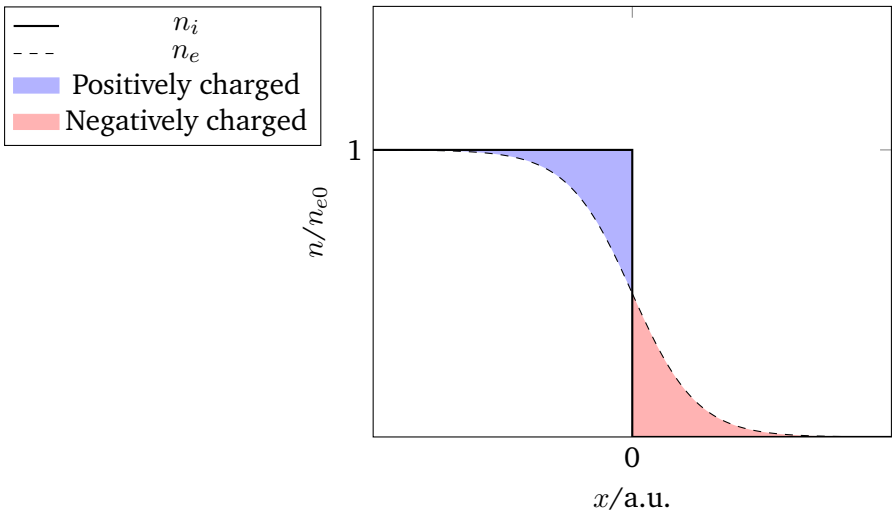

Figure 2.7.: Starting conditions for the charge and particle distribution in Moras model at $t = 0$.

2.3.1. Moras Model

In several publications, Patrick Mora developed models for TNSA ion acceleration (Mora and Thomas M. Antonsen 1997) (Quesnel et al. 1998) (Mora 2003) (Mora 2005) (Mora 2020). The model, discussed here, assumes a simple representation of the plasma expansion into a vacuum, driven by hot electrons (Mora 2003).

The model assumes a one-dimensional, one-species plasma. It consists of one type of cold ions, occupying the half-space $x < 0$, and hot electrons following the Boltzmann distribution with the characteristic hot electron temperature T_e.

$$n_{\mathrm{i}}(x) = \begin{cases} n_{\mathrm{io}} & \text{for } x < 0 \\ 0 & \text{for } x > 0 \end{cases} \qquad \text{and} \qquad n_{\mathrm{e}} = n_{\mathrm{e0}} \exp\left(\frac{e\Phi}{k_B T_{\mathrm{e}}}\right), \tag{2.19}$$

where n_{i0} is the homogeneous distributed ion density, Φ is the electrostatic potential, and k_B Boltzmann's constant.

The expressions above hold for the starting time $t = 0$, it is displayed in Figure 2.7 Taking the equation of motion and the continuity equation allows determining a self-similar solution for the ion expansion in a vacuum. The model yields four core results for the problem, which can be given with some dedicated quantities: Euler's constant is denoted with $\mathfrak{e}$, c_s is the ion's acoustic velocity, and $\omega_{\mathbf{pi}}$ is the ion's plasma frequency. Firstly, the electric field at the ion front position can be calculated by solving Poisson's equation with the given distribution in Equation 2.19. The solution of the full-space integration to acquire the expression for the electric field at the ion front is

$$E_{\mathrm{front}}(t) = \frac{\left(\frac{n_{\mathrm{e0}} k_B T_e}{\varepsilon_0}\right)^{1/2}}{\left(2\mathfrak{e} + \omega_{\mathrm{pi}}^2 t^2\right)^{1/2}} \tag{2.20}$$

Secondly, the velocity of the ion front is given by solving the equation of motion after inserting the given electric field by integrating the field over time from the start $t' = 0$ to the time $t' = t$ as

$$v_{\mathrm{front}}(t) = 2c_s \ln\left(\frac{\omega_{\mathrm{pi}} t}{\sqrt{2\mathfrak{e}}} + \sqrt{\left(\frac{\omega_{\mathrm{pi}} t}{\sqrt{2\mathfrak{e}}}\right)^2 + 1}\right). \tag{2.21}$$

Thirdly, the position of the ion front can be acquired by again integrating the velocity from 0 to t as

$$x_{\text{front}}(t) = 2\sqrt{2\mathfrak{e}} \underbrace{\left(\frac{\varepsilon_0 k_B T_e}{n_{\text{e0}} e^2}\right)^{1/2}}_{=\lambda_{\text{D0}}} \left[\frac{\omega_{\text{pi}} t}{\sqrt{2\mathfrak{e}}} \ln\left(\frac{\omega_{\text{pi}} t}{\sqrt{2\mathfrak{e}}} + \sqrt{\left(\frac{\omega_{\text{pi}} t}{\sqrt{2\mathfrak{e}}}\right)^2 + 1}\right) - \sqrt{\left(\frac{\omega_{\text{pi}} t}{\sqrt{2\mathfrak{e}}}\right)^2 + 1} + 1\right]. \tag{2.22}$$

Fourthly, the energy spectrum is given by the shape dN/dE and the cut-off energy $E_c(t)$

$$\frac{dN}{dE}(E,t) = \frac{n_{\text{i0}} c_s t}{\sqrt{2EZk_BT_e}} \exp\left(-\sqrt{\frac{2E}{Zk_BT_e}}\right) \quad \text{and} \quad E_c = 2Zk_BT_e \left[\ln\left(2\frac{\omega_{\text{pi}} t}{\sqrt{2\mathfrak{e}}}\right)\right]^2 \tag{2.23}$$

c_s is the ion acoustic velocity while ω_{pi} is the ion plasma frequency and $\mathfrak{e}$ is Euler's constant. They are defined by the relations:

$$c_s = \left(\frac{Zk_BT_e}{m_i}\right)^{1/2} \qquad \omega_{\text{pi}} = \left(\frac{n_{\text{e0}} Ze^2}{m_i \varepsilon_0}\right)^{1/2} \tag{2.24}$$

These results are powerful in interpreting numerical and physical experimentation and are widely used. The results are implemented for example in radiochromic film evaluation software (Schmitz, Metternich, et al. 2022) (Schmitz and Endl 2022) or are generally used as reference. It is noteworthy, that the model only takes one ion species into account. Huebl et al. (Huebl et al. 2020) extended the discussion towards a second heavier ion species, showing that the output spectrum varies and effects on the lighter spectrum can be seen. A further addition to the model incorporating an arbitrary number of ion species is, together with a detailed explanation of Huebl et al. model presented in subsection 2.3.2.

2.3.2. Multi Species Effect

As presented in the already mentioned study by Huebl et al. (Huebl et al. 2020) having several particle species in an expanding plasma, these particles interact. This deviates from Mora's exponential particle spectrum of a mono-species plasma by a compression of the lighter ion spectrum.

Starting with Mora's model, each ion species deviates from the others by density, charge, and mass. For each combination, the electric field from the acceleration is constant and applies to all species at once if the plasma is homogeneous. The driving source of the acceleration is the electric field, counteracted by the particles' inertia. As a result of this lower inertia particles are accelerated first, followed by those of higher inertia. The higher inertia particles co-propagate then with the lower energy particles with a lower inertia and both are following the higher energy particles with higher inertia.

The particles interact then via coulomb interaction locally, so the particles of lower inertia get pushed away from the higher inertia particles. This accelerates the low energy low inertia particles causing a compression of the particle spectrum as displayed in Figure 2.8. As displayed, the resulting spectra deviate from the classical Mora in the interaction region. The spectrum for lower energies, where both particle species are co-propagating is not as smooth, because the particles share the acceleration field, which randomizes which particle species gets a kick from the acceleration field. This behavior was also measured by Alejo (Alejo et al. 2014) using a differential Thomson Parabola setup. The spectrum, extracted from the paper is displayed in Figure 2.9. Due to the nature of the experiment, only one species could be measured, but the deviation from an exponential shape is a sufficient indicator for a multi-species effect. The effect is further smoother than the one presented in Figure 2.8, which is due to the lack of transverse moments in the PIC simulations, which will be discussed further in section 3.1 and section 6.1.

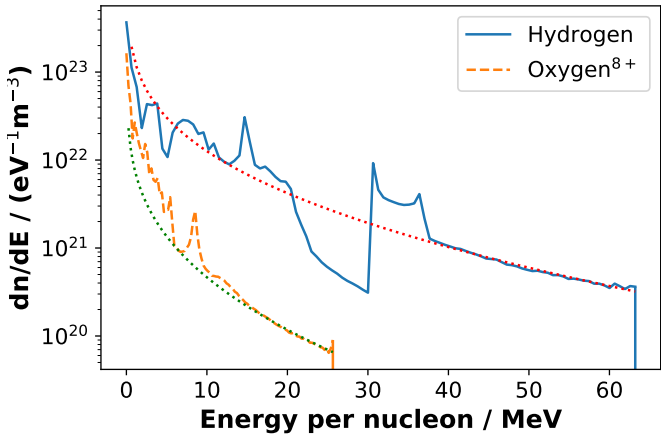

Figure 2.8.: PIC simulated multi-species system. Consisting of H_2O with eight-fold ionized Oxygen. Classical Mora solution is indicated with dotted lines, while the solid and dashed lines give the simulated spectra, respectively.

2.3.3. Divergence of the Beam

Experiments and simulations (Schmitz, Metternich, et al. 2022, and the sources therein) have shown that the opening angle is energy dependent. Studies have shown that larger energies have smaller opening angles and a laminar behavior, which is also shown by Lecsz et al. (Lécz 2013, Sec. 6.3.) (Lécz et al. 2015, Eq. 6, Fig. 11). While the TNSA accelerated ions have a close to zero transverse temperature (Roth and M. Schollmeier 2016b, Eq. 43, p.250) the full beam can have a large divergence in the order of $20°$. This is not a contradiction, since the transverse temperature, also designated as transverse emittance, is an inter-particle quantity describing momentum deviation and turbulent flow or the lack thereof inside the particle beam, while the divergence is a global description of the particle beam envelope. The beam is opening up while being laminar inside.

The physical reason for this is the already mentioned shape of the electron cloud and the shock waves expanding inside the target. A good plot of this and a describing model can be found in the work of Zeil et al (Zeil et al. 2010, Fig 8). This deformation curves the planar back side and strengthens the off-axis acceleration. Since the fastest ions see the highest field in the center the deviation for slower ions increases. In addition to the model from Lecz, two empirical functions are used to describe the angle envelope. They are discussed by Schmitz et al. (Schmitz, Metternich, et al. 2022) and are repeated here for completeness. The easiest function is a simple quadratic polynomial

$$\Theta(E) = a + b \cdot E + c \cdot E^2, \tag{2.25}$$

which behaves nonphysical in the high energy limit but explains the typical plateau visible at low energies. In the low energy limit, the function goes towards a plateau and stays there, the value a is a measure of the maximum angle achieved.

A more sophisticated model is the partial function model: Laser-accelerated ion beams, accelerated via the TNSA mechanism, have a specific cut-off energy. RCFs only allow measuring particles with energy higher or equal to the Bragg-peak energy of the first active layer. This means that the definition interval is limited. It, therefore, makes sense to force the functional values in the upper and lower interval limits to zero. An ansatz for the angle dependency is then

$$\Theta(E) = a \cdot \sqrt{-2 \ln\left(\frac{E}{b}\right)} \cdot \left(\frac{E-d}{b}\right)^{1/c}. \tag{2.26}$$

The parameter b is the maximal energy of the ion beam while d is the value for the lower energy cut-off. This

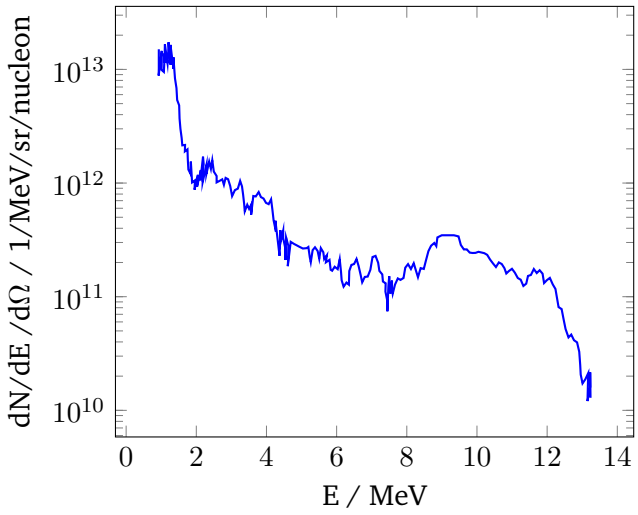

Figure 2.9.: Deuterium spectrum from a multi-species target, reproduced from (Alejo et al. 2014). A Thompson parabola setup joined with a particle filter is used to measure the spectrum.

scales the function from d to the cut-off energy. c and a scale the curvature of the function accordingly. For low energies, the distribution approaches 0 indicating a finite beam size. The function approaches zero for high energies as well, limiting the beam's maximum energy as well.

The model from Lecz is more complicated and is developed in detail in the corresponding thesis. All three models are plotted in Figure 2.10. The plot shows all 3 models. It is evident, that the model from Lecz does not reproduce the plateau at low energies, which results from assuming a point like heating on the backside of the target. This assumption is not true due to the hot electron's broadening as shown by Marius Schollmeier in his thesis (M. S. Schollmeier 2009, Ch. 4.1.). A hybrid model cutting of the model at a specific point can be a better description of the angle.

2.3.4. Targetry for Laser-Driven Ion Acceleration

As already mentioned above, the divergence and the ion species to be accelerated are relevant. An important part of the whole process is the plasma target itself. The schematics in Figure 2.11 display some of the more conventional targets used for particle acceleration via TNSA. From advanced studies for approaches like proton fast ignition even more complex targets are known (Prencipe et al. 2017, e.g. Fig. 5). This includes several modifications like cones to guide the laser or coils to modify the exiting ion beam characteristics.

This thesis aims to optimize a system for high-repetition usage. The more complex a target, the less suited it is for high-repetition operation. A good overview of the current state of the art for high repetition rate targets is given in (Prencipe et al. 2017). Several complications are evident, especially for the rapid supply of targets and positioning. It is therefore advisable to use simple targets and find a way to replace them quickly.

The simplest way is to use a foil, as displayed in Figure 2.11a. It can be fixed easily in the position needed for the experiment. The particles being accelerated in this case usually come from a contamination layer on the back of the foil. This can be used to accelerate heavier particles if the contamination layer and the lower mass particles can be removed. Unfortunately, a mounted foil is unfeasible in continuous operation due to difficulty exchanging the targets quickly and precisely. An additional problem that comes up with foil targets is the debris caused by the irradiation. The debris consists of target shrapnels which are not accelerated properly but get ejected with the resulting shock wave. The debris damages optics and surrounding components and is problematic, especially for high repetition rates. In the long term, when the laser interaction is done, the target

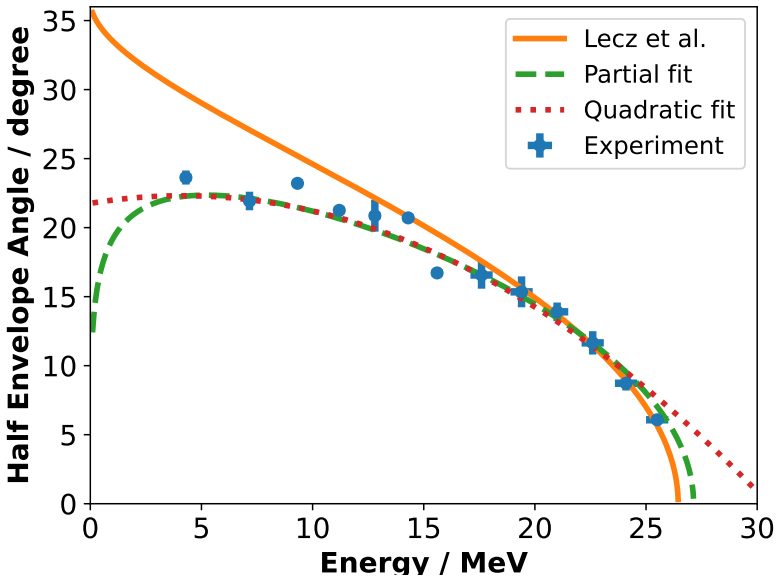

Figure 2.10.: Lecz et al. divergence model with the two mentioned empirical models. The solid line gives the best fit for the data set for Lecz's model. The dotted line is the result of the Quadratic Function (Equation 2.25) and the dashed line represents the best fit for the Partial Function (Equation 2.26). The blue data points are taken from the beamtime P218, which was performed at the PHELIX facility at the GSI Helmholtzzentrum f□ur Schwerionenforschung, Darmstadt (Germany) in the frame of FAIR Phase-0. This plot was taken from the corresponding publication by Schmitz et al. (Schmitz, Metternich, et al. 2022).

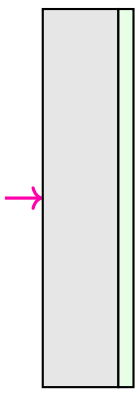

(a) Thin foil based target, green is the species to be accelerated, gray marks the area of heavier ions which works as substrate.

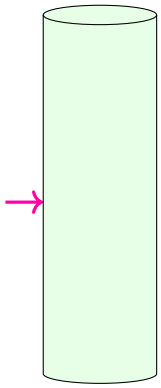

(b) Jet target, normally supplied as a liquid or in a gaseous state. Characteristic cylindrical shape. Acceleration-ready low-mass particles are distributed homogeneously.

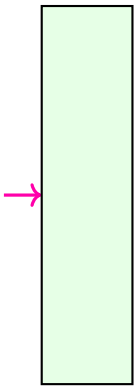

(c) Liquid leaf target or modified gas jet. The irradiated area is basically as plane as a thin foil target. Acceleration-ready low-mass particles are distributed homogeneously.

Figure 2.11.: Different targets as used in TNSA experiments. The red arrow indicates the incoming laser wave.

is basically evaporated. The resulting vapor is then coating all optics and components in the experimental area, reducing the efficiency of the optical elements.

A regular cylindrical jet is the simplest way for a flowing liquid or gaseous target as displayed in Figure 2.11b. This is simple to create and is quickly replaceable, no mechanical interlock has to be set and regeneration of the target is fast. The cylindrical geometry has a major disadvantage though. Target Normal Sheath Acceleration, accelerates the particles along the normal of the target's surface. With a cylindrical surface, the curvature is high and accelerated particles diverge more than for a comparable flat target (Obst et al. 2017, Fig. 3, Fig. 4, Fig. 5).

Figure 2.11c then displays a geometry that combines both advantages, a flat target with a homogeneous particle distribution. An example of such a target is given by George et al. (George et al. 2019, Fig. 4, Fig. 5). This can be achieved by colliding two cylindrical liquid jets under an angle Θ and utilizing momentum conservation and surface tension. The collision causes for example water to fan out into the normal with respect to the axis of collision. This leaf which is perpendicular to the laser is furthermore planar in the focus area of the laser. This work is investigating a liquid leaf target for the production of the primary particle. Its assumed parameters are discussed in detail in subsection 6.1.1.

TNSA Models in the Literature

Much of the literature about laser-driven ions consists of simplified relations and scaling laws based on different experiments or simulations. All of them use solid thin foils with adsorbed layers and the general quantity of interest is the cut-off energy of the ion spectrum (Fuchs et al. 2005) (Zeil et al. 2010) (Borghesi et al. 2013) (Fourmaux et al. 2013) (Brenner et al. 2011) (Perego, Zani, et al. 2011) (Keppler, Elkina, et al. 2022) (J. Schreiber et al. 2006).

The pre-plasma can be described as an exponential plasma skirt extending the central main part of the target. An exponential function is fully characterized by its decay constant and the starting amplitude. The decay constant in literature is called scale length- The pre-pulse can indirectly influence this scale length and an influence on the acceleration process is measurable (Keppler, Elkina, et al. 2022). If proper reproducible pre-plasma shaping is achieved, then an improvement of this can be utilized as well.

An interesting notion is that a laser-irradiated target gets hotter and then simultaneously expands in forward and backward directions. It has been shown in simulations that both bunches, propagating in different directions have spectra that are similar to each other (Fourmaux et al. 2013). It might therefore be possible to use two bunches simultaneously, doubling the number of accelerated ions.

The scaling laws developed based on experimental data are of interest for the ion scaling discussion and for our own data rescaling and validation. A reduced model that takes the acceleration time into account was developed by Karl Zeil et al. (Zeil et al. 2010, Eq. 3). It describes only the cutoff energy and neglects or simplifies the acceleration dynamics as

$$E_{\text{max}} = E_\infty \tanh^2\left(\frac{\tau_L}{2\tau_0}\right) \quad \text{with: } E_\infty = 2m_e c^2\sqrt{\frac{\eta P_L}{P_e}} \quad \text{and: } \tau_0 = \frac{R}{\sqrt{2E_\infty/m}}, \tag{2.27}$$

where τ_L is the laser pulse length, P_L the laser power, R is the size of the hot electron spot at the rear side of the target, $P_e = 8.7\,\text{GW}$ the relativistic power unit and η is the conversion efficiency (around $20\,\%$).

A more advanced model considering the process dynamics is the model proposed by Schreiber et al. (J. Schreiber et al. 2006). The model does not provide an explicit dependence from hot electron energies which is a good trait since it does not give wrong estimates due to over- or underestimation of T_e.

$$\frac{\tau_L}{\tau_0} = X\left(1 + \frac{1}{2}\frac{1}{1+X^2}\right) + \frac{1}{4}\ln\left(\frac{1+X}{1-X}\right) \quad \text{with} \quad \tau_0 = B/v(\infty) \tag{2.28}$$

where, $B = r_L d \tan\Theta$ and $X = \sqrt{E_m / E_{i,\infty}}$. One important result of this model is the prediction of an optimal pulse length.

2.4. Neutron Conversion Processes and Characteristics

So far the acceleration process has been discussed. Therefore the acceleration or part of the full setup is done, what remains is the conversion part as displayed in Figure 2.12. Therefore, this section focuses on

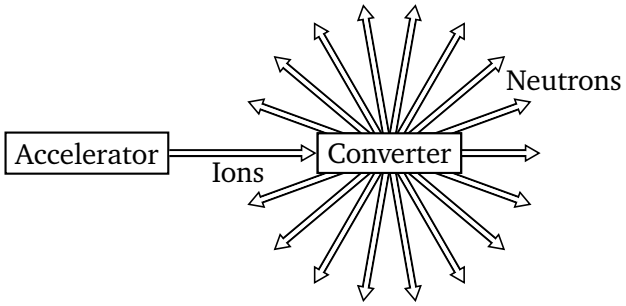

Figure 2.12.: Accelerator as a pitcher of ions, converter as catcher of ions. The ions are converted to neutrons and emitted from the converter.

understanding neutron production from light ion projectiles. It summarizes the nuclear physics relevant for producing neutrons and is based on (Mayer-Kuckuk 2013). Several parts in this section are calculated by the author to complement missing numerical values in literature, to discuss traits of the converter to be determined, or to construct geometric formulas needed in the conclusion of the proposed design.

A nuclear process is initialized by a collision of the projectile a with the target atom A. Both particles must be close, approximately some fm, so the short-range strong interaction can trigger an interaction between the particles. A considerable amount of kinetic energy is needed to get so close together since the projectile has to overcome the target's Coulomb potential. The heavier the atoms are, the higher the corresponding charge number Z and the more energy is necessary to overcome the Coulomb barrier. It is therefore advisable to use the lightest ions with the lowest Z that are reasonably usable.

As soon as the particles undergo a reaction in general a number of particles have to go out of the reaction. Analog to the ingoing particles, the outgoing is denoted b for the ejectile and B for the heavy nucleus. This reaction equation fulfills several conservation laws: energy, momentum, charge, and baryon number conservation. These laws limit the number of possible reactions. The reaction itself can be noted comparably to chemical reactions as $a + A \rightarrow B + b$ or more compact as $A(a, b)B$. The reaction probability is given by the cross-section σ of the reaction, which means that a higher cross-section implies a higher probability of this reaction occurring. This cross-section depends on the particle dynamics and the input energies, which means that the prevalent reaction can change for different conditions. The cross-section is measured in barn, equal to $100\,\mathrm{fm}^2$.

The nuclear reactions relevant to this work are the reactions for generating neutrons. Since different applications vary in the neutron energies, beam quality, and the number of neutrons needed, a model optimizing and predicting a source has to be able to deal with different conditions and be adaptable. This implied that the nature of the neutron and the production process has to be understood, the production process is one part of this work.

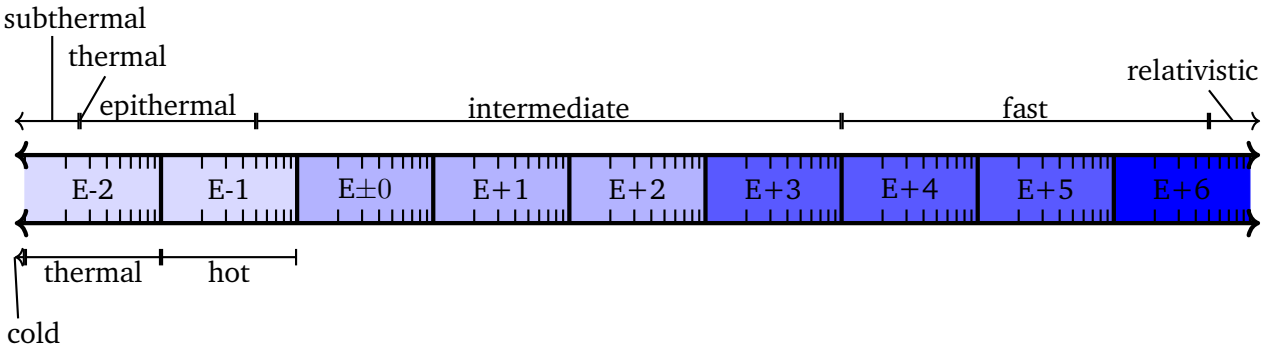

Figure 2.13.: Overview of the neutron energy and the termini used. The blue strip denotes the order of magnitude of the kinetic neutron energy in eV with an indicated logarithmic scale. Above the scale are the formal definitions, while below the scale are definitions from the neutron radiography community. Data taken from (Krieger 2018, pp. 354-355, Tab. 13.1, Tab. 13.2).

2.4.1. Neutron Traits, Production, and Yields

The importance of neutrons for different applications has already been discussed in chapter 1. Why are neutrons of interest for applications and what is different from other types of radiation? The most distinct difference is that neutrons have no electric charge to cause Coulomb repulsion. They, therefore, do not scatter at the shell of an atom but only on the nucleus itself. They, as mentioned previously, do not interact with Coulomb potential but only with the strong nuclear force This results in a higher resolution of features in scattering experiments but they can also easily initiate nuclear reactions inside a target. Which one happens depends on the incoming energies and again cross-sections express the probability of a reaction happening (Krieger 2018, Sec. 13.8) (Mayer-Kuckuk 2013, Sec. 5.2.).

As a rule of thumb, it can be assumed that the probability of inducing a nuclear reaction increases the lower the energy of the incoming neutron. Low energy means low velocity; with low velocity, the time to interact with a target nucleus increases, increasing the cross-section. Several definitions for the neutron energy's nomenclature exist in literature two of the often used variants are displayed in Figure 2.13. This work will directly take energy value to avoid confusion and ambiguities in the discussion. Neutron energies can be adjusted by moderating the beam. Moderation is the process of scattering inside a material. Neutrons traveling through the moderator are scattering with the surrounding atoms. Due to this, the energy of the neutrons changes and it converges towards the converter's thermal energy. While it is usually the case, that the neutron energy is reduced, energy can also be gained if the converter has higher thermal energy than the incoming neutron beam.

Neutron sources can be constructed with four different mechanisms (Krieger 2018, Pages 332-344). Radioactive isotopes (e.g. Americium-Beryllium sources or Californium) can be used. They have a fixed emission behavior and follow a distribution defined by their decay process. They normally do not exceed some MeV kinetic energy. Secondly, nuclear reactors can be utilized as neutron sources, since fast neutrons are a product of nuclear fission. While reactor neutrons can reach high energies, a large support system is needed and the process of fission creates a large amount of nuclear waste. Thirdly, fusion approaches using for example pyroelectric fusion (Naranjo et al. 2011) or a Farnsworth-Hirsch Fusor (Miley et al. 2000) can be used. They are commercially available but have rather low neutron rates. The fixed maximum energies on this would be 10^{11} n/s for 14 MeV neutrons for the Farnsworth-Hirsch Fusor and 10^{5} n/s for 14 MeV neutrons for the pyroelectric approach. Fourthly, accelerator-based methods can be used. This approach is discussed further since the work in this thesis is part of the accelerator-based approach.

Accelerator-based methods use light ions as projectiles and can be distinguished by the target and the energy, high Z targets and high energy create neutrons through spallation. Spallation is based on crushing nuclei with incoming particles, which is for example used at the European Spallation Source (Garoby et al. 2017, pp. 66ff) (Krieger 2018, Sec. 13.5.1). Spallation needs a high particle energy starting at $200\,\mathrm{MeV}$, while the European Spallation Source for example aims to operate at $2\,\mathrm{GeV}$. A realistic concept utilizing a compact particle accelerator for producing neutrons has to produce neutrons utilizing light ion reactions with low energies up to approximately $100\,\mathrm{MeV}$. Yang et al. demonstrated the neutron production from TNSA ions in 2004 (Yang et al. 2004).

Light ion induced Neutron Reaction with low Z Targets

As discussed in section 2.3 about TNSA, light ions with the highest Z/m ratio are accelerated to the highest energies and are therefore preferable. This means that reactions mainly from impinging protons and deuterons are evaluated. Higher ionized heavy ions can reach the same Z/m ratio, their effect on the neutron thick target yield is negligible. High ionized oxygen (which can get the highest energies and is therefore the most relevant) is strongly dominated by the Coulomb interaction, which reduces the neutron production further. Therefore, with comparable kinetic energies, the yield of for example Oxygen is assumed to be negligible. The governing reactions for the low Z projectiles and a selected number of targets at energies below the spallation threshold are

$$\text{Be-Target} \begin{cases} \mathrm{d} + {}^{9}_{4}\mathrm{Be} & \rightarrow & {}^{10}_{5}\mathrm{B} + n + 4.36\,\mathrm{MeV} \\ \mathrm{p} + {}^{9}_{4}\mathrm{Be} & \rightarrow & {}^{9}_{5}\mathrm{B} + n - 1.85\,\mathrm{MeV} \end{cases} \tag{2.29}$$

$$\text{Li-Target} \begin{cases} \mathrm{d} + {}^{7}_{3}\mathrm{Li} & \rightarrow & {}^{8}_{4}\mathrm{Be} + n + 15.03\,\mathrm{MeV} \\ \mathrm{p} + {}^{7}_{3}\mathrm{Li} & \rightarrow & {}^{7}_{4}\mathrm{Be} + n - 1.65\,\mathrm{MeV} \end{cases} \tag{2.30}$$

$$\text{V-Target} \begin{cases} \mathrm{d} + {}^{51}_{23}\mathrm{V} & \rightarrow & {}^{52}_{24}\mathrm{Cr} + n + 8.28\,\mathrm{MeV} \\ \mathrm{p} + {}^{51}_{23}\mathrm{V} & \rightarrow & {}^{51}_{24}\mathrm{Cr} + n - 1.54\,\mathrm{MeV} \end{cases} \tag{2.31}$$

$$\text{Ta-Target} \begin{cases} \mathrm{d} + {}^{181}_{73}\mathrm{Ta} & \rightarrow & {}^{182}_{74}\mathrm{W} + n + 4.87\,\mathrm{MeV} \\ \mathrm{p} + {}^{181}_{73}\mathrm{Ta} & \rightarrow & {}^{181}_{74}\mathrm{W} + n - 0.97\,\mathrm{MeV}. \end{cases} \tag{2.32}$$

$$\text{F-Target} \begin{cases} \mathrm{d} + {}^{19}_{9}\mathrm{F} & \rightarrow & {}^{20}_{10}\mathrm{Ne} + n + 10.62\,\mathrm{MeV} \\ \mathrm{p} + {}^{19}_{9}\mathrm{F} & \rightarrow & {}^{19}_{10}\mathrm{Ne} + n - 4.02\,\mathrm{MeV}. \end{cases} \tag{2.33}$$

Each reaction has a Q-value which describes whether the reaction is endo- ($Q < 0$) or exotherm ($Q > 0$). If it is exotherm, then the reaction will pass additional energy to the emitted neutron, if it is endotherm, then it needs at least the given energy to undergo the reaction. This energy does not completely go to the ejected neutron but can also be passed to the remaining nucleus, exciting it. The excited nucleus can then enter its ground state by emitting a photon of the corresponding energy, triggering further reactions. Formally written, the maximum energy of an ejectile can be calculated by

$$\max\left(E_{\mathrm{kin}}^{\mathrm{ejectile}}\right) \approx E_{\mathrm{kin}}^{\mathrm{proj}} + Q. \tag{2.34}$$

The Q-value is a direct result of the mass difference before and after the reaction and can therefore be calculated by the equation

$$Q = M_{\mathrm{projectile}} + M_{\mathrm{Target}} - M_{\mathrm{ejectile}} - M_{\mathrm{Product}}. \tag{2.35}$$

As displayed in the list of reactions above, Beryllium, Lithium, Vanadium, and Tantalum targets are investigated. Fluorine is only investigated as part of a LiF Target which is used to mitigate the difficult material parameters

of Lithium which are mentioned below. The materials were selected due to their promising results in literature (Rücker et al. 2016, Fig. 1, Fig. 2, Tab. 1).

Reactions, Cross Sections, and Thick Target Yields

A projectile can either cause direct nuclear reactions or start compound reactions. A major difference between these processes is the characteristic time it takes the particle to interact. The direct reactions emit the ejectile directly after the interaction. The characteristic time is therefore the time it takes the projectile to pass by the target nucleus, which is with 10^{-22} s. Compound reactions on the other hand form a compound nucleus, consisting of the projectile and the target nucleus, which then emits the neutron.

The compound nucleus's components are indistinguishable, effectively adding both nuclei's baryons together. This resulting compound nucleus decays in a timescale of 10^{-16} s to 10^{-18} s, leaving the nucleus enough time to reach the thermal equilibrium. Decaying nuclei in thermal equilibrium have no information about the original momenta and the emission is therefore isotropic. The equilibrium might not be reached for kinetic energies larger than the binding energy, and a reaction can occur in pre-equilibrium. Pre-equilibrium reactions have not lost all of their momenta and did not thermalize, such that a residual momentum is passed on to the neutron, causing preferred emission into the forward direction (Kleinschmidt 2017, Sec. 3.2, p. 52).

It has been calculated, that the process of deuteron break up is only relevant for targets with a high Z (Zimmer 2020, Sec. 2.4.1). This can be understood if the deuteron is assumed as a proton and a neutron, traveling together confined with a binding energy of 2.225 MeV. Since the neutron is electrically neutral, the Coulomb field of the target acts only on the proton. If the force on the proton is larger than the binding energy, the proton splits from the neutron and reacts independently with the target. This process, therefore, has a low cross-section. The dominant process for light target nuclei is deuteron stripping. It occurs when the deuteron's wavefunction overlaps with the target's wavefunction. In this configuration, either of the two projectile nucleons can form a compound nucleus with the target, while the other continues through the target and undergoes further reactions. This is supported by the three-body treatment (Johnson et al. 1974, Sec. 2).

All of these reactions and the corresponding channels have a reaction probability. The quantity describing this on a microscopic scale is the cross-section of the reaction. In experiments, special effort has to be taken to measure this cross-section directly, the targets are as thin as possible such that ideally, only one interaction happens. Created ejectiles (neutrons in this case) interact with the rest of the converter, reducing energy and direction information. The spectrum that can be measured directly after the converter is therefore already partly moderated and deviates from the spectrum expected from the cross-sections alone. If the effects of the converter's finite size are considered, the resulting spectrum is called thick target yield. Since the thick target yield is the observable of interest for a real experiment all subsequent modeling in this work takes the thick target yield and not the cross-section into account.

Nuclear Converter

Different projectile and target combinations can penetrate the corresponding converter differently. All ion beams impinging on the converter should be stopped to convert as many ions to neutrons as possible. A key measure is the penetration depth of particles. An analytical estimate for this would be the Bethe-Bloch formula (Bethe 1930, Sec. 20, pp. 397-400) (Bloch 1933, Eq. 71) which is still commonly used but got several extensions and corrections over time. A well-known tool to calculate the ion stopping power and the penetration depth is the software tool SRIM (Biersack et al. 1980). These relations can then be used to determine the needed converter length if the maximum ion energies are known. SRIM results are displayed in Figure 2.14. Independent of their physical performance in creating neutrons, engineering problems, and material traits must also be considered. Lithium for example is an alkali metal and as such highly reactive.

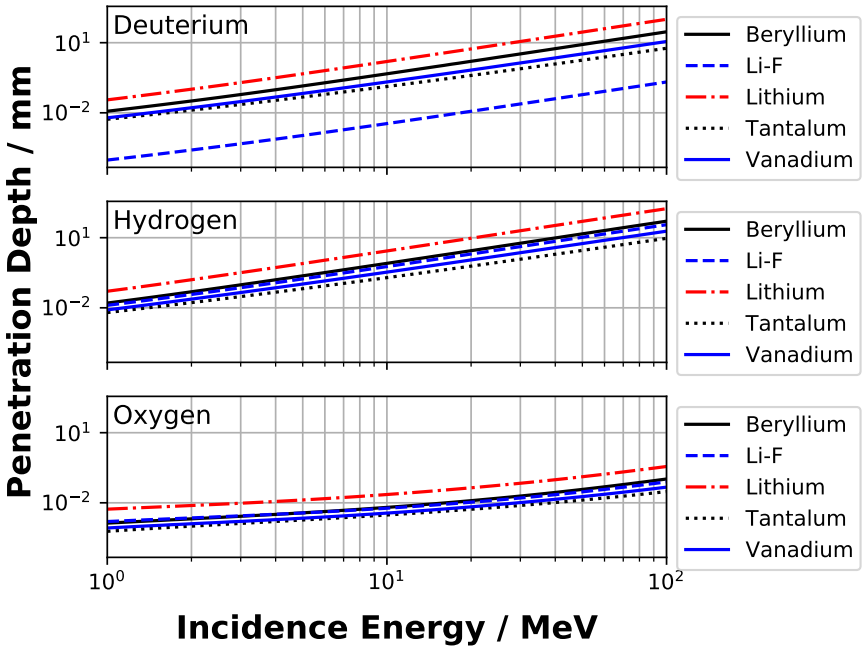

Figure 2.14.: The traveling ranges for three different projectiles and five targets. Curves calculated using SRIM.

Literature tells us it is a good neutron converter, but its stability is an issue due to its reactivity. Contact with hydrogen, oxygen, or water triggers chemical reactions and creates hydrogen gas. A way to mitigate this Lithium problem is by using compound materials, e.g. LiF. The fluoride component causes the material to stabilize but on the other hand, reduces the number of neutrons produced. Beryllium on the other hand is highly toxic and problematic if parts of it evaporate. Each converter's traits must be considered for the actual implementation. For the task of finding ideal parameters and optimizing the yield, these traits can be neglected.

When the material is known, the converter's transverse and longitudinal expansion must be determined. This correlates largely with the incoming beam's transverse divergence. Assuming a point source as the origin and the laminar flow for the ion as in subsection 2.3.3, allows a construction based on the outermost particle trajectory as displayed in Figure 2.15. Due to the already mentioned nuclear reactions, particles inside matter straggle lateral and longitudinal. This straggling is an additional uncertainty that has to be quantified and considered. The maximum angle Θ_{max} can also be determined by fitting an example data set as in subsection 2.3.3. As displayed in Figure 2.15b the effective length S_{eff} can be calculated using the Pythagorean theorem.

The converter is generally placed close to the source d, the only condition is that potential plasma debris does not damage the target. A liquid leaf targeted with water does not produce damaging debris. The TNSA ions are space charge negated, due to co-moving electrons, so the impinging protons do not charge the target. The converter can therefore be placed closely at the plasma target with arbitrary small values of d. Due to the small distance, the beam dynamics for this application can be neglected. Each particle that exceeds the mentioned minimal energy for neutron production has a chance to create neutrons and contributes to the thick target yield. Particles with energies below the necessary energy can be neglected. Therefore, applying TNSA as

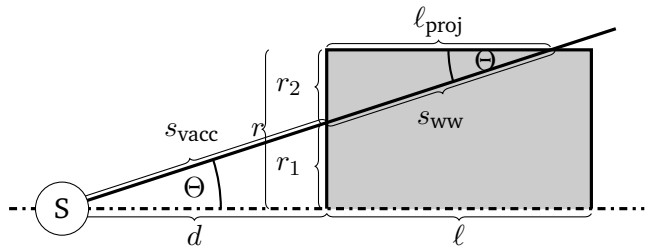

(a) Sketch of the full converter geometry with the corresponding labels.

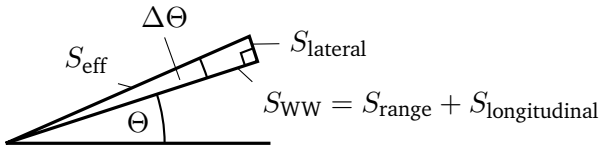

(b) Effects of lateral and longitudinal staggering of the projectile particles inside the catcher.

Figure 2.15.: Sketch of the full converter geometry and positioning and straggling inside the converter. All parameters of a cylindrical target can be expressed by the maximum angle Θ and the distance from the source. The rotational axis in (a) is denoted by a dash-dotted line.

Table 2.2.: Parameters and relations for constructing the converter's geometry.

Parameter	Conditions	Equation
Θ		
$\Delta\Theta$		$\Delta\Theta = \arctan\left(\frac{S_{\text{lateral}}}{S_{\text{WW}}}\right)$
d	Plasma Debris	
r_1	$r_1 < r$	$r_1 = \tan\Theta \cdot d$
r_2		$r_2 = r - r_1$
		$r_2 = s_{\text{WW}} \cos\left(90° - \Theta\right)$
s_{ww}	Dependent of energy	$\left(s_{\text{ww}} + s_{\text{vacc}}\right) / s_{\text{vacc}} = r / r_1$
s_{vacc}	Distance in vacuum	$s_{\text{vacc}} = d / \cos\Theta$
S_{eff}	Incorporate straggling	$S_{\text{eff}} = \sqrt{S_{\text{WW}}^2 + S_{\text{lateral}}^2}$
ℓ_{proj}	$\ell_{\text{proj}} \leq \ell$	$\ell_{\text{proj}} = r_2 / \tan\Theta$
ℓ	Maximum penetration depth	

a neutron source is easy to implement, since no dedicated acceptance for the beam or specific mono-energetic bunches has to be used.

2.4.2. Moving Source Model of Thick Target Yield

Now going one step further from the microscopic view of single atoms to the full spectrum Y, a description of Y is needed that reproduces the input parameter's dependency. This can be achieved for example with measurements or Monte Carlo simulations as explained in section 3.2. These results can be used to create a model $\mathcal{F}$, which can be evaluated quickly for arbitrary inputs. A fast model allows performing optimizations, which usually take in the order of 1000 iterations to find maxima. If the model further allows for different optimization conditions to be used, then the model is ideal. The model $\mathcal{F}$ to aid in the optimization is called a surrogate model and it is supposed to describe the double differential thick target neutron yield.

$$\left.\frac{\mathrm{d}^2 Y}{\mathrm{d}\Theta\ \mathrm{d}E_\mathrm{n}}\right|_{\substack{\text{Bunch}\\\text{Converter}}} = \mathcal{F}\left(\text{Bunch}, \text{Converter}\right), \tag{2.36}$$

Bunch is the sum of all incoming projectile particles and Converter is the specific target that creates the neutron spectrum. A full description of the bunch includes the projectile's kinetic energy E_p, the ion species, and the number of particles $N_p\left(E_p\right)$. For the converter, the main quantities are material and geometry.

A model used in the literature is the moving source model (Lawrence Heilbronn 2005, Sec. 6, and the sources therein). This model assumes that the source particle poops out neutrons according to a Maxwellian distribution. Assuming that several of these sources exist and superposing them allows describing the thick target yields.

$$\frac{\mathrm{d}^2 Y}{\mathrm{d}\Theta\ \mathrm{d}E_\mathrm{n}} = \sum_i \frac{\mathrm{d}^2 Y_i}{\mathrm{d}\Theta\ \mathrm{d}E_\mathrm{n}} \tag{2.37}$$

The functional relationship taken from the mentioned literature yields a full expression for a thick target yield spectrum as

$$\begin{aligned}\frac{\mathrm{d}^2 Y}{\mathrm{d}\Theta\,\mathrm{d}E_n} = {} & \frac{N_0(\Theta)}{\sqrt{2\pi\sigma_c(\Theta)^2}} \exp\left(-\frac{\left[E_n - E_c(\Theta)\right]^2}{2\sigma_c(\Theta)^2}\right) \\ & + \sum_{i=1}^{2} \frac{N_i\sqrt{E_n}}{2(\pi T_i)^{3/2}} \exp\left(-\frac{E_n - \varepsilon_i - 2\sqrt{E_n\varepsilon_i}\cos\Theta}{T_i}\right).\end{aligned} \tag{2.38}$$

The parameters in this model are defined as

$$\begin{aligned}\text{Source Intensity} &: N_1, N_2, N_3 N_{01}, N_{02}, ..., N_{0j} \\ \text{Nuclear kinetic Energy} &: \varepsilon_1, \varepsilon_2, \varepsilon_3 \\ \text{Nuclear Temperature} &: T_1, T_2, T_3 \\ \text{Peakenergy} &: E_{c1}, ..., E_{cj} \\ \text{Energyvariance} &: \sigma_{c1}, ..., \sigma_{cj} \\ \text{Total number of fit parameters} &: 3 \cdot j + 6, \text{ where } j \text{ is the number of measured scattering angles.}\end{aligned}$$

The model has many degrees of freedom and can fit and interpolate an extensive range of data. The model is not precise when the data is sparse or when the data covers several orders of magnitude in short intervals. This

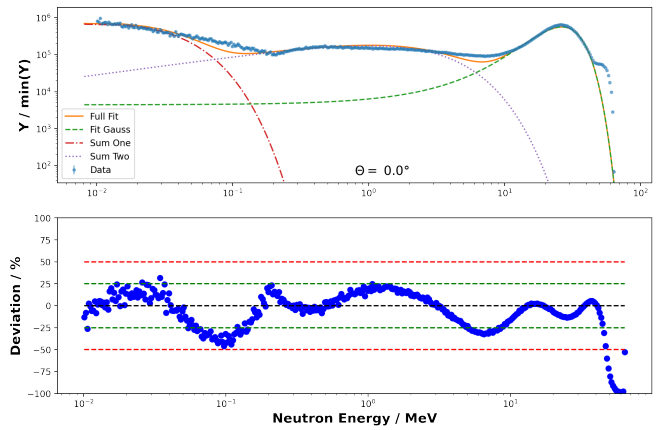

(a) Thick target neutron yield for Be(d,n)X reaction with 30 MeV/A under 0°. The yield is normalized to the minimum yield value to adjust the fit range.

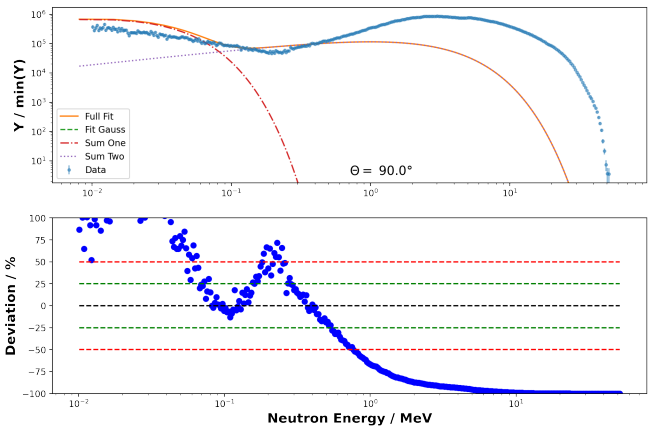

(b) Thick target neutron yield for Be(d,n)X reaction with 30 MeV/A under 90°. The yield is normalized to the minimum yield value to adjust the fit range.

Figure 2.16.: Moving source model fitted to example data. Upper plots: Blue denotes the normalized spectral data, while the non-dashed lines give the three different parts of the model. The solid line is then the superposition and, therefore, the model's result. Lower plots: Blue denotes the deviation from model and data, while the inner, green dashed line denotes the $\pm 25\,\%$ interval and the red dashed line the $\pm 50\,\%$ interval.

leads to problematic behavior at the spectrum's lower and higher energy end. As displayed in Figure 2.16, the best fit does not necessarily yield exactly the structure as measured or simulated. The model was developed for high-energy heavy ion beams. As visible, it might reproduce a dedicated spectrum to a limited extent as in Figure 2.16a. At the same time, the application on different scattering angles deviates further to the extent that the model's error gets too high to use it as in Figure 2.16b. Despite the deviation, this moving source model will be compared with its ideal result to the model developed in this thesis later.

3. Numerical Fundamentals

"'Forty-two,' said Deep Thought, with infinite majesty and calm."
– Sir Douglas Adams

The two major physics concepts explained in chapter 2 live on different scales and have different processes which are relevant to them. It is, therefore, necessary to apply disjunct methods for both cases. While the plasma dynamics of TNSA require a particle-in-cell code (section 3.1), the nuclear processes rely on Monte Carlo simulations (section 3.2). Acquiring data allows afterward to calculate surrogate models using artificial neural networks (section 3.3) which can then be used and further physically interpreted with methods from the field of uncertainty quantification and sensitivity analysis (section 3.4).

3.1. Particle-in-Cell Method

The data for the surrogate is created by the simulation code SMILEI (Derouillat et al. 2018), which uses the particle-in-cell (PIC) method. A more general approach and discussion of the method can be found in corresponding textbooks (Birdsall et al. 2004) (Arber et al. 2015). PIC is a simulation method that assumes a kinetic approach to plasma simulations: It aggregates several physical particles into a few macro particles, which are living in a continuous space, and tracks these particles' positions ($\vec{x}$) and momenta ($\vec{p}$). The relevant electromagnetic fields are not sampled continuously to save time and memory, they are sampled on a discrete grid. The PIC loop as depicted in Figure 3.1 converts during one time-step from particle quantities, sampled continuously, to field quantities sampled discretely and vice versa. For more details see (Derouillat et al. 2018, Sec. 2.6). The Newton/Lorentz pushers or the Poisson/Maxwell solvers are fully or partially used depending on the implementation. While the Poisson equation is normally used for static problems and generally calculated only at time $t = 0$, it is listed in the PIC loop where it belongs if used.

Since several physical particles are aggregated into one macro particle, the macro particles consist of distribution functions and specific weights allowing the conversion back to their physical equivalent. The distribution function for these macro particles is given in the SMILEI introduction paper as

$$f_s\left(t, \vec{x}, \vec{p}\right) = \sum_{p=1}^{N_s} w_p S\left(\vec{x} - \vec{x}_p(t)\delta\left(\vec{p} - \vec{p}_p(t)\right)\right), \tag{3.1}$$

where N_s is the number of macro particles, w_p is the macro particle weight, S the shape function and δ the Dirac delta distribution. The shape function $S(x)$ is recursively defined,

$$S(x) = \prod_{\mu=1}^{D} \hat{s}^{(n)}(x^\mu) \quad \text{with} \quad \hat{s}^{(n)}(x) = \int_{-\infty}^{+\infty} P(x' - x)\hat{s}^{(n-1)}(x')\,\mathrm{d}x', \tag{3.2}$$

where P is the Crenel function, which has the value of 1 if $\|x\| \leq \Delta x$, Δx being the distance between two grid points, and D is the number of spatial dimensions. Following the construction rule, higher-order functions are

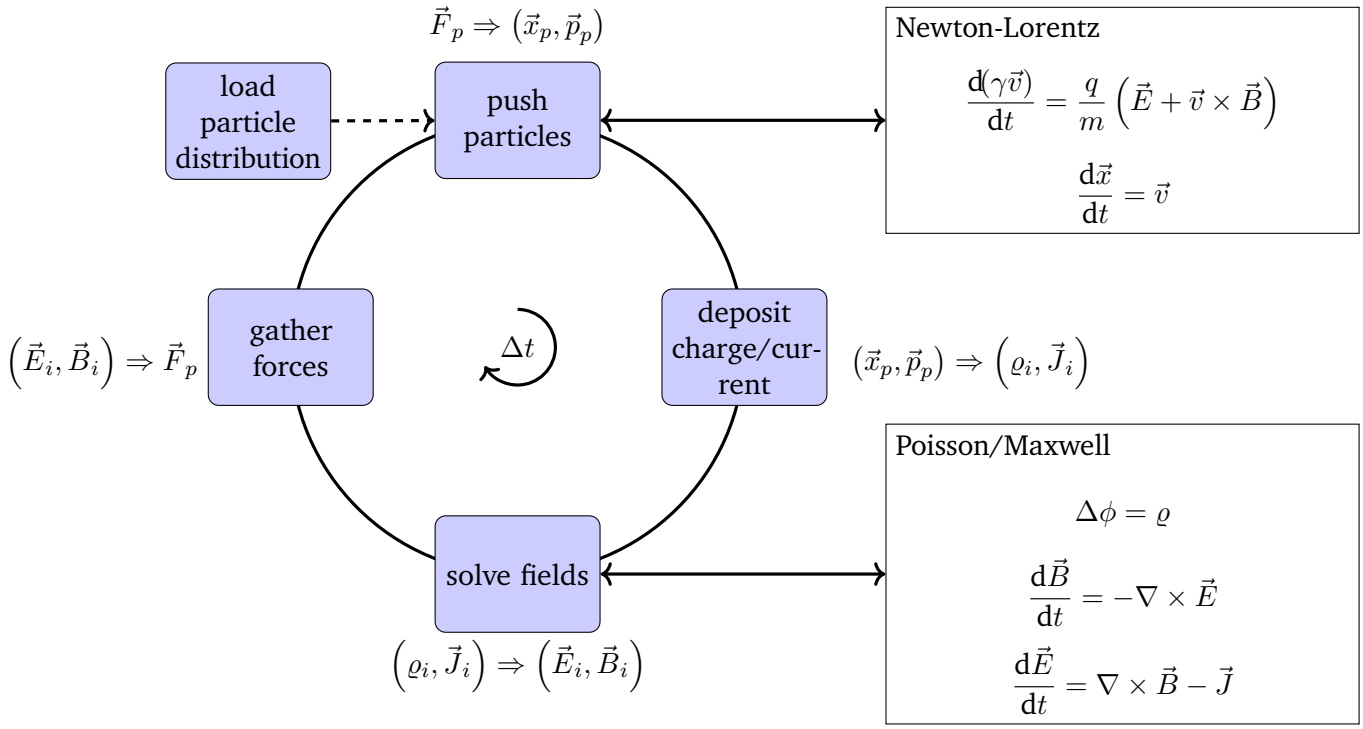

Figure 3.1.: Flow chart for the PIC cycle for one-time step. Added with double-edged arrows are the governing relations in the specific step and a short notation for conversion done. i indexes quantities living on a grid, while p indexes the macro particles living in a continuous space.

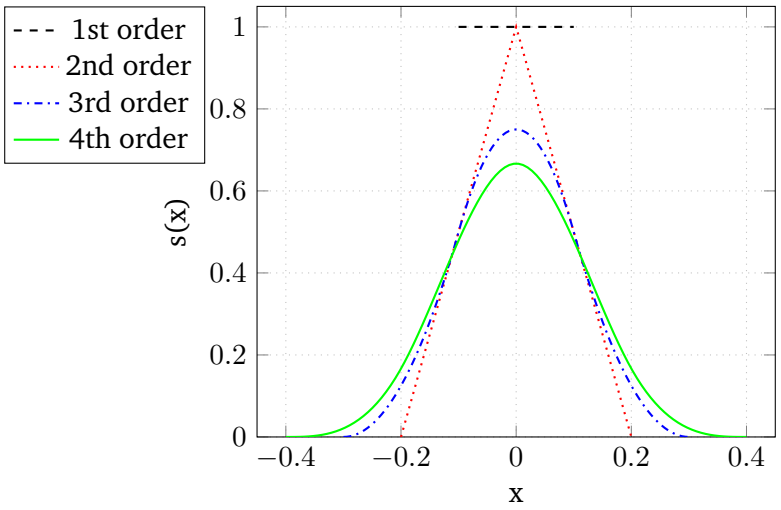

Figure 3.2.: SMILEI shape functions for one spatial component.

constructed. These functions are given in the appendix of the SMILEI introduction paper (Derouillat et al. 2018, Appendix A). For the case of one spatial dimension, the shape functions are displayed in Figure 3.2. Higher-order particle shape function causes a higher smoothing effect on the particle spectrum. Reducing the order, therefore, causes higher fluctuation in the resulting particle spectrum, while higher orders smooth the spectrum, physics might get lost if the order is too high. This trait off has to be considered when the simulation is set up.

Limitations of PIC

PIC is a widely used numerical technique for simulating the behavior of charged particles in electromagnetic fields. However, this method can be subject to a range of numerical limitations that can affect the accuracy and reliability of the simulation results. Two specific limitations that can arise in PIC simulations are the numerical Cherenkov effect and grid heating.

Grid heating is a type of numerical error that can occur when the PIC simulation is run with insufficient grid resolution. This error arises because the electric and magnetic fields are not discretized finely enough, resulting in energy being deposited into the grid instead of the particles. This can lead to inaccurate simulation results, especially when the simulation involves complex electromagnetic fields or highly energetic particles.

The choice of the time step is also an important consideration in PIC simulations. Choosing an inappropriate time step can lead to numerical instability or inaccurate results. Additionally, the time step must be large enough to ensure reasonable computational efficiency. This consideration is especially relevant in simulations of highly dynamic or complex systems. This is conditioned by the Courant–Friedrichs–Lewy condition (Courant et al. 1928). The equation

$$\mathrm{CFL} = \frac{u\Delta t}{\Delta x} \tag{3.3}$$

describes the number of cells a particle can pass during one time step. The solution will only converge if $\mathrm{CFL} < 1$, which can then be rewritten as

$$\Delta t \leq \frac{\mathrm{CFL}}{\sqrt{\frac{c^2}{\Delta x^2} + \frac{c^2}{\Delta y^2} + \frac{c^2}{\Delta z^2}}}. \tag{3.4}$$

If, however, the CFL number is too close to 1, a numerical Cherenkov effect (Godfrey 1974) might occur, which introduces further instabilities.

The numerical Cherenkov effect is a type of numerical instability that can occur in PIC simulations. It arises from discretizing the electric and magnetic fields on the numerical grid. It can lead to unphysical behaviors such as particles traveling faster than light or artificially amplified waves. Particle noise can worsen this instability, a limitation arising from the finite number of particles used to represent the plasma in the simulation.

In summary, the numerical Cherenkov effect and grid heating are two specific numerical limitations that can occur in PIC simulations. These are related to more general limitations such as particle noise, grid resolution, and time step limitations. These limitations must be carefully considered when designing and running PIC simulations, to ensure that the results are accurate and reliable.

Dimensionality in PIC Codes

PIC codes are numerically expensive. The numerical costs are higher the more dimensions are used. While one-dimensional simulations can run on a regular desktop, three-dimensional simulations with more than $40\,000$ core hours are not feasible without utilizing a large cluster. They are even more unfeasible to be used in large bulk as the basis for surrogate models. The focus of this work, therefore, revolves around one-dimensional simulations.

3.2. Nuclear Monte Carlo Code

Numerical experiments for neutron production and transport are only possible if the neutron transport equation is solved (Duderstadt 1976, Ch. 4 II). The production part is included with a dedicated source term. Determining the source term is a tedious task and needs experimental input. Several databases, e.g., JENDL, FENDL (Shibata et al. 2011) (Forrest et al. 2012) exist, already giving the needed source term data. They vary due to being measured or calculated with varying measurement methods or assumptions.

The neutron transport equation's solution can be obtained with deterministic or probabilistic methods. For the set of deterministic methods, the discrete ordinates method is the most common: The solution of the equation is calculated for average particles only. An extensive collection of different methods of discrete methods can be found in (Adams et al. 2002). The probabilistic or Monte Carlo method simulates individual particles and records specific aspects (called tallies) of their trace and behavior. A final result can be achieved by applying the central limit theorem to these tallies. While the deterministic approach generally yields more complete results than probabilistic methods, there are some compelling reasons to use Monte Carlo methods.

Therefore, Monte Carlo does not use discrete phase spaces and is not averaging. The version of the transport equation solved by Monte Carlo does not include space or time derivatives; therefore, no approximations in space or time are required. Monte Carlo is, therefore, capable of representing all aspects of physical data compared to the approximated discrete method.

Furthermore, Monte Carlo succeeds, while discrete methods can not correctly model complex problems and geometry. It succeeds in describing complex geometries and tells the whole story of a particle in this numerical experiment. From injection/creation of the particle, the entire trace is followed, and all physical interactions are calculated until the particle is stopped or decayed. Doing this for as many particles as possible finally allows for generalizing the observations.

Following the path of the particle, if it collides or interacts with matter, several nuclear reactions can take place, which of these will happen is determined by random numbers (therefore the name Monte Carlo). Cross-sections weigh the different possibilities for a dedicated reaction. Step by step, stepping through the particle's trajectory allows the later average to achieve predictions close to a real-world experiment. The interested

reader is referred to further literature about particle transport using Monte Carlo methods (Haghighat 2020). This work uses the Monte Carlo Code PHITS (Sato, Niita, et al. 2013; Sato, Iwamoto, et al. 2018) in Version 3.28. More details about the specific setup can be found in subsection 6.2.2.

3.3. Surrogate Modeling with Artificial Neural Networks

Surrogate modeling is widely applied in science, technology, engineering, and mathematics. It is used if measurements can not be easily measured or derived and a model of the outcome is used. Most design problems, in engineering or science, require a certain number of experiments and/or simulations to reach optimization goals with a function on dedicated design variables. A surrogate is mainly used in engineering sciences, but strictly speaking, all physical models are surrogates themselves.

Another way to think about a surrogate is the black box. Some input quantities or design variables go in and corresponding outputs get out. The surrogate is then the black box that directly correlates input to output and does not assume any physics or equations whatsoever. The more complicated a system is, the more design variables must be considered. If a system is easily understandable, meaning that a closed mathematical formulation exists such that an analytical solution can be found, it can be directly optimized.

Therefore, as soon as many design variables are relevant and the effort of physical or numerical experiments gets too high, sophisticated methods must be applied. Compact particle accelerators driven by laser-plasma interaction, as investigated in this thesis, are governed by complex equations, namely the Maxwell-Vlasov equation system in section 4.1 and do not allow for easy analytical calculations. This makes it necessary to thoroughly evaluate the physical process and the equations and find an effective approach to get the best parameters for the desired optimization goal.

In this work, complex surrogates based on artificial neural networks are used. Therefore some basic fundamentals of machine learning are illustrated and the general usage of these methods is discussed.

Machine Learning Fundamentals

The details of this chapter come from different sources and give a not complete bus sufficient context for the following work. Contents are collected and summarized from the book by Goodfellow (Goodfellow et al. 2016) and the extensive course by ECT* (Hjorth-Jensen et al. 2020). The fields of machine learning and artificial intelligence are closely connected. While machine learning focuses on learning relations from given data, artificial intelligence focuses more on the capability of a system to interact with its environment and learn from these interactions as well.

The methods presented and used in this thesis focus on machine learning and getting information from a structured data set. Data used in this approach was simulated and its labels and results are clearly given. The methods used are therefore from the subfield of supervised learning with labeled data sets. Artificial neural networks (ANN) are applied to the problem. Several layers are used. This classifies the problems further as deep learning problems. An illustration of the field and its different branches is displayed in Figure 3.3.

Our surrogate aims at predicting numerical values and our data is well labeled. We can therefore sort the problem into the supervised learning and regression category. Regression problems can generally be written as

$$y\left(\vec{x}, \vec{w}\right) = f\left(\sum_{j=i}^{M} w_j \Phi_j\left(\vec{x}\right)\right), \tag{3.5}$$

where f is an activation function, which defaults to the identity for linear regression, w_j are the adjustable weights of the problem, Φ_j are the nonlinear basis functions of the regression model and M is the number of basis functions.

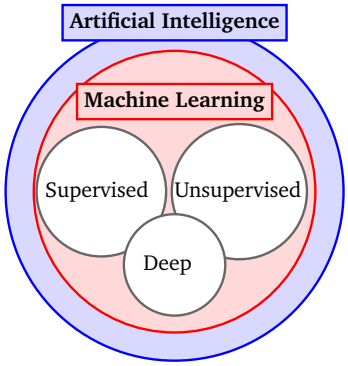

(a) Definitions of the different fields of artificial intelligence.

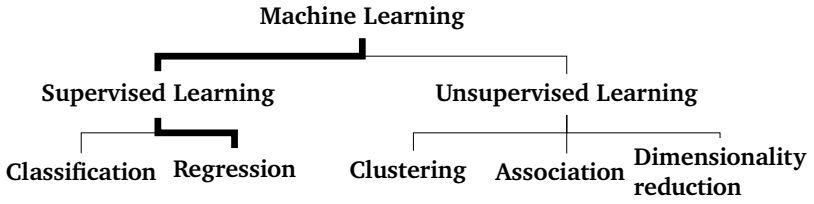

(b) Detailed tree structure of the different machine learning methods. As soon as a network introduces more than one hidden layer it gets deeper.

Figure 3.3.: Overview of the field of machine learning and its internal structure. Machine Learning has three subsets: supervised, unsupervised and deep learning. They are not mutually exclusive as deep learning methods can be applied in supervised learning problems.

The goal is to fit the given $y(\vec{x}, \vec{w})$ onto the data $y_0(\vec{x})$ by variation of $\vec{w}$. This variation is given by a loss function which has to be defined. The network is calculated by applying a minimization to the loss function.

The classical setup of a fully connected feed-forward network is displayed in Figure 3.4. A neural network has layers, each consisting of a number of neurons or nodes. "Fully connected" means that each neuron of a layer has a connection to each neuron of the following layer. Feed-forward means that the data flow is from the beginning to the end without any cycles or feedback mechanisms inside the network. When the number of layers is larger than two, we get hidden layers that are not visible from the outside. Then, a network can be regarded as being a deep neural network. The deeper a network gets, the more layers and neurons are to be considered. Thus, the complexity of the network increases, as well as the numerical costs, but also the capability of approximating even more complex functions.

Each neuron consists of three parts, the Aggregator – summing up the input from the previous neurons – the Activator – applying the activation function on the input– and the Distributor – passing the result of the activation function to each following neuron. It could be said that a piece of information (or parameters for a regression problem) has to follow a path through the network. The information that makes the network successful is the weights, which are applied to the connection between two neurons and which modify the output from the previous neurons. By setting the activation function f to identity, the regression problem from Equation 3.5 becomes a simple weighted sum and outputs the mean value. While the weights are essential to store information, the activation function and its non-linearity is important to get from a simple mean calculation towards a universal function approximation.

ANNs can have a variety of shapes, while the basic structure is always neurons ordered in layers. The weights of the connections and non-linear activation functions are essential for the approximation of complex relations.

Advantages and Drawbacks of Neural Networks

As mentioned, ANNs can approximate complex relations and functions, even if they are not explicitly given. If the parameters are chosen correctly, the network can learn and generalize these relations from input and output data alone. This includes potential higher-order dependencies of the output on the input parameters. The networks can be evaluated in milliseconds, and they can also be differentiated using gradient tape methods (Abadi et al. 2015). Both are essential parts of implementing optimization methods utilizing the

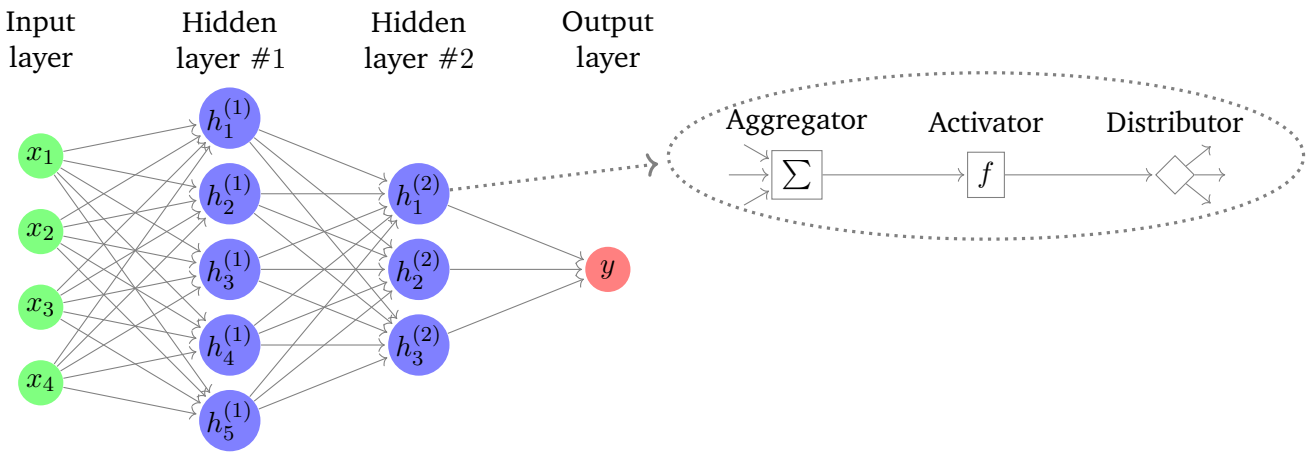

Figure 3.4.: Simple example for a neural network. A real network can vary in the number of hidden layers and the number of neurons in each layer. All paths, indicated by the arrows, have a weight. Each neuron can be separated into three smaller components, which describe the function in detail. The structure is displayed in the dotted part on the right side. The aggregator calculates the weighted sum which is then passed to the activator which applies the activation to the calculated sum. The values are passed through a distributor to the following neurons in the final step. A simple mean is calculated if the activator is set to the identity.

network.

ANNs have some drawbacks as well. First of all, ANNs are unphysical. In general, networks do not know anything about the underlying physics, except for physics-informed neural networks, which are out of scope of this thesis. It is, therefore, complicated or impossible to get the physical meaning of the approximated function. This can be counteracted by applying sensitivity analysis to the network as defined in section 3.4. The second drawback is the lack of an underlying theory. However, networks do work, it is known which parameters can be varied to achieve convergence, and networks can approximate models to arbitrary precision. But since a dedicated sound theory is lacking, networks created by different methods/scientists deviate in their structure and are therefore not fully reproducible. The third drawback is the high number of data points and extensive computing resources needed to create a converged neural network. It is unknown how much data is necessary for a defined number of input parameters nor how many neurons and layers are needed, which results in a larger number of more or less brute force methods to determine these hyperparameters.

Hyperparameter Tuning

A neural network is defined by its hyperparameters. They are fixed throughout the training but are variable on a meta-level. For each set of hyperparameters, the network performance changes. It is, therefore, difficult to get the perfect set of hyperparameters. To achieve a good set of hyperparameters, one must use experience and educated guesses or brute force, as many hyperparameter tuners do.

There is a large zoo of hyperparameters that can be tuned. The detailed set is discussed in subsection 6.1.2 and subsection 6.2.3. Due to the sheer amount of hyperparameters, their discussion is out of scope for this thesis. The reader is referred to further literature (Abadi et al. 2015, and the sources therein).

Advanced Methods

Some final remarks on advanced machine learning methods are important to understand the full scope. ANNs based on low fidelity or low dimensional simulations can easily support a low amount of high fidelity or high dimensional data model. This is done by a method called TRANSFER LEARNING (Spears et al. 2018, Sec. VIII C) (Humbird et al. 2020). A large amount of low-dimensional, quick-to-acquire data is used to pre-train the network and learn the underlying fundamental processes. The less copious data with a higher fidelity and prediction power is then used to retrain several layers while the rest is kept constant.

3.4. Sensitivity Analysis

Sensitivity analysis explores the relationship between model parameters and outcomes, while one or more parameters are perturbed over their plausible ranges or probability distributions, and corresponding effects on outcomes are examined.

In this work, two different disjunct methods are used to determine the sensitivities of the surrogate models. The combination of both methods mitigates difficulties in the interpretation of artificial neural networks. With this, the importance of specific parameters for a model can be evaluated. One way to quantify the impact of the model parameters upon the model output is with the variance-based global sensitivity analysis, also known as the SOBOL' METHOD (Sobol' 2001). The PAWN METHOD was used for a second sensitivity analysis to complement Sobol's method due to its shortcomings for the higher order of the input features.

3.4.1. Sobol' Method

A model, formally given by

$$Y = f\left(\vec{X}\right), \tag{3.6}$$

where $\vec{X}$ is the n-dimensional input vector of the model and Y its scalar output. The input vector is assumed to be independent, uniformly distributed, and scalable onto the n-dimensional hypercube. This is valid for the models developed in this work, which are based on the physical inputs.

The ANOVA representation of f is a decomposition of the model into 2^n summands, (Sobol' 2001, Sec. 2)

$$Y = f_0 + \sum_{i=1}^{n} f_i\left(X_i\right) + \sum_{i<j}^{n} f_{ij}\left(X_i, X_j\right) + \cdots + f_{1,2,\ldots,i,\ldots,n}\left(X_1, X_2, \ldots, X_i, \ldots, X_n\right). \tag{3.7}$$

The components can be determined from the model itself from the expected value $\mathbf{E}$ of the model by

$$\begin{aligned} f_0 &= \mathbf{E}\left(Y\right) \\ f_i &= \mathbf{E}\left(Y|X_i\right) - f_0 \\ f_{ij} &= \mathbf{E}\left(Y|X_i, X_j\right) - f_0 - f_i - f_j \\ &\vdots \end{aligned} \tag{3.8}$$

Herein f_i describes the effect on Y varying only the i-th component, and f_{ij} gives the effect on Y if the i-th and j-th components are varied simultaneously. Squaring and integrating each component yields the conditional variance $\mathbf{V}$ of the model

$$\mathbf{V} = \int f^2 \,\mathrm{d}X - f_0^2 \quad \text{and} \quad \mathbf{V}_{1,\ldots,n} = \int f_{1,2,\ldots,n}^2 \,\mathrm{d}X_1 \ldots \mathrm{d}X_n.$$

For these variances, the additivity of the integral holds and

$$\mathbf{V} = \sum_{i=1}^{n} \sum_{i<j}^{n} V_{1,2,\ldots,n}.$$

This allows defining the Sobol' indices as

$$S_{1,2,\ldots,n} = \frac{\mathbf{V}_{1,2,\ldots,n}}{\mathbf{V}}. \tag{3.9}$$

These indices are also known as global sensitivity indices. They describe how much variation of the output model Y can be explained by the variance of an input variable or by the variation of a combination of input variables. If only a variation of one input variable is used, it is called first-order influence, and if two input variables are varied, it is the second-order, and so on. The sum of these Sobol' indices is by construction one. If the sum is smaller than one for a defined number of indices, then the indices' order cannot explain the full model variations.

The different components can also be expressed through the total Sobol' indices, which are faster to calculate. However, they only estimate the total variation caused by a single input, including the interaction terms, which are counted several times. Its sum is, therefore, not normalized to one. The Sobol' indices are calculated utilizing a Monte Carlo sampling of parameters and the corresponding model outputs, subsequently used to determine the relevant expected values and variances. This is problematic for the higher-order interaction terms since the number of necessary samples increases, and the curse of dimensionality hinders further evaluation. The interested reader is referred to the publications from Sobol' and Satelli for further details (Sobol' 2001) (Saltelli 2002) (Saltelli et al. 2010).

Sobol's method assumes that the output is a smooth function of the input parameters and may not be appropriate for non-smooth or discontinuous functions. It also assumes that the input parameters are independent, which may not be the case in some systems, especially for systems utilizing complex representations. This makes it necessary to use a second method to evaluate sensitivities.

3.4.2. PAWN Method

The PAWN method introduced by Pianosi et al. (Pianosi et al. 2015) uses a different approach for the case, in which the variance might not be a good measure for the outcome of a system. Its idea is that the influence of a given input, measured as the variation in the output's cumulative distribution function, is determined when the uncertainty about that input is removed. This is done by computing the Kolmogorov-Smirnov test **KS** between the model output and the conditional distribution function when x_i is fixed.

$$\mathbf{KS}\left(x_i\right) = \max_{y} \left| F_y(y) - F_{y|x_i}(y) \right|. \tag{3.10}$$

Here F are the cumulative distribution functions for the conditions in the index. They can be approximated easily numerically but are also independent of statistical momenta in the data, which is their main difference from the Sobol' method. Furthermore, we can easily see that the PAWN calculation has to be done for several x_i since the result changes for different x_i. The PAWN indices T_i can then be found by any measure **measure** deemed appropriate to extract the data from the resulting data set (e.g. maximum, median, mean),

$$T_i = \underset{x_i}{\mathbf{measure}} \left[\mathbf{KS}\left(x_i\right)\right]. \tag{3.11}$$

It utilizes the traits of the Cumulative Distribution Functions with similar Monte Carlo sampling as for the Sobol' indices, giving a different approach to determine the sensitivity of a model. A combination of these two methods was also proposed by Baroni et al. (Baroni et al. 2020).

4. Dimensional Reduction and Cut-Off Modeling

"Electricity flows,
Charged particles dance and glow,
Maxwell's dance with Vlasov."

This chapter takes a deeper look into some advanced aspects of the fundamentals. First, the equations governing the collision-free part of the TNSA process are discussed. The dimensionality of the governing Maxwell-Vlasov equation system is reduced, and the resulting quantities are interpreted and used for an alternative representation of the underlying physics. The second part of this chapter is an overview of the Single Quantity Variation model. It is introduced, and its limitations are identified.

4.1. Maxwell-Vlasov System

This chapter investigates the Maxwell Vlasov System to identify relevant parameters utilizing the Buckingham Pi Theorem (Buckingham 1914) (Buckingham 1915). The assumption is that the mean free path is larger than the target thickness and the whole process can therefore be assumed as collision-free (Mulser et al. 2010, Sec. 8.3, p. 363-364). The system governing the high-power laser interaction with matter under the condition of collisionless interaction is the Maxwell-Vlasov system given in Equation 4.1 – Equation 4.5.

$$\nabla \cdot \vec{B} = 0 \tag{4.1}$$

$$\nabla \cdot \vec{E} = \frac{\varrho}{\varepsilon_0} \tag{4.2}$$

$$\nabla \times \vec{E} = -\frac{\partial \vec{B}}{\partial t} \tag{4.3}$$

$$\nabla \times \vec{B} = \mu_0 \vec{j} + \mu_0 \varepsilon_0 \frac{\partial \vec{E}}{\partial t} \tag{4.4}$$

$$0 = \frac{\partial f_\alpha}{\partial t} + \vec{v}_\alpha \cdot \nabla f_\alpha + q_\alpha \left(\vec{E} + \vec{v}_\alpha \times \vec{B} \right) \cdot \frac{\partial f_\alpha}{\partial \vec{p}} \tag{4.5}$$

The charge density ϱ, the current $\vec{j}$, and the particle's velocity in the system can be generally described by the equations given in Equation 4.6.

$$\varrho = \int \sum_\alpha f_\alpha \mathrm{d}^3\vec{p} \qquad \vec{j} = \int \sum_\alpha f_\alpha v_\alpha \mathrm{d}^3\vec{p} \qquad v_\alpha = \frac{\vec{p}}{m_\alpha} \left(1 + \frac{p^2}{m_\alpha^2 c^2} \right)^{-1/2} \tag{4.6}$$

The charge density f_α can be expressed by the product of a dimensionless distribution function $\widehat{f}_\alpha$ with the peak charge distribution n_α as $f_\alpha = n_\alpha \widehat{f}_\alpha$. The laser fields oscillate with the laser frequency ω_L.

$$\vec{E}\left(\vec{r},t\right) = E_0 \cdot \Omega\left(\vec{r},t\right) \widehat{\vec{E}} \cos\left(\vec{k} \cdot \vec{r} - \omega_L t + \Phi \right) \quad \text{and} \quad \vec{B}\left(\vec{x},t\right) = \frac{1}{c} \vec{k} \times \vec{E}, \tag{4.7}$$

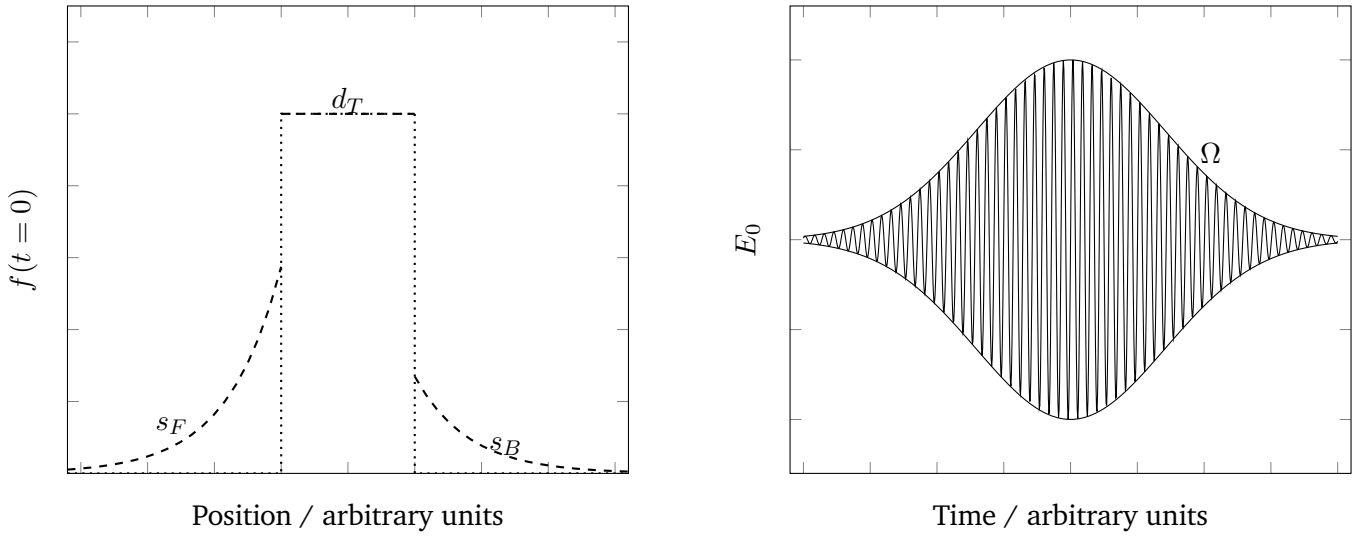

(a) Spatial distribution of the plasma components at $t = 0$. Preplasma with scale length S_F and skirt with scale length S_B included. Momentum initialization is dependent on the particle species.

(b) Laser envelope and relationship between envelope and oscillation frequency.

Figure 4.1.: Overview sketches of the plasma distribution function and the assumed Gaussian laser pulses.

where E_0 is the amplitude of the wave, $\vec{k}$ the wave vector, Φ a phase correction, Ω the envelope of the electric field as indicated in Figure 4.1 (b), and $\vec{B}$ the corresponding magnetic field. This system of equations can only properly be solved with numerical methods. The method of choice in this work is the PIC method described in section 3.1. As mentioned, the system under investigation has several quantities that must be considered. These quantities can be identified by applying normalizations through problem-relevant quantities. A rescaled electric field can also express the magnetic field.

$$\tilde{t} = \frac{t}{\tau} \qquad \tilde{r} = \frac{\vec{r}}{L} \qquad \vec{E} = E_0 \hat{\vec{E}}$$
$$\tilde{p} = \frac{\vec{p}}{p_0} \qquad p_0 = \frac{eE_0}{\omega} \qquad \vec{B} = \frac{E_0}{c} \hat{\vec{B}}$$

These substitutions have to be inserted into the Maxwell-Vlasov EQS. The substituted equations are then minimized and the fundamental quantities can be extracted. They are displayed in Table 4.1.

4.1.1. Buckingham Pi Theorem

The Buckingham Pi Theorem allows reducing the system of relevant physical quantities to effective dimensionless quantities. Their construction directly results from the theorem and are labeled as Π_i. This construction is sketched in Buckinghams publications as well. The theorem establishes a connection between the dimensionality of the equation and the physical quantities. Writing this in a formal way results in the two equations

that these parameters have to follow:

$$\Pi_j = \prod_{i=1}^{n} Q_i^{a_{ij}} \tag{4.8}$$

$$0 = \sum_{i=1}^{n} a_{ij}, \tag{4.9}$$

where Q_i denotes the dimensional parameter of the problem. The proof assumes dimensional homogeneity of equations and can be found in the corresponding paper (Buckingham 1914, pp. 350-351). Construction of the Π parameters can be achieved by following the steps below.

1. List problem's dimensional parameters
2. List primary dimensions
3. Calculate the number of dimensionless groups
4. Choose j repeating variables
5. Construct dimensionless groups

Applying Buckingham on Maxwell-Vlasov EQS

Now the theorem is applied to reduce the EQS. The first step is to list the quantities and their corresponding fundamental dimension. The Maxwell-Vlasov EQS which is to be solved is given in SI units. Table 4.1 lists the

Table 4.1.: Overview of the dimensional quantities of the Maxwell-Vlasov EQS. Dimensions are listed in SI base dimensions. Buckingham Π parameters are calculated by defining primary quantities used multiplicatively in each parameter. N is the number of parameters, and j gives the number of base dimensions. The SI base dimensions are T: Time, L: Length, C: Current, M: Mass

	Quantity	sign	Dimensions	Type
1	Laser frequency	ω_L	T^{-1}	Primary
2	Pulse length	τ_L	T	
3	Scale length	L	L	
4	Permeability	μ_0	$\mathrm{M}^1\ \mathrm{L}^1\ \mathrm{T}^{-2}\ \mathrm{C}^{-2}$	Primary
5	Permittivity	ε_0	$\mathrm{M}^{-1}\ \mathrm{L}^{-3}\ \mathrm{T}^4\ \mathrm{C}^2$	Primary
6	Charge density	n_α	$\mathrm{C}^1\ \mathrm{T}^1\ \mathrm{L}^{-3}$	
7	Charge to mass ratio	q/m	$\mathrm{C}^1\ \mathrm{T}^1\ \mathrm{M}^{-1}$	Primary
8	Electric field	E_0	$\mathrm{M}^1\ \mathrm{L}^1\ \mathrm{C}^{-1}\ \mathrm{T}^{-3}$	
		$N = 8$	$j = 4$	

problem's quantities and the relevant base dimensions used in the problem. The difference $N - j$ gives the number of Π parameters for this system.

The next step is to choose j repeating or primary variables relevant to the problem. No definite recipe for choosing the correct j values exists. In this work, the used primary quantities are marked in Table 4.1. It is important to choose 4 parameters that somehow describe the dynamics and traits of the problem as well as possible such that no trivial solutions are acquired. In this case, the laser frequency, the permittivity, the permeability, and the charge-to-mass ratio. Using this and Equation 4.8 allows to write the construction

relations of the Π parameters.

$$\Pi_1 = \omega_L^{a_1} \varepsilon_0^{b_1} \mu_0^{c_1} (q/m)_\alpha^{d_1} \cdot \tau_L^1 \tag{4.10}$$
$$\Pi_2 = \omega_L^{a_2} \varepsilon_0^{b_2} \mu_0^{c_2} (q/m)_\alpha^{d_2} \cdot L^1 \tag{4.11}$$
$$\Pi_3 = \omega_L^{a_3} \varepsilon_0^{b_3} \mu_0^{c_3} (q/m)_\alpha^{d_3} \cdot n_\alpha^1 \tag{4.12}$$
$$\Pi_4 = \omega_L^{a_4} \varepsilon_0^{b_4} \mu_0^{c_4} (q/m)_\alpha^{d_4} \cdot E_0^1 \tag{4.13}$$

Taking these Π_i and the condition from Equation 4.9 allows for constructing a linear equation system to determine the unknown exponents. The following equation shows the construction for Π_1, this is analog for the other parameters. Inserting the corresponding dimension into the construction yields Equation 4.14

$$[\Pi_1] = \left\{T^{-1}\right\}^{a_1} \left\{M^{-1}L^{-3}T^4C^2\right\}^{b_1} \left\{M^1L^1T^{-2}C^{-2}\right\}^{c_1} \left\{C^1T^1M^{-1}\right\}^{d_1} \{T\}^1 \stackrel{!}{=} 1 \tag{4.14}$$

This can be rewritten as a linear equation system using the condition given in Equation 4.9. Solving it then yields,

$$\begin{array}{l} T: \\ L: \\ M: \\ C: \end{array} \left|\begin{array}{ccccc} -a_1 & 4b_1 & -2c_1 & d_1 & = -1 \\ & -3b_1 & c_1 & & = 0 \\ & -1b_1 & c_1 & -1d_1 & = 0 \\ & 2b_1 & -2c_1 & d_1 & = 0 \end{array}\right| \Rightarrow \left|\begin{array}{l} a_1 = 1 \\ b_1 = 0 \\ c_1 = 0 \\ d_1 = 0 \end{array}\right| \Rightarrow \Pi_1 = \omega_L \tau_L \tag{4.15}$$

Solving the EQS and resubstituting the values into the original equation yields the final value for the Π_1. Repeating the above steps for all Π_i then yields a set of dimensionless parameters.

$$\Pi_1 = \omega_\mathrm{L} \tau_\mathrm{L} \tag{4.16}$$
$$\Pi_2 = \omega_\mathrm{L} L \sqrt{\mu_0 \varepsilon_0} = \frac{\omega_\mathrm{L} L}{c} \tag{4.17}$$
$$\Pi_3 = \frac{q_\alpha n_\alpha}{\varepsilon_0 m_\alpha \omega_\mathrm{L}^2} = \begin{cases} \dfrac{n_\mathrm{e} e}{\varepsilon_0 m_\mathrm{e} \omega_\mathrm{L}^2} & \text{for electrons} \\ \dfrac{n_\alpha Z_\alpha e}{\varepsilon_0 m_\alpha \omega_\mathrm{L}^2} & \text{for ions} \end{cases} \tag{4.18}$$
$$\Pi_4 = \frac{q_\alpha E_0}{m_\alpha \omega_\mathrm{L}} \sqrt{\mu_0 \varepsilon_0} = \begin{cases} \dfrac{E_0}{\omega_\mathrm{L} c} \dfrac{e}{m_\mathrm{e}} & \text{for electrons} \\ \dfrac{E_0}{\omega_\mathrm{L} c} \dfrac{Z_i e}{m_i} & \text{for ions} \end{cases} \tag{4.19}$$

Some remarks on the notation: n_α also contains the charge of the corresponding particle type, $q_\alpha n_\alpha = N_\alpha Z_\alpha^2 e^2$, where N_α is the particle density. Two of the resulting parameters are ambiguous since they contain the Z/m ratio which yields different values for the different particle species.

The calculated Πs are mathematical quantities and have a physical meaning. Each of them describes a different relevant quantity of the system.

- Π_1 measures the number of oscillations in the laser field.
- Π_2 describes the irradiation and focus size of the laser.
- Π_3 is the ratio of the electron density to the critical plasma density, measuring the plasma optical density. It combines the laser with the target.

- Π_4 describes each species' particle dynamic inside the laser's electric field. For electrons, Π_4 is identical to the dimensionless quiver velocity a_0 (Gibbon 2005, Eq. 2.19, p. 29). The meaning is equivalent for the different ion species.

These quantities are sufficient to express the Maxwell Vlasov EQS in an alternative form:

$$\tilde{\nabla} \cdot \widehat{\vec{B}} = 0 \tag{4.20}$$

$$\tilde{\nabla} \cdot \widehat{\vec{E}} = \underbrace{4\pi \int \sum_{\alpha} \frac{\Pi_2 \cdot \Pi_{3\alpha}}{\Pi_{4\alpha}} \, \mathrm{d}^3 \, \tilde{p}}_{=0 \text{ for } t=0} \tag{4.21}$$

$$\tilde{\nabla} \times \widehat{\vec{E}} = -\frac{\Pi_2}{\Pi_1} \frac{\partial \widehat{\vec{B}}}{\partial \tilde{t}} \tag{4.22}$$

$$\tilde{\nabla} \times \widehat{\vec{B}} = \frac{\Pi_2}{\Pi_1} \frac{\partial \widehat{\vec{E}}}{\partial \tilde{t}} + \int \sum_{\alpha} \frac{4\pi \Pi_2 \Pi_{3\alpha} \tilde{p}}{\sqrt{\tilde{p}^2 \Pi_{4\alpha}^2 + 1}} \widehat{f}_{\alpha} \, \mathrm{d}^3 \, \tilde{p} \tag{4.23}$$

$$0 = \frac{1}{\Pi_1} \frac{\partial \widehat{f}_{\alpha}}{\partial \tilde{t}} + \frac{1}{\Pi_2} \frac{\Pi_{4\alpha} \tilde{p}}{\sqrt{\tilde{p}^2 \Pi_{4\alpha}^2 + 1}} \frac{\partial \widehat{f}_{\alpha}}{\partial \tilde{r}} + \left(Z_{\alpha} \widehat{\vec{E}} + \frac{\Pi_{4\alpha}}{\sqrt{\tilde{p}^2 \Pi_{4\alpha}^2 + 1}} \widetilde{\vec{p}} \times \widehat{\vec{B}} \right) \frac{\partial \widehat{f}_{\alpha}}{\partial \widetilde{\vec{p}}} \tag{4.24}$$

The Z_{α} indicates the charge number of the species normalized to the elementary charge (e.g. for electron: $Z_e = -1$ or proton: $Z_p = +1$) The similitude only gives conditions for the system before a dynamical process or time evolution happens such that the full numerical solution for a set of parameters still has to be acquired. Since this set of equations defines the system at $t = 0$, where the system is still neutral, one can further assume, that both divergence equations are 0.

4.1.2. Scaling of Systems

Furthermore, if the different Π_i are the same, then all PDEs have the same prefactor and the corresponding systems are *similar*. These similarity conditions can be used to scale a system, reducing the number of simulations needed. This is because if the parameters are constant, the particle dynamics are the same and only one simulation is needed for all constant Π_i. These similar systems S1 and S2 can be determined by equating the quantities of the systems. Exemplary for Π_1:

$$\Pi_1^{\mathrm{S1}} = \Pi_1^{\mathrm{S2}} \quad \Rightarrow \quad \omega_L^{\mathrm{S1}} \tau_L^{\mathrm{S1}} = \omega_L^{\mathrm{S2}} \tau_L^{\mathrm{S2}} \tag{4.25}$$

In theory, as long as $\Pi_1, \Pi_2, \Pi_{3\alpha}, \Pi_{4\alpha}$ are the same, systems with different physical parameters are similar.

Further, the similarity can be made more powerful, e.g. by reducing the number of Π_i. One important example from literature is the S-similarity(Pukhov et al. 2006)(Ryutov et al. 2006b)(Ryutov et al. 2006a). In the limit for high-power lasers and relativistic electrons where $a_0 \gg 1$ (or $\Pi_{4e} \gg 1$), the square root terms can be simplified:

$$\sqrt{\tilde{p}^2 \Pi_{4e}^2 + 1} \overset{\Pi_{4e}^2 \gg 1}{\approx} \Pi_{4e} \tilde{p} \tag{4.26}$$

The uncertainty of this approximation is displayed in Figure 4.2. Inserting this into the Maxwell-Vlasov equation reduces the number of Π parameters and therefore the number of constraints of the EQS. The quotient between Π_3 and Π_4 can be used to eliminate both variables from the corresponding electron equations:

$$\Pi_S = \Pi_{3e} / \Pi_{4e} = \frac{\widehat{n}_e e c}{\omega_L E_0} \tag{4.27}$$

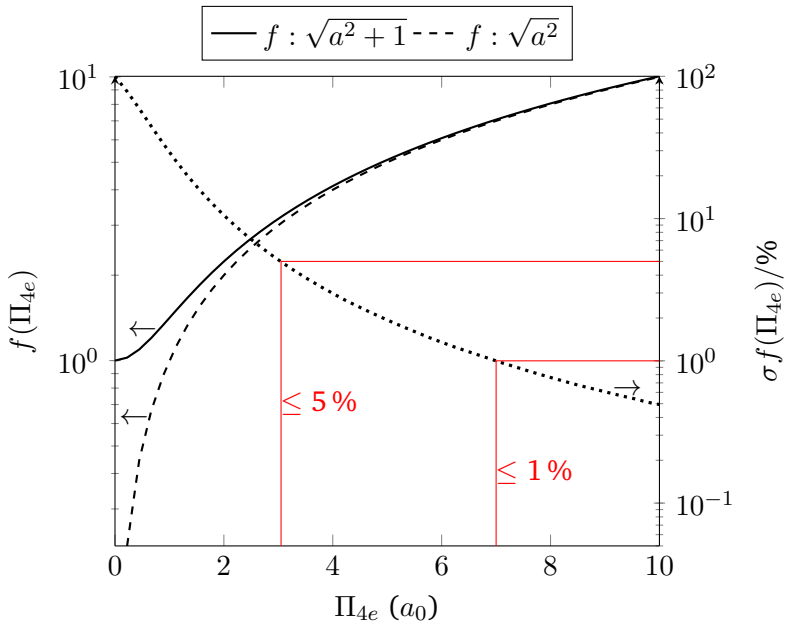

Figure 4.2.: Validity of the reduced similarity. The validity of the solution increases with higher a_0. The dotted line shows the relative uncertainty of the approximation to the real solution. The red lines indicate the area where this uncertainty is below the threshold of $5\,\%$ to $1\,\%$.

Further on it has to be taken into account that if ions are implemented with a momentum of 0, and since they have a higher mass than the corresponding electrons, they can be assumed frozen.

$$m_e \ll m_i \tag{4.28}$$

This decouples the electrons from the ions until the ions start moving. This means that the ion component in Π_3 does not contribute to the magnetic field and is therefore negligible.

4.1.3. Correlating Dimensionless Parameters and Physical Input

The system has a dedicated number of Π Parameters which must be considered. Each particle species has its own Π_3 and Π_4. In the case of a liquid leaf target investigated here, the multiplicity is at least 4: electrons, oxygen, hydrogen, and deuterium. This ambiguity can be resolved by considering the ratio of H_2O and D_2O molecules. The electron count is directly correlated to the charge states of the ions constituting the plasma (refer to section 2.2). Due to the low ionization energy (Table 2.1), hydrogen and deuterium are assumed to be fully ionized, the ambiguity in Π_3 and Π_4 can then quickly be broken down on the mean ionization state of oxygen Z_{eff} and the mixture between the lighter ions labeled mix. Defining Π_3 via oxygen and Π_4 via electrons allows resolving the ambiguity by inserting the conditions. The results are given in Table 4.2. The definitions of the Π_i are given in Equation 4.16 – Equation 4.17. Taking the definitions, inserting the mentioned particle species relations, and correcting the laser intensity due to the oblique incidence angle allows rewriting the definitions as Equation 4.29 – Equation 4.30.

$$\Pi_1 = \frac{2\pi c \tau_{\text{L}}}{\lambda_{\text{L}}} \qquad \Pi_2 = \frac{2\pi \text{FWHM}}{\lambda_{\text{L}}} \tag{4.29}$$

$$\Pi_3 = \frac{Z_{\text{eff}}^2 e^2 n_O \lambda_{\text{L}}^2}{\varepsilon_0 4\pi^2 m_O c^2} \qquad \Pi_4 = \left(\frac{E_{\text{L}} \lambda_{\text{L}}^2 \sin(\Theta_{\text{L}})}{\tau_{\text{L}} \pi \text{FWHM}^2 \cdot 1.37 \times 10^{18}} \right)^2 \tag{4.30}$$

Table 4.2.: Resolving the of Π parameters' ambiguity.

Parameter	Definition
Π_1	$\omega_L \tau_\mathrm{L}$
Π_2	$\omega_L L/c$
Π_{3O}	$Z_O^{\mathrm{eff}}/m_O \times n_O/{\omega_L}^2$
Π_{3e}	$\Pi_{3O} \times \left(Z_O^{\mathrm{eff}} + 2\right) \times \frac{m_O}{m_e} \cdot \frac{q_e}{e \cdot Z_O^{\mathrm{eff}}}$
Π_{3H}	$\Pi_{3O} \times 2\,\mathrm{mix} \times \frac{m_O}{m_H} \cdot \frac{q_H}{e \cdot Z_O^{\mathrm{eff}}}$
Π_{3D}	$\Pi_{3O} \times 2\,(1 - \mathrm{mix}) \times \frac{m_O}{m_D} \cdot \frac{q_D}{e \cdot Z_O^{\mathrm{eff}}}$
Π_{4e}	$q_e/m_e \times E_0/\omega_L c\ (a_0)$
Π_{4H}	$\Pi_{4e} \times \frac{m_e}{m_H} \cdot \frac{q_H}{q_e}$
Π_{4D}	$\Pi_{4e} \times \frac{m_e}{m_D} \cdot \frac{q_D}{q_e}$
Π_{4O}	$\Pi_{4e} \times \frac{m_e}{m_O} \cdot \frac{Z_O^{\mathrm{eff}}}{q_e}$

Table 4.3.: Two different parameterizations for describing the Maxwell-Vlasov EQS for a Liquid-Leaf Target. The analysis has shown that nine parameters are needed.

	Physical Parametrization	Buckingham Parametrization
1	Laser Pulse Time	Π_1
2	Laser Irradiation Size	Π_2
3	Laser Wavelength	Π_{3O}
4	Laser Energy	Π_{4e}
5	Ionization of oxygen Z_O^{eff}	Ionization of oxygen Z_O^{eff}
6	D/H Mixtures	D/H Mixtures
7	Laser Incidence Angle Θ_L	Laser Incidence Angle Θ_L
8	Laser Polarization	Laser Polarization
9	Plasma Slab Thickness	Plasma Slab Thickness

The final count of relevant quantities to describe the full H_2O/D_2O system is nine: Four Π_i, two parameters to deal with the ambiguity Z_O^{eff} and the mixture parameters, one parameter for the plasma slab d_T (particle density is fixed) and two for dealing with laser's polarization: Selection whether p / s linear polarization and the incidence angle Θ_L. The system can therefore be fully described by taking nine parameters into account, which is the number of parameters used for the simulation and modeling in subsection 6.1.1 and subsection 6.1.2. Two problem parametrizations are given in Table 4.3

Concluding this section: Firstly, dimension-free parameters have been found that describe the similarity of the system. Secondly, scaling based on the similarities and further reduction was investigated. Thirdly, the number of relevant parameters to describe the TNSA system for the collision-free state is nine. Fourthly, two different parametrizations for the simulations are given. These results go directly into the simulation setup and the evaluation presented in chapter 6.

4.2. Single Quantity Variation

An important step in modeling was achieved in 2021 (Zimmer et al. 2021). This study used a large number of experimental data to determine empirical scalings of proton cut-off energies.

Sources in literature (e.g. (Fuchs et al. 2005) (Torrisi 2015)) are often governed by the ponderomotive scaling, which correlates the cut-off energy to laser's a_0 and therefore also to the peak intensity I_0. The resulting relation $E_c \propto \sqrt{I_0}$ works if used in a system with similar parameters. The predictions then match the observations, but this model breaks if used to compare different systems. This is due to the multi-parameter input and variations in the individual quantities constituting the peak intensity. In the mentioned paper, the deviation of the experimental data from this model is up to $\pm 400\,\%$.

It could be shown that the prediction of the cut-off energies can be improved by splitting the intensity into its constituting components and fitting each under the constraint that the others remain constant. This single quantity variation results in a model that works well for the training data. The resulting fits can then be written as a product of the fitting functions.

$$\frac{E_c^*}{E_c^r} = \left(\frac{E_L^*}{E_L^r}\right)^{0.59\pm0.03} \left(\frac{\tau_L^*}{\tau_L^r}\right)^{-0.090\pm0.008} \left(\frac{r_s^*}{r_s^r}\right)^{-0.58\pm0.16} \left(\frac{d_T^*}{d_T^r}\right)^{-0.16\pm0.10}, \tag{4.31}$$

where E_c is the cut-off energy, E_L the laser energy, τ_L the laser pulse length, r_s the irradiation spot size of the laser, and d_T the target's thickness. * indicates the new system, while ^{r} indicates the reference system from which the new system is extrapolated. It is important to note that the model's quality depends on the selected reference system. It can only properly determine the cut-off energy if the selected reference system is as close to the new one. Mitigating this bias is possible by sampling different systems and statistically evaluating them, effectively bootstrapping the model on a discrete basis. Further uncertainties are introduced with the uncertainty on the fit parameters in the exponent and with the assumption that the entire system can be broken down into a product of power laws, neglecting higher-ordered dependencies.

It gives a lower estimate for the cut-off energy than other models (J. Schreiber et al. 2006) or (Fuchs et al. 2005) and is the first step towards a global modeling approach. The major limitation of assuming all other input quantities as a constant is overcome by the model devised in section 6.1.

5. Automatic Radiochromic Film Stack Evaluation

"Data cleaning first,
Then comes pre-processing next,
Modeling begins."

Characterization of laser-based ion sources and the corresponding optimization towards improved performance and pulse shaping demands high-resolution measurements of the three-dimensional distribution of laser-accelerated ion beams. If the ion beam traits can not be determined, any effort to find descriptions and optimizations for the full process will be more difficult, if not impossible. Numerical approaches, namely PIC simulations, are necessary to complement experiments with precise and ideal cases to fill regions of void in the global parameter space. Although numerical simulations are important, they are insufficient since they are either numerically expensive or do not allow for exact predictions of the real world, as already discussed in section 3.1.

One way to measure the entire distribution, spatially and in the momentum space radiochromic films (RCFs) (Soares 2009). RCFs are and will likely be the essential tool for the complete beam evaluation since they are in use for over two decades (Snavely et al. 2000) now and have several developments and research done with and about them. The most critical diagnostic is currently implemented with the well-known behavior and the following three points.

The first reason is their inherent safety from electromagnetic pulses, accompanying the laser-plasma interaction during the ion acceleration process. This is due to a lack of electronic components needed to operate RCF stacks.

The second reason is the possibility for absolute calibration of the RCFs that allows the determination of the total dose deposited. This enables a wide range of cross-calibration applications for other diagnostics.

The third reason is the ability to resolve the ion bunches' spatial and spectral distributions. No other diagnostic can deliver the same amount of information about an experiment in a single shot. A detailed discussion of different ion detection methods and their advantages can be found in the referenced thesis by Markus Hesse (Hesse 2022, Ch. 3).

Most applications require reproducible beams with high repetition rates, but the other beam parameters might broadly vary. RCF-based detectors are mainly assembled by hand and can only be used for single shots. For this reason, they are not practical as the primary diagnostic for high repetition rate experiments. However, many new detectors under development for high repetition rate laser ion acceleration experiments cannot be calibrated in advance. Therefore they need to be cross-calibrated using RCFs (Hesse et al. 2021) (Green et al. 2011) (Metzkes, Karsch, et al. 2012) (Huault et al. 2019) (Dover et al. 2017) (Metzkes, Zeil, et al. 2016).

An automated evaluation and reconstruction procedure of digitized RCFs is introduced to foster the modeling and increase experimental validation capabilities. This procedure is implemented in python and provided (Schmitz and Endl 2022). It comprises an algorithm for evaluating RCFs, allowing the reproducible evaluation of data and its application to large data sets. The contents of this chapter are also published by the author (Schmitz, Metternich, et al. 2022).

5.1. Radiochromic Film Stacks – Foundations and Limitations

First, a description of radiochromic films and their principle of operation is given which serves as a basis to discuss the limitations and problems in the second part.

5.1.1. Interaction of Radiation with RCF Stacks

When a RCF is irradiated, it undergoes a chemical process called polymerization, which leads to a change in the optical density (OD) of the RCF (Niroomand-Rad et al. 1998; Zhang et al. 2018). The change of the OD correlates directly to the deposited energy into this specific RCF. The deposited energy in relation to the irradiated mass is also known as dose (D). Using the stopping power relations allows us to determine the initial particle energies and estimate the corresponding number of particles.

The energy spectrum of laser plasma accelerated ions is generally not monoenergetic. This profile can be measured if several individual RCFs are combined into one RCF stack as indicated in Figure 5.4a. This configuration allows to measure the dose in dependence on the particle's penetration depth and to calculate the corresponding number of particles. The penetration depth correlates directly to the energy of the particles.

When measuring TNSA ion beams, it is important to consider the dose contribution on the RCF from all impinging types of radiation. TNSA beams consist of several ion species and electrons while additional gamma radiation is created during the laser-plasma interaction. Different types of radiation cause different changes in the OD of the individual RCF layer, the total OD can be expressed as a superposition of these contributions:

$$\mathrm{OD}_{\mathrm{total}} = \mathrm{OD}_{\mathrm{film}} + \mathrm{OD}_{\mathrm{ion}} + \mathrm{OD}_{\gamma} + \mathrm{OD}_{\mathrm{electron}} \tag{5.1}$$

where $\mathrm{OD}_{\mathrm{film}}$ is the original OD before irradiation, $\mathrm{OD}_{\mathrm{ion}}$ is the effect caused by ion irradiaton, OD_{γ} is the change caused by gamma radiation and $\mathrm{OD}_{\mathrm{electron}}$ is the change induced by electrons. A consistent evaluation is based on finding the area of the RCF, where the ions deposit energy. Ions deposit more energy inside a RCF than electrons or gamma radiation. Therefore, the area with the highest level of OD is of relevance (Clark et al. 2000; Hey et al. 2008). Electrons and gamma radiation induce a parasitic signal that must be filtered out.

The electrons are separated into two parts: the first has high energy and consists of the electrons leaving the target before the charge separation is built up. They can penetrate the full stack and their signal can be seen on EBT3 layers with a higher sensitivity to any kind of ionizing radiation than HD-v2 layers. The second part consists of electrons co-moving with the accelerated ions. Their velocities are the same as the ion distribution and they are stopped in the first passive layer, therefore not contributing to the measured signal. The gamma radiation is assumed to produce a homogeneous signal on the specific layer. The angular distribution of the photons (Brady et al. 2014; Capdessus et al. 2013; Ridgers et al. 2012; X.-B. Wang et al. 2020; Vyskočil et al. 2020) has two characteristic intensity peaks at relatively large angles. In between these angles, where the RCFs are located, the intensity of gamma rays is relatively low and comparably constant, when projected on the RCFs.

Concluding the shapes for the OD components: the gamma component comprised a constant offset, while the electron component has a low intensity while having a finite spatial distribution. The ion component has a high intensity with a finite spatial distribution.

A further remark on the differences which are visible in Figure 5.4 and, for example, in the work of F. Wagner (Wagner, Deppert, et al. 2016, Fig. 4b): Due to a decrease in energy deposition from ions and a lower number of particles, the contribution of the ion part gets less dominant the further they penetrate the stack. The electron contribution from the previously mentioned high energy part stays with a comparatively similar size and intensity, becoming measurable and more dominant on the later high-sensitivity films.

5.1.2. Limitations and Complications with RCF Evaluation

As displayed above, one essential step for the evaluation is to separate the ion signal from the parasitic contributions. This already gives the first problematic point for RCF evaluations. The current approach for filtering the measurement data relies rather on an educated guess than a systematic method. Scientists select the irradiated area on the RCFs bye eye based on the investigated radiation type. This manual selection might lead to incorrect doses and nonreproducible results, biasing the result. Furthermore, it increases the evaluation time by a significant proportion. If the aforementioned discrimination is not done properly, even fundamental properties of the spectrum, e.g. the cut-off energy, might change significantly, due to a mismatch in the stack's stopping power relations.

The dose from the ions is the core quantity for calculating the energy spectrum. A spectrum is verified by matching a calculated dose, created by the spectrum, with the measured dose. If there are deviations in the calibration or in the response function then the dose varies. If the irradiated areas vary, which can happen since the current state of the art is the manual selection of the irradiated areas, then the dose varies. Hence, the resulting fit parameters for the spectrum will vary as well. Therefore, a consistent and reproducible determination of the area irradiated by the ion beam is of utmost importance.

The user's choice of the irradiated area by ions introduces a measurable bias in the evaluation results. This bias was measured in Barbara Endl's Bachelor's Thesis (Endl 2021, Sec. 2.2.2, p. 8), created at TEMF and supervised by the author. For this study, the manually selected ion areas, defined by several scientists, were evaluated and the deposited energy in MeV for each pixel was calculated.

4 different experts (persons A-D) on RCFs participated in this study. Each expert received 2 different data sets (one shot each) to evaluate. Results of the experts' segmentations are presented in Fig. 5.1. The differences in the segmentations of the ion beam area decrease with the penetration depth, the user bias, therefore, gets less with later layers.

Some example results of the thesis are displayed in Figure 5.2. The results of two full RCF stacks employed at an experiment at the PHELIX laser at GSI, Darmstadt were evaluated, which results in a total of 15 investigated films. Displayed are only two representatives of the data sets: Figure 5.2a shows the original scan from image No 12, a later layer with low irradiation in one of the data sets used for this study. f the experts did not evaluate thislayer, because they did not identify a signal on the layer. If the data is taken into ac done by users A, C, and the algorithm, enhancing the scaling, converting to hue, and applying the filter methods, allowed to determine an existing signal. These are displayed in Figure 5.2b – Figure 5.2d.

The results do not deviate as much for a more visible contrast as presented in Figure 5.2e. It is visible that the segmentations by the algorithm and the users differ. These differences are indicated by the blue and red color coding in the whole figure.

Therefore, an algorithmic solution developed in the thesis and its different segmentation methods tested have comparable quality, and the results are similar to the experts' results (Endl 2021, Sec. 2.2.2, p. 8). The solution to keeping this deviation to a minimum is to keep the discrimination conditions constant and define an algorithm that ensures the same consistent bias utilizing a new approach based on computer vision methods and the inherent properties of the RCFs.

Another issue is the ambiguity of the species causing the observed dose. The dose, as an observable, is a superposition of different types of radiation with different intensities. This means several beam setup possibilities create the same dose profile, and additional diagnostics, for example, Thomson parabolas, are necessary to solve this ambiguity problem.

Furthermore, most evaluation methods can only calculate spectra that follow an analytical expression. On the other hand, this makes it impossible to determine multi-species effects or other deviations from the analytical expression. This last point can also be mitigated by adjusting the evaluation method. During this work, a procedure was developed to mitigate two of the mentioned issues.

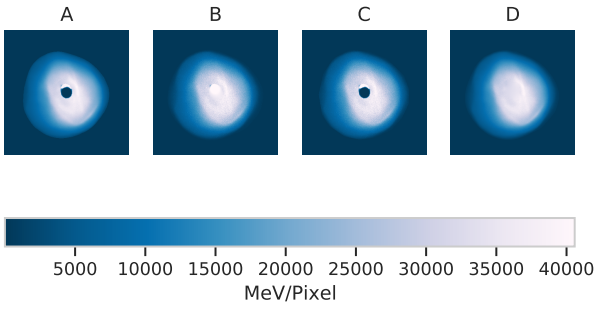

(a) MeV maps of the first data set.

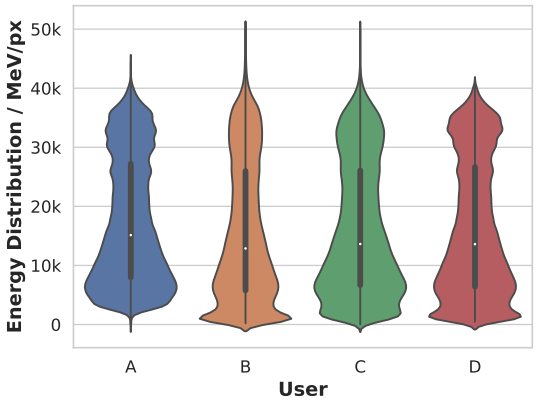

(b) Violin plot display of the first data set.

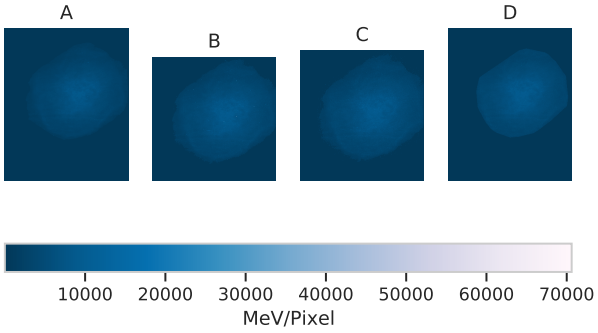

(c) MeV maps of the second data set.

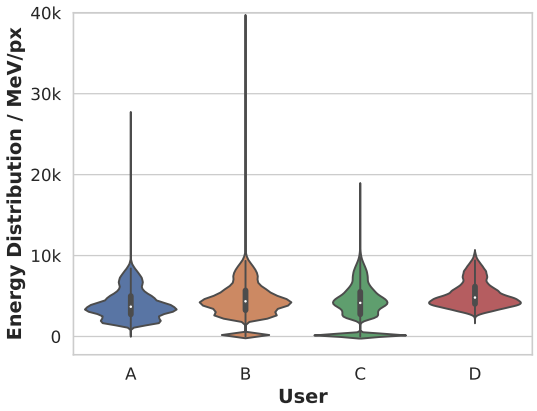

(d) Violin plot display of the second data set.

Figure 5.1.: Overview plots for the user bias study. Left is the segmented film, already converted to MeV representation. Right is the corresponding violin plot to display the differences in the final distribution.

5.2. Pythonic Radiochromic Film Evaluation Software

The pythonic Radiochromic film Evaluation Software (pyRES) implements the methods presented in this chapter. This procedure ensures the reproducibility and fast evaluation of RCF stacks. It includes routines for the deconvolution of the beam's energy distribution, accounting also for non-exponential distributions expected from other acceleration mechanisms. It further incorporates image processing methods to keep the segmentation conditions stable and reproducible.

5.2.1. Discrimination of the Radiation Types via Automatic Segmentation

The irradiated area can be identified as a segment in a picture (Jähne 2005, Ch. 16). pyRES relies on digital image processing techniques to identify these segments to identify regions of a specific type of radiation. In order to ensure reproducibility, fixed and quantifiable conditions to filter the measurement data are implemented. The algorithm for determining the segmentation boundary is displayed in Figure 5.3. Two types of automatic segmentation are implemented; one based on the Hue-Saturation-Value (HSV) representation of

the color space and one based on the converted deposited energy (MeV map) of the corresponding RCF.

While the definition of colors using the Red-Green-Blue (RGB)-triple is well known, HSV for the representation of color is less intuitive but useful. RGB is the Cartesian representation of the color space and HSV is a representation of the color space using a cylindrical coordinate system spanned by H – hue, S – saturation, and V – value (Jähne 2005, Sec. 6.3.4). The HSV branch of the algorithm converts the scanned image from the regular RGB color space into the HSV space and works on the resulting hue component. RCFs undergo a rapid change in the OD if irradiated. Converting the OD image to grayscale and applying the HSV parametrization yields that the hue is the relevant grayscale parameter. A visualization of this can be seen on the left side of Figure 5.3. The irradiated area has a light shade in this representation, while the non-irradiated area is dark. Taking a histogram for the hue allows separating the black background easily from the rest of the RCF. This allows the creation of a binary mask to separate the background from the signal. The method using HSV and more specifically the hue value is more efficient than relying on RGB-coded images since only one component has to be taken into account. If different amounts of radiations are measured, then different color value changes in the RGB space have to be compared, the projection to HSV reduces this to one component, the hue component is displayed in Figure 5.3. Segmenting this hue representation is then easily possible with the mentioned histogram method.

The MeV segmentation branch, on the other hand, converts the image directly to the corresponding deposited energies and then works on the resulting MeV map. This MeV map is generated by applying the calibration curves (Appendix A) to the image. It displays the deposited energy for each pixel given in MeV. Again, the segmentation method for this is the threshold segmentation method as in the HSV segmentation.

Both segmentation variants work rather similarly and use the inherent variation of the RCFs OD change after irradiation. Part of the algorithm is finding the corresponding thresholds. Finding absolute conditions for determining the proper segmentation threshold in computer vision is tedious, complex, and not always possible. The default values we found are presented in the corresponding paper (Schmitz, Metternich, et al. 2022). These conditions can be set and varied for the specific evaluation, such that dedicated data tests can be done and flexibility is ensured. These fixed global parameters, on the one hand, ensure reproducibility across users and experiments and on the other hand allow a high degree of automatization which is useful for data-driven modeling and its subsequent applications.

HSV segmentation as well as MeV segmentation are capable of creating fairly similar results. The MeV segmentation sometimes overestimates the threshold, especially for HD-v2 layers, irradiated with rather low intensities. Examples of these types of layers can be seen in Figure 5.4 for the 14.3 MeV and 15.6 MeV layers.

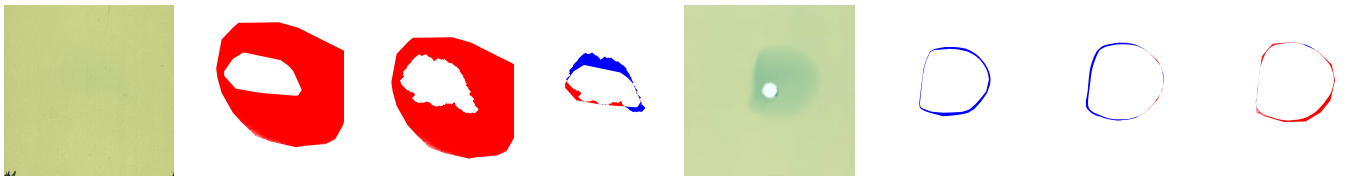

(a) Test RCF image No 12. (b) Difference between A and C. (c) Difference between C and Algorithm. (d) Difference between A and Algorithm. (e) Test RCF image No 5. (f) Difference between B and D. (g) Difference between A and Algorithm. (h) Difference between C and Algorithm.

Figure 5.2.: Evaluation plots taken from the mentioned thesis. Displayed are on the left side the original picture where the users and the algorithm worked, and on the right side, the difference between the created binary masks. The red/blue area denotes where areas are selected which are only in one of the compared masks.

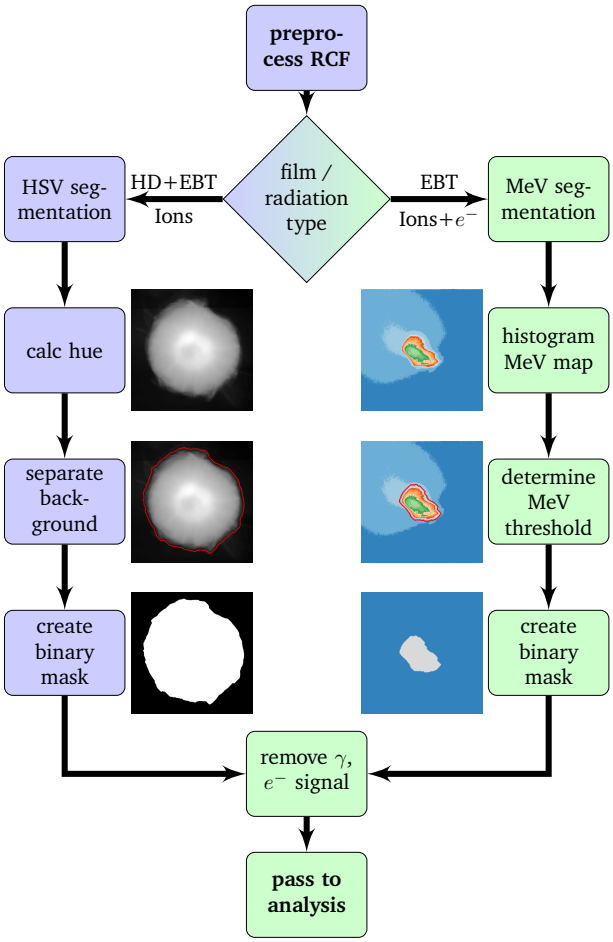

Figure 5.3.: Algorithm for determining the binary masks describing the outer ion beam contour. The colors indicate whether that part works on the original image data (blue) or the already converted energy data (green). These methods are tested for EBT3 and HD-v2 layers. Both film types can be segmented by HSV segmentation. The MeV segmentation can be used to verify the HSV segmentation for EBT3 layers and additionally allows for a more precise determination of the electron signal (light blue shade). Both methods are explained in section 5.2.2. The binary mask in the final step can then be used to define the ion beam area and to deal with background γ radiation and the electron signal on EBT3.

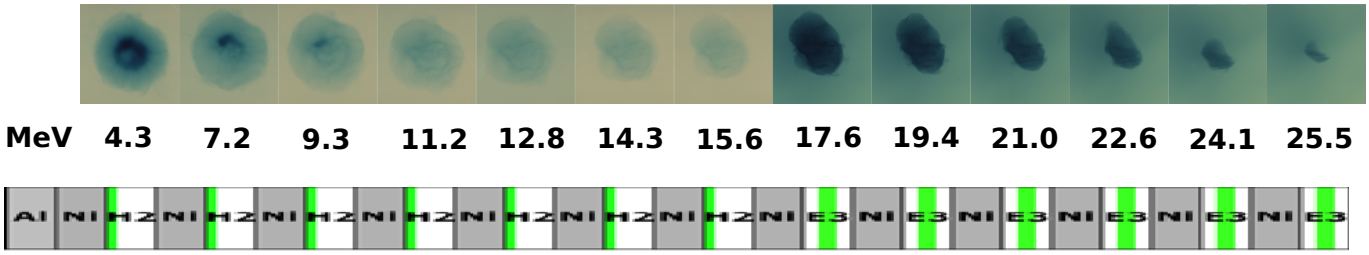

(a) Overview of a RCF stack, taken from the LIGHT beam time in January 2021 at GSI Helmholtzzentrum, Darmstadt. Displayed are the active layers which in the experiment are stacked together with passive Al and Ni layers. The energies denoted are the value of the respective Bragg Peak of the layer. While the first seven layers are HD-v2 films (lighter background), the last six layers are chosen to be EBT3 films (dark green background).

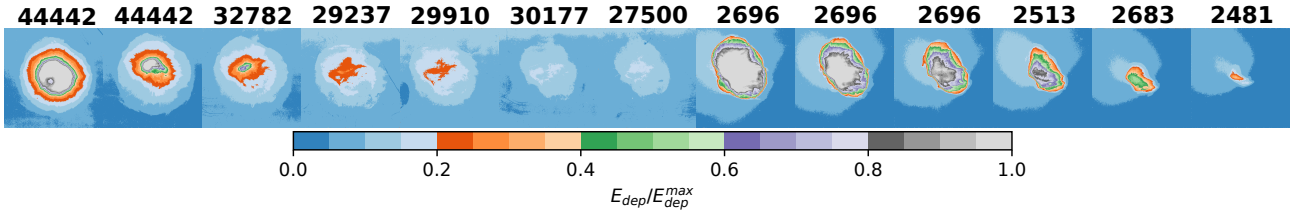

(b) Display of the corresponding MeV map for the layers displayed above. Different energy thresholds are indicated by different colors. The normalized color bar is given below the plot, while the normalized factor – the image's individual maximum deposited energy per pixel – is given above the corresponding image. Important to note is the light blueish contour on the last six EBT3 layers, which can be interpreted as an electron signal.

(c) The binary mask for the above MeV map is displayed here. This binary mask is derived by the segmentation algorithm. While HD-v2 layers are segmented via the hue segmentation approach, EBT3 layers are segmented via the MeV threshold approach.

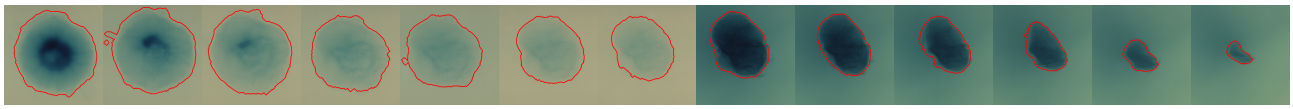

(d) Display of the binary mask on the measured RCF data.

Figure 5.4.: Intermediate results for all evaluation steps for the source shot.

Example results of the segmentation are displayed in Figure 5.3 and Figure 5.4. Combining Figure 5.4b and Figure 5.4d allows a comparison between the actual image, its calculated binary mask, and the deposited energy map. The colors indicate different energy levels normalized to the maximum dose value stored in each individual layer.

5.2.2. Automatised Ion Beam Evaluation

The beam segmentation of the RCF measurements provides the input data for automatically evaluating the ion spectrum. First, the beam's divergence is explained and its calculation is explained. Secondly, the different methods to determine the energy spectrum are explained in the section.

Table 5.1.: Parameters for the simulated RCF stack's angle fit. The parameters for the simulation are given in the Defined column, while the algorithm's output is given in the Reconstructed column. Uncertainties are given in the one-sigma interval.

Parameter	Defined	Reconstructed	Unit
a	28.19	28.83 ± 0.50	deg
b	-0.23	-0.29 ± 0.09	deg/MeV
c	-0.020	-0.016 ± 0.003	deg/MeV^2

Determination of the Ion Beams Spatial Distribution

The spatial distribution of the particle beam is one of the two intermediate results needed to reproduce the full beam. RCFs allow the measurement of the size of the beam at the position of the individual layer by taking the relevant OD change into account. Since the OD change on the layer can only properly indicate the outer radius of the beam, additional models have to be assumed for the behavior inside the beam. One possibility is that a laminar beam drifts without internal or external forces. This assumption is justified at sufficiently large distances from the target (Romagnani et al. 2005) (Lécz et al. 2015) (M. Schollmeier et al. 2014) (Nürnberg et al. 2009). For a laminar beam, the opening angle provides information about the transverse and longitudinal momenta:

$$\Theta(E) = \arctan\left(\frac{p_{\text{trans}}}{p_{\text{long}}}\right), \tag{5.2}$$

where p indicates a particle's transverse or longitudinal momentum respectively.

The laminar flow and the varying size of the RCFs imply the shape of an opening cone for each energy value. The origin of this opening cone constitutes a virtual source which, due to reconstruction, is supposed to be in front of the laser irradiated target's side (Nürnberg et al. 2009, Fig. 8). The opening angle of the beam can be experimentally evaluated by fitting the shape of a circle or an ellipsis to the aforementioned found contour for the ion signal on the individual RCF layer and applying the relevant trigonometric functions.

If a circle is fitted – as done in the course of this article – its radius can be given as the mean radius with the corresponding standard deviation. If an ellipsis is fitted, this method can result in two different opening angles for both transverse components. According to theory (Roth and M. Schollmeier 2014, pp. 235-237, Eq. 5, Fig. 3), the TNSA opening angle is an ideal circle, which might deviate due to experimental uncertainty, misalignment, laser aberrations, or the specific target structure.

The trigonometric relationships allow calculating a linear opening angle by taking the distance from the target to the individual RCF layer and the radii of the beams on these layers into account. These angle values can then be fitted with several methods for properly interpolating the full spatial spectrum.

As mentioned above, an ideally circular distribution of the RCFs allows for determining the effective radius of the distribution. This radius is the half-opening angle of the accelerated particles, its error is determined as the standard deviation of the contour from the mean radius. The experimental data for the half opening angle from the source shot in Figure 5.4 is displayed in Figure 5.8 together with fits described in subsection 2.3.3.

Figure 5.5 visualizes the corresponding angle fit with data extracted from a simulated stack, the fit results are compared to the simulation in Table 5.1. The data shows that the reproduction is close to the given simulation, which validates the automatic segmentation approach for the divergence calculation.

The importance of the laminar flow model is shown when going from the determined envelope angle toward the reconstruction of the beam's particle distribution function in the transversal components. This reconstruction assumes that the particles are homogeneously distributed on the cutting plane with the RCF layer and implies that a fixed cone exists for each energy. The half-envelope angle describes the boundary for

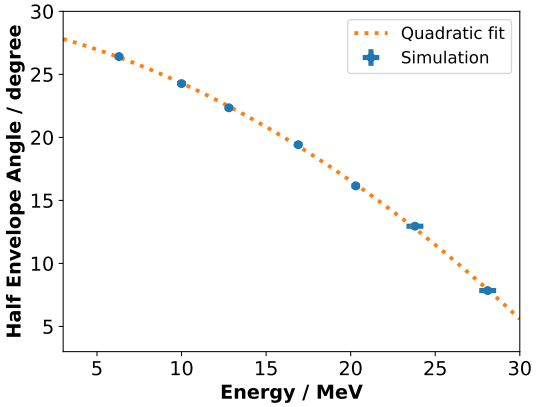

Figure 5.5.: The half envelope angle data from a simulation using the spectrum parameters given in table 5.1. Empirical fits are applied to interpolate the angle. The dashed line represents the QUADRATIC FUNCTION given in subsection 2.3.3. The parameters are calculated to be $a = 28.83$ deg, $b = -0.29$ deg/MeV, $c = -0.016$ deg/MeV^2.

this cone.

Determination of the Ion Beam's Energy Spectrum

The previously calculated energy-dependent divergence angle has to be complemented with the energy-dependent particle counts. Both are needed to reconstruct the 3D particle distribution. To calculate the spectrum, the deposited energy in the individual RCF layer has to be matched to the dose. The ideal case would be a direct deconvolution inverting

$$E_{\text{dep}} = \int_{E_{\text{min}}}^{E_c} \frac{\mathrm{d}N}{\mathrm{d}E}(E) E_{\text{loss}}(E)\,\mathrm{d}E \tag{5.3}$$

where E_{dep} is the deposited energy, $E_{\text{loss}}(E)$ is the energyloss characteristic of the individual RCF and $\mathrm{d}N/\mathrm{d}E$ is the energy distribution of the ion beam.

However, due to a stack's limited number of active layers, the resulting equation system (Equation 5.3) is under-determined. Several passive layers sandwich these active layers as for example depicted in Figure 5.4a. Charged particles continuously deposit energy while passing matter. Lower energy particles have a shorter penetration depth than higher energy particles. The higher energy particles deposit energy in all layers before they reach their corresponding Bragg peak resulting in an ambiguity in earlier layers. Only the active layers provide sampling points; information is missing for the passive layers. Increasing the number of active layers increases the preparation time needed, the accumulating costs of the diagnostic, and the time required for scanning the resulting layers. A proper inversion, for example, with the GRAVEL method (Chen et al. 2014), is therefore impossible due to underdetermination caused by ambiguity.

This sparse data issue can be overcome by applying model assumptions of the dose in the passive layers. The first approach displayed here works with the assumption of a strong model, which forces the resulting spectrum into a given distribution. This is called the Convolutional Approach and was originally presented in (Nürnberg et al. 2009). The second approach is model-free and only assumes a linear interpolation between the data points. This is called the Linear Interpolation Approach.

Further methods are for example the Graphical Subtraction Method (GSM) (Nürnberg et al. 2009), and the Image Merging Method (IMM) (M. Schollmeier et al. 2014). These methods are not considered since they

either lack numerical stability and assume strong models (GSM) or require many user inputs unsuitable for automatic application (IMM).

Convolutional Approach The main approach to dealing with the low number of sampling points resulting in the ambiguities mentioned above is using a convolution approach, described in more detail in the corresponding publication (Nürnberg et al. 2009). For this approach to work, a model for the particle spectra has to be assumed, which is in good agreement with conventional thin film TNSA targets, an exponential function e.g.

$$\frac{\mathrm{d}N(E)}{\mathrm{d}E} = \frac{N_0}{E} \exp\left(-\frac{E}{k_B T_e}\right). \tag{5.4}$$

This exponential function is convoluted with the RCFs response function given by an a priori SRIM (Ziegler et al. 2010) or Monte Carlo calculation. The function's parameters are then varied in the least squares sense until they reproduce the RCFs deposited energy values.

Due to the nature of the approach, several different models and arbitrary functions could be used, allowing for easy testing of possible new theories as soon as they emerge. It has also been shown by Wagner et al. (Wagner, Bedacht, et al. 2015, Eq. 3, Fig. 4) that this works even if different models are superposed by adding up different functions:

$$\frac{\mathrm{d}N(E)}{\mathrm{d}E} = \sum_i \left(\frac{\mathrm{d}N(E)}{\mathrm{d}E}\right)_i. \tag{5.5}$$

While this convolutional approach is numerically stable, it can only reproduce the model function given. The lower the uncertainty of the result, the higher the possibility that the assumed spectrum matches the observation. On the other hand, it does not provide information about what a deviating spectrum looks like. A result for this convolutional approach is given in Fig. 5.6.

Linear Interpolation Approach In this section, we report an additional deconvolution method that can be used to obtain the energy spectrum from the RCF data without making any assumptions about the distribution of the spectrum. This approach follows the same idea as the method by Schollmeier et al. (M. Schollmeier et al. 2014, Sec. 3.A). Since the implementation is not given in detail, it is unclear to what extent the two algorithms are identical and whether the approach of Schollmeier et al. can also be used for unconventional ion spectra. Therefore, the main difference is this algorithm's open-source implementation and the dedicated goal to investigate unconventional spectra. The algorithm presented here already takes the discretization of the data into account. The equations, therefore, differ from the ones given by Schollmeier et al..

Important to note that the spectrum is assumed to be continuous, which is achieved by linear interpolation between the sampling points. However, this assumption does not limit the shape of the resulting spectrum in any way. Each irradiated active layer has a specific Bragg peak energy, which means that the particles with this kinetic energy are stopped and deposit a significant part E_{Bragg} of their initial energy in this layer. The idea is, therefore, to take this Bragg peak energy as the sampling position in the energy spectrum, ranging from the lowest resolved Bragg peak energy E_{min} to the highest resolved Bragg peak energy E_{max}. Therefore, the sampling points E_i are part of the corresponding closed interval. To do this, one must also consider that higher energy particles do not get stopped in this layer but still deposit energy.

Only the layers that got irradiated are considered for the analysis of RCF stacks. The last layer irradiated then defines the interval's maximum energy value, and it is reasonable to assume that no higher energy component was measured. One can therefore expect that the particle count (N) on the last layer is given by the ratio of the measured deposited energy in the last layer to the particles' Bragg peak energy in the last layer only:

$$N(E_{\mathrm{max}}) = E_{\mathrm{dep}}^{\mathrm{measured}}(E_{\mathrm{max}}) / E_{\mathrm{part}}^{\mathrm{Bragg}}(E_{\mathrm{max}}). \tag{5.6}$$

After completing the first step, the stack is evaluated from the back to the front with the same method. The active layer under discussion is denoted with an integer i. The steps for this algorithm are mentioned below:

1. The first step is always to determine an initial particle number for each layer. This is done by dividing the full deposited energy by the Bragg peak energy:

$$N^{\text{max}}(E_i) = E_{\text{dep}}^{\text{measured}}(E_i)/E_{\text{part}}^{\text{Bragg}}(E_i). \tag{5.7}$$

   At this point, the particle count at E_i is calculated only with the Bragg Peak energy at E_i taken into account. No contributions from particles with an energy higher than E_i are included yet. If now the energies $E > E_i$ are included, their contributions add up, and the calculated deposited energy gets higher than the measured energy, effectively overestimating the particle count at E_i. A simple linear interpolation then does the interpolation of the particle count from two adjacent data points at E_i and E_{i+1}. Allowing for subsequent corrections as discussed in the next step.

2. To deal with the overestimation of particles at E_i, the particle count $N\,(E_i)$ has to be varied until the different deposited energies match. Starting from the last measured irradiated layer going to the front:

   a) Calculate the layers' contribution with $E_j > E_i$ to the layer with E_i and subtract it from the deposited energy.

$$E_{\text{dep}}^{\text{calc}}(E_i) = E_{\text{dep}}^{\text{measured}}(E_i) - \int_{E_j}^{E_{\text{max}}} E_{\text{part}}^{i}(j). \tag{5.8}$$

      The newly calculated deposited energy is then used to calculate a more precise particle number $N(E_i)$.

   b) Equation 5.8 subtracts every higher energy component except the part from E_i to E_{i+1}. The particle count is, therefore still overestimated. The number of particles $N(E_i)$ is reduced until the calculated deposited energy, including the area from E_i to E_{i+1} matches the assumed spectrum. The previously not included area is linearly interpolated in between the two energies.

   c) If the energies are still not matching when $N(E_i) = 0$ (this can occur if there are too many particles in the triangle formed by the linear interpolation between the sampling points $N(E_i)$ and $N(E_{i+1})$. An additional sampling point E_v is inserted between E_i and E_{i+1} with $N(E_v) = 0$ in this case. This additional sampling point in the energy domain is increased until the measured and calculated deposited energies matched. With this mechanism, increasing the spectrum's cut-off energy is possible by setting a virtual sampling point at higher energy.

The final spectrum reproduces the measured deposited energy in the RCF stack precisely to an allowed uncertainty that can be fixed a priori. An ambiguity still exists since the spectrum determined is only a representation of all possible solutions reproducing the deposited energy. Keeping the input parameters, cut-off energy, and maximum dose deviation constant ensures a reproducible data evaluation. Furthermore, additional diagnostics might be used to verify the particle spectrum's shape and reduce the number of ambiguities. This ambiguity in the spectrum can also be reduced by applying theoretical models that default to the convolutional approach. In other words: this method uses measured values without considering any measurement errors.

The energy distribution by the linear method is more susceptible to measurement errors than the convolutional approach, as seen in Figure 5.6. This is caused by the nature of the different approaches. The linear approach directly works on the measured deposited energy and is therefore susceptible to the fluctuations measured from each data point, which directly converts into the displayed fluctuations. Conversely, the convolutional approach implicitly fulfills a regression on the data and is, therefore, smooth. Less variation in the data results in less variation in the resulting spectra, as shown in Figure 5.7a.

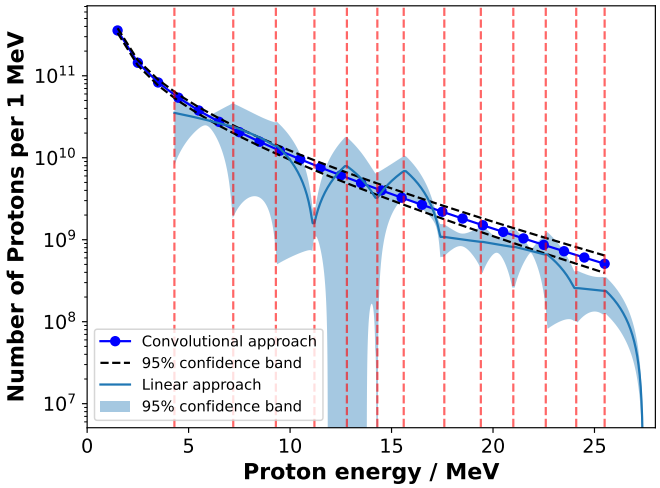

Figure 5.6.: Results for both deconvolution methods. Differences are due to the different approaches' behaviors. The red lines indicate the Bragg peak energies of the stack used and, therefore, the resolution of the data. The first set of curves consists of the blue dotted line, and the black dashed lines. They describe the result of the convolutional approach together with its corresponding confidence band. The second set of curves is the solid blue line and the light blue area giving the 1-σ interval of the linear approach.

The spectra also have dedicated features at the lower and higher energy end: The linear approach can not extrapolate beyond the lower end, where no signal could be measured. The spectrums behavior before the first active layer can not be determined, the algorithm assigns a constant value, but it has no deeper physical meaning. On the higher energy part a more consistent statement for the cut-off energy can be found, a small extrapolation is possible. The convolutional approach, on the other hand, allows extrapolation following the given model function. Still, finding a good cut-off energy is problematic, such that additional information has to be put into the complete representation, e.g. from the geometry of the used stack.

For unconventional spectra, as predicted for example by Huebl et al. (Huebl et al. 2020), Hegelich et al. (Hegelich et al. 2006) and which are under investigation for high repetition rate experiments, the linear interpolation has to be used.

5.3. RCF Application

5.3.1. Energy Spectrum Verification with Simulated RCF Stacks

The second part of the algorithm, namely the spectrum's deconvolution, is also validated. This is achieved by comparing the algorithm's output to well-defined input spectra. The input spectra are defined by two distribution functions: The exponential function is given in Equation 5.9 as

$$\frac{\mathrm{d}N}{\mathrm{d}E} = \frac{N_0}{E} \exp\left(-\frac{E}{k_B T}\right), \tag{5.9}$$

Table 5.2.: Parameters for the RCF stacks. Results are given for a simulated 7- and a 14-layer stack. Defined denotes the simulation parameters, while Reconstructed denotes the output of the evaluation algorithm. The uncertainties are passed as one-sigma intervals.

Exponential spectrum				
Parameter	Defined	Reconstructed		Unit
		14 Layers	7 Layers	
N_0	1.36	1.16 ± 0.04	1.18 ± 0.33	10^{12}
k_BT	6.37	7.11 ± 0.20	8.86 ± 2.17	MeV
Step spectrum				
Parameter	Defined	Reconstructed		Unit
		14 Layers	7 Layers	
N_0	1.36	2.5	2	10^{12}
E_0	20.00	18.25	19.5	MeV
ΔE	6.00	6.55	9.5	MeV
Experimental spectrum from Figure 5.4a				
N_0		3.7 ± 0.2		10^{11}
k_BT		7.4 ± 0.4		MeV
E_c		25.5		MeV

while the step wise function is displayed in equation 5.10 as

$$\frac{\mathrm{d}N}{\mathrm{d}E} = \begin{cases} 0 & \text{for } E < E_0 - \Delta E \\ N_0 & \text{for } E_0 - \Delta E < E < E_0 + \Delta E \\ 0 & \text{for } E > E_0 + \Delta E. \end{cases} \tag{5.10}$$

Table 5.2 gives the chosen parameters and the evaluation results. The results show that both implemented algorithms are capable of reproducing the defined spectra as presented in Figure 5.7a. The uncertainties are inherent to the dosimetry approach which can be counteracted in the experiment by using more active layers and adjusting passive layers to prevent saturated signals. The deconvolution presented in Figure 5.7b shows a step function as proton distribution. Due to its shape, the conventional convolutional method does not achieve a meaningful conclusion, if these functional dependencies are not inserted. The linear deconvolution method reaches the displayed solution. One can see that the plateau varies but is still in the same order of magnitude and that the two steps are drifted apart. This drift is caused by the lack of measurement precision since only the active layers in the stack give sampling points. The method is therefore not precise enough to fix the step's sharp boundaries.

One important restriction has to be addressed though: All evaluation methods are based on matching calculated deposited energy from the fitted spectrum to the measured deposited energy. This means a spectrum is a valid solution if it reproduces the measured dose distributions. Thus, each particle distribution reproducing the dose distribution is a valid result. The results can still vary within the given models or methods uncertainties. The final spectrum resulting from the evaluation methods (confer to section 5.2.2) therefore always represents all possible solutions. Using the same evaluation conditions and algorithm ensures

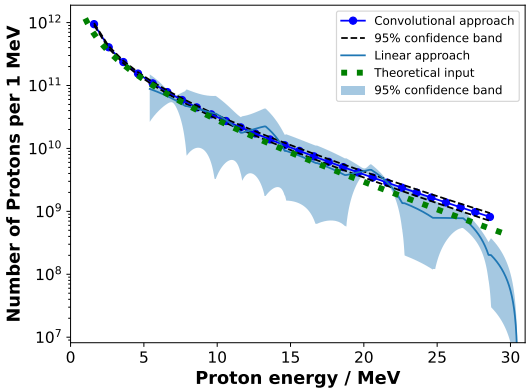

(a) Results for a simulated 14 layer stack. Displayed are the results from the Convolutional and Linear approaches. Also displayed is the theoretical input used to create the simulated stack.

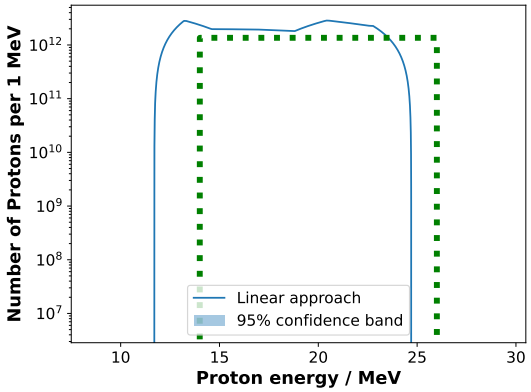

(b) Result for the linear interpolation method for a step function like particle bunch as defined in table5.2. The dashed line denotes the actually given distribution. The uncertainty exists along the full curve but is low. This is a direct result of the shape of the function in combination with a low uncertainty from the simulation.

Figure 5.7.: Consistency plots for the algorithm. The numerical parameters are displayed in table 5.2.

that comparable representatives are returned. The conclusion is that the algorithmic approach ensures the reproducibility of the evaluation inside the methodological constraints.

As mentioned in subsection 5.1.1, the different radiation components influence the evaluation results and an exact differentiation of the radiation types is only possible to a certain extent.

5.3.2. Comparison with the Analytical Model by Lecz et al.

The previous sections have shown that our segmentation scheme can isolate the ion signal on the RCFs and thereby reconstruct the beam energy-dependent divergence angle. In addition, we can reconstruct the beam energy distribution.

As an application, we discuss the comparison to the analytical model by Lecz et al. (Lécz et al. 2015, Eq. 15, Fig. 11) for the transverse divergence of TNSA beams from solid targets. This model is a 2D extension of Mora's plasma expansion subsection 2.3.1 and considers several experimental parameters and assumptions. Unknown parameters of the model can then be fitted to the reconstructed divergence angle data via a least squares approach and result in physical predictions of the cut-off energy, the hot electron spread angle inside the target, and the hot electron density. Results are displayed in Table 5.3.

The empirical models from section 5.2.2 do not have a supporting theoretical model but apparently reproduce the measured results over a more extensive energy range (see Figure 5.8). The model by Lecz et al. has a good agreement for the high energy part (here for $E > 18\,\mathrm{MeV}$) and also the capability to fit the behavior of the envelope at the top part of the spectrum. The deviation in the low energy (here for $E < 18\,\mathrm{MeV}$) part is caused by its theoretical assumptions, as mentioned in the corresponding publication. The threshold of $18\,\mathrm{MeV}$ is determined for this data set by comparing the differences of the fitted curve to the experimental data and varies according to the specific experimental parameters.

Important to note is that the model by Lecz et al. can predict the spectrum's ion cut-off energy. This 2D model, taking the ion opening angle into account, can model the angle opening angle above the highest energy until the curve reaches 0. The model helps extrapolate the fit until it hits the axis of the abscissa. The energy

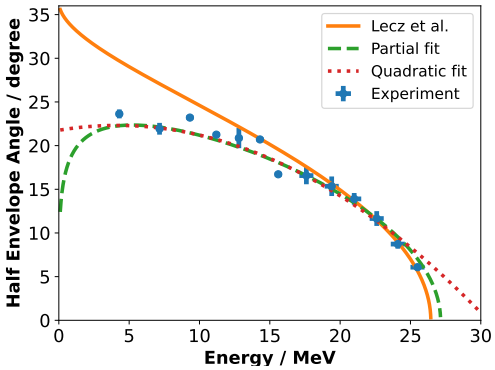

Figure 5.8.: Comparison of Lecz et al. model with two standardized empirical models. The blue data points are taken from the source shot under investigation in this paper. The solid line gives the best fit for the dataset for Lecz's model. The dashed line is the result for the PARTIAL FUNCTION and the dotted line represents the best fit for the QUADRATIC FUNCTION given in subsection 2.3.3. Both of the last functions are purely empirical.

value at the intersection of fit and the axis of abscissa is then the value of the cut-off energy. As shown in Figure 5.8, the model yields a smaller cut-off energy than the partial function. The discrepancy might result from some of the conditions assumed by Lecz and can therefore vary. Comparing the cut-off energy to the one calculated by the deconvolution, it is larger than the $25.5\,\mathrm{MeV}$ calculated (confer to Table 5.2). The fit could therefore be used to correct the cut-off energy towards higher values. However, whether this value is more "correct" has to be measured using a more detailed RCF stack which is seldom used due to the relatively high costs.

5.3.3. Full Reconstruction of TNSA Ions

A full reconstruction of the ion beam can be attempted by utilizing the evaluation method and the numerical relations given in this chapter and in chapter 2. A representation of this reconstruction is displayed in Figure 5.9. Due to the exponential energy distribution, and the variation in the envelope, values at different energies have to be sampled. This shape could be achieved by assuming the laminar flow model, which means having each energy uniformly distributed on the corresponding circle. For each energy, the weight is known, meaning that the total dose and behavior can be estimated as if it were the entire beam. Further, for each particle, the momenta are known, such that tracking of the particles can be added.

The sampling is randomized within the measured boundaries, so the model quality increases if more samples are used. However, this result has a significant problem: the same assumptions are taken to evaluate the RCF stacks. Particle distribution is assumed to follow the laminar flow model, space charge effects are neglected, and only one type of particle is considered. Both describe the visible results but do not describe the dynamic process happening.

Extending the model to incorporate space charge, different distributions, and several particle species is possible and doable if the corresponding data can resolve this.

Table 5.3.: Relevant quantities and results for Lecz et al. model. The upper part has values that must be inserted into the model and given by the experiment, while the lower quantities are the two degrees of freedom the model fits. The cut-off energy is an additional value the fit yields but is not a degree of freedom for this fit.

Physical quantity	Source shot
Pulse duration / fs	650
Normalized vector potential a_0	11.46
Irradiation size FWHM /µm	3.5
Target thickness / µm	10
Hot electron temperature / MeV	1.9
Fit Results:	
Electron spread-angle / °	46
Hot electron density / m^{-3}	0.79×10^{26}
Additional Result:	
Cut-off energy / MeV	26.44

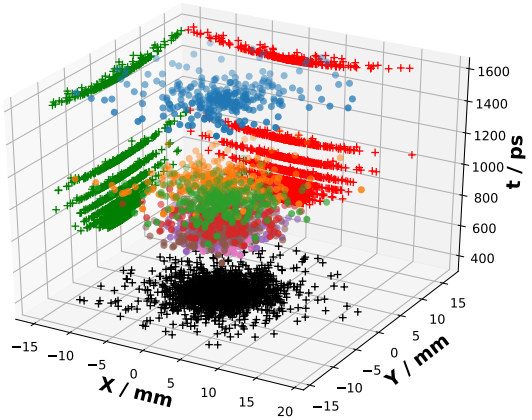

(a) 10 energy samples were taken, and each step in the energy spectrum was resampled with 300 particles each. Time-dependent for the constant position of 46 cm behind the target.

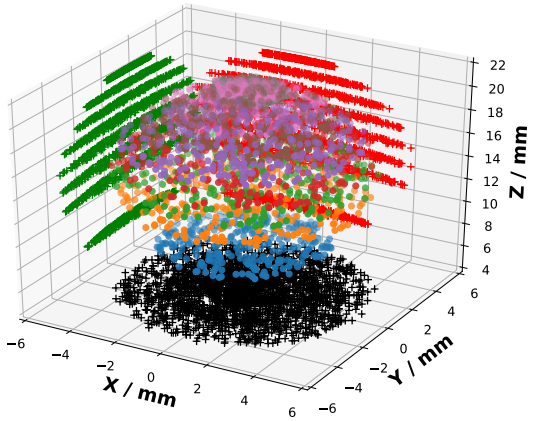

(b) 10 energy samples were taken, and each step in the energy spectrum was resampled with 300 particles each. Displayed at the time step of 300 ps after the beginning of the acceleration.

Figure 5.9.: Full reconstruction of a TNSA proton bunch. The divergence and energy spectrum was determined using pyRES.

6. Surrogate Model for the Compact Laser-Driven Neutron Source

"Data points in hand,
Surrogate models take a stand,
Simplify the world."

This chapter's goal is the full description of the surrogate models, based on artificial neural networks. Two models were developed for a final model that maps laser and target parameters. The first model aims to describe the laser plasma TNSA process and maps from the laser and plasma parameters onto the resulting proton spectrum, while the second model describes the neutron production and maps from incoming particles to outgoing neutron spectra.

For each model first, the numerical basis is explained, which for the first model are PIC simulations and nuclear Monte Carlo models for the second. The model based on PIC, which aims to describe the TNSA process, is also investigated based on sensitivity analysis to discuss the order of the model that can be described. The neutron model is further evaluated using a bootstrapping method to determine the uncertainty of the full spectrum.

As mentioned in previous chapters, optimization of any kind is only possible if the algorithm optimizing has access to a fast and cheap model to evaluate. While the effort of creating training data and conditioning the networks takes a considerable amount of time, the resulting surrogate is fast and easy to evaluate. It can be used by anyone with basic knowledge of physics and minimal programming skills. Deep knowledge about the simulations, their implementations, and further detailed knowledge is not needed anymore.

6.1. Surrogate for the Laser Accelerated Ions

The surrogate model for the laser-accelerated ions is based on a large simulations study for several parameters. This simulation is discussed first, while the modeling is discussed in the second part of this section. Part of this section was done in a master's thesis supervised by the author (Kreuter 2021) and the later results and further discussion were published (Schmitz, Kreuter, et al. 2023). This section is based on the article and some further thoughts and discussions.

6.1.1. Simulation Setup of the Liquid Leaf Target

As mentioned above, the model is a result of a large number of particle-in-cell simulations (section 3.1) done with the SMILEI PIC code (Derouillat et al. 2018).

The simulations mirror a real experiment but in reduced dimensions to sample a larger parameter space in a reasonable time. 1.5D simulations are done, meaning particles can move only in 1 spatial direction but 3 momentum components are considered, while electric and magnetic fields are also sampled in 3 dimensions. This setup saves calculation time since fewer spatial dimensions must be considered. However, the calculations can still resolve higher-order effects (e.g. $j \times B$-heating).

Further, an additional method to include an angle dependency is applied by applying a transversal Lorentz boost to the system. The corresponding article (Schmitz, Kreuter, et al. 2023) introduces this Lorentz boost method, which is given in Appendix B.1. A sketch of the full setup is displayed in Figure 6.1.

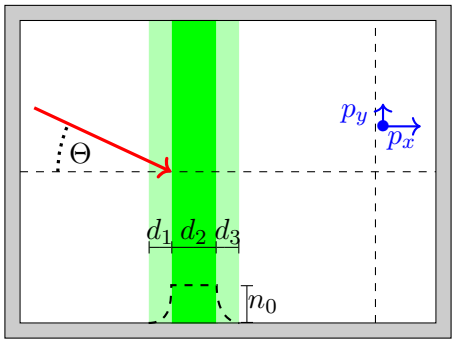

Figure 6.1.: Simulation setup for the PIC simulations. Green indicates the plasma slab of the liquid jet. The density distribution is indicated with the dashed curve. The incoming laser is displayed with a red arrow and the defined angle relative to the target's normal. At the defined acceleration time, the momenta of the particles are registered.

Plasma Target

The target in the conducted simulations models a liquid leaf target under development at TU Darmstadt Institute of Nuclear Physics and which is similar to the work by George et al. (George et al. 2019). The liquid leaf target's width is some cm, while the typical irradiation size of a laser is in the order of µm. The surface roughness is assumed to be negligible and the plasma surface can therefore be considered planar.

When the target is only dependent on one coordinate it can be described fully by its particle density profile. The simulation therefore only allows movement along the x coordinate and is then independent of y and z. It is further assumed that the plasma is expanded when the main pulse hits the target and assume that the pre-plasma and skirt follow an exponential profile. The scale length for the exponential profile as $0.4\,\mu\text{m}$ was chosen to be longer than a comparable setup with a cryogenic (i.e. less evaporative) jet target (Obst et al. 2017) while still ensuring a well-defined plasma border. The exponential profile thus takes the shape

$$n_{\text{exp}}(x) = \frac{n_0}{1 + \exp(-(x - x_{\text{front}})/l_{\text{s}})} \tag{6.1}$$

where $l_{\text{s}} = 0.4\,\mu\text{m}$ and x_{front} is the location of the target front. The skirt has an identical functional shape for the backside of the target.

Since a liquid leaf target evaporates, the typical vapor density distribution for a liquid leaf target is assumed as,

$$n_{\text{LJT}}(r) \approx n\left(r_{\text{jet}}\right)\left(\frac{r_{\text{jet}}}{r}\right)^2 \frac{L}{\sqrt{r^2 + L^2}}\,, \tag{6.2}$$

where $n\left(r_{\text{jet}}\right)$ is the water vapor density at the liquid jet surface, $L \approx 3\,\text{cm}$ is the liquid jet length, and r_{jet} is the liquid jet radius (Cappa et al. 2005, Eq. 3). Note that the second term in the above expression has been squared as we expect a faster drop-off of the liquid leaf density in our proposed experimental setup.

The assumed particle densities are $n_0 = 6.68 \times 10^{28}\,\text{m}^{-3}$ and $n\left(r_{\text{jet}}\right) = 1.62 \times 10^{23}\,\text{m}^{-3}$ stemming from the liquid density of water and the density estimated at the saturation vapor pressure at $0\,^{\circ}\text{C}$ (Cappa et al. 2005). A cut-off of the profile $4\,\mu\text{m}$ before and after the target is introduced to optimize the simulation's performance.

The multi-species effect (see subsection 2.3.2) is investigated through a variation of the ion species mixture inside the target. The simulations, therefore, included regular water, heavy water, and a potential mixture between the two. This mixture is indicated by the mixture parameter listed in Table 6.1, which was varied in discrete steps. Therefore the simulation consists of up to four species: electrons e^-, hydrogen H^+, deuterium D^+, and oxygen O^{n+}. All particle species follow the same initial distribution function defined above.

The ion species are initialized cold while the electrons received an initial temperature of $30\,\mathrm{keV}$ to simulate interaction with a pre-pulse. The length of one cell is the Debye length at the initial electron temperature. For the time resolution, a CFL number of 0.98 was used. The interpolation order of the particle shape functions is set to four and the particle per cell count is 800.

Laserpulse

In a 1.5D simulation, only the laser pulse is given by its time profile and assumed to be Gaussian. The TGAUSSIAN time profile in Smilei, which was used, has the following shape:

$$I_{\text{envelope}}(t) = \begin{cases} \exp\left(\frac{-(t-\tau_\mathrm{L})^2}{(\tau_\mathrm{L}/2)^2/\ln(2)}\right) & \text{if } t \leq 2\tau_\mathrm{L} \\ 0 & \text{otherwise} \end{cases} , \tag{6.3}$$

where τ_L is the main laser pulse duration. In this work, lasers that have a pulse duration $\tau_\mathrm{L} < 1\,\mathrm{ps}$ and an $a_0 > 1$ were assumed. The laser energy E_L, pulse length τ_L, polarization, incident angle θ_L, wavelength λ_L and the target thickness d_T are variable. They are uniformly sampled from the defined intervals in Table 6.1. The full system can be covered with 9 parameters. This count follows the discussion in section 4.1. The ranges of these parameters were chosen under two different sometimes contradictory paradigms; one is to allow the similitude equations in section 4.1 to take full effect while the second paradigm is to allow experimental validation of the model.

Table 6.1.: The physical parameters used for sampling the input files to the 1.5D PIC simulations. Mixture defines the percentage of hydrogen substituted by deuterium.

No		Attribute	Sign	Range	Units
1	Laser	Energy	E_L	[0.001, 50]	J
2	Laser	Focus-FWHM	FWHM	[2,20]	µm
3	Laser	Pulse length	τ_L	[15, 150]	fs
4	Laser	Polarization		{s, p}	
5	Laser	Incidence angle	θ_L	[0, 85]	°
6	Laser	Wavelength	λ_L	[550, 1100]	nm
7	Target	Thickness	d_T	[0.6, 3]	µm
8	Target	Mixture	Mix	[0, 100]	%
9	Target	Oxygen Charge	Z_eff	{7, 8}	

Simulation Output Quantities

The diagnostics recorded are the particles' x-coordinate, all components of the momentum $\vec{p}$, and the macro-particle weight w at the acceleration time

$$t_\mathrm{acc} = \tau_\mathrm{L} + d_\mathrm{T}/c_\mathrm{s} , \tag{6.4}$$

where c_s is the ion-acoustic velocity. Lecz (Lécz 2013, Eq. 4.1, p. 47) has found that this is a suitable acceleration time after which an isothermal plasma expansion model no longer holds. From these recorded values the energy spectrum of the particles in the lab frame is reconstructed by using Eq. (B.5). Since all energy spectra have an individual shape and cut-off energy, the spectra were each normalized to the energy range $[0, 1]$, counted into 100 bins, and stored as a list together with their respective cut-off energies. In order to keep the numbers more practical, their logarithm was used. The entry for the results of a simulation thus has the following shape: $\{\ln\left(\frac{\mathrm{d}n}{\mathrm{d}E}\right)_{\text{Bin 1}}, \ldots, \ln\left(\frac{\mathrm{d}n}{\mathrm{d}E}\right)_{\text{Bin 100}}, E_{\max}\}$. Exponentiating and re-scaling by $E_{\max}$ restores the original energy spectrum accordingly. This same recording scheme is used for all four species for all simulations.

The parameters in Table 6.1 are uniformly sampled except for the laser energy E_L which was sampled following a square root scale and the mixture was varied in discrete steps. This type of sampling results in significantly more simulations with low a_0 than with high a_0. To deal with this additional constraints for a_0 were introduced. Although the laser focus-FWHM is technically not relevant in the 1D case we sampled it nonetheless such that together with the sampled laser energy and pulse length, the correct a_0 was written in the input file. This also ensures comparability with higher-order simulations and experimental data.

Simulation Statistics

We used the setup described above to create a dataset of simulations for our subsequent surrogate model. All parameters were stochastically sampled, and their combination can be considered a sparse grid. The number of simulations varies between the different species. The number of simulations for hydrogen is $508\,200$ and the number of simulations for deuterium is $762\,426$. The reduced model, which utilizes only the pure H_2O data without D_2O component consists of a subset of the full data set and has $68\,973$ entries.

Limitations of 1.5D PIC

These low-dimensional simulations do have some drawbacks. While they, together with the introduced transversal Lorentz boost method (Appendix B.1, and Schmitz, Kreuter, et al. 2023), are capable of describing several effects, some are not possible. The main effect is the expansion of the plasma behind the target. In one spatial dimension, no transversal drift of the particles is possible. Therefore also, no decay of space charge effects exists. The expansion continues until infinity if it is not stopped. This is mitigated using the introduced t_{acc} in Equation 6.4. Furthermore, divergence opening angles cannot be evaluated because of the lack of transversal particle movement.

Data Discussion by Example

An example of the spatial distribution from the simulations is given in Figure 6.2. An example of the energy spectrum is displayed in Figure 2.8.

In this simulation, the target consists of regular water fully ionized by the implied laser pre-pulse. Thus, the three species (e^-, H^+, and O^{8+}) are initialized with a density ratio of $10 : 2 : 1$, respectively, so overall neutrality is conserved. The species' positions are displayed at $t = t_{\text{acc}}$ in Figure 6.2. In this simulation the laser incidence angle is $0°$, the target thickness is $2\,\mu\text{m}$, and the dimensionless laser amplitude is $a_0 = 20$. The figures show that the species have different positions at the measured time, which means the species are accelerated separately by the sheath field.

The ion front position at the acceleration time for different species varies due to the different charge and mass values as mentioned in subsection 2.3.2. Calculating the expected variation by numerical integration, following the relation from Huebl et al. (Huebl et al. 2020, Eq. 2), for only fully ionized oxygen and

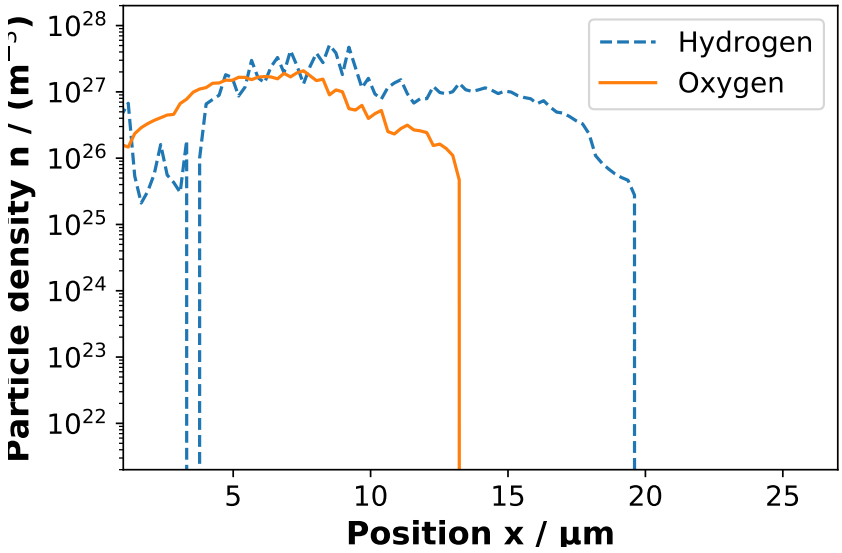

Figure 6.2.: Example PIC simulation of water leaf target TNSA experiment. The plot shows the particle distribution at the previously proposed acceleration time t_{acc} (Eq. (6.4)).

hydrogen present, yields a scaling factor of $x_F^{O^{8x}}/x_F^H \approx 0.68$. The corresponding factor from Figure 6.2 is $x_{F,\text{sim}}^{O^{8x}}/x_{F,\text{sim}}^H \approx 0.67 \pm 0.01$, where the uncertainty results from the binning.

The general TNSA mechanism is still applicable. The dynamics of the different particle species with each other are more complex, but the general behavior appears to follow classical TNSA theory. This is also more clearly displayed and backed up by the obtained kinetic energy spectra of the ion species after acceleration. An example of kinetic spectra can be found in Figure 2.8. It displays the hydrogen and oxygen ion energy spectra and Mora's predicted ideal curve.

6.1.2. Surrogate for the Liquid Leaf Target

Different simulations have to be correlated to each other in order to find relations. The resulting interpolation then allows an optimization of the full setup. This was acquired by a neural network approach with fully connected topologies utilizing Keras (Chollet et al. 2015) and Tensorflow 2 (Abadi et al. 2015).

Model Training

To predict a particle spectrum two models are needed. One model continuously maps

$$\{E, \text{mix}, E_\text{L}, r_\text{L}, \tau_\text{L}, \text{s/p-pol.}, \theta_\text{L}, \lambda_\text{L}, d_\text{T}\} \rightarrow \ln\left(\frac{\mathrm{d}n}{\mathrm{d}E}(E)\right), \tag{6.5}$$

while a second model only predicts the maximum energy (i.e. when to cut off the continuous spectrum from the first model). Two models for each particle species of interest were developed, one pair for protons and one pair for deuterons. Both model pairs contain different ratios between H_2O and D_2O. In the corresponding publication (Schmitz, Kreuter, et al. 2023) only proton models are discussed, incorporating a reduced and a full model, which is used to show that the full model reproduces the reduced model in the limit.

Table 6.2.: Architectures of the fully connected network (FCN) for the reduced and full model pair. The dN/dE columns describe the full spectrum models, while the cutoff column describes the maximum energy model for hydrogen ions. The inputs to the networks are 7,8 or 9-dimensional vectors respectively while the outputs are scalar. The numbered layers are the hidden layers.

Layer	dN/dE	Cutoff
Input	9	8
1	460	320
2	460	284
3	460	288
4	460	512
5	460	32
6	460	480
7	460	512
8	460	32
9	460	–
10	460	–
11	460	–
Output	1	1

The energy spectrum is a graph of a continuous function f, the first model maps $\{x, [\text{system parameters}]\}$ to $f(x)$ while the second model predicts the point x at which the graph gets cut off. Details about the training parameters and the procedure are given in Appendix B.3. Schematics of the finished models can be seen in Table 6.2.

Hydrogen Model Pair The precision of the maximum energy models, which attempt to map the physical parameters onto E_{max} can be estimated rather easily. The model achieved a mean squared error of $7.25\,\text{MeV}^2$ (confer to appendix B.3)., meaning the average error on the prediction of the hydrogen spectrum's maximum energy is projected to be around $\pm 2.7\,\text{MeV}$.

The model predicting the spectral shape is a little bit more complicated: To more intuitively evaluate the model's predicting capabilities and potential shortcomings, ten simulations with equal parameters (except for random seed) were computed such that their hydrogen ion energy spectra could be compared to the predicted spectrum of the model. All the spectra are plotted in Figure 6.3a. The overall agreement of the model with the simulations is evident. The maximum energy predicted by the model falls centrally between the maximum energies of the ten simulations, only differing from the simulation average by $0.2\,\text{MeV}$. Looking at more intricate features of the simulation spectra, however, it is clear that the model possibly generalized slightly too much. At around $10\,\text{MeV}$ a dip, possibly due to multi-species effects, can be observed in most simulations and is barely present in the model prediction. Generally, the fluctuations in the simulation spectra are greatly reduced in the neural network predicted spectrum. A reason for this is likely the sheer vastness of differing spectra the model was trained on. Since the parameter space for the training simulations was so large, the model had to generalize to many different output spectra. From the paper, the plot in Figure 6.3b is displayed which correlates the reduced model with the full model and therefore shows, that the models reproduce each other in the corresponding limit. This is expected behavior since there is a statistical variation in the training of neural networks. Important to note is the deviation in the spectra for different mixture ratios. An influence of the mixture parameter on the spectrum is visible and tuning, utilizing this effect, is possible.

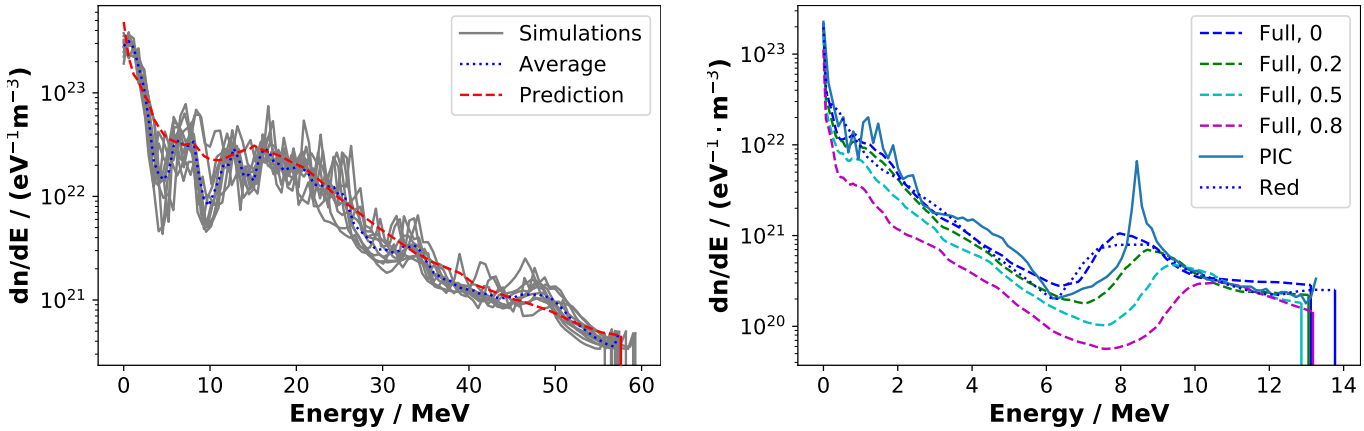

(a) Reconstructed hydrogen ion energy spectra of ten simulations differing only in their random seed. The energy spectrum prediction by the trained neural network model is indicated with a red dashed line, while the average of the simulations is indicated by the blue dotted line.

(b) Model comparison for hydrogen spectra with reference PIC simulation. Dashed lines give the result for the full model, the number indicates the value for the mixture parameter. The PIC reference (for mixture = 0) is displayed with a solid line and the reduced model with a dotted line. Taken from (Schmitz, Kreuter, et al. 2023).

Figure 6.3.: Hydrogen model plots.

Deuteron Model Pair The deuteron model pair was trained exactly the same as the hydrogen model pair but with an additional parameter and a larger dataset. They converged with a mean squared error of $6.76\,\mathrm{MeV}^2$ resulting in a prediction error of $\pm 2.6\,\mathrm{MeV}$ for the maximum energy of the hydrogen spectrum (confer to appendix B.3). Again, as given above, the sensitivity of the spectral model is more complicated to estimate. The shape however is not smooth, which might result from the co-propagating particles occupying the same space.

Model Efficiency

Calling the models in a Python code environment is similar to calling any other function and takes around $20\,\mathrm{ms}$ on a personal laptop. This time is in stark contrast to the four hours on 16 CPUs taken to run a similar 1D PIC simulation on the HPC cluster. To put this in perspective, the model can run inference roughly $720\,000$ times, while one PIC simulation calculates.

Other attempts at fitting the regression problem using various kernel combinations and Gaussian Process Regression (Bishop 2006) were made, however, they never produced energy spectrum predictions that even came close to the neural network prediction seen in Figure 6.3a, usually being off from simulations by orders of magnitude. As expected, the adaptability of modern unparameterized machine learning methods such as neural network models stands out from other regressors.

6.1.3. Application of the Model

With a trained surrogate in hand, it is possible to take advantage of the model to perform a numerical optimization of an experiment and evaluate the model's interpretability.

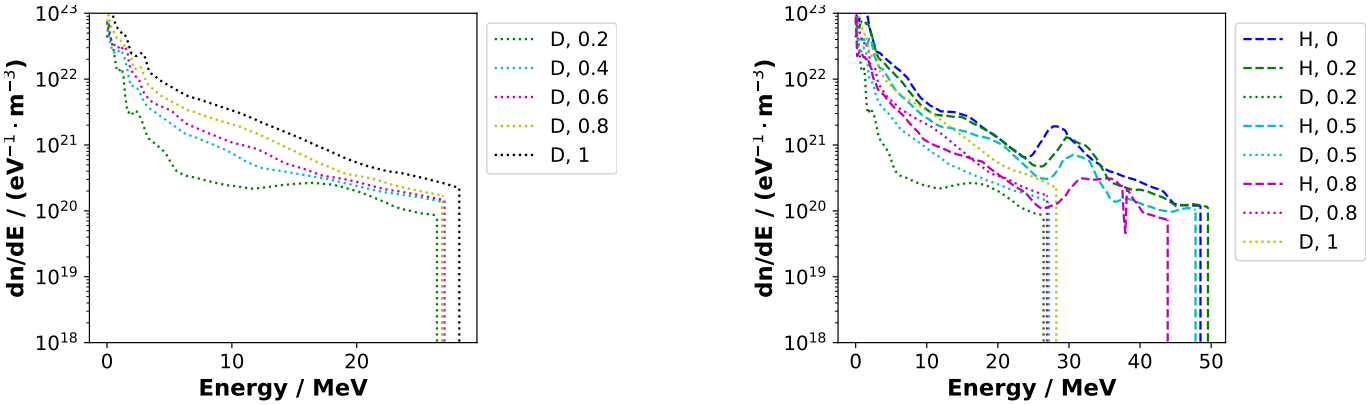

(a) Deuterium curves for different mixtures.

(b) Results for the combined deuterium and hydrogen model with different mixtures.

Figure 6.4.: Deuteron predictions for the optimum proton energy deposition. Input parameters are taken from Table 6.3 The mixture is given as a deuterium ratio in the legend.

Optimization of Parameters for Laser Plasma Interactions

In this section, a TNSA experiment with a water-leaf target is optimized. The aim is to get an ideal set of laser and target parameters and apply the previously obtained reduced machine-learning model pair.

Some base parameters are fixed. They are chosen based on a reals system that has a proven repetition rate of at least $1\,\mathrm{Hz}$: Ti:Sa lasers with a central wavelength of $800\,\mathrm{nm}$ and p polarized laser light. Exemplary systems would be the VEGA-3 laser at the Centro De Laseres Pulsados in Salamanca, Spain (CLPU) (VEGA 2022) or the DRACO laser at the Helmholt-Zentrum Dresden-Rossendorf (Schramm et al. 2017). Following the procedure in this section, the model can also be applied to any other system, if its parameters are inside the model's minimal and maximal physical parameters (see Table 6.1). If the system's parameters are not included, the model could be expanded by retraining with additional data, using transfer learning (Spears et al. 2018), or other modern domain adaptation methods (M. Wang et al. 2018). The assumed initial parameters are stated in Table 6.3. Optimization can have different meanings, therefore, two different goals are investigated in this section. The first goal is to find the maximum cut-off energy, while the second goal is to maximize the laser energy deposition into the plasma.

As mentioned, the polarization and central laser wavelength were fixed but all other parameters were allowed change, as long as they stayed within the given physical constraints. Since the obvious solution to maximizing output energy is to maximize input energy (as seen in Zimmer et al. 2021 and section 4.2), the optimizations were computed under the constraint of a constant dimensionless laser amplitude a_0. This ensures optimization by exploiting complicated relationships between the physical parameters of the system; a task that can only be feasibly solved with a rapidly callable model.

The optimization was implement using *SciPy* Python library (Virtanen et al. 2020) and the Byrd-Omojokun algorithm (Lalee et al. 1998). The Byrd-Omojokun algorithm allows to include both, boundary conditions according to Table 6.1 and the equality constraint of constant a_0, to leverage the aforementioned non-trivialities of the system.

The optimized parameters are displayed in Table 6.3. The optimizer seems to have taken advantage of incidence angle-dependent absorption effects such as resonance absorption. Additionally, by dramatically increasing laser focus while simultaneously decreasing laser power (energy over time) the maximum ion energy could be optimized without changing the dimensionless laser amplitude a_0. Overall, the optimizer increased the maximum ion output energy by a factor of roughly 4. The hydrogen energy spectra for these

Table 6.3.: Table of the physical parameters to be optimized for the laser system. Both initial and optimized values are shown. Rows in bold remained fixed during optimization. The dimensionless laser amplitude a_0 also remained fixed during optimization to encourage the convergence towards non-trivial parameter combinations. η_{conv} is a measure for energy conversion efficiency (see Eq. (6.6)), normalized to the initial parameter case.

No	Attribute	Initial	Optimized (E_{max})	Optimized (E-conversion)	Units
1	Laser energy	30	6.6	1.4	J
2	Focus-FWHM	20	4.2	2	µm
3	Pulse length	30	149.9	137.6	fs
4	**Polarization**	**p**	**p**	**p**	
5	Incidence angle	12.2	32.2	29.3	°
6	**Wavelength**	**800**	**800**	**800**	**nm**
7	Thickness	2	3.0	3.0	µm
	E_{max}	13.8	51.5	51.2	MeV
	η_{conv}	1.0	7.8	41.3	

optimized parameters and the initial parameters are depicted in Figure 6.5.

A more intricate measure of a TNSA experimental system is the laser-ion energy conversion efficiency, i.e. the measure of how much of the laser's input energy gets transported into the accelerated particles. Consider thus the optimization of the ratio of the total kinetic energy of the ions E_{H} to the laser pulse energy E_{L}:

$$\underset{x\in\{\text{params}\}}{\arg\max}\ \frac{E_{\text{H}}(x)}{E_{\text{L}}} = \underset{x\in\{\text{params}\}}{\arg\max}\ \frac{1}{E_{\text{L}}} \cdot \int_0^{E_{\text{max}}} \frac{\mathrm{d}N}{\mathrm{d}E} \cdot E\,\mathrm{d}E\ , \tag{6.6}$$

where $\frac{\mathrm{d}N}{\mathrm{d}E}(E,x)$ and E_{max} are given by the neural network models, and {params} is the set of all parameter combinations within the ranges specified in Table 6.1. It is important to note that the SMILEI output gives $\frac{\mathrm{d}n}{\mathrm{d}E}$, which must be scaled by a unit volume V to arrive at the expression needed. For further explanation of how to arrive at the above integral term, the reader is referred to Appendix B.2. Allowing the variation of laser energy E_{L} increases the complexity of the problem, but the optimization is still successful. The optimization described in Eq. (6.6) was carried out by solving the numerical integration using the composite trapezoidal rule and once again employing the Byrd-Omojokun algorithm. The optimized parameters are displayed in Table 6.3.

Surprisingly, despite having a slightly lower maximum ion energy than the first optimization task, the calculated energy conversion efficiency is more than five times greater. This strongly indicates that laser coupling into the target in a laser-plasma experiment depends on the system's physical parameters in a highly non-trivial way.

Sensitivity Analysis

Artificial neural networks are generally difficult to interpret. Nevertheless, the importance of specific parameters for a model can be evaluated. One way to quantify the impact of the model parameters upon the model output is with the variance-based global sensitivity analysis, also known as the Sobol method and the complementary PAWN method introduced in section 3.4. The number of evaluations of the model is $N \times (2D + 2)$, where D is the number of input features and N is the number of samples drawn. N is ideally

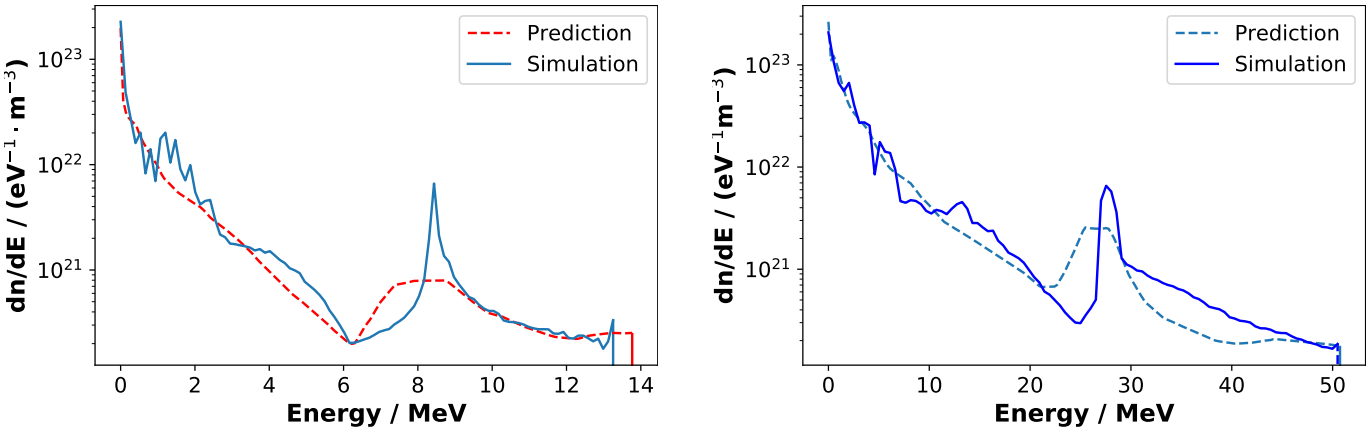

(a) Initial parameter selection.

(b) Optimized parameter selection with respect to maximum ion energy.

Figure 6.5.: Energy spectra of H-ions for a TNSA water leaf target experiment using both initial VEGA-3 as well as optimized parameters with respect to the maximum ion energy. Predicted spectra by the neural network model and spectra from a 1D PIC simulation are shown. The parameters are given in Table 6.3.

selected as 2^n, where we selected $n = 18$ resulting in 262144 drawn samples and they were used for both methods.

Hydrogen Model The Hydrogen model has 8 cut-off energy features mapped to 1 output prediction for the maximal energy. The results of the Sobol analysis are given in Figure 6.6.

The larger the value of a Sobol index is, the more influence the independent parameter has on the result. The total Sobol indices, normally referred to as S_T, measure the features' total importance. The total Sobol indices can neither describe how much of the variance is attributed to which combination of parameters nor are they normalized for the total expression. This is due to multiple counting of effects, e.g. if there is a second-order contribution for Θ_L and r_L, then this contribution is added to both of the values in the total representation. It doubles the counting for the second order, triples for the third order, and so on.

Due to this complication, determining higher-order dependencies makes it necessary to display the first and second-order Sobol indices, as done in Figure 6.6b. The values are displayed in a matrix, so the interaction between (x_i, y_j) can be displayed. The first-order Sobol indices are shown on the main diagonal ($x_i = y_j$). It is evident from the plot, that the sum does not add up to 1, leaving approximately $10\,\%$ of data variance unexplained. The consequence is that even higher-order interactions are necessary to explain the variation of the model fully. Full calculation of higher orders has been omitted as it was deemed unfeasible due to the extreme computational cost for higher dimensions.

The results of the PAWN method are displayed in Figure 6.7. PAWN can only measure the full importance of the individual parameters. A subsequent division into main effects and higher order is not possible. The importance ranking from PAWN does not entirely match the order found by the Sobol method but is rather close. If not the total, but the sum of first and second-order Sobol is taken, then the first two features change places.

The Conclusions from the sensitivity analysis are thus: Higher-order interactions are important in this model and a simple optimization (e.g. maximizing only one quantity) is not sufficient. The previously presented optimizations take this implicitly into account. Furthermore, the incidence angle and the irradiation

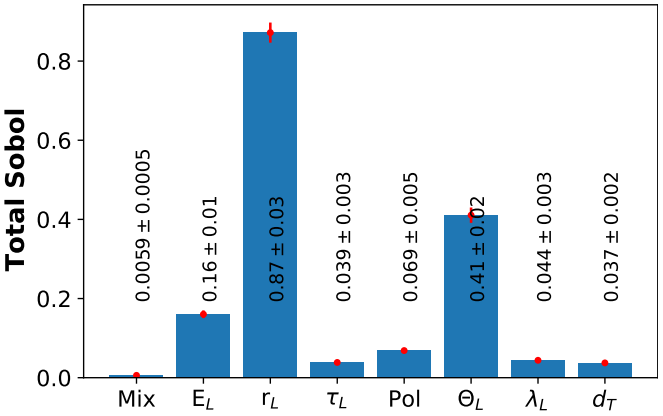

(a) Total variation which explains the cut-off energy variation.

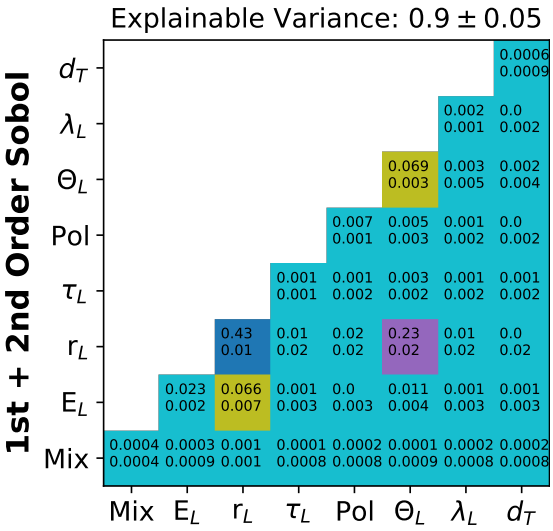

(b) Matrix of dependencies to explain the cut-off energy variation. The diagonal gives first-order Sobol indices, while the lower gives the second-order Sobol indices for the corresponding variables. The upper line is the numerical value, and the lower line gives the corresponding error.

Figure 6.6.: Sobol sensitivity analysis results showing the influence of various physical parameters on the cut-off energy of H-ions for a TNSA water leaf target experiment, for the full model utilizing only the H_2O data. Errors are given in the $95\,\%$ confidence level.

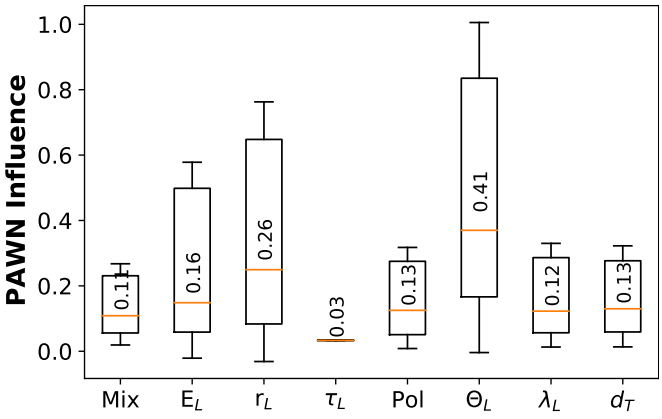

Figure 6.7.: PAWN indices for the full model as a measure for parameter importance. Boxes consist of uncertainty values, minimum, median, maximum, and upper uncertainty values. The numerical value given is the median.

Table 6.4.: Importance ranking of the model parameters as calculated by the Sobol and PAWN methods.

Importance	Sobol	PAWN
1	r_L	Θ_L
2	Θ_L	r_L
3	E_L	E_L
4	τ_L	τ_L
5	λ_L	λ_L
6	d_T	d_T
7	Pol	Pol

area appear to be important. The angle Θ_L's high influence is expected, considering laser-ion absorption mechanisms, and is faithfully implemented into the 1D simulation space using the Lorentz boosted geometry (see Appendix B.1). While the third quantity, the laser energy, directly scales the laser's dimensionless amplitude a_0, the irradiation radius r_L's influence is more difficult to understand. The irradiation area is not directly represented in a 1.5D PIC simulation. However, since a_0 is dependent on r_L an indirect influence is included.

Deuteron Model Calculating the same sensitivity indices for the deuterons results in the corresponding Sobol and PAWN indices, given in Figure 6.8 and Figure 6.9.

Sensitivity Analysis Discussion

The performed sensitivity analysis on the models allows evaluation of the importance of the different parameters. Since not all variations can be explained, it is evident that the model describing the laser-plasma system is non-linear. It should be noted that a deep learning model approximates the physical system very well. It does not, however, provide a closed-form solution for the underlying physics, which would require further theoretical work.

The models apply regression for the simulated data and, as such, can reproduce a mean curve for the data, which is, for example, displayed in Figure 6.5 or in Figure 6.3a. The spectral models consider the energy bin value and predict the continuum of accelerated ions. This means the dependency on the bin's energy would also be included. An explainable analysis of considering all energy bin values becomes infeasible as each bin would require a separate Sobol/PAWN analysis.

The cut-off energy of a TNSA spectrum is the main parameter investigated in the literature, which is also discussed in section 4.2 and in the corresponding paper (Zimmer et al. 2021). The Sobol analysis indicates that several parameters are of importance. Therefore, having only a single parameter to describe the cut-off is insufficient. Since second-order Sobol indices are not zero, the parameters' interaction must also be considered.

Since the model is not explaining the cut-off variation thoroughly, when only 1st and 2nd-order variations are considered, even higher-order variations have to be used to describe the total variation of cut-off energy. Such a significant reliance on higher-order interactions implies that simple scaling models are not ideal for optimizations since these effects can not be considered. A model capable of approximating highly non-linear effects, such as this neural network model, should thus be preferred.

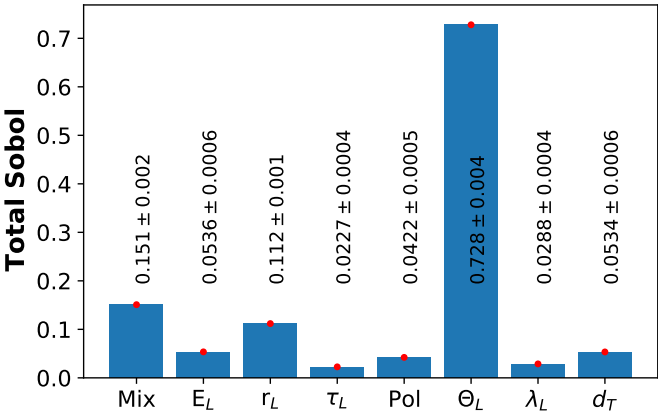

(a) Total variation which explains the cut-off energy variation.

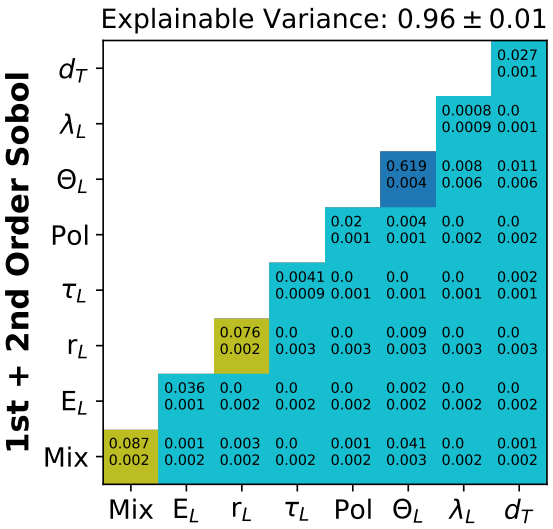

(b) Matrix of dependencies to explain the cut-off energy variation. The diagonal gives first-order Sobol indices, while the lower gives the second-order Sobol indices for the corresponding variables. The upper line is the numerical value, and the lower line gives the corresponding error.

Figure 6.8.: Sobol sensitivity analysis results showing the influence of various physical parameters on the cut-off energy of Deuterons for a TNSA water leaf target experiment, for the full model utilizing only the D_2O data. Errors are given in the $95\,\%$ confidence level.

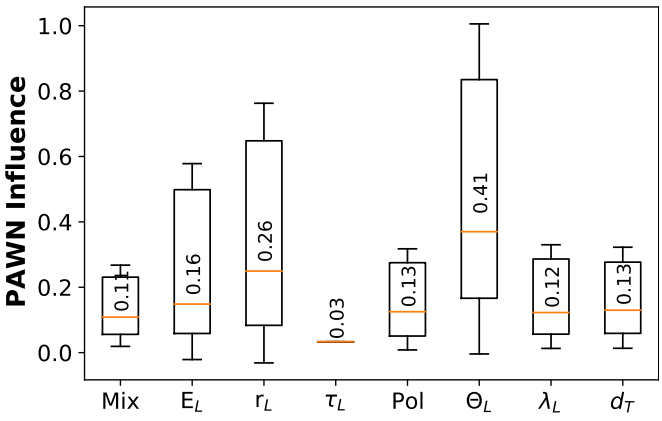

Figure 6.9.: PAWN indices for the Deuteron model as a measure for parameter importance. Boxes consist of uncertainty values, minimum, median, maximum, and upper uncertainty values. The numerical value given is the median.

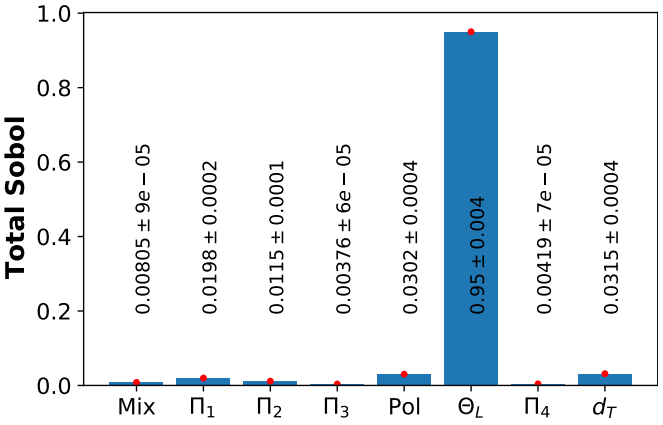

(a) Total variation which explains the cut-off energy variation for the full model.

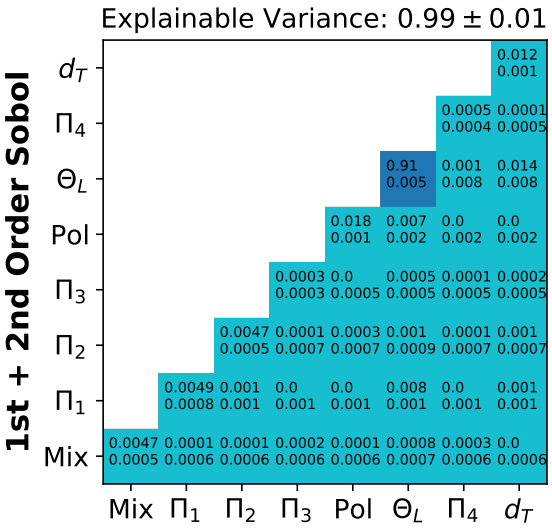

(b) Matrix of dependencies to explain the cut-off energy variation. The diagonal gives first-order Sobol indices, while the lower gives the second-order Sobol indices for the corresponding variables. The upper line is the numerical value. The lower line gives the corresponding error.

Figure 6.10.: Sobol sensitivity analysis results showing the influence of various physical parameters on the cut-off energy of H-ions for a TNSA water leaf target experiment for the full model utilizing only the H_2O data and the Buckingham parametrization. Errors are given in the $95\,\%$ confidence level.

Ion Surrogate using Buckingham Parameters

Going one step further in the modeling, the determined parameters in section 4.1 can fully represent the physical system. This is based on the construction in Table 4.2.

Taking these relations and mapping the physical parameters onto the corresponding Buckingham space allows for retraining the models. With this representation, all advantages of dimensional analysis can be applied, and systems can be scaled. The sensitivity analysis plots for the cut-off energy model for the Buckingham parameter model are presented in Figure 6.10 and Figure 6.11. The Sobol' indices show a large dependent significance angle and mostly negligible values for all other parameters. This has a very obvious s,elf-evident construction of the model, that the angle Θ_L is also relevant to calculate Π_4, such that the input variables are not independent of each other. This is one of the reasons for the introduction of a second complementary method. The PAWN indices show that the importance of the angle is still high, but the difference between other parameters is not as high as for the Sobol indices.

As seen for all three cases investigated, the incidence angle always has high importance in these models. This also correlates to the results of the Lorentz boost method presented in (Schmitz, Kreuter, et al. 2023) and section B.1. The governing effect in the heating process follows the same characteristic as the resonance absorption explained in subsection 2.2.3. Furthermore, the angle and the focus size defined are essential in the definition of irradiation. This directly biases the laser a_0, which is a direct indicator of the strength of the laser, and it, according to the relations calculated in section 4.1, is the component that defines the plasma dynamics.

Due to the use of the Lorentz boost method, the capability to simulate the angle variation in 1D PIC is

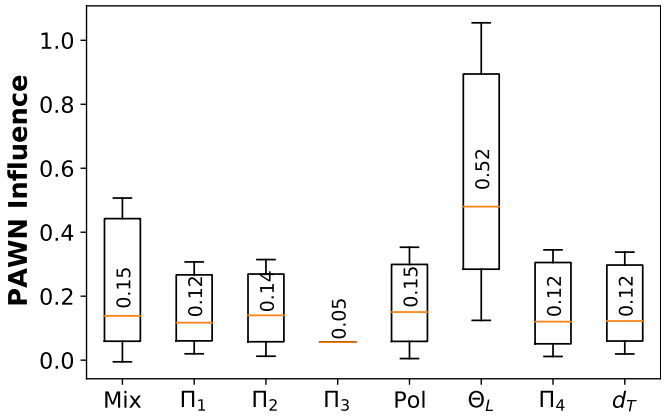

Figure 6.11.: PAWN indices for the full model in Buckingham parametrization as a measure for parameter importance. Boxes consist of uncertainty values, minimum, median, maximum, and upper uncertainty values. The numerical value given is the median.

acquired. Since higher dimensional effects, which can be represented only in 2D or 3D PIC simulations, are neglected, the resonance absorption process is dominant. Mitigation is possible if higher-order simulations or experimental data are also used for the model. This could be done with transfer learning (confer to section 3.3).

6.2. Surrogate for the Neutron Thick Target Yields

After the ions are accelerated the conversion to neutrons has to be modeled, such that it is possible to optimize and predict the relevant spectra. This implies two conditions: Firstly a quick evaluation and high inference speed are necessary, and secondly, a large parameter space has to allow for significant changes. The model should further be capable of comparing both conventional and laser-driven ion sources.

Conventional accelerators produce monoenergetic particle bunches. These mono-energetic bunches are simple to deal with in a modeling and optimization sense. On the other hand, the particle bunches created by laser-driven ions are more complex and not necessarily stable. Furthermore, the variation introduced by the multi-species effect complicates the spectrum further. Optimization tasks take in the order of 1000 evaluations, making optimizing the system even more unfeasible without a fast and reliable model.

To mitigate these problems, neutron production samples in the full parameter range of the ion spectrum were put together.

This allows predicting the full double differential neutron yield $\mathfrak{Y}$ by solving

$$\mathfrak{Y}(\Theta, E_\mathrm{n}) = \int_{E_\mathrm{min}}^{E_c} \underbrace{\frac{\mathrm{d}N}{\mathrm{d}E'}(E_\mathrm{p})}_{\text{Ion spectrum}} \cdot \underbrace{\frac{\mathrm{d}^2 Y}{\mathrm{d}\Theta\,\mathrm{d}E_\mathrm{n}}(E_\mathrm{p})}_{\text{Surrogate } \mathfrak{F}} \mathrm{d}E_\mathrm{p}, \tag{6.7}$$

where E' is the spectral binning width, E_n the neutron's energy, E_p the projectile's energy, E_c is the cut-off energy of the spectrum, and E_min the minimal relevant energy of the spectrum.

The minimal relevant energy is either determined by the minimal measured energy of the ion spectrum or the minimum neutron production energy, whichever is higher. The minimum neutron production energy is approximately given by the Q-values introduced in section 2.4, Equation 2.29 – Equation 2.33. If the model is evaluated for a mono-energetic beam, the ion spectrum is a Dirac delta distribution and is only evaluated at

the defined constant projectile energy. Such a model would ideally utilize experimental and simulated data to acquire a resulting surrogate as presented in Figure 6.12.

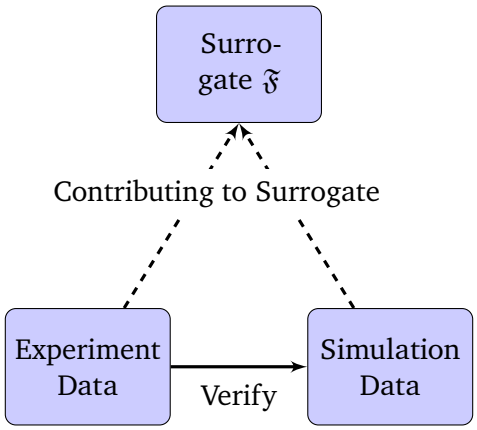

Figure 6.12.: Ideal setup of a neutron surrogate.

6.2.1. Experimental Data

The model's first pillar is experimental data, which is problematic for several reasons. Firstly, not much data was measured (or published) in the range of interest. Most data was measured for high energy beams and higher Z material as usable with the approach presented here.

Secondly, the type of data. Most were measured to determine the reaction cross-section, which made it necessary to use thin targets. These thin targets neglect the scattering and further reactions a thick target has on the resulting neutron beam, which makes the data not comparable. The difference was thoroughly discussed in section 2.4. The thin target data was also used to create the databases for the Monte Carlo codes, which are necessary for all relevant simulation codes. To avoid circular reasoning, results should not be compared with the same data used to calculate them.

Thirdly, experiments for this model were planned but ultimately did not result in usable neutron spectra due to a mismatch in the conventional accelerator parameters. Either energies were unreachable, or bunch lengths were too long to calculate the neutron's respective energies. The few remaining usable data sets are insufficient to contribute to the surrogate.

The model, therefore, only relies on simulated data. This results in potential offsets to the actual neutron yield. Still, since validating any arbitrary setup in the competitor range with the same model is possible, this systematic deviation does not matter. It is further not necessary to rely on the varying rigor of the different groups, publications, and models to be comparable since they can all be reproduced by the achieved surrogate.

The potential global offset can be corrected. If, at later times, sufficient experimental data is available. If so, the transfer learning approach can be applied to fit the model onto the experimental data. For now, the model is purely simulation-based. Since the simulations are important for the surrogate, how are they acquired?

6.2.2. Simulation for the Neutron Surrogate

The data for the surrogate is created by Monte Carlo simulations of the relevant physical processes as described in section 3.2. Simulations are done using the PHITS (Sato, Iwamoto, et al. 2018) code in Version 3.28A with the FENDL (Forrest et al. 2012) library.

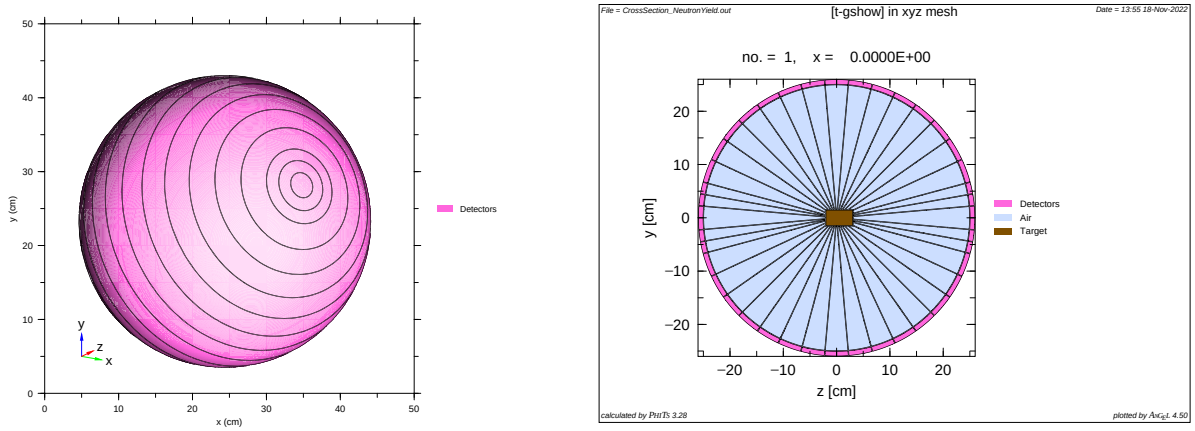

(a) 3D view of the simulation setup used in the PHITS simulations.

(b) 2D Cross section of the simulation geometry.

Figure 6.13.: Simulation description plots. They are created using PHITS Angel tool.

Table 6.5.: Monte Carlo input parameters. The maximum number of sampled parameters is given in the last column. Rectangular brackets indicate numerical intervals with the lower value left and the upper value right inside the bracket.

Quantity	Values	Possibilities
projectile	deuterons, protons	2
E_{kin} / MeV	$[3, 97]$	56
Element	Li, LiF, Be, Va, Ta	5
Length / mm	$[0.02, 104.45]$	356
Angle / °	$[0, 180]$	21

The observable is the double differential neutron yield $\mathfrak{Y}$ which is determined by measuring the number of neutrons crossing a detector surface. Several detectors are implemented to resolve the scattering angle. The detectors are implemented as rings around the detector, so the solid angle is maximized and the individual scattering angle stays constant. This is illustrated in Figure 6.13a and Figure 6.13b, where the black lines indicate the boundaries for each individual detector. Concrete parameters for the scattering angle (center of the detector) Θ and its size $\Delta\Theta$ are listed in the appendix in table C.1. The results have to be normalized to keep the different rates comparable.

$$\frac{\mathrm{d}^2 Y_0}{\mathrm{d}\Theta\,\mathrm{d}E_n}(E,\Theta) = \frac{1}{\Delta E}\frac{1}{\Delta A}\cdot\Phi_n(E,\Theta) \tag{6.8}$$

where Φ_n denotes the measured neutron flux, ΔE the measured neutrons energy bin width, Θ the scattering angle, and ΔA the detector's area.

The cylindrical particle beam is inserted at position $(0, 0, -9)$ into positive z direction with a radius of $r_0 = 0.5\,\text{cm}$. Energy and particle type of the incoming particles are subject to variation as indicated by Table 6.5. The target is implemented as a cylinder along the z-axis centered around $(0, 0, 0)$ with a radius $r = 1.5\,\text{cm}$ and a variable length as well as a variable material, as indicated by Table 6.5, too. One condition has been fulfilled in the random sampling of the domain. The full bunch had to be stopped inside the target.

It is possible, however, that the target is longer than necessary. This was allowed because the effect of low neutron absorption and moderation in a longer target is included. The target cylinder's radius was fixed at $2.5\,\mathrm{cm}$. A total $54\,768$ neutron yield simulations in the mentioned setup were acquired for the surrogate model.

6.2.3. Thick Target Yield Model

With the large amount of data calculated for the modeling, a numerical surrogate can be directly calculated. Due to the complicated nonlinear relation coming together, a neural network is applied. The moving source model (subsection 2.4.2) did not lead to a sufficiently good result, so the approach using an artificial neural network was chosen.

Data Preparation

For an efficient surrogate, the input data was organized following the concept of one hot encoding (OHE). The categorical features of data were labeled according to a binary representation of the values, while the continuous data was scaled from 0 to 1.

For the one hot encoded data, the 2 different projectiles can be labeled by a single bit: Deuterium is labeled with 1 and Hydrogen is labeled with 0. For the converter materials under investigation, this makes it necessary to have 3 bits to describe all possibilities fully: 'Li'–'000', 'LiF'–'001', 'Be'– '010', 'Va'–'011', 'Ta'– '100'
In total the number of inputs has to be adjusted: Neutron Energy, Projectile Energy, Length, Angle, Projectile OHE, $3\times$ Target OHE, which totals 8 input parameters. The neutron energy is a normalized measure for the position of the determined count rate.

A further important note, which is relevant to the convergence of the system is the preparation of the training data itself. Without preparation, convergence is bad and not existent. The data was first resampled to increase the density of the data points in the higher energy part of the spectrum. This resampling was done with cubic spline interpolation of the Monte Carlos output data and joined with the raw data, doubling the number of data points for learning while keeping the spectral shape intact.

Because of the large range of input data, varying by several orders of magnitude, numerical stability is an issue. While some data points contribute much to the mean squared error training quantity, some with a lower numerical value did not contribute much. As a result, the training process was highly unstable, which needed to be mitigated. This was fixed by applying a transformation to the data. First, the logarithm to the base 10 was taken, then the full data set was renormalized, to the smallest value. The final data reached from 1 to the normalized maximal value and all data was larger than 0.

Cut-Off Energy of a Neutron Spectrum

The same approach for the model was chosen as for the ion model in subsection 6.1.2. Two models were trained, one for the spectrum and one for the cut-off energy. Training cut-off positions together with the spectrum is difficult since a cut-off represents a discontinuity in the spectrum. Discontinuities are not smooth and can only be approximated with an even larger data set.

This can be circumvented by splitting the data into spectral shapes and cut-offs, equivalent to the ion model. The spectral shape is then normalized from minimal data at 0 to maximal non-zero data at 1, while the cut-off model basically predicts the relevant scaling.

The topologies of the networks are displayed in Table 6.6. Better results might be acquired by dropout optimization or other sophisticated methods, but time constraints did not permit further optimizing the topology.

Table 6.6.: Topologies for the two networks needed to predict the thick target neutron yields. The numbered layers are the hidden layers. A

Layer	Spectrum	Cutoff
In	8	7
1	200	260
2	200	180
3	200	180
4	200	340
5	200	180
6	200	180
7	200	340
8	–	340
9	–	180
Out	1	1

Training Results and Model Validity

For these topologies, the resulting training error for the cut-off model results in a prediction uncertainty of ± 3 MeV. To understand the result for the spectrum, a set of example plots is displayed in Figure 6.14 and Figure 6.15. A few remarks on the model's validity can be derived from the figures.

1. The model is only valid in the region of fit, defined by the parameters in Table 6.5.
2. After the cutoff energy, the spectrum generally deviates, implying that the physical cutoff is not learned by the spectral model and therefore yields wrong results in the high-energy end of the spectrum.
3. The model can predict the lowest energy neutrons, which can not be seen in the Monte Carlo spectra. This has two reasons: First, the model itself is regression-based, and as can be seen, higher energy projectile energies do have neutron signals in the low energy regime. The effect of the regression is calculating a corresponding mean value from all calculated spectra and therefore yielding a non-zero contribution. Second, the reason for zero count rates is the bulky target, the lowest neutrons created by low-energy projectiles can not leave the target and are stuck there.
4. The proton Lithium reaction has a characteristic high energy peak in the forward direction. As visible Figure 6.14 (a) this peak is suppressed by the bulky target. Due to the nature of the regression model, the model further suppresses the peak and is therefore impossible to resolve it.

Despite these limitations, the model can predict spectra that are quite accurate over a large energy domain in milliseconds evaluation time and allows the needed quick evaluations of neutron production.

If compared to the results of a moving source model (confer to subsection 2.4.2), which are close to the curves presented in Figure 2.16, the accuracy and predictability of this model are significantly better in each aspect. As already mentioned in the corresponding section and the given source, this is because of the moving source model's bad fit for the low-energy regime.

Uncertainty Quantification for the Model

The uncertainty bands given in Figure 6.14 and Figure 6.15 are the $95\,\%$ are calculated by a Monte Carlo approach themselves. The data has been resampled and evaluated several times in a bootstrapping sense (Efron et al. 1994). The data from the simulation had uncertainties, which were used to resample data according to their uncertainty and the likelihood of the distribution. With this variation, 10 different spectra

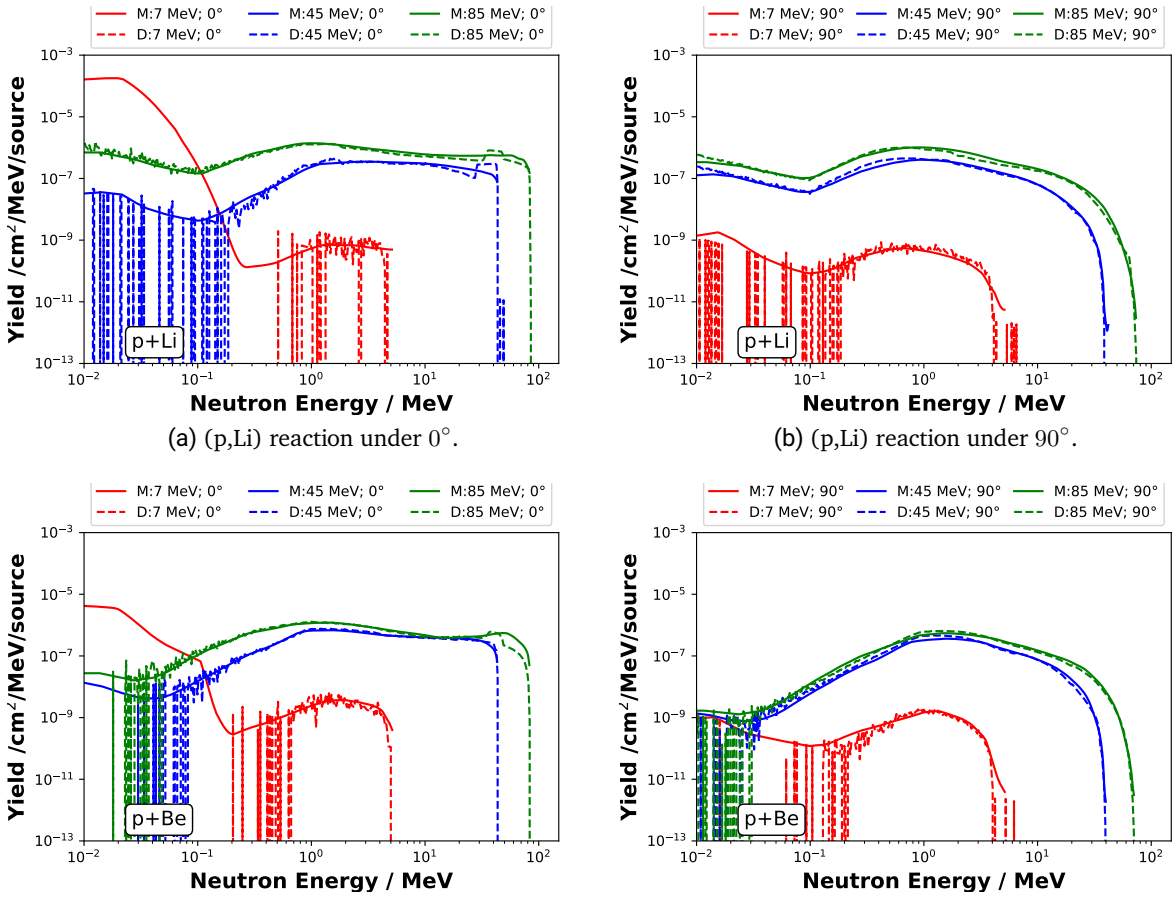

(a) (p,Li) reaction under $0°$.

(b) (p,Li) reaction under $90°$.

(c) (p,Be) reaction under $0°$.

(d) (p,Be) reaction under $90°$.

Figure 6.14.: Comparison of our model with results from PHITS. Displayed are samples for proton-induced neutron production. Dashed lines indicate the Monte Carlo data indicated by D and solid lines give the corresponding model output indicated by M.

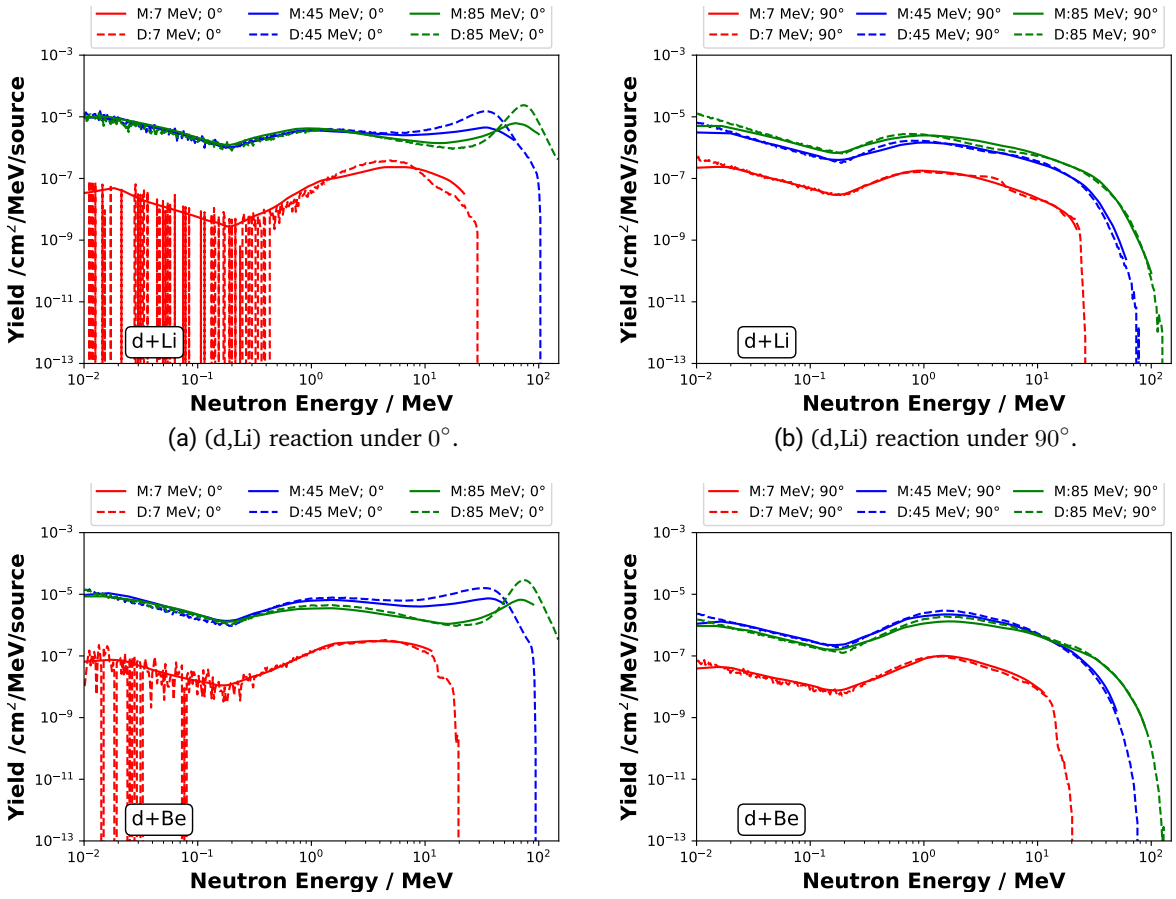

(a) (d,Li) reaction under $0°$.

(b) (d,Li) reaction under $90°$.

(c) (d,Be) reaction under $0°$.

(d) (d,Be) reaction under $90°$.

Figure 6.15.: Comparison of our model with results from PHITS. Displayed are samples for deuterium-induced neutron production. Dashed lines indicate the Monte Carlo data indicated by D and solid lines give the corresponding model output indicated by M.

Table 6.7.: Parameters for several compact neutron source accelerators. The same projectile and target types are fixed to compare different spectra. The source is given in the text.

Name	Projectile	Energy /MeV	Target	Current / 10^{-4} A	d_T / mm
IAEA2	p	40	Be	50	20
IAEA4	p	40	Be	1250	20
RANS	p	7	Be	1	0.3
HBS	p	70	Be	1000	16
SONATE	p	20	Be	1000	2

were acquired. For each spectrum 10 models were evaluated, its mean and deviation calculated, and the results are the spectra displayed here. With this method, the direct uncertainty of the network-based model could be acquired and a more quantitative description of the results is possible.

6.2.4. Application of the Model

The trained model can be quickly applied to determine spatially distributed neutron spectra. This model can now be used to validate different ion beam parameters against each other.

TNSA's exponential spectra must be separated into quasi-mono-energetic pieces to calculate the yield. The neutron spectrum for each piece has to be calculated and superposed with the multiplicity in the particle count to reach the final spectrum. This can be formally written as

$$\frac{\mathrm{d}^2 Y}{\mathrm{d}\Theta\,\mathrm{d}E_n} = \sum_{E_\mathrm{p}} N_\mathrm{p}\left(E_\mathrm{p}\right) \cdot \hat{\mathfrak{F}}\left(E_n, \Theta, E_\mathrm{p}\right) \tag{6.9}$$

and with the infinitesimal limit for $E_p \to 0$:

$$= \int N_\mathrm{p}\left(E_\mathrm{p}\right) \cdot \hat{\mathfrak{F}}\left(E_n, \Theta, E_\mathrm{p}\right) \mathrm{d}E_\mathrm{p}, \tag{6.10}$$

where Y is the neutron yield, Θ the scattering angle, E_n the energy of the neutron, N_p the number of incoming projectiles, E_p the energy of the projectile, and $\hat{\mathfrak{F}}$ is the unit surrogate model, which is normalized to one projectile particle. E_p is sampled according to the needed precision. We used a bin width of $\Delta E = 1\,\mathrm{MeV}$. Setting the model up like this allows to apply and verify this model on mono-energetic spectra and on laser-accelerated ions and ensure their direct comparability. Furthermore, the model after the limit is a convolution of the spectrum with the production model, similar to the integral equation given in Equation 5.3. The model will now be applied to conventional accelerators and some already-done TNSA experiments.

Neutron Production from Conventional Accelerators

The parameters for the conventional accelerator are extracted from several reports focused on developing compact ion-based neutron sources. Namely the projects HBS in Jülich (Rücker et al. 2016), RANS at RIKEN in Japan (Otake 2018), SONATE at CEA-Saclay (Thulliez, Loïc et al. 2020), and from the technical report of the IAEA in Vienna (*Compact Accelerator Based Neutron Sources* 2021). A first exemplary set is tabulated in Table 6.7 and the model's results are displayed in Figure 6.16a and Figure 6.16b. Differences in the spectrum result from the different particle energies, and level differences from the different particle counts. A difference in the spectral shape in dependence on the angle also appears obvious. This variation

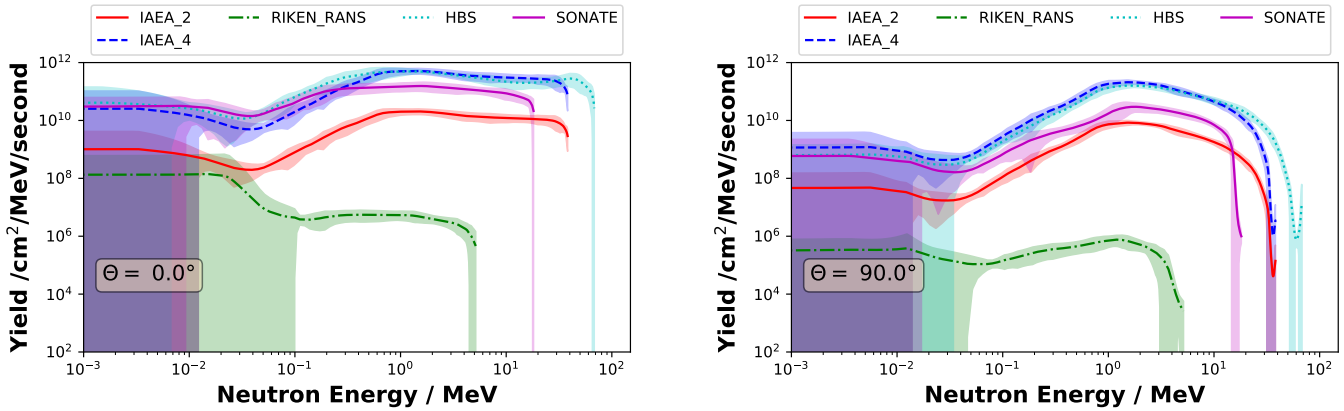

(a) Signal under $0°$.

(b) Signal under $90°$.

Figure 6.16.: Model output for the conventional accelerators in p+Be configuration.

indicates that pre-equilibrium reactions (section 2.4) are more dominant in the forward direction, which shows that the understanding of the processes happening is in good agreement. The neutron counts are realistic compared to publications of the respective collaboration. SONATE, for example, has around 10^6 neutrons in the forward direction for neutrons below $400\,\text{keV}$ and after a moderator, the loss, therefore, is the same order of magnitude. HBS also, according to the design reports, is supposed to achieve something in the order of 10^{12}. All these numbers are not exactly comparable, due to the already mentioned complications between simulation, experiment, and different simulation databases. Despite these problems, the model is in the same order of magnitude as other calculations. It can therefore be concluded, that it reproduces the physics quite well and the next step in comparing laser-driven sources can be taken.

Neutron Production from Laser-Driven Ion Accelerators

In this section we calculate the neutron yield for TNSA accelerated spectra and assume the functional dependency given in Equation 5.9.

These not mono energetic beams can be dealt with with the already mentioned split along several energies. For this first part, four different spectra are used. Two from DRACO with a $10\,\text{J}$ and $18\,\text{J}$ laser respectively (Kroll et al. 2022) and two from PHELIX, where one of the highest energy spectra (Hornung et al. 2020) and the lower one is the source shot evaluated in chapter 5. The proton + Beryllium case spectra are displayed together with the conventional spectra in Figure 6.17. The laser spectra are similarly scaled as the conventional ones. All spectra give the mean neutron yield for 1 second of operation. The TNSA sources are all below conventional accelerators, this is due to the low repetition rate of the dedicated laser system. For PHELIX a repetition rate of 1/5400 Hz reduces the yields considerably, while the $1\,\text{Hz}$ of DRACO further does not improve the signal.

Considering a sweep of the full angle space, integrating over all neutrons yields Figure 6.18.

The solution for the problem of TNSA-based neutron sources can only be the scaling of the repetition rate, hence the discussion of the liquid leaf as a target that enables high repetition rates.

6.3. Neutron Yields from Liquid-Leaf Protons

This section puts everything investigated so far together. The aim is to get a pitcher-catcher setup for proton-induced nuclear reactions to produce neutrons. Starting on the design the physical laser parameters already

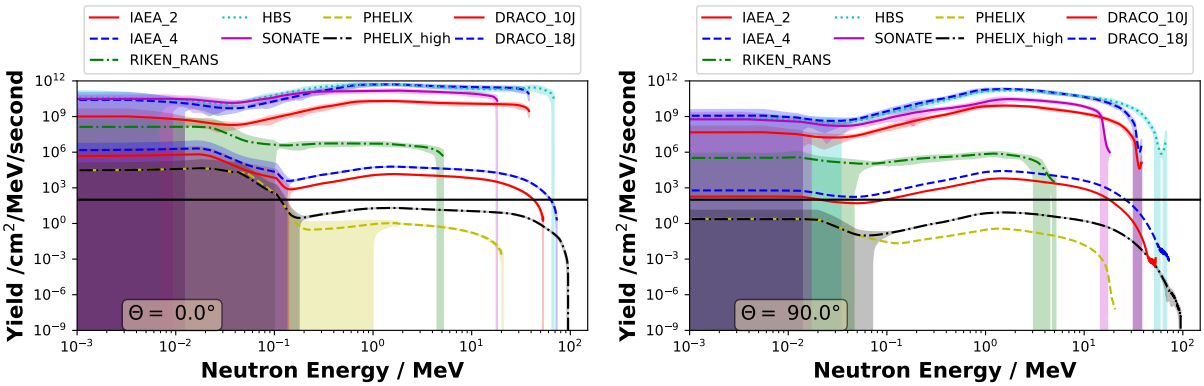

(a) (p,Be) reaction under $0°$.

(b) (p,Be) reaction under $90°$.

Figure 6.17.: Comparison of the result for conventional machines with TNSA-based laser accelerated spectra. The thick black line denotes the lower boundary of the plots in Figure 6.16.

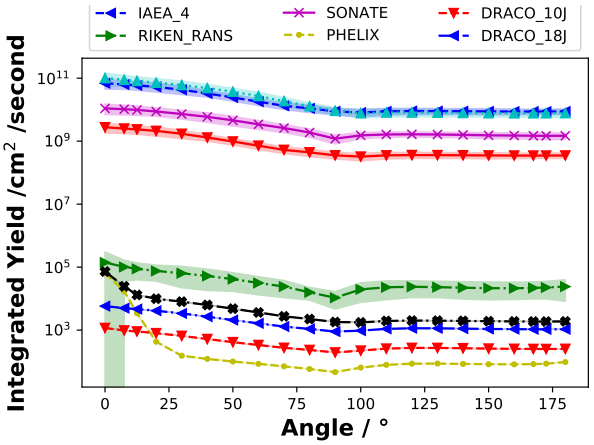

Figure 6.18.: Energy integrated neutron yield for (p,Be) reactions

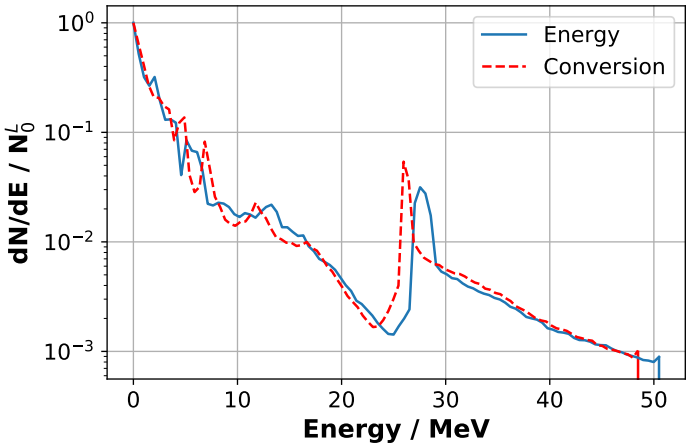

Figure 6.19.: Normalized plots of the simulated spectra. The simulation for the setup with maximum cut-off energy is marked in a blue solid line and denoted as Energy, while the spectrum for the maximum energy conversion is marked with a red dashed line.

found in section 6.1.3 and displayed in Table 6.3 are used. Fixing a Ti:Sa system, with p-polarized laser light, allows fixing $\lambda_L = 800\,\mathrm{nm}$. With this, the optimization leaves basically two reasonable solutions, once a laser pulse is optimized for the maximum cut-off energy, and once the laser is optimized for maximal energy deposition.

The ion spectra calculated by the ion model are from a one-dimensional model; no experimental data were available to validate the model. This leads to one major issue, the unit for the count-rate $\mathrm{d}n/\mathrm{d}E$ is in $\mathrm{eV}^{-1}\,\mathrm{m}^{-3}$ which needs to be corrected. In one dimension the transversal directions extend to infinity. As a result, the n is a surface density and as such has to be multiplied with a proper volume for a physical particle count. A new parameter for this model is introduced to solve this problem, which scales the full count rate onto the interval from 0 to 1. This parameter has the same meaning as n_{i0} in subsection 2.3.1 and as N_0 in chapter 5. The initial ion rate can later be extracted from higher-order simulations or experiments. This parameter can then be defined as

$$N_0^L = \max_{\forall E}\left(\frac{\mathrm{d}\,n}{\mathrm{dE}}(E)\right). \tag{6.11}$$

For each spectrum, this normalization is applied. Due to the additive nature of the neutron model, a global scaling factor of the result can be factored out. The resulting model is a normalized weighted sum, and the true scaling factor can be determined with an experimental input. A RCF (confer to chapter 5) or a comparable measurement could be done to determine this factor.

Physical Optimization

New particle-in-cell simulations were done for the two parameter sets, given in Table 6.3. These spectra are normalized by N_0^L and displayed in Figure 6.19. Compared to the results in the table, the simulation does deviate. The cut-off energies are lower, than predicted, but are still inside the model's uncertainty. The simulation for the maximal cut-off energy gives the cut-off at $50.5\,\mathrm{MeV}$, where the model's prediction is $(51.5 \pm 2.7)\,\mathrm{MeV}$. The cut-off position for the maximized conversion efficiency from the test simulation is $48.5\,\mathrm{MeV}$, where the model's prediction is $(51.2 \pm 2.7)\,\mathrm{MeV}$. Example plots are displayed in Figure 6.20 and are directly scalable with the product of the introduced factor and the repetition rate of the laser $N_0^L \times \nu_{\mathrm{rep}}$. These plots complement Figure 6.16 and Figure 6.17. For this case, the results for the conventional accelerators are used as a benchmark. The calculated combined scaling factor is given in Figure 6.21. Only the curves

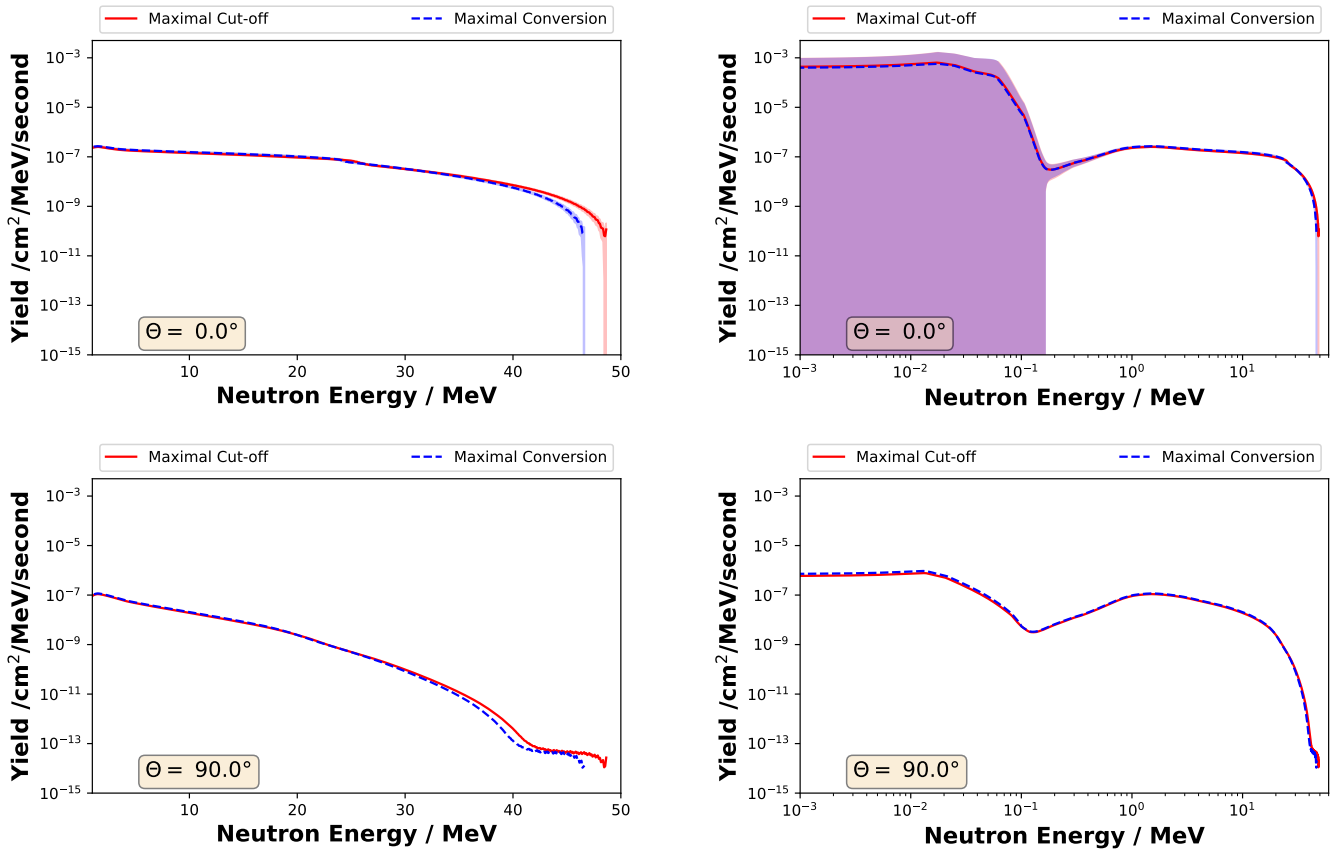

Figure 6.20.: Exemplary plots for both optimized liquid leaf parameter sets with a Beryllium target. Ion input for the model was scaled with N_0^L and a $1\,\mathrm{Hz}$.

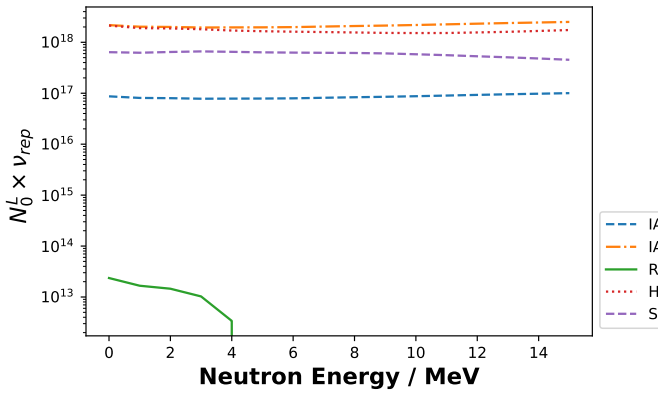

Figure 6.21.: Comparison of the scaling differences for the Liquid Leaf's maximum energy data compared to the conventional accelerators.

Table 6.8.: Numerical values for the $N_0^L \times \nu$ product and the calculated ν for two exemplary N_0^L values.

	IAEA2	IAEA4	HBS	SONATE	RANS	
Cut-off	10^{17}	3×10^{18}	2×10^{18}	8×10^{17}	2×10^{13}	
$N_0^L = 10^{10}$	10^{7}	3×10^{8}	2×10^{8}	8×10^{7}	2×10^{3}	Hz
$N_0^L = 10^{12}$	10^{5}	3×10^{6}	2×10^{6}	8×10^{5}	2×10^{1}	Hz

for the maximized cut-off energy case are given. The results for maximized energy conversion only deviate minimally from these curves. The results are essentially the same. Extracting the numerical values for the curves in Table 6.8. As visible, a competitive setup is difficult to reach for the large accelerator-based concepts. According to the dedicated application, this competitive setup assumes a higher neutron yield in each energy bin and might not be necessary. For the low energy machines, for example, RANS, a repetition rate of some Hz appears to be sufficient.

The yield can be boosted by an additional factor of two if the expanding plasma from the front side (confer to section 2.3 or (Fourmaux et al. 2013)) is used as well. Utilizing both beams is complicated; whether it is applicable depends on application and usability. The main problem is that the neutron yield from both catchers superpose and signals can be misinterpreted during the experiment.

Deuterons have a higher yield but are not discussed in this combined part. They have the same Z/m ratio as the eightfold ionized oxygen and contributed significantly to the accelerated particles. Due to the higher plasma frequency $\propto Z^2/m$, it started to move earlier than deuterium and significantly reduced its acceleration efficiency. This caused the model for deuterium to be suppressed in yield and maximum energy and increased the model's fluctuations.

This has to be tackled by an additional campaign to fix the proper ionization rates of oxygen to yield realistic behavior for deuterium.

7. Final Review and Conclusion

"Neutrons probe deep,
Unveiling secrets within,
Science finds truth there."

As presented in the previous chapters two components for a joined surrogate model were determined. Both parts can be used to understand and optimize an ion source or compare the neutron yield from proton and deuteron reactions. First, both models and their respective traits and problems are reviewed. Then in the second part, the application to the real world is discussed. The last two parts then conclude and make an outlook for further developments.

7.1. Model Review

Both models' capabilities and drawbacks are reviewed in this section.

The ion surrogate can predict ion spectra, especially protons, depending on the physical parameters. The model focuses on the proton behavior, since the model for the deuterium spectrum resulted in some unexpected behavior, contradicting higher-order PIC simulations. Sensitivity analyses have made it possible to predict the existence of proton cut-off energy variations, depending on higher-order combinations of their respective input parameters. These higher-order input dependencies allow for non-trivial optimization of the full system. Because the model, as mentioned in section 6.1, is trained exclusively on 1D PIC data it has certain limitations.

- One dimensional simulation as mentioned in subsection 6.1.1 would accelerate particles into infinity and it can therefore overestimate the spectral energy cut-off. This was successfully dealt with using the acceleration time determined by (Lécz 2013, Eq. 4.1, p. 47). Proper scaling of such an improved system towards a 2D or 3D PIC simulation also exists, such that the model can be regarded as scalable towards higher dimensional simulations (Sinigardi et al. 2018).
- Effects of transverse particle movement can not be taken into account. The lack of transverse movement results that the multi-species-based variation being more discontinuous than measured in the experiments.
- The spectral predicted value dn/dE is not equal to the particle counts dN/dE, n is particle density with the number of particles per volume. Taking the output in particles per cubic meter overestimates the direct count by several orders of magnitude since the irradiated volume is much smaller than cubic meters.
- Further limitations arise from the ionization state of the Oxygen particles used in the simulations. While the ionization energies necessary (confer to Table 2.1) are known, it is not clear how the charge state distribution inside the plasma behaves. Applying a tunnel ionization model for the acceleration field on the back side ions underestimates the ionization state because collisions are not taken into account. Full ionized oxygen was assumed for the model presented here, which is also not the ideal representation of the system. As discussed in section 6.1 the high ionized oxygen suppresses the acceleration efficiency of deuterium. The fewer oxygen ions are highly ionized, the better the acceleration for deuterium.

These limitations can be overcome by applying the transfer learning method using higher dimensional simulations and experimental data or introducing a better model for the ionization of oxygen.

The neutron model is successfully used to evaluate and compare different types of accelerators. The behavior for the same machine with different particle intensities is consistent. The uncertainty is small in a large energy range and the cutoff values determined correlate well with the expected cut-off from the Q-values (confer to section 2.4). Although the predictions are good in the area where they are needed the model has some limitations.

- The geometry of the converter was fixed as a cylinder with a constant diameter and a flexible length. This does not allow for optimization in the geometry shape.
- Some data sets were not successfully calculated, this implies that there might be issues with the code and that the predictions for Vanadium targets might not be true.
- The model lacks absolute validation. As mentioned in subsection 6.2.3 the ideal workflow, verifying simulated data with experimental data and applying a correction was not possible. The lack of comparable experimental data makes it further difficult to verify the simulation model with other published studies. The results, therefore, have to be compared with the same model.

The neutron transport equation, which is a basis for the neutron production simulations could be solved more efficiently by applying more sophisticated methods from the field of machine learning. Further comparable experimental data to introduce a numerical benchmark of the model with the real world can increase the model's performance and validity.

7.2. Application to Real-World Machines

These models should be used to identify ideal working points to aid the design and setup of machines and experiments. Since the assumed physical parameters are not directly measured in an experiment, some transfer has to be done to make the models applicable. For example, the laser irradiation size on the target can not even be measured at all, during the experiment. This makes it necessary to correlate the measurable parameters to the needed physical parameters. This means that if the system is known well enough a map between the systems' observables O and the physical parameters P used in this thesis can be constructed.

$$P = f(O), \tag{7.1}$$

strictly speaking, f is a surrogate model itself. f can be determined by dedicated experiments and supported with simulations of the corresponding laser facility under investigation. This surrogate f is then machine-dependent and can vary, while the model presented here is universally valid as long as it is not extrapolated beyond the region of input parameters.

The inversion of f allows determining the observable parameters needed for the ideal work point. As soon as the different optima for a system are known, the ideal machine values can be used to regulate a machine. This is exemplarily sketched in Figure 7.1.

Experimental Validations

Experimental validations of the neutron model are straightforward since the model allows to predict neutron yields for laser-driven and accelerator-driven spectra simultaneously.

Validation of the ion model needs a little bit more work to be validated. First, the whole spectrum has to be measured, and the deviations from the exponential curve must be measurable. To achieve this, an experimental setup that can resolve particle species and spectral distribution has to be used (Alejo et al. 2014).

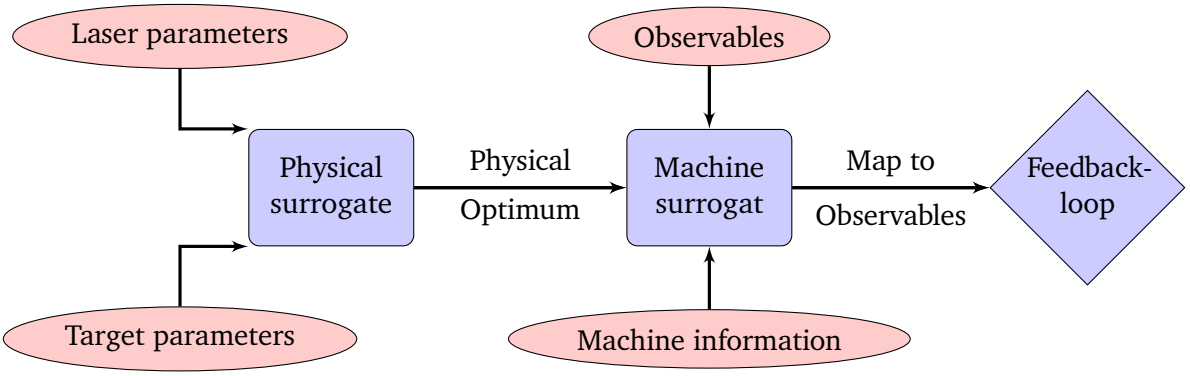

Figure 7.1.: Application flow in a real machine.

If RCFs are supposed to be used, their setup and traits must be aligned with proper calibrations (Appendix A) to get remotely close to the sensitivity needed. Secondly, when the data is available, the model has to be scaled or retrained in a transfer learning sense to fit the data onto a real system.

Even if the system is not adjusted as explained, the model's prediction can still lead to islands of efficient acceleration parameters, which can be directly checked. The calculations in section 4.1 have shown that the governing equation system can be reduced to the Buckingham representation. In this representation, each set of physical parameters resulting in the same Π_i result in the same particle dynamics and therefore yield the same result. It is, therefore, possible to verify the results for other laser systems that were not investigated. An example calculation was given in subsection 4.1.2.

7.3. Conclusion

In the course of this thesis, the fundamentals for compact laser-driven ion accelerators using TNSA have been discussed. This led to a discussion of the fundamental equations systems and the investigation of their similarities. Due to the non-existence of closed-form solutions, data-driven modeling was attempted. The proposition and implementation of an algorithmic data processing tool mitigated problems with the experimental data sets. The modeling approach using neural networks and numerical simulations allows, for the first time, to quickly predict full particle spectra and generate insight into the governing equation system. Finding a nontrivial optimum for energy deposition in a laser-driven proton beam was achieved. Furthermore, comparable spectra for conventional and laser-driven neutron sources were calculated.

These results can be applied to real machines and deliver pointers toward more efficient usage.

7.4. Outlook

The results presented so far have some limitations, as discussed above. The models are set up so that further improvement is possible. Both models can be improved by including relevant experimental data and applying, for example, transfer learning better to fit the models onto the physical domain of interest.

The ion prediction model can further be improved by including 2D or 3D particle-in-cell simulations. This would then incorporate transverse motion inside the target and is expected to smooth out the multi-species effects on the spectrum.

The developed tool for the enhanced evaluation of radiochromic film stacks can also further be improved by adding additional capabilities. When all supporting data is supplied by the tool itself, and the evaluations no

longer rely on externally generated data, the reproducibility of the data sets is further strengthened.

For a possible design study for new machines based on liquid leaf targets, these imprecisions should be tackled further to enhance the prediction level of the models. It should, as mentioned previously, be supported by an experimental study, to fix the scaling parameter N_0^L and to show the system's high repetition rate operation capabilities.

A. Radiochromic Films – Functionality, Calibrations, and Limitations

Radiochromic films, mainly conceived and designed for dose verification in radiotherapy, are also widely used to characterize and quantify the ultra-intense proton pulses produced in laser-particle acceleration. Their capability to withstand and measure high doses and insensitivity to electromagnetic disturbances make them ideal for the harsh environment encountered in relativistic laser-matter interaction experiments. The film's response, i.e. the amount of darkening per absorbed dose, is non-linear. Consequently, quantitative dose measurements require a calibration of the response curve over the application dose range. With new generations of RCF being developed, these calibrations must be redone. Differences in thickness, density, and composition of the active layer, and even the crystallinity of the color molecules affect the response, and a simple scaling from one generation to the next is generally impossible. Even for the same film type, the manufacturer advises that "...the thickness of the active layer will vary slightly between different production lots..." (Ashland Global Holdings Inc, Delaware, U.S. 2022), leading to different response curves for films from different production batches.

A.1. Calibration Model

The first part of this section describes the data pipeline to enable calibration and describes the relations necessary to express the relevant quantities. The second part of this section gives then the actual fit model and describes the concrete bootstrap steps to determine the model's uncertainty.

Preparing Input Data

The relevant quantities, color, and dose, have to determine from the measured data.

Determining the Color Values

Experimental data are taken for several dose values. Each dose value can be assigned a color value triple Ξ consisting of the R, G, B values for the dose. All equations, therefore, apply for each of these components individually as indicated by the index i. They are obtained from the scanned RCFs by

$$\Xi_i = \frac{\left(65535 - \overline{\mathrm{PH}}_i\right) - \left(65535 - \overline{\mathrm{BG}}_i\right)}{65535} = \frac{\overline{\mathrm{BG}}_i - \overline{\mathrm{PH}}_i}{65535} \tag{A.1}$$

where $\overline{\mathrm{PH}}$ is the pixels mean value and $\overline{\mathrm{BG}}$ corresponds to the mean background value. $\overline{\mathrm{BG}}$ is determined from samples before calibration and $\overline{\mathrm{PH}}$ is the current signal during calibration or later also the measured signal. Equation A.1 also implies that the Ξ ranges from 0 to 1 while 0 corresponds to a white and 1 to a black pixel. The scanned RCFs' color scaling is given by 16-bit integers, such that 65535 is the maximum achievable integer in the scanning range.

The uncertainty on this value can be assumed to be determined via the quadratic addition of both components

$$\sigma\Xi_i = \frac{\sqrt{\sigma\overline{\mathrm{BG}}_i^2 + \sigma\overline{\mathrm{PH}}_i^2}}{65535} \tag{A.2}$$

Determining the Dose Value

The dose D can be calculated with the relation given in Equation A.3. This relation is valid for a fixed energy target, in this case for protons impinging on the RCF with $68\,\mathrm{MeV}$.

$$D = \frac{Q \cdot E_{\mathrm{loss}}[\mathrm{eV}]}{A \cdot x \cdot \varrho} \tag{A.3}$$

where Q is the charge crossing the RCF, E_{loss} is the energy loss of the projectile inside the RCF, A the irradiated area, x the thickness of the RCF and ϱ the density of the irradiated RCF.

All of these quantities have uncertainties. The value and the uncertainty for E_{loss} are calculated by Monte Carlo simulations, while the other parameters are measured quantities. These values are assumed to be statistically uncorrelated, therefore the covariance terms are equal zero, which allows the final uncertainty to be calculated as

$$(\sigma D)^2 = \left(\frac{E_{\mathrm{loss}}}{A \cdot x \cdot \varrho}\sigma Q\right)^2 + \left(\frac{Q}{A \cdot x \cdot \varrho}\sigma E_{\mathrm{loss}}\right)^2 + \left(\frac{Q \cdot E_{\mathrm{loss}}}{A^2 \cdot x \cdot \varrho}\sigma A\right)^2 + \left(\frac{Q \cdot E_{\mathrm{loss}}}{A \cdot x^2 \cdot \varrho}\sigma x\right)^2 + \left(\frac{Q \cdot E_{\mathrm{loss}}}{A \cdot x \cdot \varrho^2}\sigma \varrho\right)^2 \tag{A.4}$$

By construction and normalization, the calibration function is forced through the origin, which is an additional point that has to be taken into account.

Calibration Function

The calibration function to be fitted for each R, G, and B component is a rational function. This prevents polynomial overshoot and reproduces the physics and saturation behavior observed in RCFs. It is also, except for a small modification the same as presented in the GafChromic manual.

$$\Xi(D)_i = D\frac{a_i + b_i D}{c_i + D}. \tag{A.5}$$

a, b, c are the calibration parameters. If b is set to zero the function is the same as given in the manual. This parameter will appear to be very small in the current results. It is still important since it changes the saturating behavior if higher doses are applied.

Uncertainty on the Fit Parameters

A large problem now is minimizing the resulting uncertainties and finding the best fit for the data. Normally a least-squares problem is used to minimize the residuals using an established algorithm. This is problematic since a least-squares problem can not deal with the 2-dimensional uncertainties in the input data. The data has, as discussed above, uncertainties in the color value and in the dose value creating a non-linear optimization problem. A proposed way to deal with this is using a Monte Carlo approach re-sampling N data points according to the specific uncertainties and doing descriptive statistics on the $N + 1$ variants:

1. Define probability density function for each dimension:

D: Normal distribution with
$\mu = D$ and $\sigma_{\text{Gauß}} = \sigma D$.

Ξ: Normal distribution with
$\mu = \Xi$ and $\sigma_{\text{Gauß}} = \sigma \Xi$

2. Resample data N times with random variables following the distribution functions above.
3. Fit each of the $N + 1$ data sets with unweighted least-squares fits.
4. Descriptive statistics on the resulting parameters to get mean values, variances, and covariances.

Applying these steps and supplying the relevant quantities to the evaluation is necessary. A final remark for the calibration is that it is advantageous to limit the fit parameters value to $\mathbb{R}^+$, such that the resulting rational function is invertible.

A.2. Application and Uncertainty Quantification

The fit values a, b, c and their corresponding uncertainties and covariances are the results of the calibration. With the inverted fit function (Equation A.5), color can then be correlated to the deposited dose in the RCF. All 3 RGB components have to be taken into account.

$$D_i(\Xi_i) = \begin{cases} \dfrac{-a_i + \Xi_i + \sqrt{(a_i^2 - 2a_i\Xi_i + 4b_ic_i\Xi_i + \Xi_i^2}}{2b_i} \\ \dfrac{c_i\Xi_i}{(a_i - \Xi_i)^2} \quad \text{for } b = 0 \end{cases} \tag{A.6}$$

Weighting

All RGB channels have to be considered for calculating the proper dose value since different channels saturate at different dose values. The valid use range of the RCF can therefore be increased. It has been shown in the past, that RCFs could be used for ranges up to 4 times higher than the manufacturer gave. This is a feature that is important for our application in dosimetry for laser-driven proton beams.

Taking these different saturation ranges into account makes it necessary to define the weight of the individual color channel. The weight in this case is a measure of the degree of saturation which can be determined by the derivative of the fit function with respect to the dose value. If the derivative goes toward 0 the signal is saturated, as long as this is not the case, the signal can be properly used. The derivative is given as

$$\frac{\partial \Xi(D)}{\partial D} = \frac{ac + bD(2c + D)}{(c + D)^2} \tag{A.7}$$

This approach applies only the conversion for the color codes still in the dynamic range when the derivative is not close to zero.

Uncertainty Quantification

In the following section, a detailed discussion of the uncertainties is presented. The base equation for this discussion is given by

$$\sigma^2(y) = \sum_{i=1}^{N} \sum_{j=1}^{N} \frac{\partial f}{\partial x_i} \frac{\partial f}{\partial x_i} \sigma(x_i, x_j), \tag{A.8}$$

where y is the measured or output value, x_i the input value, f is the functional relation and σ describes the corresponding uncertainties. For $i = j$ this defaults to the Gaussian error propagation while in the full expression, $i \neq j$ yields the corresponding covariance terms.

The numerical data and the results taken from the calculation show, that the covariance terms are non-zero and can also be negative. Therefore, the resulting uncertainty might be reduced by considering the covariances.

Components for the Dose Error

Applying the Equation A.8 on the converted equation yields the final uncertainty on the dose value. This makes it necessary to determine the partial derivatives which are given below:

$$\frac{\partial D}{\partial a} = \begin{cases} \frac{1}{2b}\left(-1 + \frac{a-\Xi}{\sqrt{a^2 - 2a\Xi + \Xi(4bc+\Xi)}}\right) \\ -\frac{c\Xi}{(a-\Xi)^2} \quad \text{for } b = 0 \end{cases} \tag{A.9}$$

$$\frac{\partial D}{\partial b} = \begin{cases} \frac{-1}{2b}\frac{2bc\Xi}{\sqrt{a^2 - 2a\Xi + 4bc\Xi + \Xi^2}} + \\ \frac{-a + \Xi + \sqrt{a^2 - 2a\Xi + 4bc\Xi + \Xi^2}}{2b} \\ 0 \quad \text{for } b = 0 \end{cases} \tag{A.10}$$

$$\frac{\partial D}{\partial c} = \begin{cases} \frac{\Xi}{\sqrt{a^2 + -2a\Xi + \Xi\,(4bc+\Xi)}} \\ \frac{\Xi_i}{(a_i - \Xi_i)^2} \quad \text{for } b = 0 \end{cases} \tag{A.11}$$

$$\frac{\partial D}{\partial \Xi} = \begin{cases} \frac{1}{2b}\left(1 + \frac{-a+2bc+\Xi}{\sqrt{a^2 - 2a\Xi + \Xi(4bc\Xi)}}\right) \\ \frac{c_i\,(a_i + \Xi_i)}{(a_i - \Xi_i)^3} \quad \text{for } b = 0 \end{cases} \tag{A.12}$$

A.3. Experimental Data

These methods have been applied to several sets of calibration data, to make it usable for the developed routine and its implementation presented in chapter 5 and (Schmitz, Metternich, et al. 2022) (Schmitz and Endl 2022). The plasma physics groups at GSI and IKP TU Darmstadt supplied the data and reevaluated during this study.

Calibration was done for two of the latest GAF-ChromicTM films, EBT3 and HD-V2. The dose range was dynamic from 0.1 Gy to 20 Gy and 10 Gy to 1000 Gy respectively. These film types cover a wide dose range, and their combinations are often used to cover the entire spectrum of proton pulses produced in laser-driven proton acceleration experiments. The Calibration measurements were done for several RCFs with ionization chambers located directly behind the aperture. The proton therapy scattering system was employed to achieve a high spatial homogeneity ($< 2\,\%$) of the proton beam over an area of 22x12 mm, defined by a rectangular aperture located a few cm in front of the films to be irradiated. The total number of protons reaching the RCF during

irradiation was measured by an ionization chamber located directly behind the aperture. The uncertainty in this measurement is estimated to be approximately $\pm 3\,\%$, based on cross-calibration measurements against a second ionization chamber. The ionization chamber was initially calibrated against the absolute beam current measurement from a Faraday cup.

The analyzed data is presented below. As can be seen, the relative dose error, the maximum error in dose determination using the calibration from a different batch, can be as high as $50\,\%$ to $200\,\%$. Having the calibration data for the actual production batch, though, allows measuring the dose with an uncertainty on the level of a few percent.

A.4. Limitation of the Data and Improvements

As visible in the data, only a few calibration curves are saturated with the current radiation levels. It has been shown that, if the different sensitivities of each RGB component are taken into account, dose values of up to $5\,\mathrm{kGy}$ or more can be measured (A. Schreiber 2012). It is, therefore, advisable to calibrate to higher energies. Furthermore, accelerators provide the dose in a longer time scale which further introduces uncertainty and has to verify to increase precision.

The low energies of the calibration are problematic during evaluation. Irradiated RCFs acquire dose in dependence on the particle count, their energy, and the governing spectrum. For laser systems such as PHELIX at GSI, evaluation using the data below saturates too early. The maximum irradiated energy and its corresponding color values determine this early saturation threshold. Suppose these color values are passed, and further change is measured. In that case, it is not advisable to extrapolate the fit function since the non-linear saturation behavior is not precisely known. This introduces a maximal measurable dose that strongly biases the output since it underestimates particle counts.

A.5. Collection of Evaluated Calibration Data

This section lists the calibration results for both types of functions and both film types investigated.

calibration_campaign	CAL-2019-1
calibration_date	15.11.2019
calibration_done_by	Paul Neumayer, Abel Blazevic
calibration_description	Irradiation at HZB (Berlin) with 68MeV protons
film_type	EBT
film_LOT	03161503
film_number	2

Fit results if b is set to zero.

	a	b	c
R	5.23E-1	0.00	3.22
G	6.23E-1	0.00	1.18E1
B	4.75E-1	0.00	4.13E1

Fit results if b is left variable.

	a	b	c
R	4.69E-1	2.35E-3	2.69
G	4.82E-1	3.87E-3	8.49
B	3.89E-1	1.16E-3	3.33E1

Covariance matrix values if b is set to zero.

	σ_{aa}	σ_{bb}	σ_{cc}	σ_{ab}	σ_{ac}	σ_{bc}
R	8.28E-5	0.00	3.83E-2	0.00	0.00	1.54E-3
G	9.65E-4	0.00	1.39	0.00	0.00	3.49E-2
B	1.57E-2	0.00	2.17E2	0.00	0.00	1.83

Covariance matrix values if b is left variable.

	σ_{aa}	σ_{bb}	σ_{cc}	σ_{ab}	σ_{ac}	σ_{bc}
R	8.20E-4	1.36E-6	1.06E-1	-3.18E-5	-3.22E-4	8.81E-3
G	1.04E-2	7.99E-6	5.73	-2.77E-4	-6.19E-3	2.40E-1
B	2.58E-2	4.02E-6	2.65E2	-2.56E-4	-2.29E-2	2.58

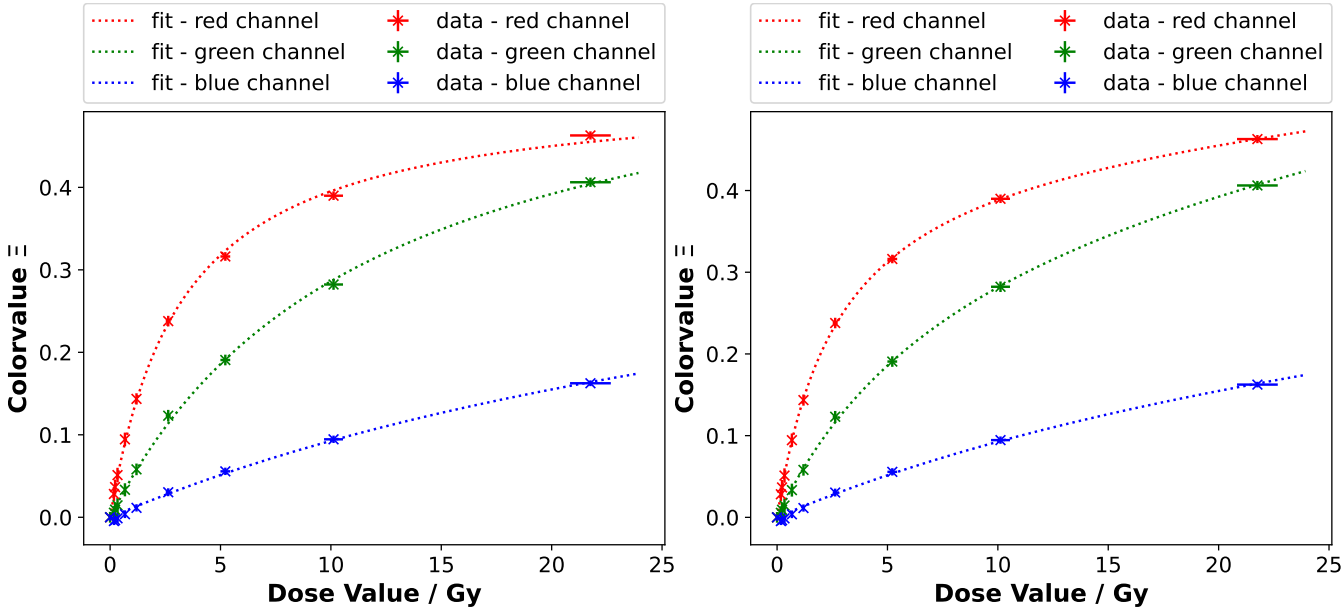

calibration_campaign	CAL-2019-1
calibration_date	15.11.2019
calibration_done_by	Paul Neumayer, Abel Blazevic
calibration_description	Irradiation at HZB (Berlin) with 68MeV protons
film_type	EBT
film_LOT	05191502
film_number	1

Fit results if b is set to zero.

	a	b	c
R	5.13E-1	0.00	3.60
G	6.02E-1	0.00	1.19E1
B	3.84E-1	0.00	3.13E1

Fit results if b is left variable.

	a	b	c
R	4.61E-1	2.20E-3	3.03
G	3.82E-1	5.98E-3	6.63
B	1.74E-1	3.55E-3	1.28E1

Covariance matrix values if b is set to zero.

	σ_{aa}	σ_{bb}	σ_{cc}	σ_{ab}	σ_{ac}	σ_{bc}
R	1.35E-4	0.00	6.79E-2	0.00	0.00	2.64E-3
G	8.55E-4	0.00	1.39	0.00	0.00	3.30E-2
B	3.83E-3	0.00	5.70E1	0.00	0.00	4.62E-1

Covariance matrix values if b is left variable.

	σ_{aa}	σ_{bb}	σ_{cc}	σ_{ab}	σ_{ac}	σ_{bc}
R	1.22E-3	1.88E-6	1.91E-1	-4.56E-5	-5.12E-4	1.45E-2
G	8.16E-3	6.46E-6	4.72	-2.22E-4	-5.13E-3	1.94E-1
B	1.50E-2	4.88E-6	1.12E2	-2.61E-4	-2.18E-2	1.29

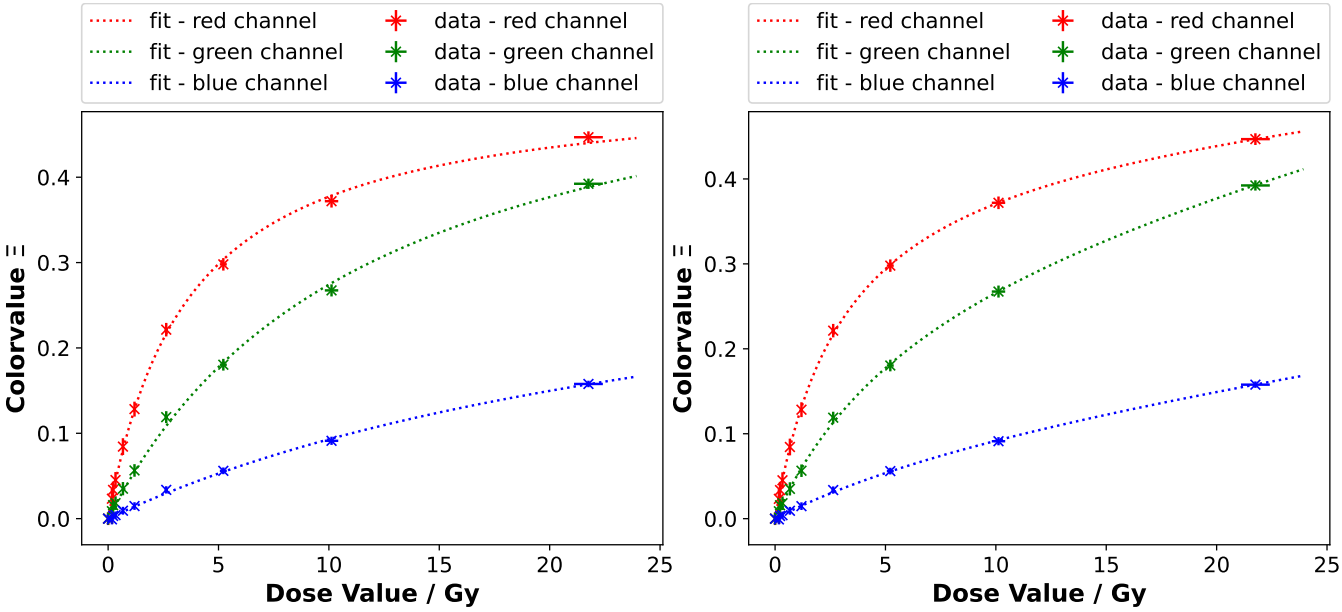

calibration_campaign	CAL-2019-1
calibration_date	15.11.2019
calibration_done_by	Paul Neumayer, Abel Blazevic
calibration_description	Irradiation at HZB (Berlin) with 68MeV protons
film_type	EBT
film_LOT	07291902
film_number	6

Fit results if b is set to zero.

	a	b	c
R	6.02E-1	0.00	2.10
G	5.78E-1	0.00	6.70
B	4.05E-1	0.00	1.51E1

Fit results if b is left variable.

	a	b	c
R	5.18E-1	4.31E-3	1.59
G	4.47E-1	4.49E-3	4.61
B	2.92E-1	2.80E-3	1.02E1

Covariance matrix values if b is set to zero.

	σ_{aa}	σ_{bb}	σ_{cc}	σ_{ab}	σ_{ac}	σ_{bc}
R	1.18E-4	0.00	2.18E-2	0.00	0.00	1.32E-3
G	3.94E-4	0.00	3.22E-1	0.00	0.00	1.04E-2
B	1.32E-3	0.00	6.05	0.00	0.00	8.62E-2

Covariance matrix values if b is left variable.

	σ_{aa}	σ_{bb}	σ_{cc}	σ_{ab}	σ_{ac}	σ_{bc}
R	7.94E-4	1.84E-6	3.71E-2	-3.56E-5	-2.08E-4	4.98E-3
G	3.45E-3	4.45E-6	8.80E-1	-1.18E-4	-1.74E-3	5.35E-2
B	9.63E-3	6.25E-6	1.94E1	-2.34E-4	-9.92E-3	4.26E-1

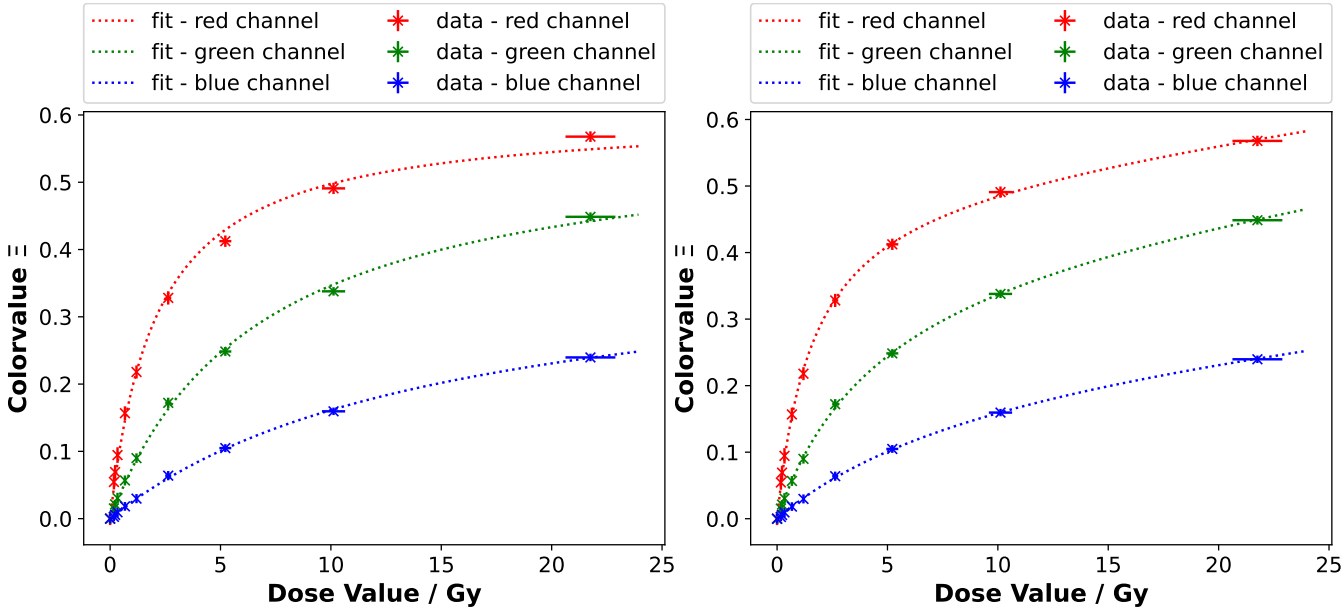

calibration_campaign	CAL-2019-1
calibration_date	15.11.2019
calibration_done_by	Paul Neumayer, Abel Blazevic
calibration_description	Irradiation at HZB (Berlin) with 68MeV protons
film_type	EBT
film_LOT	09121802
film_number	8

Fit results if b is set to zero.

	a	b	c
R	5.56E-1	0.00	2.44
G	5.53E-1	0.00	7.01
B	3.79E-1	0.00	1.51E1

Fit results if b is left variable.

	a	b	c
R	4.65E-1	4.44E-3	1.77
G	3.95E-1	5.34E-3	4.31
B	2.05E-1	4.31E-3	6.94

Covariance matrix values if b is set to zero.

	σ_{aa}	σ_{bb}	σ_{cc}	σ_{ab}	σ_{ac}	σ_{bc}
R	1.97E-4	0.00	4.93E-2	0.00	0.00	2.62E-3
G	4.38E-4	0.00	4.13E-1	0.00	0.00	1.23E-2
B	1.44E-3	0.00	7.64	0.00	0.00	1.01E-1

Covariance matrix values if b is left variable.

	σ_{aa}	σ_{bb}	σ_{cc}	σ_{ab}	σ_{ac}	σ_{bc}
R	1.29E-3	2.83E-6	8.50E-2	-5.63E-5	-3.97E-4	9.73E-3
G	3.64E-3	4.87E-6	1.01	-1.26E-4	-1.96E-3	5.91E-2
B	8.64E-3	6.26E-6	1.77E1	-2.23E-4	-9.65E-3	3.87E-1

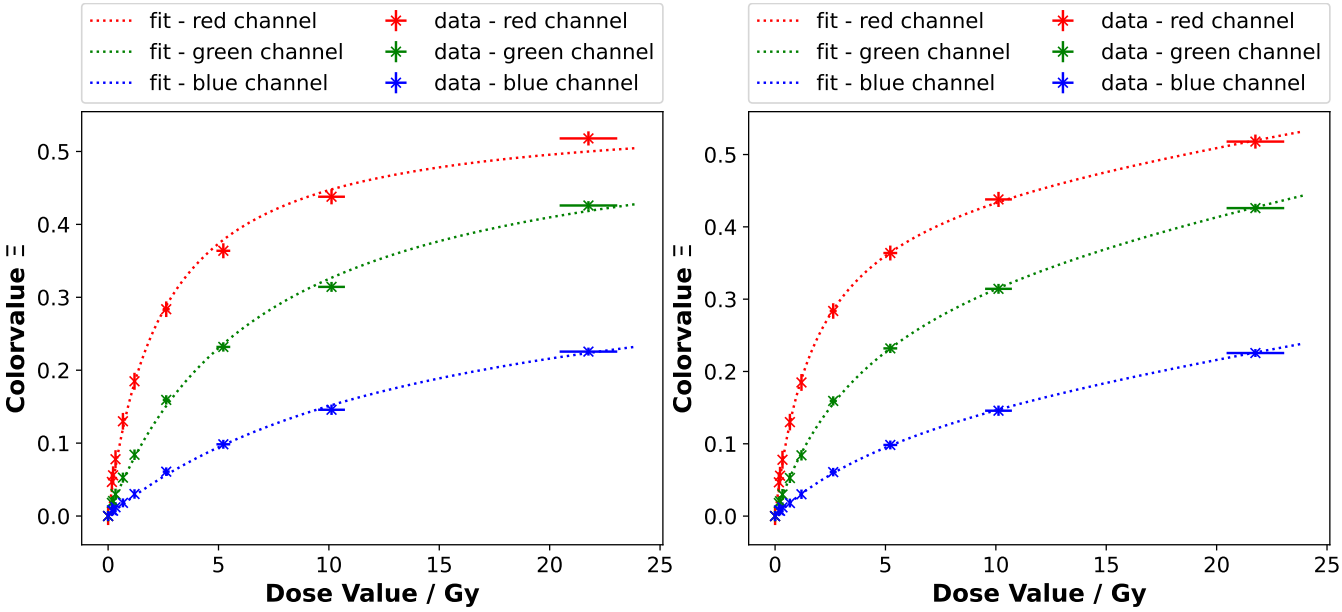

calibration_campaign	CAL-2019-1
calibration_date	15.11.2019
calibration_done_by	Paul Neumayer, Abel Blazevic
calibration_description	Irradiation at HZB (Berlin) with 68MeV protons
film_type	HD
film_LOT	01091801
film_number	7

Fit results if b is set to zero.

	a	b	c
R	5.44E-1	0.00	1.78E1
G	5.35E-1	0.00	7.17E1
B	4.11E-1	0.00	1.62E2

Fit results if b is left variable.

	a	b	c
R	5.33E-1	1.55E-5	1.69E1
G	4.96E-1	3.75E-5	6.13E1
B	3.32E-1	5.98E-5	1.10E2

Covariance matrix values if b is set to zero.

	σ_{aa}	σ_{bb}	σ_{cc}	σ_{ab}	σ_{ac}	σ_{bc}
R	1.37E-5	0.00	6.34E-1	0.00	0.00	1.59E-3
G	2.43E-5	0.00	1.28E1	0.00	0.00	1.31E-2
B	4.12E-5	0.00	9.52E1	0.00	0.00	5.34E-2

Covariance matrix values if b is left variable.

	σ_{aa}	σ_{bb}	σ_{cc}	σ_{ab}	σ_{ac}	σ_{bc}
R	5.74E-5	6.56E-11	8.44E-1	-5.44E-8	-4.26E-6	4.94E-3
G	1.58E-4	1.25E-10	1.91E1	-1.30E-7	-3.46E-5	4.63E-2
B	2.90E-4	1.80E-10	1.53E2	-2.14E-7	-1.35E-4	1.95E-1

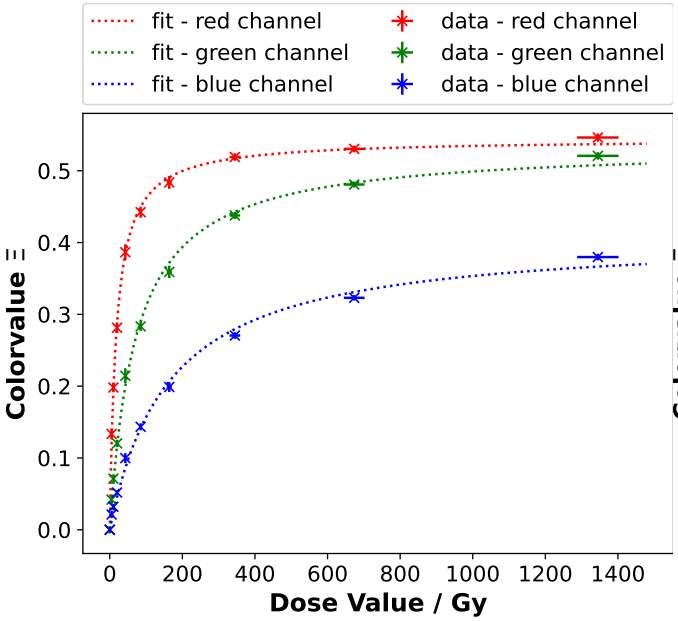

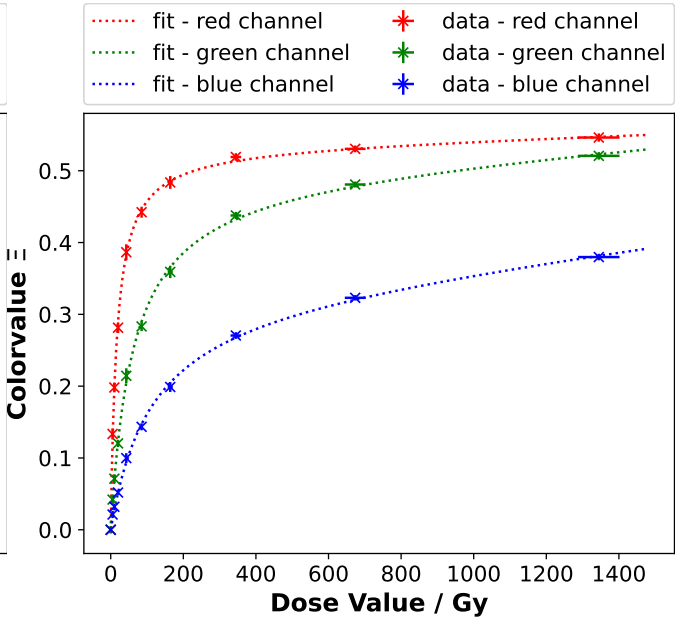

calibration_campaign	CAL-2019-1
calibration_date	15.11.2019
calibration_done_by	Paul Neumayer, Abel Blazevic
calibration_description	Irradiation at HZB (Berlin) with 68MeV protons
film_type	HD
film_LOT	11171501
film_number	4

Fit results if b is set to zero.

	a	b	c
R	5.93E-1	0.00	1.19E2
G	5.51E-1	0.00	3.72E2
B	3.57E-1	0.00	7.04E2

Fit results if b is left variable.

	a	b	c
R	5.21E-1	5.99E-5	9.27E1
G	3.77E-1	1.00E-4	2.08E2
B	2.06E-1	6.83E-5	3.40E2

Covariance matrix values if b is set to zero.

	σ_{aa}	σ_{bb}	σ_{cc}	σ_{ab}	σ_{ac}	σ_{bc}
R	1.27E-4	0.00	9.85E1	0.00	0.00	9.27E-2
G	3.17E-4	0.00	1.04E3	0.00	0.00	5.34E-1
B	6.11E-4	0.00	1.03E4	0.00	0.00	2.41

Covariance matrix values if b is left variable.

	σ_{aa}	σ_{bb}	σ_{cc}	σ_{ab}	σ_{ac}	σ_{bc}
R	1.00E-3	5.70E-10	1.90E2	-7.18E-7	-2.69E-4	4.01E-1
G	2.23E-3	8.21E-10	2.06E3	-1.30E-6	-1.15E-3	2.08
B	4.28E-3	9.73E-10	2.59E4	-1.97E-6	-4.62E-3	1.04E1

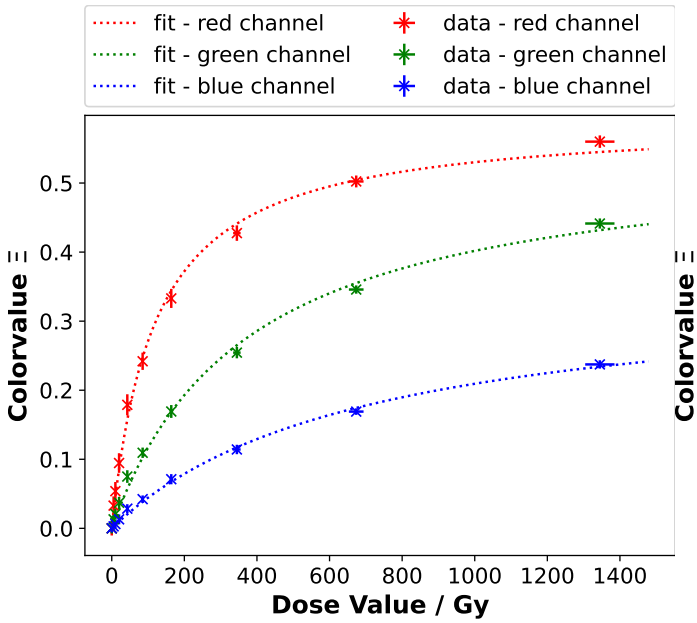

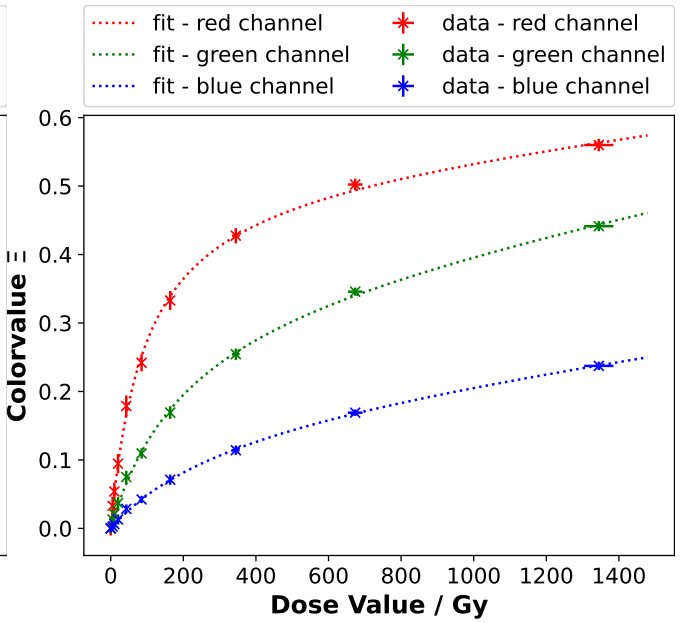

calibration_campaign	CAL-2019-1
calibration_date	15.11.2019
calibration_done_by	Paul Neumayer, Abel Blazevic
calibration_description	Irradiation at HZB (Berlin) with 68MeV protons
film_type	HD
film_LOT	12151402
film_number	3

Fit results if b is set to zero.

	a	b	c
R	6.96E-1	0.00	2.89E2
G	7.24E-1	0.00	9.29E2
B	4.46E-1	0.00	1.78E3

Fit results if b is left variable.

	a	b	c
R	6.51E-1	2.87E-5	2.62E2
G	6.15E-1	4.27E-5	7.63E2
B	3.63E-1	2.26E-5	1.41E3

Covariance matrix values if b is set to zero.

	σ_{aa}	σ_{bb}	σ_{cc}	σ_{ab}	σ_{ac}	σ_{bc}
R	4.51E-4	0.00	7.06E2	0.00	0.00	4.89E-1
G	4.82E-3	0.00	2.99E4	0.00	0.00	1.16E1
B	2.11E-2	0.00	8.18E5	0.00	0.00	1.30E2

Covariance matrix values if b is left variable.

	σ_{aa}	σ_{bb}	σ_{cc}	σ_{ab}	σ_{ac}	σ_{bc}
R	3.43E-3	1.22E-9	1.65E3	-1.91E-6	-1.13E-3	2.21
G	2.17E-2	3.50E-9	5.70E4	-7.99E-6	-1.13E-2	3.39E1
B	3.11E-2	1.49E-9	8.71E5	-4.90E-6	-2.09E-2	1.61E2

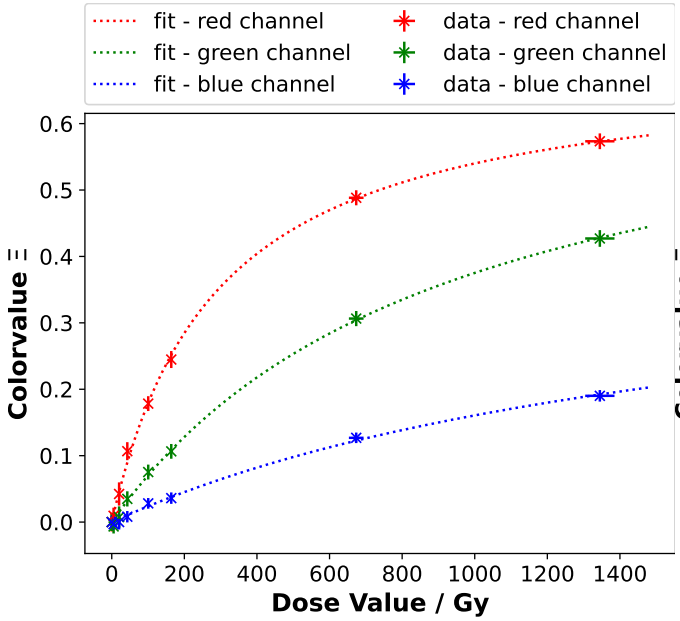

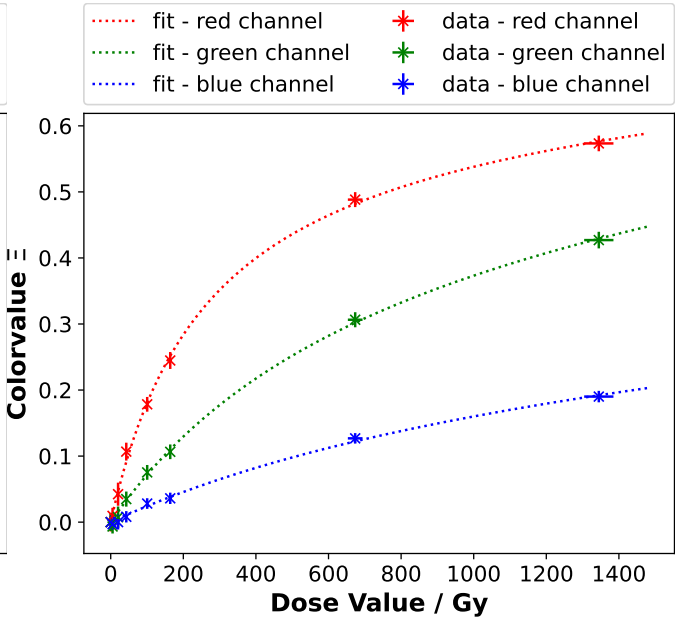

B. Ion Model Remarks

B.1. Transversal Lorentz Boosted 1.5D PIC Simulations

Modeling oblique laser incidence onto a target is inherently at least a 2D problem, which requires substantially more computational power than a similar 1D geometry to simulate. Bourdier (Bourdier 1983) thus proposed a method in which a relativistic Lorentz boost is applied to the frame of reference in the simulation. This method has later been employed by Gibbon et al. (Gibbon et al. 1999) in a PIC code.

Here, we would like to present the implementation of this technique yet again for a modern PIC code while also correcting some mistakes in the calculations by Gibbon et al.. A schematic of the general principle is shown in Figure B.1. To obtain the results in the lab frame a back transformation must be applied to the diagnostics obtained from the simulation. For finding the transformations, a simple Lorentz boost in

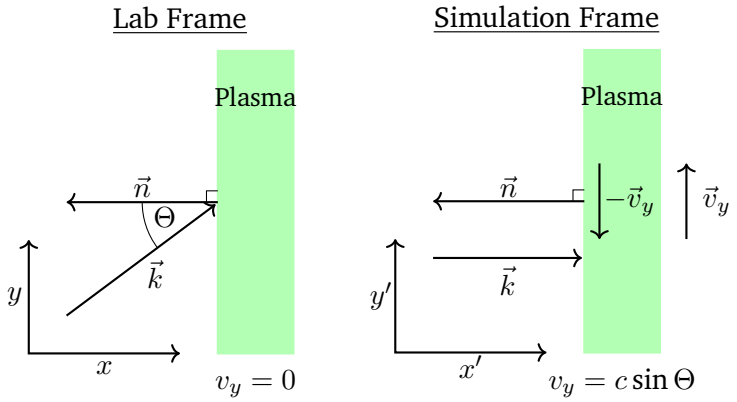

Figure B.1.: Schematic of the Lorentz boosted simulation frame versus the implied lab frame. In the simulation frame, the laser appears to be at normal incidence onto the target while the particles appear to drift in negative y-direction with velocity v_y.

y-direction by the velocity $v_y = c \cdot \sin(\theta)$ is applied. In matrix form, this can be represented by:

$$\Lambda = \begin{pmatrix} 1/\cos(\theta) & 0 & -\tan(\theta) & 0 \\ 0 & 1 & 0 & 0 \\ -\tan(\theta) & 0 & 1/\cos(\theta) & 0 \\ 0 & 0 & 0 & 1 \end{pmatrix}, \tag{B.1}$$

since $\gamma_0 = \left(1 - (v_y/c)^2\right)^{-1/2} = 1/\cos(\theta)$. This transformation matrix can be used to transform all the quantities of the particles and the electromagnetic fields. Indicating quantities in the transformed system with

a prime, we find after carrying out all transformations

$$\begin{aligned} k_y' &= 0 \\ \omega_\mathrm{L}' &= \omega_\mathrm{L}/\gamma_0 \\ a_0' &= a_0 \ , \end{aligned} \tag{B.2}$$

where k_y' is the y-component of the wave vector in the boosted system, showing that the laser is now at normal incidence. Note that the dimensionless laser amplitude a_0 is invariant under the transformation (Gibbon et al. 1999). Further, denoting PIC code units with a tilde, we find

$$\begin{aligned} \tilde{x}' &= \tilde{x}/\gamma_0 \\ \tilde{t}' &= \tilde{t}/\gamma_0^2 \end{aligned} \tag{B.3}$$

giving a re-scaling of both the simulation time as well as the cell grid. The initial particle density is also affected by

$$\tilde{n}_0' = \tilde{n}_0 \cdot \gamma_0^3 \ . \tag{B.4}$$

With these conditions, the particles can be initialized in the boosted frame. The relative velocity v_y is added as a permanent drift which is handled and relativistically added to the particles by the code.
From the diagnostics in the simulation, we can obtain desired quantities via a back transformation. For the particle kinetic energies, we find using the energy-momentum relation:

$$\begin{aligned} \tilde{E} &= \gamma_0(\tilde{E}' + \tilde{v}_y\tilde{p}_y') \\ &= \gamma_0 \left(\frac{1}{m_\mathrm{e}c^2}\sqrt{p'^2c^2 + (m_0c^2)^2} + \tilde{v}_y\tilde{p}_y' \right) \\ \Rightarrow E_\mathrm{kin} &= \gamma_0 m_\mathrm{e}c^2 \left(\sqrt{\tilde{p}'^2 + \frac{m_0^2}{m_\mathrm{e}^2}} + \tilde{v}_y\tilde{p}_y' \right) - m_0c^2 \ , \end{aligned} \tag{B.5}$$

where m_0 is the particle rest mass. Noting that $\tilde{B}_x' = 0$, we can find relations to recover the fields of the laser. The non-zero fields are:

For s-polarization:

$$\begin{aligned} \tilde{E}_z &= \tilde{E}_z' \\ \tilde{B}_x &= \tilde{v}_y\tilde{E}_z' \\ \tilde{B}_y &= \tilde{B}_y'/\gamma_0 \end{aligned} \tag{B.6}$$

For p-polarization:

$$\begin{aligned} \tilde{E}_x &= \tilde{E}_x' - \tilde{v}_y\tilde{B}_z' \\ \tilde{E}_y &= \tilde{E}_y'/\gamma_0 \\ \tilde{B}_z &= \tilde{B}_z' - \tilde{v}_y\tilde{E}_x' \end{aligned} \tag{B.7}$$

Using the field transformations and assuming that reflection at the plasma surface does not change polarization, we find for the absolute magnitude of the Poynting vector:

$$|\vec{S}| = |\vec{S}'| \cdot \gamma_0^2 \ , \tag{B.8}$$

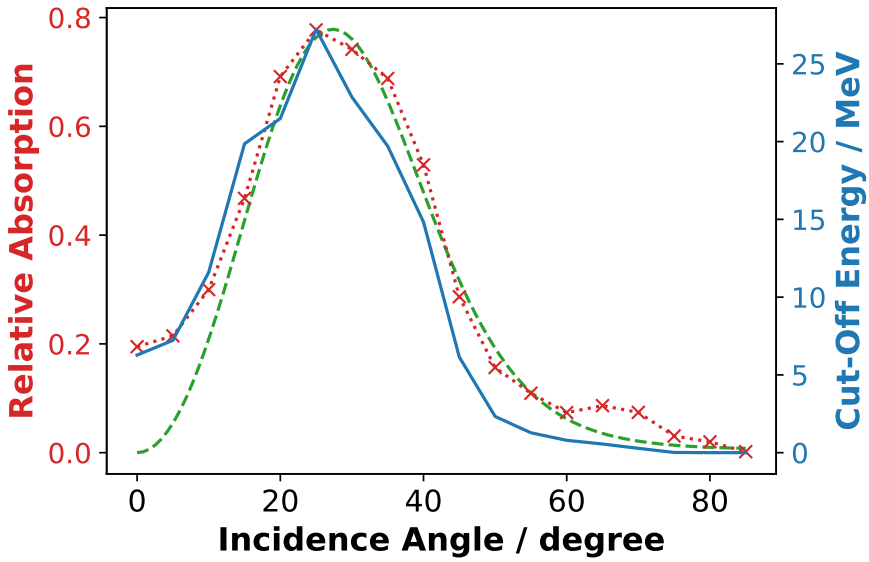

Figure B.2.: Simulation of laser incidence angles between $0°$ and $85°$. The plot shows the incidence angle versus the relative absorption of a laser into a hydrogen plasma target (dotted red line) and the maximum proton kinetic energy behind the target (blue solid line). The laser impinges on the target with p-polarized fields. Classical resonance absorption, also known as the Desinov curve (Gibbon 2005), is shown as a dashed line.

with which the relative absorption of the laser into the plasma can be calculated by dividing the incoming Poynting flux by the outgoing Poynting flux.

It should be noted that while the Lorentz boosted frame method can replicate incidence angle-based behavior, it cannot replace a 2D or even 3D simulation on all accounts (Gibbon et al. 1999). Firstly, in general, all physical quantities depend separately on the transformed coordinates $x, y, z, t, p_x, p_y, p_z$. Thus, the Lorentz-boosted simulation can only be used for a problem independent of y and z. Additionally, reducing the geometry after the boost to 1D limits the spatial dynamics of the particles. Since only the x-axis is present, all particles (while having 3D velocities) can only move along a straight line (i.e. have only 1 spatial dimension). This disregards the angular spread at the back of the target so that the particles can be accelerated for longer times and thus end up with higher energies than a similar 2D simulation. Distinctly 2D effects such as hole boring can also not be modeled accurately.

To illustrate the capabilities of this method, however, the relative laser absorption of a p-polarized laser impinging on a hydrogen plasma target was measured for varying laser incidence angles using the above method in the Smilei PIC code. The resulting absorption curve is shown in Figure B.2. The results agree well with 2D simulations by Cui et al. (Cui et al. 2013) using a similar target and laser (see Figure B.4 for a comparison).

Explicit Lorentz Boost for Oblique Laser Incidence

In the following section, the full transformation is discussed in more detail, and explicitly calculate the relations we mentioned before:

The transformation matrix for the considered boost in y-direction by $v_y = c \cdot \sin(\theta)$ is given by

$$\Lambda = \begin{pmatrix} 1/\cos(\theta) & 0 & -\tan(\theta) & 0 \\ 0 & 1 & 0 & 0 \\ -\tan(\theta) & 0 & 1/\cos(\theta) & 0 \\ 0 & 0 & 0 & 1 \end{pmatrix} , \tag{B.9}$$

since $\gamma_0 = \left(1 - (v_y/c)^2\right)^{-1/2} = 1/\cos(\theta)$. Now all relevant quantities of the system are transformed using the matrix Λ.
Firstly, the four-position R, the four-momentum P, the four-wave vector K and the four-current J are given as follows:

$$\begin{aligned} R &= (ct, x, y, z)^\top \\ P &= (\gamma m_0 c, p_x, p_y, p_z)^\top \\ K &= (\omega_\mathrm{L}/c, k \cdot \cos(\theta), k \cdot \sin(\theta), 0)^\top \\ J &= (c\rho, j_x, j_y, j_z)^\top \end{aligned} \tag{B.10}$$

where $k = \omega_\mathrm{L}/c$ is the magnitude of the wave vector, ρ is the charge density and $\vec{j}$ is the current density. Here, the geometry of the wave vector from Figure B.1 has already been applied, reducing the wave vector to two spatial dimensions. By left multiplication of Λ these quantities can be transformed into the boosted frame. This multiplication yields

$$\begin{aligned} R' &= (\gamma_0(ct - y\beta_0), x, \gamma_0(y - ct\beta_0), z)^\top \\ P' &= (\gamma_0(\gamma m_0 c - p_y\beta_0), p_x, \gamma_0(p_y - \gamma m_0 c\beta_0), p_z)^\top \\ K' &= (\omega_\mathrm{L}/(c\gamma_0), k_0/\gamma_0, 0, 0)^\top \\ J' &= (\gamma_0(c\rho - j_y\beta_0), j_x, \gamma_0(j_y - c\rho\beta_0), j_z)^\top \end{aligned} \tag{B.11}$$

where a prime indicates quantities in the transformed system and $\beta_0 = v_y/c = \sin(\theta)$. Most importantly here we find $k'_y = 0$ and $\omega'_\mathrm{L} = \omega_\mathrm{L}/\gamma_0$. Also, since the particles are assumed cold at $t = 0$, we find for the initial density $\rho'_0 = \gamma_0\rho_0$.
The next transformation is for the electromagnetic fields. Here, s- and p-polarized incidence lasers have to be distinguished. To transform the electric and magnetic fields of the incoming laser, the electromagnetic tensor is used:

$$F^{\mu\nu}_{\text{s-pol}} = \begin{pmatrix} 0 & 0 & 0 & -E_z/c \\ 0 & 0 & 0 & B_y \\ 0 & 0 & 0 & -B_x \\ E_z/c & -B_y & B_x & 0 \end{pmatrix} \tag{B.12}$$

$$F^{\mu\nu}_{\text{p-pol}} = \begin{pmatrix} 0 & -E_x/c & -E_y/c & 0 \\ E_x/c & 0 & -B_z & 0 \\ E_y/c & B_z & 0 & 0 \\ 0 & 0 & 0 & 0 \end{pmatrix} . \tag{B.13}$$

The Lorentz transformation of such a tensor is given by:

$$F^{\mu'\nu'} = \Lambda^{\mu'}{}_{\mu}\Lambda^{\nu'}{}_{\nu}F^{\mu\nu} , \tag{B.14}$$

where a prime again indicates quantities in the transformed system. The calculated fields are

$$\left.\begin{aligned} E'_x &= 0 \\ E'_y &= 0 \\ E'_z &= \gamma_0(E_z - v_y B_x) \\ B'_x &= \gamma_0(B_x - E_z v_y/c^2) \\ B'_y &= B_y \\ B'_z &= 0 \end{aligned}\right\} \text{ s-pol} \tag{B.15}$$

$$\left.\begin{aligned} E'_x &= \gamma_0(E_x + v_y B_z) \\ E'_y &= E_y \\ E'_z &= 0 \\ B'_x &= 0 \\ B'_y &= 0 \\ B'_z &= \gamma_0(B_z + E_x v_y/c^2) \end{aligned}\right\} \text{ p-pol} \tag{B.16}$$

where $E'_x, B'_x \stackrel{!}{=} 0$ since the laser is at normal incidence in the boosted system. For absorption measurements, it is useful to have a look at the transformation of the Poynting Vector $\vec{S}$. The definition in a vacuum is

$$\vec{S} = \frac{1}{\mu_0}\vec{E} \times \vec{B}\ , \tag{B.17}$$

where μ_0 is the vacuum permeability. As an example, only the calculation in the p-polarization case is presented. The s-polarization calculation is equivalent.

$$\vec{S}_{\text{p-pol}} = \frac{1}{\mu_0}\left(E_y B_z, -E_x B_z, 0\right)^\top \tag{B.18}$$

$$\Rightarrow \vec{S}'_{\text{p-pol}} = \frac{1}{\mu_0}(E'_y B'_z, \underbrace{-E'_x B'_z}_{=0}, 0)^\top \tag{B.19}$$

$$= \frac{1}{\mu_0}\left(E'_y B'_z, 0, 0\right)^\top\ . \tag{B.20}$$

The magnitude of the transformed Poynting Vector is determined as

$$|\vec{S}'_{\text{p-pol}}| = \frac{1}{\mu_0}\sqrt{E'^2_y B'^2_z} \tag{B.21}$$

$$= \frac{1}{\mu_0 c}E'^2_y\ , \tag{B.22}$$

since $|\vec{B}| = |\vec{E}|/c$. On the other hand, inserting the transformation into $\vec{S}$, yields

$$\vec{S}_{\text{p-pol}} = \frac{1}{\mu_0}\begin{pmatrix} E'_y\gamma_0\left(B'_z - E'_x\frac{v_y}{c^2}\right) \\ -\gamma_0\left(E'_x - v_y B'_z\right)\gamma_0\left(B'_z - E'_x\frac{v_y}{c^2}\right) \\ 0 \end{pmatrix} \tag{B.23}$$

$$= \frac{1}{\mu_0}\begin{pmatrix} \gamma_0 E'_y B'_z \\ \gamma_0^2 v_y B'^2_z \\ 0 \end{pmatrix} \tag{B.24}$$

such that the magnitude is given by

$$|\vec{S}_{\text{p-pol}}| = \frac{\gamma_0}{\mu_0}\sqrt{E_y'^2 B_z'^2 + \gamma_0^2 v_y^2 B_z'^4} \tag{B.25}$$

$$= \frac{E_y'^2 \gamma_0}{\mu_0 c}\sqrt{1 + \gamma_0^2 \frac{v_y^2}{c^2}}\ . \tag{B.26}$$

The term in the square root can be resolved elegantly once the definition of v_y is inserted:

$$1 + \gamma_0^2 \frac{v_y^2}{c^2} = 1 + \frac{1}{\cos^2(\theta)} \frac{c^2 \sin^2(\theta)}{c^2} \tag{B.27}$$

$$= \frac{1}{\cos^2(\theta)} \tag{B.28}$$

$$= \gamma_0^2\ , \tag{B.29}$$

and with that

$$|\vec{S}_{\text{p-pol}}| = \frac{E_y'^2 \gamma_0}{\mu_0 c}\ \gamma_0 \tag{B.30}$$

$$= |\vec{S}'_{\text{p-pol}}| \cdot \gamma_0^2\ . \tag{B.31}$$

Next, the transformed quantities in code units are considered, so as to initialize the particles correctly in the PIC code. For space coordinate,

$$\tilde{x}' = \frac{\omega' x'}{c} = \tilde{x}/\gamma_0\ , \tag{B.32}$$

while for the time coordinate, since $\tilde{y}' \stackrel{!}{=} 0$:

$$0 \stackrel{!}{=} \tilde{y}' = \frac{\omega'}{c}\gamma_0(y - ct\beta_0) \tag{B.33}$$

$$= \tilde{y} - \tilde{t}\tilde{v}_y \tag{B.34}$$

$$\Rightarrow \tilde{t}' = \omega'\gamma_0\left(t - \frac{y}{c}\beta_0\right) \tag{B.35}$$

$$= \tilde{t} - \tilde{y}\tilde{v}_y \tag{B.36}$$

$$= \tilde{t} - \tilde{t}\tilde{v}_y^2 \tag{B.37}$$

$$= \tilde{t}/\gamma_0^2 \tag{B.38}$$

Finally, the critical density transforms as

$$\frac{n'_{\text{c}}}{n_{\text{c}}} = \frac{\omega'^2}{\omega^2} = \frac{1}{\gamma_0^2}\ , \tag{B.39}$$

such that the initial particle densities in code units become

$$\tilde{n}'_0 = \frac{n'_0}{n'_{\text{c}}} = \tilde{n}_0 \cdot \gamma_0^3\ . \tag{B.40}$$

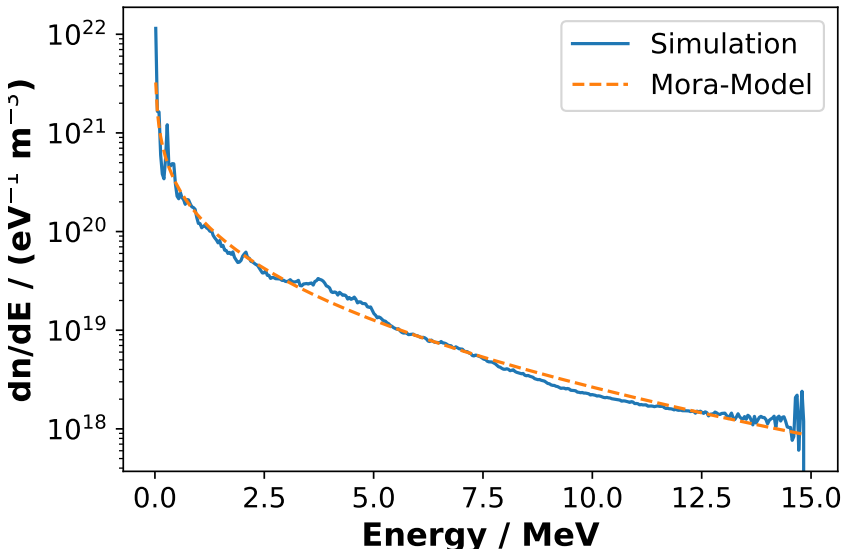

Figure B.3.: Example results for a Lorentz-boosted simulation with an angle of 40 degrees. The dashed line denotes the fit of Mora's model (refer to subsection 2.3.1) to the data.

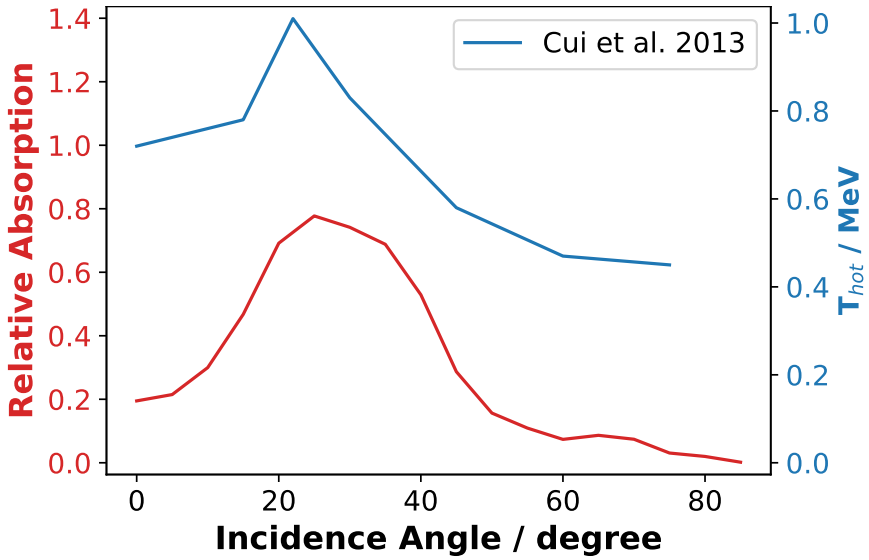

Figure B.4.: Plot of the absorption of energy in the Lorentz boosted simulation in comparison to the data from Cui et al. (Cui et al. 2013) and discussed in subsection 2.2.3.

B.2. Laser Conversion Efficiency

The laser conversion efficiency is important to characterize particle acceleration, especially laser-plasma acceleration. To retrieve information about the energy in the output spectrum of a TNSA experiment, consider first a spectrum $\mathrm{d}N/\mathrm{d}E$ recorded in multiple energy bins of width ΔE. In this case, the number of particles in bin i is given by the bin's height multiplied by its width, i.e.

$$N_i = \left(\frac{\mathrm{d}N}{\mathrm{d}E}\right)_i \cdot \Delta E \ . \tag{B.41}$$

Hence, the total energy of the particles within the bin could be approximated by multiplying the particles in the bin by the bin's central energy E_i. Summing over all bins yields the total energy of the particles

$$E_{\mathrm{tot}} = \sum_i \left(\frac{\mathrm{d}N}{\mathrm{d}E}\right)_i \cdot \Delta E \cdot E_i \ , \tag{B.42}$$

which can be generalized in the continuous limit $\Delta E \to 0$, giving

$$E_{\mathrm{tot}} = \int_0^\infty \frac{\mathrm{d}N}{\mathrm{d}E} \cdot E \, \mathrm{d}E \ . \tag{B.43}$$

Concretely, adjusting for the output format of the neural network models the total energy is given by

$$E_{\mathrm{tot}} = V \cdot \int_0^{E_{\mathrm{max}}} \exp\left(\ln\left(\frac{\mathrm{d}n}{\mathrm{d}E}\right)\right) \cdot E \, \mathrm{d}E \ , \tag{B.44}$$

where $\ln\left(\frac{\mathrm{d}n}{\mathrm{d}E}\right)$ and E_{max} are given by the neural network models and V is a unit volume. To obtain a measure for the energy conversion efficiency then, the above integral should be weighted by the laser pulse energy E_{L}, resulting in the maximization problem shown in Eq. (6.6).

B.3. Neural Network Training and Preparation

This section discusses the chosen parameter ranges for the surrogate models based on neural networks.

Training surrogate models is a tedious and numerically expensive task. This means that the training process's parameters and data must be defined clearly and reproducible. This section focuses on the data preparation task and the numerical hyperparameters chosen for the model. Both parts are important if we want to create fast converging models.

Data Preparation

Neural networks can only be as good as the data used for training them. Convergence is important and data, therefore, has to be prepared properly. We can only investigate the multi-species effect and subsequent optimizations if we consider the full spectrum.

The spectral data for the output spectrum is taken on a logarithmic scale since the count rates vary over several orders of magnitude. The logarithmic data can be directly used to train a model. We tried using the data directly, but convergence was problematic. This is due to the noise of the data and the mixture-depending shifts of multi-species plateaus. The signal variation in both cases is similar and it is therefore difficult for the network to fit the dependencies. To mitigate this we applied a Savitzky-Golay filter with a window size of 7 points and a 3rd-order polynomial (Savitzky et al. 1964). This filter decreased the noise-based fluctuations and allowed subsequent convergence. We display a comparison for filtered and unfiltered data in Figure B.5, showing that the major behavior of the curves is reproduced. Still, the bin-to-bin fluctuations in the mid to high-energy range are minimized.

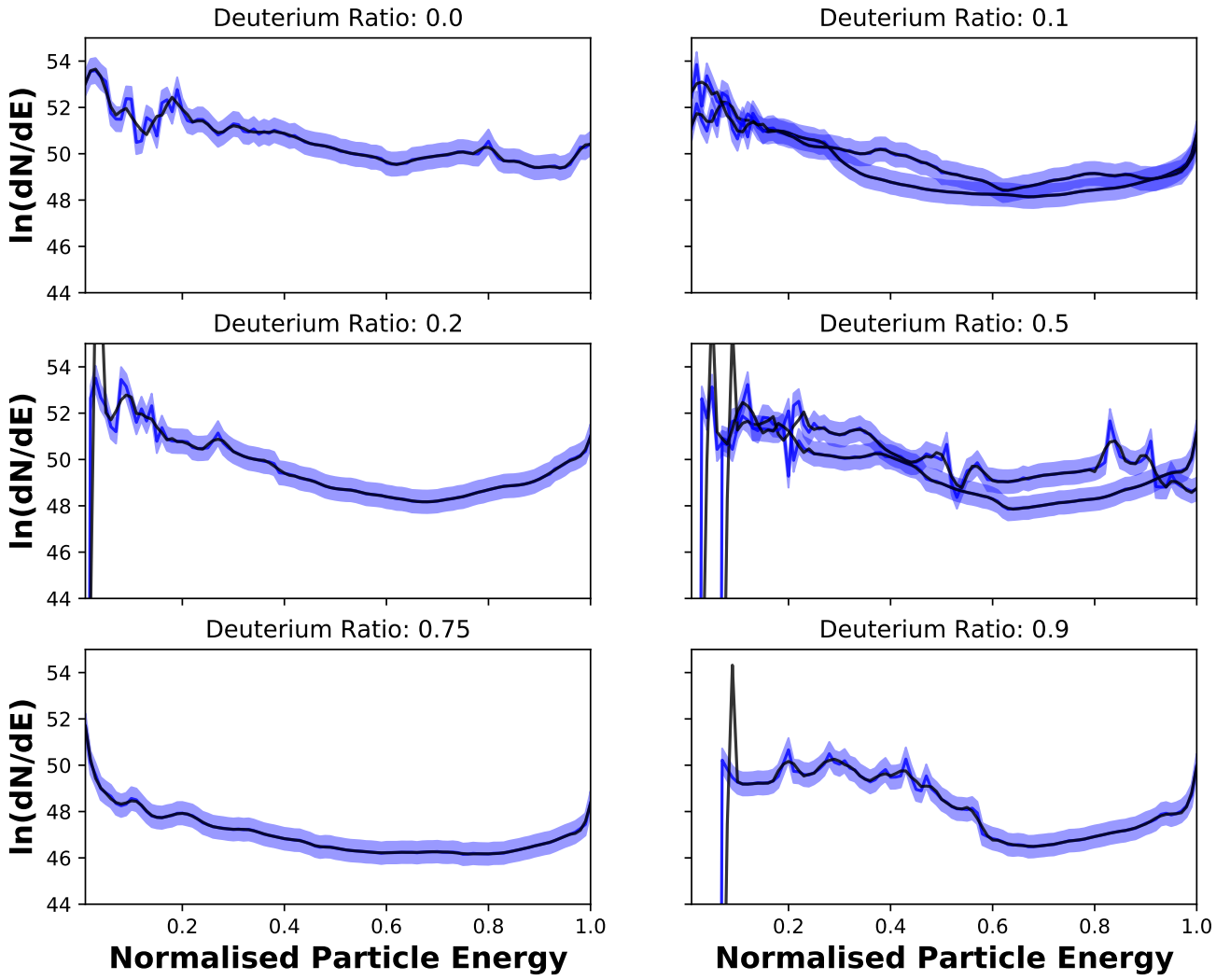

Figure B.5.: Savitzky-Golay filter with window size 7 and a 3rd order polynomial. Blue indicates the raw data, projected to a wider range for visibility and black indicates the filtered signal.

Numerical Parameters, Training, and Topology

As none of the architectural parameters for these models were known, some outlying hyperparameters were decided first. For a regression problem, the Rectified Linear Unit (ReLU) activation function is widely used and was added to every network layer except the output layer which used the identity activation. Similarly, we chose the mean squared error, suited for regression problems, as loss and it was minimized using the Adam optimizer with $\beta_1 = 0.9$, $\beta_2 = 0.999$ and $\epsilon = 1 \times 10^{-7}$. The initial learning rate was 0.001 which was lowered to a minimum of 0.0001 during training should the optimizer detect a plateau in the validation loss value (Keras' ReduceLROnPlateau feature). In order for the physical parameters to be more manageable numerically, all parameters were divided by the maximum value in their range (see Table 6.1) before being given to the model.
With these outlying parameters in place, the architecture of the FCNs, i.e. the number of layers and the number of neurons in each layer, was left variable and was optimized for the problem using a hyperparameter tuning method. Keras Tuner allows for extensive hyperparameter tuning using various optimization algorithms (O'Malley et al. 2019).

Recalling section 6.1 and in the corresponding publication (Schmitz, Kreuter, et al. 2023), each simulation output contains information about 100 locations in the energy spectrum of the particles. Hence, the available data length for the reduced continuous model was $68973 \times 100 = 6897300$ data points. Of these, 81% were used for training, 9% were used for validation, and 10% were used for testing. Running Keras Tuner on Google Cloud Compute Engine API from a Google Colab Notebook, Bayesian Optimization could be performed for the hyperparameters of the continuous model of hydrogen ions. In order to find a model architecture that most accurately describes the simulation results the number of layers and the number of neurons for each layer was first optimized to achieve the lowest possible training loss. Every training used a batch size of 256 and an early stopping mechanism. After 50 trials, each running training twice in order to lower the chance of a bad local minimum, a suitable architecture was found. However, this optimized model was only tuned to minimize the training loss of the model without considering the validation data at all. To generalize the model, hyperparameter tuning was run again on the optimized architecture, this time with L1 and L2 regularization on each layer as the hyperparameters to be tuned and with the tuning objective set to the mean squared error on the validation set. A schematic of the final optimized model for the continuous energy spectrum of hydrogen ions is shown in Table 6.2 (a).
Each hidden layer in the network has L1 regularization strength of 1.98×10^{-6} and L2 regularization strength of 3.07×10^{-8}. The network achieved a mean squared error of 3.38 on the 620 757 randomly selected validation data points. As a reminder, this number is equal to the mean squared error on the $\ln\left(\frac{\mathrm{d}n}{\mathrm{d}E}(E)\right)$ prediction for input parameters $\{E, [\text{physical parameters}]\}$.
Equivalently, the second model predicting the maximum ion energy could be tuned and optimized. Since the maximum energy is only predicted per simulation and not per energy bin of the energy spectra, the second model was trained on 68 973 unique data points. This significantly smaller dataset made the model training on a home computer feasible. The optimized model for the maximum energy found L1 regularization strength of 2.3×10^{-4} and L2 regularization strength of 1.1×10^{-7}.

C. Modeling of Neutron Production

Table C.1.: Data for detectors implemented in the Monte Carlo model. Radius of the detector sphere is 25 cm. Area gives the absolute covered area of the specific detector, while Ratio gives the percentage of full coverage. Every second value is grayed to guide the eye. Θ_{min} and Θ_{max} values describe the minimum and maximum scattering angle which the detector can measure. Θ_{mean} is the central scattering angle of the detector.

Index	Θ_{min} °	Θ_{max} °	Θ_{mean} °	$\sigma\Theta$ °	Area cm^2	Ratio %
D01	0	5	0.0	5.0	14.94	0.19
D02	5	10	7.5	2.5	44.72	0.57
D03	10	15	12.5	2.5	74.15	0.94
D04	15	25	20.0	5.0	234.12	2.98
D05	25	35	30.0	5.0	342.26	4.36
D06	35	45	40.0	5.0	440.00	5.60
D07	45	55	50.0	5.0	524.37	6.68
D08	55	65	60.0	5.0	592.81	7.55
D09	65	75	70.0	5.0	643.24	8.19
D10	75	85	80.0	5.0	674.12	8.58
D11	85	95	90.0	5.0	684.52	8.72
D12	95	105	100.0	5.0	674.12	8.58
D13	105	115	110.0	5.0	643.24	8.19
D14	115	125	120.0	5.0	592.81	7.55
D15	125	135	130.0	5.0	524.37	6.68
D16	135	145	140.0	5.0	440.00	5.60
D17	145	155	150.0	5.0	342.26	4.36
D18	155	165	160.0	5.0	234.12	2.98
D19	165	170	167.5	2.5	74.15	0.94
D20	170	175	172.5	2.5	44.72	0.57
D21	175	180	180.0	5.0	14.94	0.19

Bibliography

Abadi, M., A. Agarwal, P. Barham, E. Brevdo, Z. Chen, C. Citro, G. S. Corrado, A. Davis, J. Dean, M. Devin, S. Ghemawat, I. Goodfellow, A. Harp, G. Irving, M. Isard, Y. Jia, R. Jozefowicz, L. Kaiser, M. Kudlur, J. Levenberg, D. Mané, R. Monga, S. Moore, D. Murray, C. Olah, M. Schuster, J. Shlens, B. Steiner, I. Sutskever, K. Talwar, P. Tucker, V. Vanhoucke, V. Vasudevan, F. Viégas, O. Vinyals, P. Warden, M. Wattenberg, M. Wicke, Y. Yu, and X. Zheng (2015). *TensorFlow: Large-Scale Machine Learning on Heterogeneous Systems*. Software available from tensorflow.org. URL: https://www.tensorflow.org/.

Adams, M. L. and E. W. Larsen (Jan. 2002). "Fast iterative methods for discrete-ordinates particle transport calculations". In: *Progress in Nuclear Energy* 40.1, pp. 3–159. DOI: 10.1016/s0149-1970(01)00023-3.

Alejo, A., S. Kar, H. Ahmed, A. G. Krygier, D. Doria, R. Clarke, J. Fernandez, R. R. Freeman, J. Fuchs, A. Green, J. S. Green, D. Jung, A. Kleinschmidt, C. L. S. Lewis, J. T. Morrison, Z. Najmudin, H. Nakamura, G. Nersisyan, P. Norreys, M. Notley, M. Oliver, M. Roth, J. A. Ruiz, L. Vassura, M. Zepf, and M. Borghesi (Sept. 2014). "Characterisation of deuterium spectra from laser driven multi-species sources by employing differentially filtered image plate detectors in Thomson spectrometers". In: *Review of Scientific Instruments* 85.9, p. 093303. DOI: 10.1063/1.4893780.

Alfvén, H. (Oct. 1942). "Existence of Electromagnetic-Hydrodynamic Waves". In: *Nature* 150.3805, pp. 405–406. DOI: 10.1038/150405d0.

Alvarez, J., J. Fernández-Tobias, K. Mima, S. Nakai, S. Kar, Y. Kato, and J. Perlado (2014). "Laser Driven Neutron Sources: Characteristics, Applications and Prospects". In: *Physics Procedia* 60, pp. 29–38. DOI: 10.1016/j.phpro.2014.11.006.

Arber, T. D., K. Bennett, C. S. Brady, A. Lawrence-Douglas, M. G. Ramsay, N. J. Sircombe, P. Gillies, R. G. Evans, H. Schmitz, A. R. Bell, and C. P. Ridgers (Sept. 2015). "Contemporary particle-in-cell approach to laser-plasma modelling". In: *Plasma Physics and Controlled Fusion* 57.11, p. 113001. DOI: 10.1088/0741-3335/57/11/113001.

Ashkar, R., H. Z. Bilheux, H. Bordallo, R. Briber, D. J. E. Callaway, X. Cheng, X.-Q. Chu, J. E. Curtis, M. Dadmun, P. Fenimore, D. Fushman, F. Gabel, K. Gupta, F. Herberle, F. Heinrich, L. Hong, J. Katsaras, Z. Kelman, E. Kharlampieva, G. R. Kneller, A. Kovalevsky, S. Krueger, P. Langan, R. Lieberman, Y. Liu, M. Losche, E. Lyman, Y. Mao, J. Marino, C. Mattos, F. Meilleur, P. Moody, J. D. Nickels, W. B. O'Dell, H. O'Neill, U. Perez-Salas, J. Peters, L. Petridis, A. P. Sokolov, C. Stanley, N. Wagner, M. Weinrich, K. Weiss, T. Wymore, Y. Zhang, and J. C. Smith (Dec. 2018). "Neutron scattering in the biological sciences: progress and prospects". In: *Acta Crystallographica Section D Structural Biology* 74.12, pp. 1129–1168. DOI: 10.1107/s2059798318017503.

Ashland Global Holdings Inc, Delaware, U.S. (Feb. 8, 2022). "Gafchromic Film". In: *www.gafchromic.com*. Ed. by U. Ashland Global Holdings Inc Delaware. URL: www.gafchromic.com.

Aymar, G., T. Becker, S. Boogert, M. Borghesi, R. Bingham, C. Brenner, P. N. Burrows, O. C. Ettlinger, T. Dascalu, S. Gibson, T. Greenshaw, S. Gruber, D. Gujral, C. Hardiman, J. Hughes, W. G. Jones, K. Kirkby, A. Kurup, J.-B. Lagrange, K. Long, W. Luk, J. Matheson, P. McKenna, R. McLauchlan, Z. Najmudin, H. T. Lau, J. L. Parsons, J. Pasternak, J. Pozimski, K. Prise, M. Puchalska, P. Ratoff, G. Schettino, W. Shields, S. Smith, J. Thomason, S. Towe, P. Weightman, C. Whyte, and R. Xiao (Sept. 2020). "LhARA: The Laser-hybrid Accelerator for Radiobiological Applications". In: *Frontiers in Physics* 8. DOI: 10.3389/fphy.2020.567738.

Baroni, G. and T. Francke (Dec. 2020). “An effective strategy for combining variance- and distribution-based global sensitivity analysis”. In: *Environmental Modelling & Software* 134, p. 104851. DOI: 10.1016/j.envsoft.2020.104851.

Berglund, M., L. Rymell, H. M. Hertz, and T. Wilhein (June 1998). “Cryogenic liquid-jet target for debris-free laser-plasma soft x-ray generation”. In: *Review of Scientific Instruments* 69.6, pp. 2361–2364. DOI: 10.1063/1.1148944.

Bethe, H. (1930). “Zur Theorie des Durchgangs schneller Korpuskularstrahlen durch Materie”. In: *Annalen der Physik* 397.3, pp. 325–400. DOI: 10.1002/andp.19303970303.

Biersack, J. and L. Haggmark (Aug. 1980). “A Monte Carlo computer program for the transport of energetic ions in amorphous targets”. In: *Nuclear Instruments and Methods* 174.1-2, pp. 257–269. DOI: 10.1016/0029-554x(80)90440-1.

Birdsall, C. and A. Langdon (2004). *Plasma Physics via Computer Simulation*. Series in Plasma Physics and Fluid Dynamics. Taylor & Francis. ISBN: 9780750310253.

Bishop, C. M. (Aug. 2006). *Pattern Recognition and Machine Learning*. Springer-Verlag New York Inc. 738 pp. ISBN: 0387310738. URL: https://www.ebook.de/de/product/5324937/christopher_m_bishop_pattern_recognition_and_machine_learning.html.

Bloch, F. (1933). “Zur Bremsung rasch bewegter Teilchen beim Durchgang durch Materie”. In: *Annalen der Physik* 408.3, pp. 285–320. DOI: 10.1002/andp.19334080303.

Borghesi, M., S. Kar, and D. Margarone (2013). “Laser-ion accelerators: State-of-the-art and scaling laws”. In: *AIP Conference Proceedings*. AIP. DOI: 10.1063/1.4816600.

Bourdier, A. (1983). “Oblique incidence of a strong electromagnetic wave on a cold inhomogeneous electron plasma. Relativistic effects”. In: *Physics of Fluids* 26.7, p. 1804. DOI: 10.1063/1.864355.

Brady, C. S., C. P. Ridgers, T. D. Arber, and A. R. Bell (Mar. 2014). “Synchrotron radiation, pair production, and longitudinal electron motion during 10-100 PW laser solid interactions”. In: *Physics of Plasmas* 21.3, p. 033108. DOI: 10.1063/1.4869245.

Brenner, C., J. Green, A. Robinson, D. Carroll, B. Dromey, P. Foster, S. Kar, Y. Li, K. Markey, C. Spindloe, M. Streeter, M. Tolley, C.-G. Wahlström, M. Xu, M. Zepf, P. McKenna, and D. Neely (Sept. 2011). “Dependence of laser accelerated protons on laser energy following the interaction of defocused, intense laser pulses with ultra-thin targets”. In: *Laser and Particle Beams* 29.3, pp. 345–351. DOI: 10.1017/s0263034611000395.

Brunel, F. (July 1987). “Not-so-resonant, resonant absorption”. In: *Physical Review Letters* 59.1, pp. 52–55. DOI: 10.1103/physrevlett.59.52.

Bryant, P. (1994). “A brief history and review of accelerators”. In.

Büchner, J., M. Scholer, and C. T. Dum (Dec. 4, 2010). *Space Plasma Simulation*. Springer Berlin Heidelberg. 372 pp. ISBN: 3642056342. URL: https://www.ebook.de/de/product/13905179/space_plasma_simulation.html.

Buckingham, E. (Oct. 1914). “On Physically Similar Systems: Illustrations of the Use of Dimensional Equations”. In: *Physical Review* 4.4, pp. 345–376. DOI: 10.1103/physrev.4.345.

– (Dec. 1915). “The Principle of Similitude”. In: *Nature* 96.2406, pp. 396–397. DOI: 10.1038/096396d0.

Capdessus, R., E. d’Humières, and V. T. Tikhonchuk (May 2013). “Influence of Ion Mass on Laser-Energy Absorption and Synchrotron Radiation at Ultrahigh Laser Intensities”. In: *Physical Review Letters* 110.21. DOI: 10.1103/physrevlett.110.215003.

Cappa, C. D., W. S. Drisdell, J. D. Smith, R. J. Saykally, and R. C. Cohen (Dec. 2005). “Isotope Fractionation of Water during Evaporation without Condensation”. In: *The Journal of Physical Chemistry B* 109.51, pp. 24391–24400. DOI: 10.1021/jp0539066.

Chadwick, J. (1932). “The existence of a neutron”. In: *Proceedings of the Royal Society of London. Series A, Containing Papers of a Mathematical and Physical Character* 136.830, pp. 692–708. DOI: 10.1098/rspa.

1932.0112. eprint: https://royalsocietypublishing.org/doi/pdf/10.1098/rspa.1932.0112. URL: https://royalsocietypublishing.org/doi/abs/10.1098/rspa.1932.0112.

Chen, Y., X. Chen, J. Lei, L. An, X. Zhang, J. Shao, P. Zheng, and X. Wang (June 2014). "Unfolding the fast neutron spectra of a BC501A liquid scintillation detector using GRAVEL method". In: *Science China Physics, Mechanics & Astronomy* 57.10, pp. 1885–1890. DOI: 10.1007/s11433-014-5553-7.

Chollet, F. et al. (2015). *Keras*. https://keras.io.

Cialfi, L., L. Fedeli, and M. Passoni (Nov. 2016). "Electron heating in subpicosecond laser interaction with overdense and near-critical plasmas". In: *Physical Review E* 94.5, p. 053201. DOI: 10.1103/physreve.94.053201.

Clark, E. L., K. Krushelnick, J. R. Davies, M. Zepf, M. Tatarakis, F. N. Beg, A. Machacek, P. A. Norreys, M. I. K. Santala, I. Watts, and A. E. Dangor (Jan. 2000). "Measurements of Energetic Proton Transport through Magnetized Plasma from Intense Laser Interactions with Solids". In: *Physical Review Letters* 84.4, pp. 670–673. DOI: 10.1103/physrevlett.84.670.

CLIC et al. (2018). "The Compact Linear Collider (CLIC) - 2018 Summary Report". In: DOI: 10.48550/ARXIV.1812.06018.

Compact Accelerator Based Neutron Sources (2021). TECDOC Series 1981. Vienna: INTERNATIONAL ATOMIC ENERGY AGENCY. ISBN: 978-92-0-127022-1. URL: https://www.iaea.org/publications/14948/compact-accelerator-based-neutron-sources.

Courant, R., K. Friedrichs, and H. Lewy (1928). "Über die partiellen Differenzengleichungen der mathematischen Physik". In: *Mathematische annalen* 100.1, pp. 32–74.

Crockcroft, J. and E. Walton (1932). "Experiments with high velocity ions". In: *Proc. Royal Soc., Series A*. Vol. 136, pp. 619–30.

Cui, Y.-Q., W.-M. Wang, Z.-M. Sheng, Y.-T. Li, and J. Zhang (June 2013). "Laser absorption and hot electron temperature scalings in laser–plasma interactions". In: *Plasma Physics and Controlled Fusion* 55.8, p. 085008. DOI: 10.1088/0741-3335/55/8/085008.

Davies, J. (June 2006). "The Alfvén limit revisited and its relevance to laser-plasma interactions". In: *Laser and Particle Beams* 24.2, pp. 299–310. DOI: 10.1017/s0263034606060460.

Demtröder, W. (June 24, 2016). *Experimentalphysik 3*. Springer Berlin Heidelberg. 612 pp. ISBN: 3662490935.

Derouillat, J., A. Beck, F. Pérez, T. Vinci, M. Chiaramello, A. Grassi, M. Flé, G. Bouchard, I. Plotnikov, N. Aunai, J. Dargent, C. Riconda, and M. Grech (Jan. 2018). "Smilei : A collaborative, open-source, multi-purpose particle-in-cell code for plasma simulation". In: *Computer Physics Communications* 222, pp. 351–373. DOI: 10.1016/j.cpc.2017.09.024.

Didenko, N. V., A. V. Konyashchenko, A. P. Lutsenko, and S. Y. Tenyakov (2008). "Contrast degradation in a chirped-pulse amplifier due to generation of prepulses by postpulses". In: *Optics Express* 16.5, p. 3178. DOI: 10.1364/oe.16.003178.

Dover, N. P., M. Nishiuchi, H. Sakaki, M. A. Alkhimova, A. Y. Faenov, Y. Fukuda, H. Kiriyama, A. Kon, K. Kondo, K. Nishitani, K. Ogura, T. A. Pikuz, A. S. Pirozhkov, A. Sagisaka, M. Kando, and K. Kondo (July 2017). "Scintillator-based transverse proton beam profiler for laser-plasma ion sources". In: *Review of Scientific Instruments* 88.7, p. 073304. DOI: 10.1063/1.4994732.

Duderstadt, E. H. (Jan. 2, 1976). *Nuclear Reactor Analysis*. John Wiley & Sons, Inc. 672 pp. ISBN: 0471223638. URL: https://www.ebook.de/de/product/3597336/duderstadt_e_hamilton_nuclear_reactor_analysis.html.

Efron, B. and R. J. Tibshirani (1994). "An Introduction to the Bootstrap". In: *Chapman and Hall/CRC*, p. 456. DOI: 10.1201/9780429246593.

Egenolf, T. (2020). "Intensity Effects in Dielectric Laser Accelerator Structures". PhD Thesis. TU Darmstadt. DOI: 10.25534/TUPRINTS-00014139.

Eickhoff, H., R. Bar, A. Dolinskii, T. Haberer, B. Schlitt, P. Spiller, and U. Weinrich (2003). “HICAT - the German hospital-based light ion cancer therapy project”. In: *Proceedings of the 2003 Bipolar/BiCMOS Circuits and Technology Meeting (IEEE Cat. No.03CH37440)*. IEEE. DOI: 10.1109/pac.2003.1289012.

Endl, B. (2021). “Automatisierte Bilderverarbeitung für Ionenstrahldiagnostik”. B.Sc. Thesis. TU Darmstadt.

ESFRI Physical Sciences and Engineering Strategy Working Group - NeutronLandscape Group (Sept. 30, 2015). *Neutron scattering facilities in Europe - Present status and future perspectives*. ESFRI Scripta. Ed. by C. Carlile and C. Petrillo. Vol. 1. URL: https://www.esfri.eu/sites/default/files/NGL_CombinedReport_230816_Complete%20document_0209-1.pdf.

Favalli, A., N. Guler, D. Henzlova, S. Croft, K. Falk, D. C. Gautier, K. D. Ianakiev, M. Iliev, S. Palaniyappan, M. Roth, J. C. Fernandez, and M. T. Swinhoe (Feb. 2019). “Characterizing laser-plasma ion accelerators driving an intense neutron beam via nuclear signatures”. In: *Scientific Reports* 9.1. DOI: 10.1038/s41598-019-39054-z.

Flacco, A., F. Sylla, M. Veltcheva, M. Carrié, R. Nuter, E. Lefebvre, D. Batani, and V. Malka (Mar. 2010). “Dependence on pulse duration and foil thickness in high-contrast-laser proton acceleration”. In: *Physical Review E* 81.3, p. 036405. DOI: 10.1103/physreve.81.036405.

Forrest, R., R. Capote, N. Otsuka, T. Kawano, A. Koning, S. Kunieda, J.-C. Sublet, and Y. Watanabe (2012). *FENDL-3 Library Summary documentation*. Tech. rep. International Atomic Energy Agency, Vienna, Austria. URL: https://nds.iaea.org/publications/indc/indc-nds-0628/.

Fourmaux, S., S. Buffechoux, B. Albertazzi, D. Capelli, A. Lévy, S. Gnedyuk, L. Lecherbourg, P. Lassonde, S. Payeur, P. Antici, H. Pépin, R. S. Marjoribanks, J. Fuchs, and J. C. Kieffer (Jan. 2013). “Investigation of laser-driven proton acceleration using ultra-short, ultra-intense laser pulses”. In: *Physics of Plasmas* 20.1, p. 013110. DOI: 10.1063/1.4789748.

FRM II – Forschungs-Neutronenquelle Heinz Maier-Leibnitz (2016). *Joint Annual Report 2015 of the MLZ and FRM II*. Tech. rep. DOI: 10.14459/2015MD1292666.

– (2017). *Joint Annual Report 2016 of the MLZ and FRM II*. Tech. rep. DOI: 10.14459/2017MD1352771.

– (2018). *Joint Annual Report 2017 of the MLZ and FRM II*. Tech. rep. DOI: 10.14459/2018MD1431530.

– (2019). *Joint Annual Report 2018 of the MLZ and FRM II*. Tech. rep. DOI: 10.14459/2019md1474027.

– (2020). *Joint Annual Report 2019 of the MLZ and FRM II*. Tech. rep. DOI: 10.14459/2020MD1535058.

– (2021). *Joint Annual Report 2020 of the MLZ and FRM II*. Tech. rep. DOI: 10.14459/2021MD1601341.

– (2022). *Joint Annual Report 2021 of the MLZ and FRM II*. Tech. rep. DOI: 10.14459/2022MD1639756.

Fryxell, B., K. Olson, P. Ricker, F. X. Timmes, M. Zingale, D. Q. Lamb, P. MacNeice, R. Rosner, J. W. Truran, and H. Tufo (Nov. 2000). “FLASH: An Adaptive Mesh Hydrodynamics Code for Modeling Astrophysical Thermonuclear Flashes”. In: *The Astrophysical Journal Supplement Series* 131.1, pp. 273–334. DOI: 10.1086/317361.

Fuchs, J., P. Antici, E. d’Humières, E. Lefebvre, M. Borghesi, E. Brambrink, C. A. Cecchetti, M. Kaluza, V. Malka, M. Manclossi, S. Meyroneinc, P. Mora, J. Schreiber, T. Toncian, H. Pépin, and P. Audebert (Dec. 2005). “Laser-driven proton scaling laws and new paths towards energy increase”. In: *Nature Physics* 2.1, pp. 48–54. DOI: 10.1038/nphys199.

Garoby, R., A. Vergara, H. Danared, I. Alonso, E. Bargallo, B. Cheymol, C. Darve, M. Eshraqi, H. Hassanzadegan, A. Jansson, I. Kittelmann, Y. Levinsen, M. Lindroos, C. Martins, Ø. Midttun, R. Miyamoto, S. Molloy, D. Phan, A. Ponton, E. Sargsyan, T. Shea, A. Sunesson, L. Tchelidze, C. Thomas, M. Jensen, W. Hees, P. Arnold, M. Juni-Ferreira, F. Jensen, A. Lundmark, D. McGinnis, N. Gazis, J. W. II, M. Anthony, E. Pitcher, L. Coney, M. Gohran, J. Haines, R. Linander, D. Lyngh, U. Oden, H. Carling, R. Andersson, S. Birch, J. Cereijo, T. Friedrich, T. Korhonen, E. Laface, M. Mansouri-Sharifabad, A. Monera-Martinez, A. Nordt, D. Paulic, D. Piso, S. Regnell, M. Zaera-Sanz, M. Aberg, K. Breimer, K. Batkov, Y. Lee, L. Zanini, M. Kickulies, Y. Bessler, J. Ringnér, J. Jurns, A. Sadeghzadeh, P. Nilsson, M. Olsson, J.-E. Presteng, H. Carlsson, A. Polato, J. Harborn,

K. Sjögreen, G. Muhrer, and F. Sordo (Dec. 2017). “The European Spallation Source Design”. In: *Physica Scripta* 93.1, p. 014001. DOI: 10.1088/1402-4896/aa9bff.

George, K. M., J. T. Morrison, S. Feister, G. K. Ngirmang, J. R. Smith, A. J. Klim, J. Snyder, D. Austin, W. Erbsen, K. D. Frische, J. Nees, C. Orban, E. A. Chowdhury, and W. M. Roquemore (2019). “High-repetition-rate (kHz) targets and optics from liquid microjets for high-intensity laser–plasma interactions”. In: *High Power Laser Science and Engineering* 7. DOI: 10.1017/hpl.2019.35.

Gibbon, P., A. Andreev, E. Lefebvre, G. Bonnaud, H. Ruhl, J. Delettrez, and A. R. Bell (Mar. 1999). “Calibration of one-dimensional boosted kinetic codes for modeling high-intensity laser–solid interactions”. In: *Physics of Plasmas* 6.3, pp. 947–953. DOI: 10.1063/1.873335.

Gibbon, P. (Sept. 5, 2005). *Short Pulse Laser Interactions with Matter*. Imperial College Press. 328 pp. ISBN: 1860941354. URL: https://www.ebook.de/de/product/3747267/paul_gibbon_short_pulse_laser_interactions_with_matter.html.

Godfrey, B. B. (Aug. 1974). “Numerical Cherenkov instabilities in electromagnetic particle codes”. In: *Journal of Computational Physics* 15.4, pp. 504–521. DOI: 10.1016/0021-9991(74)90076-x.

Goodfellow, I., Y. Bengio, and A. Courville (Nov. 2016). *Deep Learning*. The MIT Press. 775 pp. ISBN: 0262035618. URL: https://www.ebook.de/de/product/26337726/ian_goodfellow_yoshua_bengio_aaron_courville_deep_learning.html.

Green, J. S., M. Borghesi, C. M. Brenner, D. C. Carroll, N. P. Dover, P. S. Foster, P. Gallegos, S. Green, D. Kirby, K. J. Kirkby, P. McKenna, M. J. Merchant, Z. Najmudin, C. A. J. Palmer, D. Parker, R. Prasad, K. E. Quinn, P. P. Rajeev, M. P. Read, L. Romagnani, J. Schreiber, M. J. V. Streeter, O. Tresca, C.-G. Wahlström, M. Zepf, and D. Neely (May 2011). “Scintillator-based ion beam profiler for diagnosing laser-accelerated ion beams”. In: *SPIE Proceedings*. Ed. by K. W. D. Ledingham, W. P. Leemans, E. Esarey, S. M. Hooker, K. Spohr, and P. McKenna. SPIE. DOI: 10.1117/12.888967.

Gutberlet, T., D. Tunger, P. Zeitler, and T. Brückel (Apr. 2018). “Do neutrons publish? A neutron publication survey, 2005–2015”. In: *Neutron News* 29.2, pp. 18–24. DOI: 10.1080/10448632.2018.1514199.

Haghighat, A. (Aug. 2020). *Monte Carlo Methods for Particle Transport*. 2nd ed. CRC Press, p. 320. ISBN: 9780429198397. DOI: 10.1201/9780429198397.

Hahn, O. and F. Strassmann (Feb. 1939). “Nachweis der Entstehung aktiver Bariumisotope aus Uran und Thorium durch Neutronenbestrahlung; Nachweis weiterer aktiver Bruchstücke bei der Uranspaltung”. In: *Die Naturwissenschaften* 27.6, pp. 89–95. DOI: 10.1007/bf01488988.

He, Z.-H., B. Hou, J. A. Nees, J. H. Easter, J. Faure, K. Krushelnick, and A. G. R. Thomas (May 2013). “High repetition-rate wakefield electron source generated by few-millijoule, 30 fs laser pulses on a density downramp”. In: *New Journal of Physics* 15.5, p. 053016. DOI: 10.1088/1367-2630/15/5/053016. URL: https://dx.doi.org/10.1088/1367-2630/15/5/053016.

Hegelich, B. M., B. J. Albright, J. Cobble, K. Flippo, S. Letzring, M. Paffett, H. Ruhl, J. Schreiber, R. K. Schulze, and J. C. Fernández (Jan. 2006). “Laser acceleration of quasi-monoenergetic MeV ion beams”. In: *Nature* 439.7075, pp. 441–444. DOI: 10.1038/nature04400.

Hesse, M., T. Ebert, M. Zimmer, S. Scheuren, G. Schaumann, and M. Roth (Sept. 2021). “Spatially resolved online particle detector using scintillators for laser-driven particle sources”. In: *Review of Scientific Instruments* 92.9, p. 093302. DOI: 10.1063/5.0052507.

Hesse, M. (2022). “OCTOPUS – A High Repetition Rate Detector for Laser-Accelerated Particles”. PhD thesis. TU Darmstadt. DOI: 10.26083/TUPRINTS-00020248.

Hey, D. S., M. H. Key, A. J. Mackinnon, A. G. MacPhee, P. K. Patel, R. R. Freeman, L. D. V. Woerkom, and C. M. Castaneda (May 2008). “Use of GafChromic film to diagnose laser generated proton beams”. In: *Review of Scientific Instruments* 79.5, p. 053501. DOI: 10.1063/1.2901603.

Hjorth-Jensen, M., M. Kuchera, R. Ramanjuan, S. Liddick, and D. Bazin (2020). *Machine Learning and Data Analysis for Nuclear Physics, a Nuclear TALENT Course at the ECT**. URL: https://github.com/NuclearTalent/MachineLearningECT.

Hornung, J., Y. Zobus, P. Boller, C. Brabetz, U. Eisenbarth, T. Kühl, Z. Major, J. Ohland, M. Zepf, B. Zielbauer, et al. (2020). "Enhancement of the laser-driven proton source at PHELIX". In: *High Power Laser Science and Engineering* 8, e24.

Huault, M., D. D. Luis, J. I. Api naniz, M. D. Marco, C. Salgado, N. Gordillo, C. G. Neira, J. A. Pérez-Hernández, R. Fedosejevs, G. Gatti, L. Roso, and L. Volpe (2019). "A 2D scintillator-based proton detector for high repetition rate experiments". In: *High Power Laser Science and Engineering* 7. DOI: 10.1017/hpl.2019.43.

Huebl, A., M. Rehwald, L. Obst-Huebl, T. Ziegler, M. Garten, R. Widera, K. Zeil, T. E. Cowan, M. Bussmann, U. Schramm, and T. Kluge (Oct. 2020). "Spectral control via multi-species effects in PW-class laser-ion acceleration". In: *Plasma Physics and Controlled Fusion* 62.12, p. 124003. DOI: 10.1088/1361-6587/abbe33.

Humbird, K. D., J. L. Peterson, B. K. Spears, and R. G. McClarren (Jan. 2020). "Transfer Learning to Model Inertial Confinement Fusion Experiments". In: *IEEE Transactions on Plasma Science* 48.1, pp. 61–70. DOI: 10.1109/tps.2019.2955098.

Jähne, B. (2005). *Digital Image Processing*. 6th ed. Berlin/Heidelberg: Springer, p. 608. ISBN: 3-540-24035-7. DOI: 10.1007/3-540-27563-0.

Johnson, R. and P. Tandy (Dec. 1974). "An approximate three-body theory of deuteron stripping". In: *Nuclear Physics A* 235.1, pp. 56–74. DOI: 10.1016/0375-9474(74)90178-x.

Jüttner, F. (1911a). "Das Maxwellsche Gesetz der Geschwindigkeitsverteilung in der Relativtheorie". In: *Annalen der Physik* 339.5, pp. 856–882. DOI: 10.1002/andp.19113390503.

– (1911b). "Die Dynamik eines bewegten Gases in der Relativtheorie". In: *Annalen der Physik* 340.6, pp. 145–161. DOI: 10.1002/andp.19113400608.

Katayama, R., E. Kako, S. Yamaguchi, S. Michizono, K. Umemori, and Y. Kondo (Feb. 2022). "Design study of compact medical accelerator using superconducting rf quadrupole for boron neutron capture therapy". In: *Physical Review Accelerators and Beams* 25.2. DOI: 10.1103/physrevaccelbeams.25.021601.

Keppler, S., N. Elkina, G. A. Becker, J. Hein, M. Hornung, M. Mäusezahl, C. Rödel, I. Tamer, M. Zepf, and M. C. Kaluza (Jan. 2022). "Intensity scaling limitations of laser-driven proton acceleration in the TNSA-regime". In: *Physical Review Research* 4.1, p. 013065. DOI: 10.1103/physrevresearch.4.013065.

Keppler, S., A. Sävert, J. Körner, M. Hornung, H. Liebetrau, J. Hein, and M. C. Kaluza (Dec. 2015). "The generation of amplified spontaneous emission in high-power CPA laser systems". In: *Laser & Photonics Reviews* 10.2, pp. 264–277. DOI: 10.1002/lpor.201500186.

Kleinschmidt, A., V. Bagnoud, O. Deppert, A. Favalli, S. Frydrych, J. Hornung, D. Jahn, G. Schaumann, A. Tebartz, F. Wagner, G. Wurden, B. Zielbauer, and M. Roth (May 2018). "Intense, directed neutron beams from a laser-driven neutron source at PHELIX". In: *Physics of Plasmas* 25.5, p. 053101. DOI: 10.1063/1.5006613.

Kleinschmidt, A. (2017). "Investigation of a laser-driven neutron source with respect to different fields of application". en. PhD thesis. Darmstadt: Technische Universität. URL: http://tuprints.ulb.tu-darmstadt.de/6753/.

Kluge, T., T. Cowan, A. Debus, U. Schramm, K. Zeil, and M. Bussmann (Nov. 2011). "Electron Temperature Scaling in Laser Interaction with Solids". In: *Physical Review Letters* 107.20, p. 205003. DOI: 10.1103/physrevlett.107.205003.

Kramida, A. (2006). *NIST Atomic Energy Levels and Spectra Bibliographic Database*. en. DOI: 10.18434/T40K53.

Kreuter, D. (2021). "Modelling of a Liquid Leaf Target TNSA Experiment using Particle-In-Cell Simulations and Deep Learning". M.Sc. Thesis. TU Darmstadt.

Krieger, H. (2018). *Strahlungsquellen für Technik und Medizin*. Springer Berlin Heidelberg. DOI: 10.1007/978-3-662-55827-0.

Kroll, F., F.-E. Brack, C. Bernert, S. Bock, E. Bodenstein, K. Brüchner, T. E. Cowan, L. Gaus, R. Gebhardt, U. Helbig, L. Karsch, T. Kluge, S. Kraft, M. Krause, E. Lessmann, U. Masood, S. Meister, J. Metzkes-Ng, A. Nossula, J. Pawelke, J. Pietzsch, T. Püschel, M. Reimold, M. Rehwald, C. Richter, H.-P. Schlenvoigt, U. Schramm, M. E. P. Umlandt, T. Ziegler, K. Zeil, and E. Beyreuther (Mar. 2022). "Tumour irradiation in mice with a laser-accelerated proton beam". In: *Nature Physics* 18.3, pp. 316–322. DOI: 10.1038/s41567-022-01520-3.

Kruer, W. L. and K. Estabrook (Jan. 1985). "JxB heating by very intense laser light". In: *Physics of Fluids* 28.1, pp. 430–432. DOI: 10.1063/1.865171.

Lakey, J. H. (Aug. 2009). "Neutrons for biologists: a beginner's guide, or why you should consider using neutrons". In: *Journal of The Royal Society Interface* 6.suppl_5. DOI: 10.1098/rsif.2009.0156.focus.

Lalee, M., J. Nocedal, and T. Plantenga (1998). "On the implementation of an algorithm for large-scale equality constrained optimization". In: *SIAM Journal on Optimization* 8.3, pp. 682–706.

Laser-Driven Sources of High Energy Particles and Radiation (Sept. 6, 2019). Springer International Publishing. 272 pp. ISBN: 3030258491. URL: https://www.ebook.de/de/product/37135065/laser_driven_sources_of_high_energy_particles_and_radiation.html.

Lawrence Heilbronn, T. N. (Dec. 15, 2005). *Handbook on Secondary Particle Production and Transport by High-Energy Heavy Ions [With CDROM]*. WORLD SCIENTIFIC PUB CO INC. 236 pp. ISBN: 9812565582.

Lawson, J. (1975). *Rutherford Laboratory Report*. Tech. rep. RL-75-043.

Lécz, Z. (Nov. 2013). "Laser ion acceleration from a double-layer metal foil". PhD thesis. Darmstadt: Technische Universität. URL: http://tuprints.ulb.tu-darmstadt.de/3335/.

Lécz, Z., O. Boine-Frankenheim, and V. Kornilov (Feb. 2015). "Transverse divergence in target normal sheath acceleration of a thick contamination layer". In: *Nuclear Instruments and Methods in Physics Research Section A: Accelerators, Spectrometers, Detectors and Associated Equipment* 774, pp. 42–50. DOI: 10.1016/j.nima.2014.11.062.

Linz, U. and J. Alonso (Sept. 2007). "What will it take for laser driven proton accelerators to be applied to tumor therapy?" In: *Physical Review Special Topics - Accelerators and Beams* 10.9. DOI: 10.1103/physrevstab.10.094801.

Livingston, M. S. (1980). "Early History of Particle Accelerators". In: *Advances in Electronics and Electron Physics Volume 50*. Elsevier, pp. 1–88. DOI: 10.1016/s0065-2539(08)61061-6.

Mayer-Kuckuk, T. (2013). *Kernphysik: Eine Einführung*. Springer-Verlag.

Metzkes, J., L. Karsch, S. D. Kraft, J. Pawelke, C. Richter, M. Schürer, M. Sobiella, N. Stiller, K. Zeil, and U. Schramm (Dec. 2012). "A scintillator-based online detector for the angularly resolved measurement of laser-accelerated proton spectra". In: *Review of Scientific Instruments* 83.12, p. 123301. DOI: 10.1063/1.4768672.

Metzkes, J., K. Zeil, S. D. Kraft, L. Karsch, M. Sobiella, M. Rehwald, L. Obst, H.-P. Schlenvoigt, and U. Schramm (Aug. 2016). "An online, energy-resolving beam profile detector for laser-driven proton beams". In: *Review of Scientific Instruments* 87.8, p. 083310. DOI: 10.1063/1.4961576.

Miley, G. H. and J. Sved (Nov. 2000). "The IEC star-mode fusion neutron source for NAA — status and next-step designs". In: *Applied Radiation and Isotopes* 53.4-5, pp. 779–783. DOI: 10.1016/s0969-8043(00)00215-3.

Mima, K., A. Yogo, S. R. Mirfayzi, Z. Lan, Y. Arikawa, Y. Abe, and H. Nishimura (Mar. 2022). "Laser-driven neutron source and nuclear resonance absorption imaging at ILE, Osaka University: review". In: *Applied Optics* 61.9, p. 2398. DOI: 10.1364/ao.444628.

Mora, P. (May 2003). "Plasma Expansion into a Vacuum". In: *Physical Review Letters* 90.18, p. 185002. DOI: 10.1103/physrevlett.90.185002.

Mora, P. (Nov. 2005). “Thin-foil expansion into a vacuum”. In: *Physical Review E* 72.5, p. 056401. DOI: 10.1103/physreve.72.056401.

Mora, P. (Mar. 2020). “A selection of theoretical results in the context of laser-plasma interaction and inertial fusion”. In: *High Energy Density Physics* 34, p. 100744. DOI: 10.1016/j.hedp.2020.100744.

Mora, P. and J. Thomas M. Antonsen (Jan. 1997). “Kinetic modeling of intense, short laser pulses propagating in tenuous plasmas”. In: *Physics of Plasmas* 4.1, pp. 217–229. DOI: 10.1063/1.872134.

Mulser, P. and D. Bauer (2010). *High Power Laser-Matter Interaction*. Springer Berlin Heidelberg. DOI: 10.1007/978-3-540-46065-7.

Nakai, S., K. Mima, Y. Kato, K. Tanaka, Y. Ikeda, H. Azechi, K. Miyanaga, M. Nakai, M. Perlado, and R. G. Arrabal (Aug. 2010). “Industrial applications of laser neutron source”. In: *Journal of Physics: Conference Series* 244.4, p. 042027. DOI: 10.1088/1742-6596/244/4/042027.

Naranjo, B., S. Putterman, and T. Venhaus (Mar. 2011). “Pyroelectric fusion using a tritiated target”. In: *Nuclear Instruments and Methods in Physics Research Section A: Accelerators, Spectrometers, Detectors and Associated Equipment* 632.1, pp. 43–46. DOI: 10.1016/j.nima.2010.08.003.

Niedermayer, U., J. Lautenschläger, T. Egenolf, and O. Boine-Frankenheim (Aug. 2021). “Design of a Scalable Integrated Nanophotonic Electron Accelerator on a Chip”. In: *Physical Review Applied* 16.2, p. 024022. DOI: 10.1103/physrevapplied.16.024022.

Niroomand-Rad, A., C. R. Blackwell, B. M. Coursey, K. P. Gall, J. M. Galvin, W. L. McLaughlin, A. S. Meigooni, R. Nath, J. E. Rodgers, and C. G. Soares (Oct. 1998). “Radiochromic film dosimetry: Recommendations of AAPM Radiation Therapy Committee Task Group 55”. In: *Medical Physics* 25.11, pp. 2093–2115. DOI: 10.1118/1.598407.

Nürnberg, F., M. Schollmeier, E. Brambrink, A. Blažević, D. C. Carroll, K. Flippo, D. C. Gautier, M. Geißel, K. Harres, B. M. Hegelich, O. Lundh, K. Markey, P. McKenna, D. Neely, J. Schreiber, and M. Roth (Mar. 2009). “Radiochromic film imaging spectroscopy of laser-accelerated proton beams”. In: *Review of Scientific Instruments* 80.3, p. 033301. DOI: 10.1063/1.3086424.

O’Malley, T., E. Bursztein, J. Long, F. Chollet, H. Jin, L. Invernizzi, et al. (2019). *KerasTuner*. https://github.com/keras-team/keras-tuner.

Obst, L., S. Göde, M. Rehwald, F.-E. Brack, J. a. Branco, S. Bock, M. Bussmann, T. E. Cowan, C. B. Curry, F. Fiuza, M. Gauthier, R. Gebhardt, U. Helbig, A. Huebl, U. Hübner, A. Irman, L. Kazak, J. B. Kim, T. Kluge, S. Kraft, M. Loeser, J. Metzkes, R. Mishra, C. Rödel, H.-P. Schlenvoigt, M. Siebold, J. Tiggesbäumker, S. Wolter, T. Ziegler, U. Schramm, S. H. Glenzer, and K. Zeil (Aug. 2017). “Efficient laser-driven proton acceleration from cylindrical and planar cryogenic hydrogen jets”. In: *Scientific Reports* 7.1. DOI: 10.1038/s41598-017-10589-3.

Otake, Y. (2018). “RIKEN Compact Neutron Systems with Fast and Slow Neutrons”. In: *Plasma and Fusion Research* 13, pp. 2401017–2401017. DOI: 10.1585/pfr.13.2401017.

Padamsee, H., J. Knobloch, and T. Hays (1998). “RF Superconductivity for Accelerators John Wiley & Sons”. In: *Inc., New York*, p. 199.

Passoni, M., A. Zani, A. Sgattoni, D. Dellasega, A. Macchi, I. Prencipe, V. Floquet, P. Martin, T. V. Liseykina, and T. Ceccotti (Mar. 2014). “Energetic ions at moderate laser intensities using foam-based multi-layered targets”. In: *Plasma Physics and Controlled Fusion* 56.4, p. 045001. DOI: 10.1088/0741-3335/56/4/045001.

Passoni, M., L. Bertagna, and A. Zani (Apr. 2010). “Target normal sheath acceleration: theory, comparison with experiments and future perspectives”. In: *New Journal of Physics* 12.4, p. 045012. DOI: 10.1088/1367-2630/12/4/045012.

Perego, C., D. Batani, A. Zani, and M. Passoni (Feb. 2012). “Target normal sheath acceleration analytical modeling, comparative study and developments”. In: *Review of Scientific Instruments* 83.2, 02B502. DOI: 10.1063/1.3666188.

Perego, C., A. Zani, D. Batani, and M. Passoni (Oct. 2011). “Extensive comparison among Target Normal Sheath Acceleration theoretical models”. In: *Nuclear Instruments and Methods in Physics Research Section A: Accelerators, Spectrometers, Detectors and Associated Equipment* 653.1, pp. 89–93. DOI: 10.1016/j.nima.2011.01.100.

Pianosi, F. and T. Wagener (May 2015). “A simple and efficient method for global sensitivity analysis based on cumulative distribution functions”. In: *Environmental Modelling & Software* 67, pp. 1–11. DOI: 10.1016/j.envsoft.2015.01.004.

Piel, A. (2017). *Plasma physics: an introduction to laboratory, space, and fusion plasmas*. Springer.

Prencipe, I., J. Fuchs, S. Pascarelli, D. W. Schumacher, R. B. Stephens, N. B. Alexander, R. Briggs, M. Büscher, M. O. Cernaianu, A. Choukourov, M. D. Marco, A. Erbe, J. Fassbender, G. Fiquet, P. Fitzsimmons, C. Gheorghiu, J. Hund, L. G. Huang, M. Harmand, N. J. Hartley, A. Irman, T. Kluge, Z. Konopkova, S. Kraft, D. Kraus, V. Leca, D. Margarone, J. Metzkes, K. Nagai, W. Nazarov, P. Lutoslawski, D. Papp, M. Passoni, A. Pelka, J. P. Perin, J. Schulz, M. Smid, C. Spindloe, S. Steinke, R. Torchio, C. Vass, T. Wiste, R. Zaffino, K. Zeil, T. Tschentscher, U. Schramm, and T. E. Cowan (2017). “Targets for high repetition rate laser facilities: needs, challenges and perspectives”. In: *High Power Laser Science and Engineering* 5. DOI: 10.1017/hpl.2017.18.

Pukhov, A. and S. Gordienko (Jan. 2006). “Bubble regime of wake field acceleration: similarity theory and optimal scalings”. In: *Philosophical Transactions of the Royal Society A: Mathematical, Physical and Engineering Sciences* 364.1840, pp. 623–633. DOI: 10.1098/rsta.2005.1727.

Quesnel, B. and P. Mora (Sept. 1998). “Theory and simulation of the interaction of ultraintense laser pulses with electrons in vacuum”. In: *Physical Review E* 58.3, pp. 3719–3732. DOI: 10.1103/physreve.58.3719.

Ridgers, C. P., C. S. Brady, R. Duclous, J. G. Kirk, K. Bennett, T. D. Arber, A. P. L. Robinson, and A. R. Bell (Apr. 2012). “Dense Electron-Positron Plasmas and Ultraintense γ rays from Laser-Irradiated Solids”. In: *Physical Review Letters* 108.16. DOI: 10.1103/physrevlett.108.165006.

Romagnani, L., J. Fuchs, M. Borghesi, P. Antici, P. Audebert, F. Ceccherini, T. Cowan, T. Grismayer, S. Kar, A. Macchi, P. Mora, G. Pretzler, A. Schiavi, T. Toncian, and O. Willi (Oct. 2005). “Dynamics of Electric Fields Driving the Laser Acceleration of Multi-MeV Protons”. In: *Physical Review Letters* 95.19. DOI: 10.1103/physrevlett.95.195001.

Roth, M., D. Jung, K. Falk, N. Guler, O. Deppert, M. Devlin, A. Favalli, J. Fernandez, D. Gautier, M. Geissel, R. Haight, C. E. Hamilton, B. M. Hegelich, R. P. Johnson, F. Merrill, G. Schaumann, K. Schoenberg, M. Schollmeier, T. Shimada, T. Taddeucci, J. L. Tybo, F. Wagner, S. A. Wender, C. H. Wilde, and G. A. Wurden (Jan. 2013). “Bright Laser-Driven Neutron Source Based on the Relativistic Transparency of Solids”. In: *Physical Review Letters* 110.4. DOI: 10.1103/physrevlett.110.044802.

Roth, M. and M. Schollmeier (2014). “Ion Acceleration—Target Normal Sheath Acceleration”. In: *Proceedings of the CAS-CERN Accelerator School: Plasma Wake Acceleration*.

– (2016a). “Ion Acceleration - Target Normal Sheath Acceleration”. In: *arXiv: Accelerator Physics*.

– (2016b). “Ion Acceleration—Target Normal Sheath Acceleration”. en. In: *CERN Yellow Reports*, Vol 1 (2016): Proceedings of the 2014 CAS–CERN Accelerator School: Plasma Wake Acceleration. DOI: 10.5170/CERN-2016-001.231.

Rücker, U., T. Cronert, J. Voigt, J. P. Dabruck, P. .-. Doege, J. Ulrich, R. Nabbi, Y. Beßler, M. Butzek, M. Büscher, C. Lange, M. Klaus, T. Gutberlet, and T. Brückel (Jan. 2016). “The Jülich high-brilliance neutron source project”. In: *The European Physical Journal Plus* 131.1. DOI: 10.1140/epjp/i2016-16019-5.

Ryutov, D. D. and B. A. Remington (Feb. 2006a). “Similarity laws for collisionless interaction of superstrong electromagnetic fields with a plasma”. In: *Plasma Physics and Controlled Fusion* 48.3, pp. L23–L31. DOI: 10.1088/0741-3335/48/3/l01.

– (Dec. 2006b). “Scaling Laws for Collisionless Lase-Plasma Interactions of Relevance to Laboratory Astrophysics”. In: *Astrophysics and Space Science* 307.1-3, pp. 291–296. DOI: 10.1007/s10509-006-9247-0.

Saltelli, A. (May 2002). “Making best use of model evaluations to compute sensitivity indices”. In: *Computer Physics Communications* 145.2, pp. 280–297. DOI: 10.1016/s0010-4655(02)00280-1.

Saltelli, A., P. Annoni, I. Azzini, F. Campolongo, M. Ratto, and S. Tarantola (Feb. 2010). “Variance based sensitivity analysis of model output. Design and estimator for the total sensitivity index”. In: *Computer Physics Communications* 181.2, pp. 259–270. DOI: 10.1016/j.cpc.2009.09.018.

Sato, T., Y. Iwamoto, S. Hashimoto, T. Ogawa, T. Furuta, S.-i. Abe, T. Kai, P.-E. Tsai, N. Matsuda, H. Iwase, N. Shigyo, L. Sihver, and K. Niita (Jan. 2018). “Features of Particle and Heavy Ion Transport code System (PHITS) version 3.02”. In: *Journal of Nuclear Science and Technology* 55.6, pp. 684–690. DOI: 10.1080/00223131.2017.1419890.

Sato, T., K. Niita, N. Matsuda, S. Hashimoto, Y. Iwamoto, S. Noda, T. Ogawa, H. Iwase, H. Nakashima, T. Fukahori, K. Okumura, T. Kai, S. Chiba, T. Furuta, and L. Sihver (Sept. 2013). “Particle and Heavy Ion Transport code System, PHITS, version 2.52”. In: *Journal of Nuclear Science and Technology* 50.9, pp. 913–923. DOI: 10.1080/00223131.2013.814553.

Savitzky, A. and M. J. E. Golay (1964). “Smoothing and Differentiation of Data by Simplified Least Squares Procedures.” In: *Analytical Chemistry* 36.8, pp. 1627–1639. DOI: 10.1021/ac60214a047. eprint: https://doi.org/10.1021/ac60214a047. URL: https://doi.org/10.1021/ac60214a047.

Schardt, D., T. Elsässer, and D. Schulz-Ertner (Feb. 2010). “Heavy-ion tumor therapy: Physical and radiobiological benefits”. In: *Reviews of Modern Physics* 82.1, pp. 383–425. DOI: 10.1103/revmodphys.82.383.

Schmickler, H. (2020). *CAS Proceedings of the 2019 course on High Gradient Wakefield Accelerators, Sesimbra, Portugal, 11–22 March 2019. CAS Proceedings of the 2019 course on High Gradient Wakefield Accelerators, Sesimbra, Portugal, 11–22 March 2019 (Draft version September 4, 2020)*. Tech. rep. Geneva: CERN. URL: https://cds.cern.ch/record/2729705.

Schmitz, B. and B. Endl (2022). *pythonbased RCF Evaluation Software*. en. DOI: 10.5281/ZENODO.6383868.

Schmitz, B., D. Kreuter, and O. Boine-Frankenheim (Apr. 2023). “Modeling of a Liquid Leaf Target TNSA Experiment using Particle-In-Cell Simulations and Deep Learning”. In: *Laser and Particle Beams* under review.under review. DOI: underreview.

Schmitz, B., M. Metternich, and O. Boine-Frankenheim (Sept. 2022). “Automated reconstruction of the initial distribution of laser accelerated ion beams from radiochromic film (RCF) stacks”. In: *Review of Scientific Instruments* 93.9, p. 093306. DOI: 10.1063/5.0094105.

Schollmeier, M., M. Geissel, A. B. Sefkow, and K. A. Flippo (Apr. 2014). “Improved spectral data unfolding for radiochromic film imaging spectroscopy of laser-accelerated proton beams”. In: *Review of Scientific Instruments* 85.4, p. 043305. DOI: 10.1063/1.4870895.

Schollmeier, M. S. (Jan. 2009). “Optimization and control of laser-accelerated proton beams”. en. PhD thesis. Darmstadt: Technische Universität. URL: http://tuprints.ulb.tu-darmstadt.de/1232/.

Schramm, U., M. Bussmann, A. Irman, M. Siebold, K. Zeil, D. Albach, C. Bernert, S. Bock, F. Brack, J. Branco, J. Couperus, T. Cowan, A. Debus, C. Eisenmann, M. Garten, R. Gebhardt, S. Grams, U. Helbig, A. Huebl, T. Kluge, A. Köhler, J. Krämer, S. Kraft, F. Kroll, M. Kuntzsch, U. Lehnert, M. Loeser, J. Metzkes, P. Michel, L. Obst, R. Pausch, M. Rehwald, R. Sauerbrey, H. Schlenvoigt, K. Steiniger, and O. Zarini (July 2017). “First results with the novel petawatt laser acceleration facility in Dresden”. In: *Journal of Physics: Conference Series* 874, p. 012028. DOI: 10.1088/1742-6596/874/1/012028.

Schreiber, A. (2012). “RGB-Farbkalibrierung von radiochromatischen Filmen”. In: *B.Sc. Thesis at TU Darmstadt*.

Schreiber, J., F. Bell, F. Grüner, U. Schramm, M. Geissler, M. Schnürer, S. Ter-Avetisyan, B. M. Hegelich, J. Cobble, E. Brambrink, J. Fuchs, P. Audebert, and D. Habs (July 2006). “Analytical Model for Ion Acceleration by High-Intensity Laser Pulses”. In: *Physical Review Letters* 97.4, p. 045005. DOI: 10.1103/physrevlett.97.045005.

Shibata, K., O. Iwamoto, T. Nakagawa, N. Iwamoto, A. Ichihara, S. Kunieda, S. Chiba, K. Furutaka, N. Otuka, T. Ohsawa, T. Murata, H. Matsunobu, A. Zukeran, S. Kamada, and J.-i. Katakura (Jan. 2011). “JENDL-4.0:

A New Library for Nuclear Science and Engineering". In: *Journal of Nuclear Science and Technology* 48.1, pp. 1–30. DOI: 10.1080/18811248.2011.9711675.

Shull, C. G. and E. O. Wollan (July 1948). "X-Ray, Electron, and Neutron Diffraction". In: *Science* 108.2795, pp. 69–75. DOI: 10.1126/science.108.2795.69.

Sigrist, M. W. (Mar. 9, 2013). *Laser*. Teubner Studienbücher Physik. Vieweg+Teubner Verlag. 414 pp. ISBN: 9783322938756. URL: https://www.ebook.de/de/product/34417520/markus_werner_sigrist_laser.html.

Sinigardi, S., J. Babaei, and G. Turchetti (Nov. 2018). "TNSA proton maximum energy laws for 2D and 3D PIC simulations". In: *Nuclear Instruments and Methods in Physics Research Section A: Accelerators, Spectrometers, Detectors and Associated Equipment* 909, pp. 438–440. DOI: 10.1016/j.nima.2018.01.057.

Snavely, R. A., M. H. Key, S. P. Hatchett, T. E. Cowan, M. Roth, T. W. Phillips, M. A. Stoyer, E. A. Henry, T. C. Sangster, M. S. Singh, S. C. Wilks, A. MacKinnon, A. Offenberger, D. M. Pennington, K. Yasuike, A. B. Langdon, B. F. Lasinski, J. Johnson, M. D. Perry, and E. M. Campbell (Oct. 2000). "Intense High-Energy Proton Beams from Petawatt-Laser Irradiation of Solids". In: *Physical Review Letters* 85.14, pp. 2945–2948. DOI: 10.1103/physrevlett.85.2945.

Soares, C. G. (2009). "Radiochromic Film". In: *AAPM Summer School on Cllinical Dosimetry Measurements in Radiotherapy*. URL: https://www.aapm.org/meetings/09SS/documents/23Soares-RadiochromicFilm.pdf.

Sobol', I. (Feb. 2001). "Global sensitivity indices for nonlinear mathematical models and their Monte Carlo estimates". In: *Mathematics and Computers in Simulation* 55.1-3, pp. 271–280. DOI: 10.1016/s0378-4754(00)00270-6.

Spears, B. K., J. Brase, P.-T. Bremer, B. Chen, J. Field, J. Gaffney, M. Kruse, S. Langer, K. Lewis, R. Nora, J. L. Peterson, J. J. Thiagarajan, B. V. Essen, and K. Humbird (Aug. 2018). "Deep learning: A guide for practitioners in the physical sciences". In: *Physics of Plasmas* 25.8, p. 080901. DOI: 10.1063/1.5020791.

Sprangle, P., E. Esarey, J. Krall, and A. Ting (Feb. 1996). "Vacuum laser acceleration". In: *Optics Communications* 124.1-2, pp. 69–73. DOI: 10.1016/0030-4018(95)00618-4.

Strickland, D. and G. Mourou (Oct. 1985). "Compression of amplified chirped optical pulses". In: *Optics Communications* 55.6, pp. 447–449. DOI: 10.1016/0030-4018(85)90151-8.

Thulliez, Loïc, Letourneau, Alain, Schwindling, Jérôme, Chauvin, Nicolas, Sellami, Nadia, Ott, Frédéric, Menelle, Alain, and Annighöfer, Burkhard (2020). "First steps toward the development of SONATE, a Compact Accelerator driven Neutron Source". In: *EPJ Web Conf.* 239, p. 17011. DOI: 10.1051/epjconf/202023917011.

Torrisi, L. (June 2015). "Ion acceleration from intense laser-generated plasma: methods, diagnostics and possible applications". In: *Nukleonika* 60.2, pp. 207–212. DOI: 10.1515/nuka-2015-0051.

VEGA, C. P. L. S. (Oct. 2022). *https://www.clpu.es/en/VEGA_Introduction*. URL: https://www.clpu.es/en/VEGA_Introduction.

Virtanen, P., R. Gommers, T. E. Oliphant, M. Haberland, T. Reddy, D. Cournapeau, E. Burovski, P. Peterson, W. Weckesser, J. Bright, S. J. van der Walt, M. Brett, J. Wilson, K. J. Millman, N. Mayorov, A. R. J. Nelson, E. Jones, R. Kern, E. Larson, C. J. Carey, İ. Polat, Y. Feng, E. W. Moore, J. VanderPlas, D. Laxalde, J. Perktold, R. Cimrman, I. Henriksen, E. A. Quintero, C. R. Harris, A. M. Archibald, A. H. Ribeiro, F. Pedregosa, P. van Mulbregt, and SciPy 1.0 Contributors (2020). "SciPy 1.0: Fundamental Algorithms for Scientific Computing in Python". In: *Nature Methods* 17, pp. 261–272. DOI: 10.1038/s41592-019-0686-2.

Vyskočil, J., E. Gelfer, and O. Klimo (May 2020). "Inverse Compton scattering from solid targets irradiated by ultra-short laser pulses in the $10^{22} - -10^{23}$ W/cm^2 regime". In: *Plasma Physics and Controlled Fusion* 62.6, p. 064002. DOI: 10.1088/1361-6587/ab83cb.

Wagner, F., S. Bedacht, V. Bagnoud, O. Deppert, S. Geschwind, R. Jaeger, A. Ortner, A. Tebartz, B. Zielbauer, D. H. H. Hoffmann, and M. Roth (June 2015). "Simultaneous observation of angularly separated laser-

driven proton beams accelerated via two different mechanisms". In: *Physics of Plasmas* 22.6, p. 063110. DOI: 10.1063/1.4922661.

Wagner, F., O. Deppert, C. Brabetz, P. Fiala, A. Kleinschmidt, P. Poth, V. Schanz, A. Tebartz, B. Zielbauer, M. Roth, T. Stöhlker, and V. Bagnoud (May 2016). "Maximum Proton Energy above 85 MeV from the Relativistic Interaction of Laser Pulses with Micrometer ThickCH2Targets". In: *Physical Review Letters* 116.20. DOI: 10.1103/physrevlett.116.205002.

Wang, M. and W. Deng (2018). "Deep visual domain adaptation: A survey". In: *Neurocomputing* 312, pp. 135–153.

Wang, X.-B., G.-Y. Hu, Z.-M. Zhang, Y.-Q. Gu, B. Zhao, Y. Zuo, and J. Zheng (2020). "Gamma-ray generation from ultraintense laser-irradiated solid targets with preplasma". In: *High Power Laser Science and Engineering* 8. DOI: 10.1017/hpl.2020.30.

Wilks, S. C., W. L. Kruer, M. Tabak, and A. B. Langdon (Aug. 1992). "Absorption of ultra-intense laser pulses". In: *Physical Review Letters* 69.9, pp. 1383–1386. DOI: 10.1103/physrevlett.69.1383.

Yang, J. M., P. McKenna, K. W. D. Ledingham, T. McCanny, L. Robson, S. Shimizu, R. P. Singhal, M. S. Wei, K. Krushelnick, R. J. Clarke, D. Neely, and P. A. Norreys (Dec. 2004). "Neutron production by fast protons from ultraintense laser-plasma interactions". In: *Journal of Applied Physics* 96.11, pp. 6912–6918. DOI: 10.1063/1.1814421.

Zeil, K., S. D. Kraft, S. Bock, M. Bussmann, T. E. Cowan, T. Kluge, J. Metzkes, T. Richter, R. Sauerbrey, and U. Schramm (Apr. 2010). "The scaling of proton energies in ultrashort pulse laser plasma acceleration". In: *New Journal of Physics* 12.4, p. 045015. DOI: 10.1088/1367-2630/12/4/045015.

Zhang, J. X. and K. Hoshino (2018). *Molecular sensors and nanodevices: principles, designs and applications in biomedical engineering*. Academic Press.

Ziegler, J. F. (1988). *Ion Implantation Science and Technology*. 2. Sub. Academic Press. ISBN: 9780127806211.

Ziegler, J. F., M. Ziegler, and J. Biersack (June 2010). "SRIM - The stopping and range of ions in matter (2010)". In: *Nuclear Instruments and Methods in Physics Research Section B: Beam Interactions with Materials and Atoms* 268.11-12, pp. 1818–1823. DOI: 10.1016/j.nimb.2010.02.091.

Zimmer, M., S. Scheuren, T. Ebert, G. Schaumann, B. Schmitz, J. Hornung, V. Bagnoud, C. Rödel, and M. Roth (Oct. 2021). "Analysis of laser-proton acceleration experiments for development of empirical scaling laws". In: *Physical Review E* 104.4, p. 045210. DOI: 10.1103/physreve.104.045210.

Zimmer, M. (July 2020). "Laser-Driven Neutron Sources - A Compact Approach to Non-Destructive Material Analysis". PhD thesis. Darmstadt: Technische Universität Darmstadt. DOI: https://doi.org/10.25534/tuprints-00012996. URL: http://tuprints.ulb.tu-darmstadt.de/12996/.

List of Figures

List of Tables

Danksagung

Diese Arbeit wurde durch das HMWK über den LOEWE Schwerpunkt – Nukleare Photonik ermöglicht, der es mir erlaubte die letzten 4 Jahre intensiv an der lasergestützten Ionenbeschleunigung zu arbeiten. Die Modelle die das finale Resultat dieser Thesis sind waren ohne die zusätzliche Unterstützung durch die Graduate School for Computational Engineering als Teil des Centre for Computational Engineering, durch die Verwendung des Virgo HPC Clusters an der GSI im Rahmen von FAIR Phase-0, und die exzellente Infrastruktur am TEMF nicht möglich gewesen. Ich danke meinem Doktorvater Oliver Boine-Frankenheim, ohne den ich dieses Thema niemals bearbeitet hätte, für die vielen Freiräume bei dessen Bearbeitung. Ebenso danke ich Markus Roth für die Diskussionen und die Unterstützung bei meiner experimentellen Kampagne.

Durch Diskussionen, Kaffee und das eine oder andere Bier haben mich meine Kollegen, sowohl am TEMF als auch am IKP begleitet und bestärkt. Ich konnte vieles lernen und mich weiterentwickeln. Sowohl das Feld der Plasmaphysik als auch der Neutronenerzeugung waren zu Beginn Neuland für mich ohne meine Kollegen wäre das wohl auch so geblieben. Ich danke Ion Gabriel Ion, Dimitrios Loukrezis, Jonas Christ, Daria Astapovych, Luisa Riik, Felix Wolf, Yun Ouedraogo, Laura D'Angelo, Thilo Egenolf, Stefan Scheuren, Moritz von Tresckow, Armin Galetzka, Maximilian Meier, Maxim Singer und allen anderen mit denen ich im Laufe der letzten 4 Jahre intensive Diskussionen führen konnte.

Ich danke auch den Studis deren Abschlussarbeiten ich mit betreuen durfte, nämlich Robin Dexheimer-Reuter, Barbara Endl und Daniel Kreuter. Jede einzelner dieser Arbeiten hat mir neue fachliche Sichtweisen auf das Feld geliefert und auch meine Fähigkeiten für die Anleitung von Arbeiten verbessert.

Trotz der Corona Pandemie und deren Auswirkungen, welche ich voll zu spüren bekommen habe, konnte ich diese Arbeit weiter bearbeiten und abschließen. Ohne die viele Unterstützung im Privaten hätte das aber, auch ohne Corona, wohl nicht geklappt. Daher danke ich meiner Familie, meinen Freunden und meinen Kommilitonen. Danke, dass ihr mich bis zum Ende unterstützt habt. Ein besonderer Dank gilt meiner Freundin Mara. Sie half mir bei allen Problemen weiter und unterstützte mich wo sie nur konnte. Mara, ich liebe dich und danke dir für alles.

Zuletzt möchte ich auch noch meiner Fechtgruppe danken, die mir den nötigen sportlichen Ausgleich ermöglicht hatte ohne den ich das wohl auch nicht hätte zu Ende bringen können.

Vermutlich habe ich trotz der vielen namentlichen Erwähnungen Menschen vergessen, das tut mir Leid. Unter Garantie wird mir nach Druck und Einreichen der Arbeit jeder einzelne einfallen, aber das ist leider zu spät. Auch euch danke ich von ganzem Herzen für die Unterstützung in den letzten vier Jahren.